Investigation of the Mechanical Properties of the *Helicobacter pylori* Cell Envelope and Maintenance of Helical Shape by Asymmetric Peptidoglycan Synthesis

Jennifer Taylor

A dissertation

submitted in partial fulfillment of the

requirements for the degree of

Doctor of Philosophy

University of Washington

2020

Reading Committee:

Nina Salama, Chair

Caroline Harwood

E. Peter Greenberg

Program Authorized to Offer Degree:

Microbiology

University of Washington

Abstract

Investigation of the Mechanical Properties of the *Helicobacter pylori* Cell Envelope and Maintenance of Helical Shape by Asymmetric Peptidoglycan Synthesis

Jennifer Taylor

Chair of the Supervisory Committee:
Professor Nina Salama
Microbiology, University of Washington

The human stomach pathogen *Helicobacter pylori* is a helically-shaped Gram-negative bacterium. While many individual protein contributors to helical shape have been identified and partially characterized, little is known about how these proteins work in concert to achieve helical shape. The structure of the peptidoglycan (PG) cell wall is responsible for *H. pylori*'s cell shape, and many of the cell shape determining proteins modify or interact with the cell wall, yet how these modifications shape the cell wall is not understood.

We demonstrated that cell wall growth is patterned asymmetrically in helical cells, with enhanced synthesis at both the minor and major helical axis areas. We showed that the actin-like cytoskeletal protein MreB has a localization preference for negative Gaussian curvature and that the bactofilin CcmA preferentially localizes to the range of positive Gaussian curvature

corresponding to the major helical axis. We demonstrate that in Δ*ccmA* cells, which are gently curved, PG synthesis is still enhanced at negative Gaussian curvature, but there is a dramatic reduction in PG synthesis levels at positive Gaussian curvature. We therefore posit that CcmA-driven enhanced PG synthesis rates at the major helical axis help enable curvature maintenance in the presence of MreB-promoted PG synthesis and that this asymmetric synthesis is one mechanism by which *H. pylori* maintains helical shape.

During these studies we observed that while similar, there are notable differences between PG synthesis labeling patterns with the metabolic probes *N*-acetylmuramic acid-alkyne (MurNAc-alk) and D-alanine-alkyne (D-Ala-alk). MurNAc-alk is thought to be incorporated through the cytoplasmic steps of the PG biosynthetic pathway, whereas D-Ala-alk is likely incorporated through transpeptidase activity, and thus reports on sites of active crosslinking. Therefore, we performed osmotic and detergent shocks on wild-type and shape mutant *H. pylori* cells to determine if there is structural heterogeneity in the cell envelope. We observed that, unlike in other rod-like bacteria studied to date, wild-type *H. pylori* length and width changes in response to turgor pressure modulation via osmotic shock are inversely related, with cells becoming longer and narrower after hyper-osmotic shock and shorter and wider after hypo-osmotic shock. In response to hyper-osmotic shock, the major axis appears to be rigid, with changes in width largely achieved by displacement of the minor helical axis. Detergent treatment with SDS revealed that cells transition through a number of changes before finally shrinking substantially in both length and width, indicating that multiple components of the cell envelope contribute to force homeostasis and that the PG cell wall itself is approximately isotropic with no apparent subcellular heterogeneity.

TABLE OF CONTENTS

LIST OF FIGURES

LIST OF TABLES

ACKNOWLEDGEMENTS

I would like to first thank my thesis advisor, Nina Salama, for her support throughout this journey. I deeply appreciate the time and effort she has put into shaping my scientific development. Nina taught me how to intentionally foster collaboration, how to clearly present my work, and how to embrace the unique challenges and rewards of studying a fastidious organism. I am incredibly grateful for all of the past and present members of the Salama Lab, who have encouraged me through the tough times, celebrated with me for victories large and small, have been an amazing sounding board, and have helped to cultivate my ability to do science. Words alone cannot express how much you mean to me. I am grateful for my committee members Carrie Harwood, Pete Greenberg, Paul Wiggins, and Colin Manoil for their support through this process, and particularly for Carrie and Pete for serving on my reading committee. Thank you to all of the administrative staff, especially Amy Gundlach, who has always been cheering me on, and Pam Lindberg who has helped everything in the lab run smoothly and has also helped expand my culinary horizons. I am so grateful to Luna Yu, who not only has helped solve any technical issue I have encountered with the sunniest disposition, but has also helped rescue my laptop from disaster multiple times. I am deeply thankful for everyone in Shared Resources, without whom this project would not have succeeded.

I am profoundly indebted to all my collaborators. Going through a particularly challenging review process was far less daunting with the support of extraordinary scientists who have also become my friends. A tremendous thank you goes to Ben Bratton, who gave so generously of his time not only to adapt software for image analysis and build new code to answer critical questions for our eLife publication, but also spent countless hours patiently teaching me about

quantitative image analysis and bacterial physiology. Ben has been a champion for this project and has been an incredible role model. I am so grateful to Josh Shaevitz, who committed support to making our image analysis goals a reality and who never wavered in that support. Thank you to Catherine Grimes, who has been dedicated to getting the MurNAc-alk probes working for us and has been committed to supporting my personal scientific success. I also am so thankful for Kristen DeMeester, who has been both a fabulous colleague and friend. I am indebted to Erkin Kuru, who happily shared his D-alanine probes and his exuberance for bacterial cell biology. Thank you to Waldemar Vollmer and Jacob Biboy, who warmly welcomed me in Newcastle and taught me how to purify sacculi. I am so grateful to KC Huang, who graciously hosted me at Stanford during my first major SIM imaging session and has continued to foster my scientific growth. I am so appreciative of Zach Pincus, who helped me assess ideas for 3D image analysis goals and who has been so generous with his time adapting the Celltool program for the osmotic shock work and so prompt with his help. Thank you to Bob Turner and Simon Foster for performing AFM on our purified sacculi and for helping us interpret the results.

I could not have made it this far without the phenomenal community I have had cheering me on. I could justifiably spend pages thanking each of you. I am so thankful for all of the roommates I have had in Seattle, who have been on the front lines for all the ups and downs. Thank you to the many of you who have given me a ride to lab, despite the hour. For this dissertation, I want to particularly thank Dan Buffington and Caitlin Lynch for providing retreat spaces for me to write without an abundance of distractions, and Ryan Wilkerson for staying by my side and supporting me while I have been finishing my PhD.

I cannot thank my family enough. My parents have walked with me every day of this journey, have listened with unending patience, and have never stopped believing in me. I am so

grateful for my brother Mike and my sister-in-law Shelly for their love and for Daniel, Emily, Julia, and Lucy for the best hugs and for reminding me to find joy everywhere. I am incredibly thankful for all of my extended family, particularly my grandparents and for my cousins Julia and Leslie, who have been cheering me on through it all.

DEDICATION

For my parents, John and Pam Taylor.

You have sacrificed so much so that I could flourish.

Chapter 1. INTRODUCTION

1.1 PREFACE

"Nothing is in the intellect that was not first in the senses."

- Thomas Aquinas

This chapter is based on a manuscript published in the Annual Review of Microbiology 2019 73:1, 457-480 DOI: 10.1146/annurev-micro-020518-115919

1.2 DIVERSITY OF HELICAL SHAPES

C. crescentus, *V. cholerae*, *H. pylori*, and *C. jejuni* are all helical rod-shaped organisms (Figure 1.1); single *H. pylori* and *C. jejuni* cells are clearly helical, but the helical shape of *V. cholerae* and *C. crescentus* becomes clear once cells are filamented (Ausmees *et al.*, 2003, Bartlett *et al.*, 2017, Cooper, 2001, Wortinger *et al.*, 1998). Individual *V. cholerae* and *C. crescentus* cells appear to be curved cells because the pitch of the helix is greater than the average cell length, thus multiple cells are required to achieve one full helical turn (Figure 1.2). Cell shape is ultimately determined by the structure of the peptidoglycan (PG) cell wall (sacculus), as purified sacculi retain the shape of the original cell. Therefore, all of the proteins involved in cell shape discussed below are expected to either directly or indirectly influence cell wall structure.

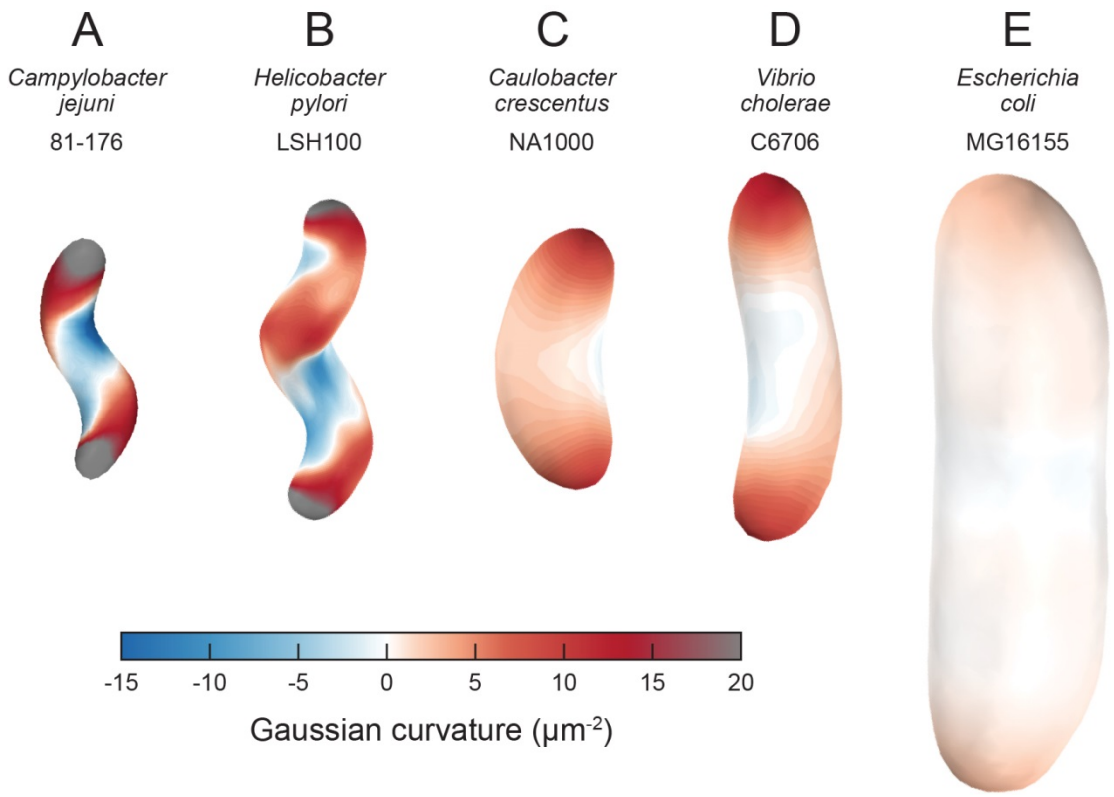

Figure 1.1. Sidewall Gaussian curvature for Gram-negative model organisms used to study cell shape.

Computational surface reconstructions of cells with Gaussian curvature plotted. Helical cells (A and B) show a substantially larger range of Gaussian curvature than curved cells (C and D) or straight rod (E) cells. All images are properly scaled to represent their true relative sizes.

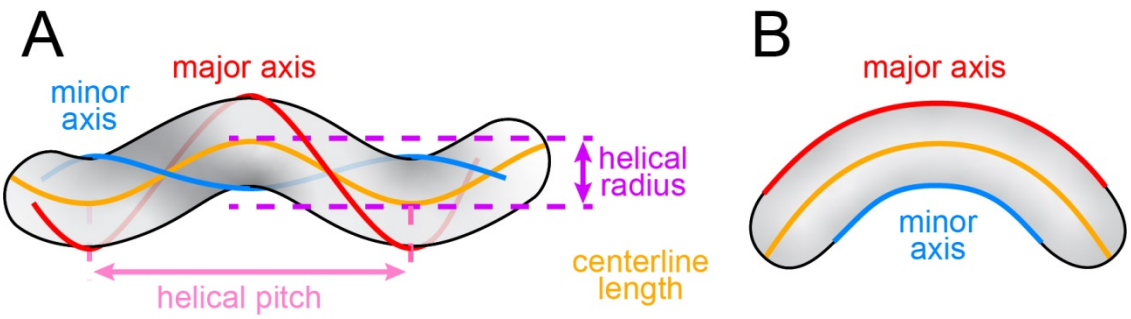

Figure 1.2. Diagram of pertinent shape parameters.

(A) Diagram of a helical cell with major (red) and minor (blue) axes, helical radius (purple), helical pitch (pink), and centerline length (gold) defined. (B) Diagram of a curved cell, with major (red) and minor (blue) axes defined as well as centerline length (gold).

Helical rod shape is a composite of two features: rod shape plus helicity (curvature and twist). *C. crescentus*, *V. cholerae*, *C. jejuni*, and *H. pylori* all encode the actin-like cytoskeletal protein MreB, which promotes straight-rod shape by directing sites of new PG incorporation (Shi *et al.*, 2018). In *C. crescentus* and *V. cholerae*, there is catastrophic loss of shape characterized by cell widening after treatment with A22, which disrupts MreB, even though curvature-determining genes are still present. It has been reported that MreB is not essential in *H. pylori* (Waidner *et al.*, 2009, Taylor *et al.*, 2020), but depletion of MreC or the elongation specific PBP2 similarly results in cell widening (El Ghachi *et al.*, 2011). While generating rod-like shape is an essential component of proper shape maintenance in these organisms, there is a fundamental opposition between the requirements for maintaining rod shape (minimizing sidewall curvature) and also maintaining a helical body (maintaining sidewall curvature).

Despite all being helical, these cells face different requirements for achieving their morphology. Both the pitch and helical diameter of the cell centerline play a substantial role in determining the distribution of surface curvature required for a given helical shape. Organisms like *V. cholerae* and *C. crescentus* that have a large pitch (stretched-out helix) only need to achieve moderate changes in surface curvature as compared to a straight rod (Figure 1.1). Organisms like *H. pylori* and *C. jejuni* with a smaller pitch (compressed helix) must achieve much more extreme curvatures and have reached a solution different from that of *V. cholerae* and *C. crescentus* to maintain their characteristic helical shapes. Here, we focus on the mechanisms allowing these bacteria to specialize their rod-like shapes by maintaining the

curvature features necessary for helicity. Major themes include cytoskeletal proteins with a curvature localization preference, PG synthesis patterning, and PG remodeling.

1.3 *V. CHOLERAE* CURVATURE DEPENDS ON THE PERISKELETAL FILAMENT CRVA

Curvature maintenance has been studied the least in the Gammaproteobacterium *V. cholerae*. A manuscript published during my thesis work provides a starting point for the field by identifying CrvA, a protein essential for driving curvature (Bartlett *et al.*, 2017). CrvA was identified by a visual screen of a transposon insertion library; loss of CrvA causes cells to become straight rods. The protein is characterized by two coiled-coil domains, a PEGA-like C-terminal domain, and a periplasmic localization sequence. Purified recombinant CrvA forms filaments in vitro, and deletion of the second coiled-coil domain prevents filament formation. In vivo, CrvA-GFP forms a cell-spanning filament in the periplasm that localizes to the minor axis. Localization and filament formation in vivo depends on the periplasmic signal sequence, potentially suggesting that polymerization depends on a factor present within the periplasm. When cells are grown in high-osmolality medium, CrvA localizes diffusely rather than as a filament and cells become straight. As these cells recover in LB, CrvA filaments form first and then cells curve around them, indicating that CrvA generates curvature. Despite its PEGA-like domain, which is associated with carboxypeptidase activity in eukaryotes, CrvA does not alter the global peptidoglycan composition.

Rather than directly altering PG, CrvA appears to bias synthesis rates. To study PG synthesis and turnover, cells were metabolically labeled with fluorescent derivatives of D-alanine, which can be incorporated into growing cell wall (Kuru *et al.*, 2012). Cells were labeled first with the blue fluorescent D-alanine HADA and then chased with the green fluorescent D-alanine NADA. Labeling revealed that the cells grow diffusely along the cell wall but not at the

poles. Taking advantage of the fact that centerlines of individual cells are essentially two-dimensional and that because of their curvature, cells tend to lie on their sides, the authors could define the major and minor axes. With these features defined, they then performed 2D analysis of PG synthesis and turnover, which they termed QuASAR. *V. cholerae* becomes more curved as cell density increases, a property which appears to be in response to regulation of CrvA. In cells with increasing curvature, they found equal cell wall turnover rates on both axes, but an increased rate of growth on the major axis compared to the minor axis. In cells maintaining curvature, both the rates of turnover and synthesis remained equal.

Whether and how other mechanisms contribute to *V. cholerae* curvature remains to be seen. Interestingly, a second PEGA domain-containing protein, VCA1077, is present in the same operon as CrvA and may also contribute to *V. cholerae* curvature. Additionally, deletion of the low molecular weight (LMW) penicillin binding protein (PBP) DacA-1 results in extra cell curvature in addition to an increase in width and length in LB (Möll *et al.*, 2015). Morphology perturbations were dependent on the presence of salt in the growth medium. DacA-1 appears to be the major pentapeptide carboxypeptidase. Global peptidoglycan analysis revealed that the Δ*dacA-1* mutant had a 50% increase in glycan strand length in addition to an 8-fold increase in pentapeptides, suggesting that the accumulation of pentapeptide muropeptides may inhibit lytic transglycosylase activity. Future studies will be necessary to establish how and to what degree PG turnover contributes to shape maintenance.

1.4 *C. CRESCENTUS* CURVATURE DEPENDS ON THE INTERMEDIATE FILAMENT-LIKE CYTOSKELETAL FILAMENT CRES

The Alphaproteobacterium *C. crescentus* forms left-handed helical cells in contrast to the right-handed helical cell bodies of *V. cholerae*, *C. jejuni*, and *H. pylori*, suggesting some divergence in

the strategy *C. crescentus* uses to achieve its shape (Ausmees *et al.*, 2003, Cabeen *et al.*, 2009). Curvature of the cell body is driven by the intermediate filament (IF)-like protein Crescentin (CreS). Crescentin is a coiled-coil rich protein that forms left-handed helices. The structure of CreS is generically similar to that of eukaryotic IF proteins; it contains a head domain, coiled-coil rod domain with interspersed linkers, and a tail domain (Ausmees *et al.*, 2003, Cabeen *et al.*, 2011). Filament formation, localization, and tethering to the membrane are all requirements for proper curvature generation, as demonstrated by the defects in CreS localization and *C. crescentus* cell shape resulting from deleting various CreS domains (Cabeen *et al.*, 2011).

In wild-type cells growing without perturbation, CreS forms a long filament that appears to be contiguous, spans the length of the sidewall on the minor axis, and is not mobile (Ausmees *et al.*, 2003, Charbon *et al.*, 2009). The protein is quite stable, undergoing slow turnover of subunits and subunit turnover appears to be distributed equally along the length of the cell, indicating that it does not undergo treadmilling (Charbon *et al.*, 2009, Esue *et al.*, 2010). CreS can be detached from the membrane by perturbing the structural integrity of the cell wall with mecillinam or A22 treatment. Investigation of a number of A22-resistant *C. crescentus* mutants revealed that amino acid substitutions clustered on the back face of MreB disrupt localization of CreS (Dye *et al.*, 2011). These results suggest that MreB and potentially other proteins related to PG synthesis may be required directly and/or indirectly for proper CreS localization. When CreS is not anchored to the membrane, it becomes motile and relaxes. The detached, relaxed CreS filament condenses to a very obviously helical filament that has a smaller pitch than the membrane-anchored filament, indicating that the anchored filament is under strain. CreS filaments appear to be anchored along their whole length, since CreS detachment as a result of perturbations occurs gradually and processively (Cabeen *et al.*, 2009).

Similarly to CrvA, it appears that CreS generates curvature by influencing PG synthesis patterning (Figure 1.3 B). Unlike *V. cholerae* and the other organisms discussed in this review, *C. crescentus* undergoes an asymmetric growth pattern (Terrana & Newton, 1975). A motile swarmer cell is generated by division of an elongated, stalked progenitor. The swarmer cell then elongates via diffuse, MreB-patterned PG insertion. Once it begins to differentiate into a stalked cell, elongation switches to a midcell insertion mode that is dependent on both MreB and FtsZ (Aaron *et al.*, 2007, Figge *et al.*, 2004). While the curvature-based distribution of the diffuse MreB-directed PG synthesis has yet to be analyzed, midcell elongation PG is inserted in a wedge-like pattern such that more PG synthesis occurs at the major axis of the cell compared to the minor axis (Cabeen *et al.*, 2009). This growth pattern depends on CreS, as midcell elongation occurs as a straight, symmetrical band in a Δ*creS* strain. The proposed model is that the CreS filament exerts a mechanical force on the minor axis, locally restricting PG insertion and enhancing relative synthesis rates on the opposite face (the major axis). This is consistent with the results of computational modeling (Kim & Sun, 2009). Furthermore, ectopic expression of CreS in *E. coli* is sufficient to curve the cells, suggesting that the CreS-dependent mechanism of curvature generation is simple and depends on well-conserved cellular machinery (Cabeen *et al.*, 2009).

Numerous curvature-defective mutants have been described in *C. crescentus*, but almost all of these have been attributed to a downstream effect on CreS. Deletion of *wbqL*, which functions in lipopolysaccharide (LPS) biogenesis, results in the accumulation of altered O-polysaccharide species, shedding of the S-layer, and straight cell morphology (Cabeen *et al.*, 2010). Aberrant O-polysaccharides, but neither loss of O-polysaccharides nor of the S-layer, prevents CreS tethering to the membrane, thus explaining loss of curvature. Another modulator of curvature linked to

CreS is the essential protein CTP synthase (CtpS) (Ingerson-Mahar *et al.*, 2010). CtpS forms long filaments on the minor axis colocalized with CreS. Overproduction of CtpS diminishes cell curvature while CtpS depletion yields hyper-curved cells (Ingerson-Mahar *et al.*, 2010). The ability of CtpS to influence shape depends on its ability to form filaments but not catalytic activity. Curvature modulation was dependent on CreS; overproduction of CtpS causes CreS to localize as a single focus within the cell, while depletion of *ctpS* is unable to curve cells in a Δ*creS* background.

There remain a few examples of *C. crescentus* cell curvature perturbations that remain unexplored and/or unexplained. Overexpression of the essential tyrosine phosphatase homolog CtpA results in straight cells, but depletion of CtpA causes cells to filament and form outer membrane blebs without any apparent curvature alteration (Shapland *et al.*, 2011). The authors show using widefield fluorescence microscopy that CreS is still able to form cell-spanning, immobile tethered filaments when CtpA is overexpressed, but it is unclear if a more subtle filamentation or localization defect occurs. Super-resolution microscopy paired with one of the recently-described compatible CreS tags, photoswitchable eYFP (Biteen *et al.*, 2008, Lew *et al.*, 2011) or dL5 paired with Malachite Green (Saurabh *et al.*, 2016), would be a powerful tool to assay CreS for proper filament formation and localization.

Interestingly, perturbation of central metabolism also appears to be able to perturb cell curvature. Deletion of the master regulator Hfq in *C. crescentus* causes a substantial growth defect, fosfomycin hypersensitivity, and a striking increase of width and length (Irnov *et al.*, 2017). Although not noted by the authors, Δ*hfq* cells in the published phase contrast images also appear to be less curved. Hfq deletion appears to perturb cell shape by altering PG biosynthesis; the TCA cycle intermediate α-ketoglutarate (KG) accumulates due to insufficient CoA levels,

and accumulation of KG interferes with an upstream step of mDAP synthesis. mDAP is the third-position amino acid in the PG peptide stem. Supplementation with the mDAP precursor DAP restores cell length and width. However, the published phase contrast image shows that supplemented cells are largely straight and may also be narrower and shorter than wild-type. DAP supplementation failed to restore wild-type growth rate, but supplementation with pantothenate, an intermediate upstream of CoA synthesis, restored length, width, curvature, growth rate, and fosfomycin sensitivity. Thus some other Hfq-mediated effect seems to influence curvature. Imaging CreS to check filament formation and localization could be helpful in deciphering this effect.

Another possible contributor to curvature is the M23 family protein DipM. DipM has four LysM domains, which are essential for its proper localization in vivo and ability to bind purified sacculi in vitro, and a C-terminal LytM domain, which has substitutions at two of the three predicted catalytic residues and indicates that it does not have hydrolytic activity (Goley *et al.*, 2010, Möll *et al.*, 2010, Poggio *et al.*, 2010). DipM-depleted or Δ*dipM* cells are wider than wild-type and are filamented, with branches sometimes seen extending from the main cell body. Although not explicitly stated in the corresponding publications, the cell filaments formed by loss of DipM appear to have notable curvature heterogeneity, with some regions appearing completely straight and other regions appearing highly-curved (Goley *et al.*, 2010, Meier *et al.*, 2016, Möll *et al.*, 2010, Poggio *et al.*, 2010, Zielinska *et al.*, 2017). The curvature disruption and heterogeneity is reminiscent of the morphology of *H. pylori* cells with one of their three M23-family proteins deleted (see next section). DipM localizes to the middle of the cell in early division in an FtsZ-dependent (Goley *et al.*, 2010, Möll *et al.*, 2010, Poggio *et al.*, 2010), MreB-independent (Goley *et al.*, 2010, Poggio *et al.*, 2010) manner. PG thickening was observed in

Δ*dipM* or DipM-depleted sacculi (Goley *et al.*, 2010, Möll *et al.*, 2010, Poggio *et al.*, 2010), and an m-Cherry fusion to DipM with the LytM domain truncated can localizes to foci along the length of the filamented cell. This patchy localization pattern is dependent on FtsZ (Poggio *et al.*, 2010) and suggests that DipM may have a role in remodeling FtsZ-patterned cell wall synthesis. Analysis of PG synthesis patterning, PG turnover, global muropeptide composition, and CreS functionality in Δ*dipM* and DipM-depleted cells will help clarify the mechanisms behind the curvature heterogeneity.

1.5 *H. PYLORI* AND *C. JEJUNI* EMPLOY A MULTIFACTORIAL SHAPE SYSTEM

The right-handed helical Epsilonproteobacteria *H. pylori* and *C. jejuni* employ a more complicated and enigmatic strategy for shape determination than *V. cholerae* and *C. crescentus*, both in terms of the number of components involved and the underlying mechanisms. As shown in (Figure 1.1), there are substantial differences in the helical parameters and, as a result, the cell surface curvatures of these organisms, which might necessitate more substantial modification of the PG. Furthermore, there is considerable strain variation in morphology of both wild-type and cell shape mutants. This was demonstrated quantitatively by 2D curvature analysis using Celltool (Lacayo *et al.*, 2007, Sycuro *et al.*, 2010), which uses principle component analysis or defined parameters to compare the shape features of cell silhouettes derived from micrographs.

H. pylori uses a suite of PG-modifying enzymes (Csd1, Csd3/HdpA, Csd4, Csd6, Slt), several cytoskeletal proteins (CcmA, Ccrp58, Ccrp59, Ccrp1142, and Ccrp1143), and three putative scaffolding proteins (Csd2, Csd5, Csd7) for maintaining helical shape (Figure 1.3 C-D) (Bonis *et al.*, 2010, Specht *et al.*, 2011, Sycuro *et al.*, 2010, Sycuro *et al.*, 2013, Sycuro *et al.*, 2012, Waidner *et al.*, 2009, Yang *et al.*, 2019). *H. pylori* has been reported to require four coiled-coil rich cytoskeletal proteins (Ccrps) (Specht *et al.*, 2011, Waidner *et al.*, 2009) as well as a

member of the bactofilin class of cytoskeletal elements, CcmA (Sycuro *et al.*, 2010) for maintaining helical shape. There has been a conflicting report on the non-redundant essentiality of the Ccrps for morphology in a different strain background (Yang *et al.*, 2019), which may suggest that these proteins play a more-redundant role in other *H. pylori* strains.

The outstanding question about the mechanism(s) of helical shape maintenance in *H. pylori* is how the various cell shape-determining proteins play into generating the pronounced cell surface curvature and twist. Two of the PG-modifying enzymes are endopeptidases: Csd1 and Csd3/HdpA (Bonis *et al.*, 2010, Sycuro *et al.*, 2010). Another protein required for cell shape is Csd2, a homolog of Csd1 that has an inactive catalytic site, which interacts with and is essential for Csd1 stability (An *et al.*, 2016, Yang *et al.*, 2019). Deletion of *csd1* or *csd2* results in curved-rod cells (pitch increased to greater than the cell length), while deletion of *csd3* results in a pleomorphic population in LSH100 (a derivative of strain G27 (Baltrus *et al.*, 2009, Lowenthal *et al.*, 2009, Sycuro *et al.*, 2010)) and branched cells in the N6 strain (Bonis *et al.*, 2010). Both proteins break tetra-pentapeptide crosslinks, and Csd3 appears to also exhibit weak carboxypeptidase activity on pentapeptides. Endopeptidase activity is required for the insertion of new cell wall material into the existing peptidoglycan network, thus Csd1 and Csd3 may help enhance local cell wall growth.

How the carboxypeptidases Csd6 and Csd4, as well as the soluble lytic transpeptidase Slt contribute to helical morphology is far more perplexing. Csd6 trims tetrapeptides to tripeptides and Csd4 trims tripeptides to dipeptides (Sycuro *et al.*, 2013, Sycuro *et al.*, 2012). Loss of either protein results in straight rod morphology. Deletion of *slt* results in curved-rod cells that have an increase in tripeptides (Chaput *et al.*, 2007, Yang *et al.*, 2019), potentially linking Slt to Csd4. Csd4 and Csd6 may contribute to helical shape maintenance by spatially regulating the

generation of dipeptides. Once mDAP at the third position of the peptide stem has been removed, peptides are no longer able to participate in crosslinking, which may influence the structure of the PG and/or synthesis locally.

Fewer proteins necessary for helical cell shape have been elucidated in the closely-related *C. jejuni*, which is also a right-handed helix, but is smaller than *H. pylori* in both length and width (Figure 1.2). Pgp1 (peptidoglycan peptidase 1) and Pgp2 are required for helical cell shape; loss of either protein results in straight-rod cells (Frirdich *et al.*, 2012, Frirdich *et al.*, 2014). Pgp1 and Pgp2 are homologous to *H. pylori*'s Csd4 and Csd6, respectively. Global muropeptide analysis and in vitro studies confirmed that like Csd6 and Csd4, Pgp2 and Pgp1 are carboxypeptidases and that Pgp2 trim tetrapeptides to tripeptides and Pgp1 trims tripeptides to dipeptides. *C. jejuni* has also been reported to have homologues of CcmA (CJJ81176_1104), Csd1 (CJJ81176_1105), and Csd3 (CJJ81176_1228), but biochemical validation is still forthcoming (Esson *et al.*, 2017, Frirdich *et al.*, 2017, Stahl *et al.*, 2016). Loss of CJJ81176_1104 has been reported to alter cell curvature (Frirdich *et al.*, 2017), and loss of CJJ81176_1105 or CJJ81176_1228 has been shown visually to yield cells with an increased pitch, which means the cells have a decrease in the magnitude of their sidewall curvature (Esson *et al.*, 2017, Stahl *et al.*, 2016). The phenotype for Δ*CJJ81176_1105* is reminiscent of the morphology of the corresponding Δ*csd1* mutant in *H. pylori* (Esson *et al.*, 2017, Sycuro *et al.*, 2010). However, the phenotype of Δ*CJJ81176_1228* more resembles that of Δ*csd1* rather than of Δ*csd3*, which is pleomorphic or branched in *H. pylori*, depending on the parent strain (Bonis *et al.*, 2010, Esson *et al.*, 2017, Stahl *et al.*, 2016, Sycuro *et al.*, 2010).

Finally, in addition to achieving helical cell shape, *H. pylori* and *C. jejuni* can modulate their helical parameters. In *H. pylori*, helical radius is increased by deletion of *mviN* (Sycuro *et*

al., 2013) or *mltD* (our unpublished observations and also not noted but visible in the published SEM (Chaput *et al.*, 2007)) and possibly a decrease in pitch. In *C. jejuni*, deletion of the *O*-acetylpeptidodoglycan esterase Ape1, which causes a significant increase in *O*-acetylation of peptidoglycan and increases glycan chain length, increases helical radius (Ha *et al.*, 2016). In contrast, deletion of the hypothetical protein HPG27_1093 yields cells with a substantial decrease in both helical radius and pitch (Yang *et al.*, 2019).

1.6 CONCLUSIONS

Substantial progress has been made in identifying proteins that contribute to helical cell shape, their activities, and some of the corresponding mechanisms involved in shape homeostasis. However, many questions remain, particularly for *H. pylori*. While the predicted bactofilin CcmA and the intermediate filament-like Ccrps have been reported to be required for proper helical shape in *H. pylori*, it is unclear if one or more of these forms a cell-spanning filament similar to CreS in *C. crescentus* and CrvA in *V. cholerae*. Furthermore, it is unknown if spatially-biased PG synthesis and/or subcellular variation in cell wall mechanical properties contribute to helical shape maintenance. To address these knowledge gaps, I investigated cell wall growth patterning (Chapter 2); the localization, polymerization extent, and functional requirements of candidate cell spanning cytoskeletal elements (Chapters 2 and 3); and the subcellular asymmetry of cell envelope structural features (Chapter 3). These studies have yielded new insights that allow us to present a more complete model of *H. pylori* helical cell shape maintenance and set the stage for future investigation (Chapter 4).

1.7 BIBLIOGRAPHY

Aaron, M., Charbon, G., Lam, H., Schwarz, H., Vollmer, W., and Jacobs-Wagner, C. (2007) The tubulin homologue FtsZ contributes to cell elongation by guiding cell wall precursor synthesis in *Caulobacter crescentus*. *Mol Microbiol* **64**: 938-952.

An, D.R., Im, H.N., Jang, J.Y., Kim, H.S., Kim, J., Yoon, H.J., Hesek, D., Lee, M., Mobashery, S., Kim, S.J., and Suh, S.W. (2016) Structural Basis of the Heterodimer Formation between Cell Shape-Determining Proteins Csd1 and Csd2 from *Helicobacter pylori*. *PLoS One* **11**: e0164243.

Ausmees, N., Kühn, J.R., and Jacobs-Wagner, C. (2003) The Bacterial Cytoskeleton: An Intermediate Filament-Like Function in Cell Shape. *Cell* **115**: 705-713.

Baltrus, D.A., Amieva, M.R., Covacci, A., Lowe, T.M., Merrell, D.S., Ottemann, K.M., Stein, M., Salama, N.R., and Guillemin, K. (2009) The complete genome sequence of *Helicobacter pylori* strain G27. *J Bacteriol* **191**: 447-448.

Bartlett, T.M., Bratton, B.P., Duvshani, A., Miguel, A., Sheng, Y., Martin, N.R., Nguyen, J.P., Persat, A., Desmarais, S.M., VanNieuwenhze, M.S., Huang, K.C., Zhu, J., Shaevitz, J.W., and Gitai, Z. (2017) A Periplasmic Polymer Curves *Vibrio cholerae* and Promotes Pathogenesis. *Cell* **168**: 172-185 e115.

Biteen, J.S., Thompson, M.A., Tselentis, N.K., Bowman, G.R., Shapiro, L., and Moerner, W.E. (2008) Super-resolution imaging in live *Caulobacter crescentus* cells using photoswitchable EYFP. *Nat Methods* **5**: 947-949.

Bonis, M., Ecobichon, C., Guadagnini, S., Prevost, M.C., and Boneca, I.G. (2010) A M23B family metallopeptidase of *Helicobacter pylori* required for cell shape, pole formation and virulence. *Mol Microbiol* **78**: 809-819.

Cabeen, M.T., Charbon, G., Vollmer, W., Born, P., Ausmees, N., Weibel, D.B., and Jacobs-Wagner, C. (2009) Bacterial cell curvature through mechanical control of cell growth. *EMBO J* **28**: 1208-1219.

Cabeen, M.T., Herrmann, H., and Jacobs-Wagner, C. (2011) The domain organization of the bacterial intermediate filament-like protein crescentin is important for assembly and function. *Cytoskeleton (Hoboken)* **68**: 205-219.

Cabeen, M.T., Murolo, M.A., Briegel, A., Bui, N.K., Vollmer, W., Ausmees, N., Jensen, G.J., and Jacobs-Wagner, C. (2010) Mutations in the Lipopolysaccharide biosynthesis pathway interfere with crescentin-mediated cell curvature in *Caulobacter crescentus*. *J Bacteriol* **192**: 3368-3378.

Chaput, C., Labigne, A., and Boneca, I.G. (2007) Characterization of *Helicobacter pylori* lytic transglycosylases Slt and MltD. *J Bacteriol* **189**: 422-429.

Charbon, G., Cabeen, M.T., and Jacobs-Wagner, C. (2009) Bacterial intermediate filaments: *in vivo* assembly, organization, and dynamics of crescentin. *Genes Dev* **23**: 1131-1144.

Cooper, S. (2001) Helical growth and the curved shape of *Vibrio cholerae*. *FEMS Microbiology Letters* **198**: 123-124.

Dye, N.A., Pincus, Z., Fisher, I.C., Shapiro, L., and Theriot, J.A. (2011) Mutations in the nucleotide binding pocket of MreB can alter cell curvature and polar morphology in *Caulobacter*. *Mol Microbiol* **81**: 368-394.

El Ghachi, M., Mattei, P.J., Ecobichon, C., Martins, A., Hoos, S., Schmitt, C., Colland, F., Ebel, C., Prevost, M.C., Gabel, F., England, P., Dessen, A., and Boneca, I.G. (2011) Characterization of the elongasome core PBP2 : MreC complex of *Helicobacter pylori*. *Mol Microbiol* **82**: 68-86.

Esson, D., Gupta, S., Bailey, D., Wigley, P., Wedley, A., Mather, A.E., Meric, G., Mastroeni, P., Sheppard, S.K., Thomson, N.R., Parkhill, J., Maskell, D.J., Christie, G., and Grant, A.J. (2017) Identification and initial characterisation of a protein involved in *Campylobacter jejuni* cell shape. *Microb Pathog* **104**: 202-211.

Esue, O., Rupprecht, L., Sun, S.X., and Wirtz, D. (2010) Dynamics of the bacterial intermediate filament crescentin *in vitro* and *in vivo*. *PLoS One* **5**: e8855.

Figge, R.M., Divakaruni, A.V., and Gober, J.W. (2004) MreB, the cell shape-determining bacterial actin homologue, co-ordinates cell wall morphogenesis in *Caulobacter crescentus*. *Molecular Microbiology* **51**: 1321-1332.

Frirdich, E., Biboy, J., Adams, C., Lee, J., Ellermeier, J., Gielda, L.D., Dirita, V.J., Girardin, S.E., Vollmer, W., and Gaynor, E.C. (2012) Peptidoglycan-modifying enzyme Pgp1 is required for helical cell shape and pathogenicity traits in *Campylobacter jejuni*. *PLoS Pathog* **8**: e1002602.

Frirdich, E., Biboy, J., Huynh, S., Parker, C.T., Vollmer, W., and Gaynor, E.C. (2017) Morphology heterogeneity within a *Campylobacter jejuni* helical population: the use of calcofluor white to generate rod-shaped *C. jejuni* 81-176 clones and the genetic determinants responsible for differences in morphology within 11168 strains. *Mol Microbiol* **104**: 948-971.

Frirdich, E., Vermeulen, J., Biboy, J., Soares, F., Taveirne, M.E., Johnson, J.G., DiRita, V.J., Girardin, S.E., Vollmer, W., and Gaynor, E.C. (2014) Peptidoglycan LD-carboxypeptidase Pgp2 influences *Campylobacter jejuni* helical cell shape and pathogenic properties and provides the substrate for the DL-carboxypeptidase Pgp1. *J Biol Chem* **289**: 8007-8018.

Goley, E.D., Comolli, L.R., Fero, K.E., Downing, K.H., and Shapiro, L. (2010) DipM links peptidoglycan remodelling to outer membrane organization in *Caulobacter*. *Mol Microbiol* **77**: 56-73.

Ha, R., Frirdich, E., Sychantha, D., Biboy, J., Taveirne, M.E., Johnson, J.G., DiRita, V.J., Vollmer, W., Clarke, A.J., and Gaynor, E.C. (2016) Accumulation of Peptidoglycan *O*-Acetylation Leads to Altered Cell Wall Biochemistry and Negatively Impacts Pathogenesis Factors of *Campylobacter jejuni*. *J Biol Chem* **291**: 22686-22702.

Ingerson-Mahar, M., Briegel, A., Werner, J.N., Jensen, G.J., and Gitai, Z. (2010) The metabolic enzyme CTP synthase forms cytoskeletal filaments. *Nat Cell Biol* **12**: 739-746.

Irnov, I., Wang, Z., Jannetty, N.D., Bustamante, J.A., Rhee, K.Y., and Jacobs-Wagner, C. (2017) Crosstalk between the tricarboxylic acid cycle and peptidoglycan synthesis in *Caulobacter crescentus* through the homeostatic control of alpha-ketoglutarate. *PLoS Genet* **13**: e1006978.

Kim, J.S., and Sun, S.X. (2009) Morphology of *Caulobacter crescentus* and the Mechanical Role of Crescentin. *Biophys J* **96**: L47-49.

Kuru, E., Hughes, H.V., Brown, P.J., Hall, E., Tekkam, S., Cava, F., de Pedro, M.A., Brun, Y.V., and VanNieuwenhze, M.S. (2012) *In situ* probing of newly synthesized peptidoglycan in live bacteria with fluorescent D-amino acids. *Angew Chem Int Ed Engl* **51**: 12519-12523.

Lacayo, C.I., Pincus, Z., VanDuijn, M.M., Wilson, C.A., Fletcher, D.A., Gertler, F.B., Mogilner, A., and Theriot, J.A. (2007) Emergence of large-scale cell morphology and movement from local actin filament growth dynamics. *PLoS Biol* **5**: e233.

Lew, M.D., Lee, S.F., Ptacin, J.L., Lee, M.K., Twieg, R.J., Shapiro, L., and Moerner, W.E. (2011) Three-dimensional superresolution colocalization of intracellular protein

superstructures and the cell surface in live *Caulobacter crescentus*. *Proc Natl Acad Sci U S A* **108**: E1102-1110.

Lowenthal, A.C., Hill, M., Sycuro, L.K., Mehmood, K., Salama, N.R., and Ottemann, K.M. (2009) Functional analysis of the *Helicobacter pylori* flagellar switch proteins. *J Bacteriol* **191**: 7147-7156.

Meier, E.L., Razavi, S., Inoue, T., and Goley, E.D. (2016) A novel membrane anchor for FtsZ is linked to cell wall hydrolysis in *Caulobacter crescentus*. *Mol Microbiol* **101**: 265-280.

Möll, A., Dörr, T., Alvarez, L., Davis, B.M., Cava, F., and Waldor, M.K. (2015) A D, D-carboxypeptidase is required for *Vibrio cholerae* halotolerance. *Environ Microbiol* **17**: 527-540.

Möll, A., Schlimpert, S., Briegel, A., Jensen, G.J., and Thanbichler, M. (2010) DipM, a new factor required for peptidoglycan remodelling during cell division in *Caulobacter crescentus*. *Mol Microbiol* **77**: 90-107.

Poggio, S., Takacs, C.N., Vollmer, W., and Jacobs-Wagner, C. (2010) A protein critical for cell constriction in the Gram-negative bacterium *Caulobacter crescentus* localizes at the division site through its peptidoglycan-binding LysM domains. *Mol Microbiol* **77**: 74-89.

Saurabh, S., Perez, A.M., Comerci, C.J., Shapiro, L., and Moerner, W.E. (2016) Super-resolution Imaging of Live Bacteria Cells Using a Genetically Directed, Highly Photostable Fluoromodule. *J Am Chem Soc* **138**: 10398-10401.

Shapland, E.B., Reisinger, S.J., Bajwa, A.K., and Ryan, K.R. (2011) An essential tyrosine phosphatase homolog regulates cell separation, outer membrane integrity, and morphology in *Caulobacter crescentus*. *J Bacteriol* **193**: 4361-4370.

Shi, H., Bratton, B.P., Gitai, Z., and Huang, K.C. (2018) How to Build a Bacterial Cell: MreB as the Foreman of *E. coli* Construction. *Cell* **172**: 1294-1305.

Specht, M., Schatzle, S., Graumann, P.L., and Waidner, B. (2011) *Helicobacter pylori* possesses four coiled-coil-rich proteins that form extended filamentous structures and control cell shape and motility. *J Bacteriol* **193**: 4523-4530.

Stahl, M., Frirdich, E., Vermeulen, J., Badayeva, Y., Li, X., Vallance, B.A., and Gaynor, E.C. (2016) The Helical Shape of *Campylobacter jejuni* Promotes *in vivo* Pathogenesis by Aiding Transit through Intestinal Mucus and Colonization of Crypts. *Infect Immun* **84**: 3399-3407.

Sycuro, L.K., Pincus, Z., Gutierrez, K.D., Biboy, J., Stern, C.A., Vollmer, W., and Salama, N.R. (2010) Peptidoglycan crosslinking relaxation promotes *Helicobacter pylori*'s helical shape and stomach colonization. *Cell* **141**: 822-833.

Sycuro, L.K., Rule, C.S., Petersen, T.W., Wyckoff, T.J., Sessler, T., Nagarkar, D.B., Khalid, F., Pincus, Z., Biboy, J., Vollmer, W., and Salama, N.R. (2013) Flow cytometry-based enrichment for cell shape mutants identifies multiple genes that influence *Helicobacter pylori* morphology. *Mol Microbiol* **90**: 869-883.

Sycuro, L.K., Wyckoff, T.J., Biboy, J., Born, P., Pincus, Z., Vollmer, W., and Salama, N.R. (2012) Multiple peptidoglycan modification networks modulate *Helicobacter pylori*'s cell shape, motility, and colonization potential. *PLoS Pathog* **8**: e1002603.

Taylor, J.A., Bratton, B.P., Sichel, S.R., Blair, K.M., Jacobs, H.M., DeMeester, K.E., Kuru, E., Gray, J., Biboy, J., VanNieuwenhze, M.S., Vollmer, W., Grimes, C.L., Shaevitz, J.W., and Salama, N.R. (2020) Distinct cytoskeletal proteins define zones of enhanced cell wall synthesis in *Helicobacter pylori*. *eLife* **9**.

Terrana, B., and Newton, A. (1975) Pattern of Unequal Cell Division and Development *Caulobacter crescentus*. *Developmental Biology* **44**: 380-385.

Waidner, B., Specht, M., Dempwolff, F., Haeberer, K., Schaetzle, S., Speth, V., Kist, M., and Graumann, P.L. (2009) A novel system of cytoskeletal elements in the human pathogen *Helicobacter pylori*. *PLoS Pathog* **5**: e1000669.

Wortinger, M.A., Quardokus, E.M., and Brun, Y.V. (1998) Morphological adaptation and inhibition of cell division during stationary phase in *Caulobacter crescentus*. *Molecular Microbiology* **29**.

Yang, D.C., Blair, K.M., Taylor, J.A., Petersen, T.W., Sessler, T., Tull, C.M., Leverich, C.K., Collar, A.L., Wyckoff, T.J., Biboy, J., Vollmer, W., and Salama, N.R. (2019) A Genome-Wide *Helicobacter pylori* Morphology Screen Uncovers a Membrane-Spanning Helical Cell Shape Complex. *J Bacteriol* **201**.

Zielinska, A., Billini, M., Möll, A., Kremer, K., Briegel, A., Izquierdo Martinez, A., Jensen, G.J., and Thanbichler, M. (2017) LytM factors affect the recruitment of autolysins to the cell division site in *Caulobacter crescentus*. *Mol Microbiol* **106**: 419-438.

Chapter 2. DISTINCT CYTOSKELETAL PROTEINS DEFINE ZONES OF ENHANCED CELL WALL SYNTHESIS IN *HELICOBACTER PYLORI*

2.1 PREFACE

This chapter is based on a manuscript published in eLife 2020; 9:e52482 DOI: 10.7554/eLife.52482

2.2 ABSTRACT

Helical cell shape is necessary for efficient stomach colonization by *Helicobacter pylori*, but the molecular mechanisms for generating helical shape remain unclear. The helical centerline pitch and radius of wild-type *H. pylori* cells dictate surface curvatures of considerably higher positive and negative Gaussian curvatures than those present in straight- or curved-rod *H. pylori*. Quantitative 3D microscopy analysis of short pulses with either *N*-acetylmuramic acid or D-alanine metabolic probes showed that cell wall growth is enhanced at both sidewall curvature extremes. Immunofluorescence revealed MreB is most abundant at negative Gaussian curvature, while the bactofilin CcmA is most abundant at positive Gaussian curvature. Strains expressing CcmA variants with altered polymerization properties lose helical shape and associated positive Gaussian curvatures. We thus propose a model where CcmA and MreB promote PG synthesis at positive and negative Gaussian curvatures, respectively, and that this patterning is one mechanism necessary for maintaining helical shape.

2.3 INTRODUCTION

Helicobacter pylori is a helical Gram-negative bacterium that colonizes the human stomach and can cause stomach ulcers and gastric cancers (Correa, 1988). Helical cell shape is necessary for efficient stomach colonization (Bonis *et al.*, 2010, Sycuro *et al.*, 2010, Sycuro *et al.*, 2012), underscoring its importance. *H. pylori* is a main model organism for studying helical cell shape, in part because it is a genetically tractable organism with a compact genome that minimizes redundancy (Tomb *et al.*, 1997). Key non-redundant, non-essential contributors to cell shape have been identified, but the question of how they enable *H. pylori* to be helical remains largely unsolved.

As is the case for most bacteria (Höltje, 1998), the structure of the *H. pylori* peptidoglycan (PG) cell wall (sacculus) is ultimately responsible for the shape of the cell; purified cell walls maintain helical shape (Sycuro *et al.*, 2010). PG is a polymer of alternating *N*-acetylglucosamine (GlcNAc) and *N*-acetylmuramic acid (MurNAc) with an attached peptide stem that can be crosslinked to a peptide stem of an adjacent PG strand. Crosslinked PG strands form the cell wall, a large mesh-like macromolecule that surrounds the cell and counteracts the cell's turgor pressure (Höltje, 1998, Typas *et al.*, 2012). The PG monomer is synthesized in the cytoplasm and subsequently flipped across the inner membrane and incorporated into the existing PG by the glycosyltransferase activities of penicillin binding proteins (PBPs) and shape, elongation, division and sporulation (SEDS) proteins and the transpeptidation activities of PBPs (Meeske *et al.*, 2016, Sauvage *et al.*, 2008).

Helical cell shape maintenance in *H. pylori* requires a suite of both PG-modifying enzymes (Csd1, Csd3/HdpA, Csd4, Csd6) to remodel the cell wall and non-enzymatic proteins (Csd2, Csd5, CcmA, and Csd7) that may act as scaffolds or play other structural roles (Bonis *et al.*,

2010, Sycuro *et al.*, 2013, Sycuro *et al.*, 2012, Sycuro *et al.*, 2010, Yang *et al.*, 2019). One of the non-enzymatic proteins is the putative bactofilin CcmA. Bactofilins are bacteria-specific cytoskeletal proteins with diverse functions, including playing a role in stalk elongation in *Caulobacter crescentus* (Kühn *et al.*, 2010) and helical pitch modulation in *Leptospira biflexa* (Jackson *et al.*, 2018). CcmA loss in *H. pylori* results in rod-shaped cells with minimal sidewall curvature (Sycuro *et al.*, 2010). As with other organisms, *H. pylori* CcmA has been shown to self-oligomerize (Holtrup *et al.*, 2019). Recently CcmA was shown to co-purify with Csd5 and the PG biosynthetic enzyme MurF (Blair *et al.*, 2018), suggesting CcmA may influence cell wall growth.

Patterning PG synthesis has been shown to be an important mechanism for cell shape maintenance in several model organisms. In the rod-shaped Escherichia coli, MreB helps direct synthesis preferentially to sites at or below zero Gaussian curvature. One working model is that this growth pattern promotes rod shape by accelerating growth at dents and restricting growth at bulges along the sidewall, thereby enforcing diameter control (Bratton *et al.*, 2018, Ursell *et al.*, 2014). In the Gram-positive *Bacillus subtilis*, MreB filaments have been shown to move in paths oriented approximately perpendicular to the long axis of rod shaped cells. The relative organization of path orientations decreases with an increase in rod diameter, suggesting that filament orientation is sensitive to changes in cell surface curvatures (Hussain *et al.*, 2018).

Here, we demonstrate that the surface of helical *H. pylori* cells is characterized by large regions of both positive and negative Gaussian curvature. To investigate how *H. pylori* achieves diameter control while simultaneously maintaining sidewall curvature, we employed two metabolic probes to investigate PG synthesis patterning in *H. pylori*. Using superresolution microscopy and 3D quantitative image analysis, we show that synthesis is enhanced at negative

Gaussian curvature as well as at a limited range of positive Gaussian curvatures. We furthermore investigate the localization of cytoskeletal proteins MreB and CcmA. We demonstrate that, as in straight-rod shaped *E. coli* cells, MreB is enriched at negative curvature. CcmA is enriched at the window of positive Gaussian curvatures where enhanced synthesis is observed. We propose that both MreB and CcmA help maintain PG synthesis activity locally and that PG synthesis patterning is one mechanism that plays a fundamental role in helical cell shape maintenance.

2.4 RESULTS

2.4.1 *Helical cells maintain areas of positive and negative Gaussian curvature on the sidewall*

Unlike straight rod-shaped bacteria, helical *H. pylori* cells maintain distinct and diverse cell surface curvatures along the sidewall (Figure 2.1 and 2.2). To characterize the cell surface curvature features of *H. pylori* in detail, we stained permeabilized cells with fluorescent wheat germ agglutinin (WGA), which binds GlcNAc and thus labels the cell wall. Since the dimensions of *H. pylori* cells (1.5-3.5 μm in length and 0.45 μm in diameter (Figure 2.3)) are near the limit of light microscopy resolution, we employed 3D structured illumination microscopy (SIM) to more clearly resolve cells in three dimensions (Figure 2.1 A). We adapted previous image processing software (Bartlett *et al.*, 2017, Morgenstein *et al.*, 2015) to accommodate characteristic SIM artifacts and enhanced resolution in order to generate a 3D triangular meshwork surface with roughly 30 nm precision from the SIM z-stack images (Figure 2.1 A and B, matched SIM image volumes and surface reconstructions). Display of the Gaussian curvature, which is the product of the two principal curvatures, at each point on the meshwork shows the distinct curvatures on opposite sides of helical cells (Figure 2.1 B). Using Gaussian curvature allows us to focus on local curvature geometry. We operationally define the minor helical axis as

the shortest helical path along the sidewall within the zone of moderate negative curvature (minor helical axis area, -15 to -5 μm^{-2}, blue), and define the major axis as the path opposite the minor helical axis, which resides within the zone of moderate positive curvature (major helical axis area, 5 to 15 μm^{-2}, red) (Figure 2.1 C). The cell poles are characterized by high positive curvature (>15 μm^{-2}, gray).

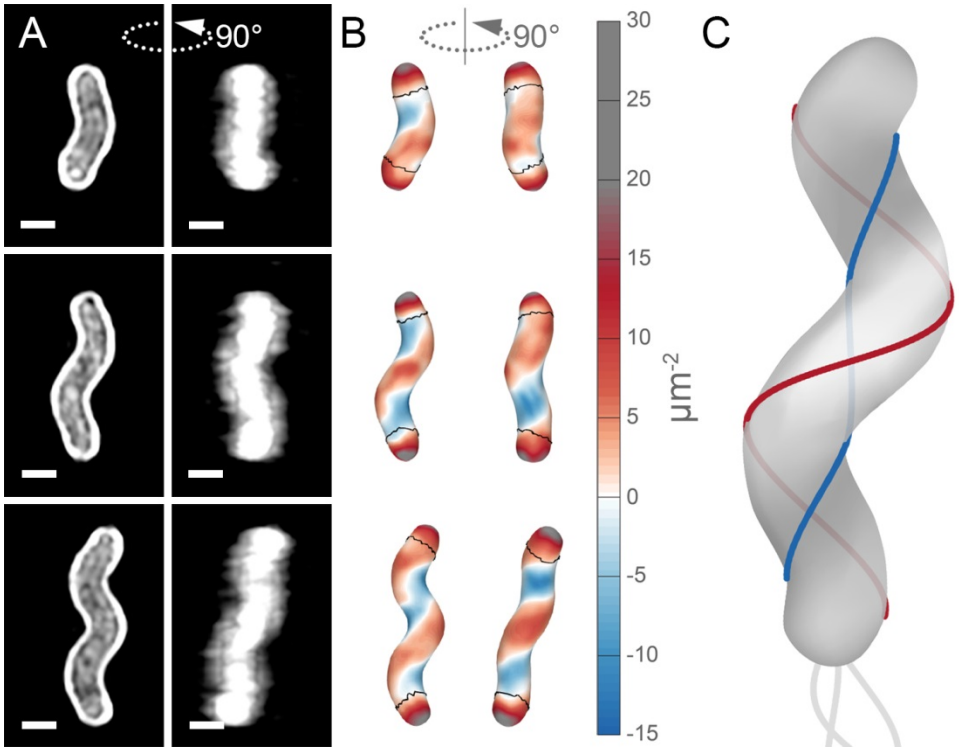

Figure 2.1. Helical cell surface feature areas of distinct curvatures.

(A) 3D SIM images of individual *H. pylori* cells stained with fluorescent wheat germ agglutinin (WGA). Top-down view (left) and 90-degree rotation about the long axis (right). Scale bar = 0.5 μm; images from one experiment. (B) Corresponding views of computational surface reconstructions of cells in A. with Gaussian curvature plotted (scale at right - blue: moderate negative; white: zero; red: moderate positive; gray: high positive). Computationally-defined polar regions are delineated by the thin black line. Polar regions correspond to regions whose centerline points are within 0.75 of a cell diameter to the terminal pole positions. (C) Schematic of minor (blue line) and major (red line) helical axes.

Our image reconstruction method performs faithful reconstructions of straight- and curved-rod cells (Figure 2.2, inset). To compare the surface curvatures maintained by helical (wild-type), curved-rod (Δ*csd2*), and straight-rod (Δ*csd6*) cells, we pooled reconstructions of hundreds of non-septating cells for each genotype and plotted a histogram of the proportion of surface curvature points with a given Gaussian curvature value (Figure 2.2). All three cell shapes share a tail of high positive curvatures from the cell poles (Figure 2.2 A, right of the dotted line). In order to study the sidewall alone, we developed an algorithm to computationally define and exclude poles (Figure 2.1 B, black lines). With the poles removed, the extended tail disappears for each cell shape. In contrast to the other shapes, helical cells have a large proportion of sidewall area with curvatures less than -5 μm^{-2} and an even larger proportion with curvatures greater than 5 μm^{-2} (Figure 2.2 B). Rather than having a unimodal distribution, helical cells have a multimodal distribution that includes an apparent peak at negative curvature and another at positive curvature.

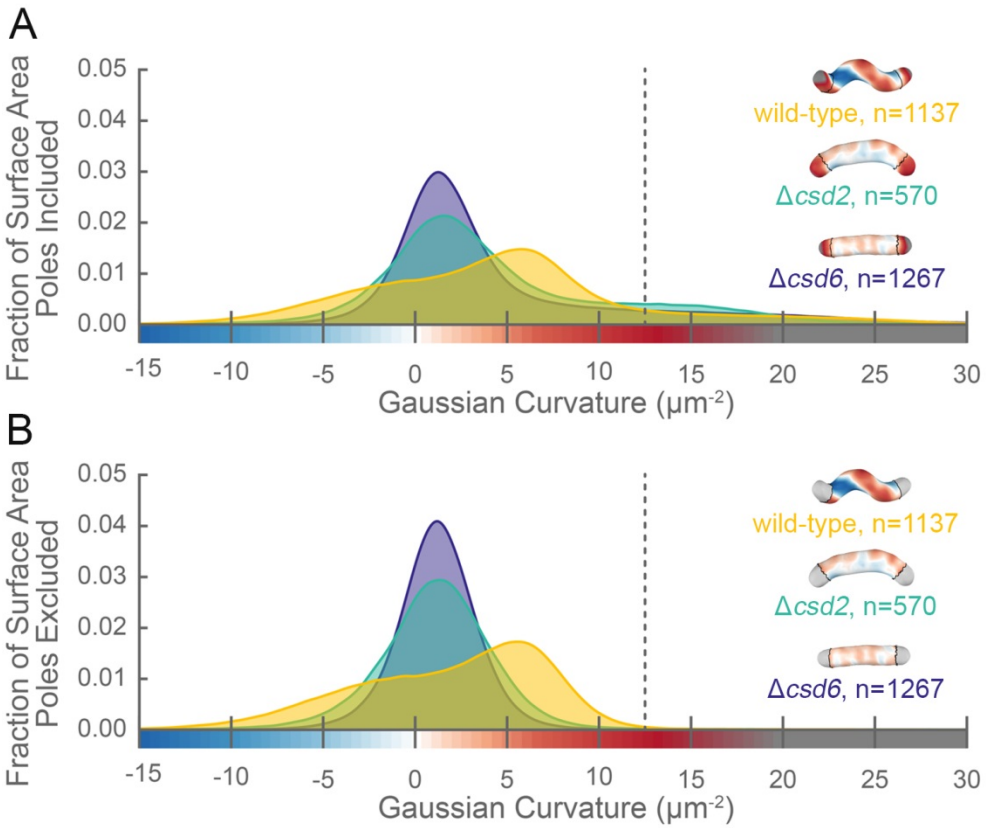

Figure 2.2. The distribution of surface Gaussian curvature for helical cells is distinct from that of curved- and straight-rod cells.

Smooth histograms of the distribution of surface Gaussian curvatures for a population of cells (wild-type helical, yellow; curved-rod Δ*csd2*, teal; straight-rod Δ*csd6*, indigo) with poles included (A) or sidewall only (B, poles excluded). The region to the right of the dotted vertical lines corresponds to curvatures contributed almost exclusively by the poles. Histograms are derived using a bin size of 0.2 μm^{-2}. Example computational surface reconstructions (top right of each histogram) of a wild-type helical, curved-rod Δ*csd2*, and straight-rod Δ*csd6* cell with Gaussian curvatures displayed as in Figure 2.1. The data represented are from one replicate.

The sidewall curvature distribution informed us about the overall types of surface curvature wild-type cells need to achieve, but was not sufficient to let us directly compare the surface properties of the major and minor axes, specifically the relative lengths of the major and minor axes and the average Gaussian curvature along both axes. Furthermore, prior shape parameter

characterizations of *H. pylori* have been performed using 2D images (Martinez *et al.*, 2016, Sycuro *et al.*, 2010, Sycuro *et al.*, 2012, Sycuro *et al.*, 2013, Yang *et al.*, 2019); measurement of pitch and helical radius from 2D images is subject to systematic errors for short cells (approximately <1.5 helical turns) depending on their orientation on the coverslip. Therefore, we also wished to determine *H. pylori* population shape parameters from our 3D dataset. To characterize the major and minor axes, we needed to find these axes on each reconstructed cell surface. While cells in our experiments appear helical, in reality they have surface imperfections and centerlines with kinks, bends, or variation in pitch along the centerline (Sycuro *et al.*, 2010). We therefore limited ourselves to considering the relative length of the major and minor helical axes of a population of simulated, idealized cells, each of which mimics a cell from the wild-type population described in Figure 2.2 (for full details see Appendix 1). In brief, to both derive the cell shape parameters necessary to generate the simulated cells and to further characterize the 3D shape parameters of the wild-type population, we measured the cell lengths from one pole to the other along the curved centerlines (Figure 2.3 A and C, gray); the diameters of the cells (Figure 2.3 A and D, purple); the helical pitches of the centerlines (Figure 2.3 A and E, pink); and the helical diameters of the centerlines (Figure 2.3 A and F, green).

Wild-type cells are 2.5 ± 0.5 μm long and 0.45 ± 0.02 μm in diameter, have a helical pitch of 1.7 ± 1 μm, and have a helical diameter of 0.3 ± 0.1 μm (mean ± standard deviation, Figure 2.3 C-F). These parameters are derived from a subset of the wild-type population that can be modeled as a uniform helix (Figure 2.4). The distribution of cell lengths, diameters, and surface curvatures of the subset closely match that of the whole population (Figure 2.4 C-E).

Using the simulated counterparts to these cells, we determined that the average major to minor length ratio is 1.69±0.16, meaning that the major axis is on average 70% longer than the

minor axis (Figure 2.3 G). We also determined from the simulated cells that the average Gaussian curvature at the major axis is 5±1 μm^{-2}, and the average Gaussian curvature at the minor axis is -11±4 μm^{-2} (Figure 2.3 H).

We next used our simulation framework to explore how the four helical-rod shape parameters affect the length ratio of the major to minor helical axes. Changes in cell length and cell diameter had almost no effect, whereas increasing the helical diameter or decreasing the helical pitch increased the relative length of the major axis (Figure 2.5, right column), consistent with the idea that a helix is formed by differential expansion of the major and minor axes. We then investigated how each of these parameters influences the distribution of surface curvatures along the sidewall. We began with a cell simulated from the population average of all four parameters (cell length, cell diameter, helical pitch, and helical diameter), and changed each property individually within the range of variation represented in the wild-type population (± 1.5 standard deviations) while holding the other three constant (Figure 2.5 and 2.6). Each of the dashed colored lines in Figure 2.3 C-F correspond to the parameters used to simulate these altered cell shapes. Changing cell length had a negligible impact on the distribution of surface curvatures along the sidewall (Figure 2.5 A). Decreasing the cell diameter had a relatively small effect given the narrow distribution of cell diameters observed in the wild-type population (Figure 2.5 B). Changing the two parameters describing the properties of the helix had a larger impact on the distribution of Gaussian curvatures. Decreasing the pitch resulted in a helix with tighter coils and a greater distance between the peak of negative and positive Gaussian surface curvatures (Figure 2.5 C). Increasing the helical diameter resulted in cells that looked less like straight-rod cells and had a greater distance between the peak of negative and positive Gaussian surface curvatures (Figure 2.5 D). In holding with the Gauss-Bonnet theorem, cells had a greater

proportion of sidewall area with positive Gaussian curvature than with negative, and the magnitude of the positive Gaussian curvature was less than that of the negative Gaussian curvature.

Having established the substantial difference in the length of the major and minor axes, we wondered if differential synthesis at these cellular landmarks might help explain helical shape maintenance. Although it is not currently possible to computationally define the helical axes on surface reconstructions of actual cells due to their imperfections, our data indicate that we can use Gaussian curvature of 5 μm^{-2} and -11 μm^{-2} as a proxy for the major and minor axes, respectively, in population level data.

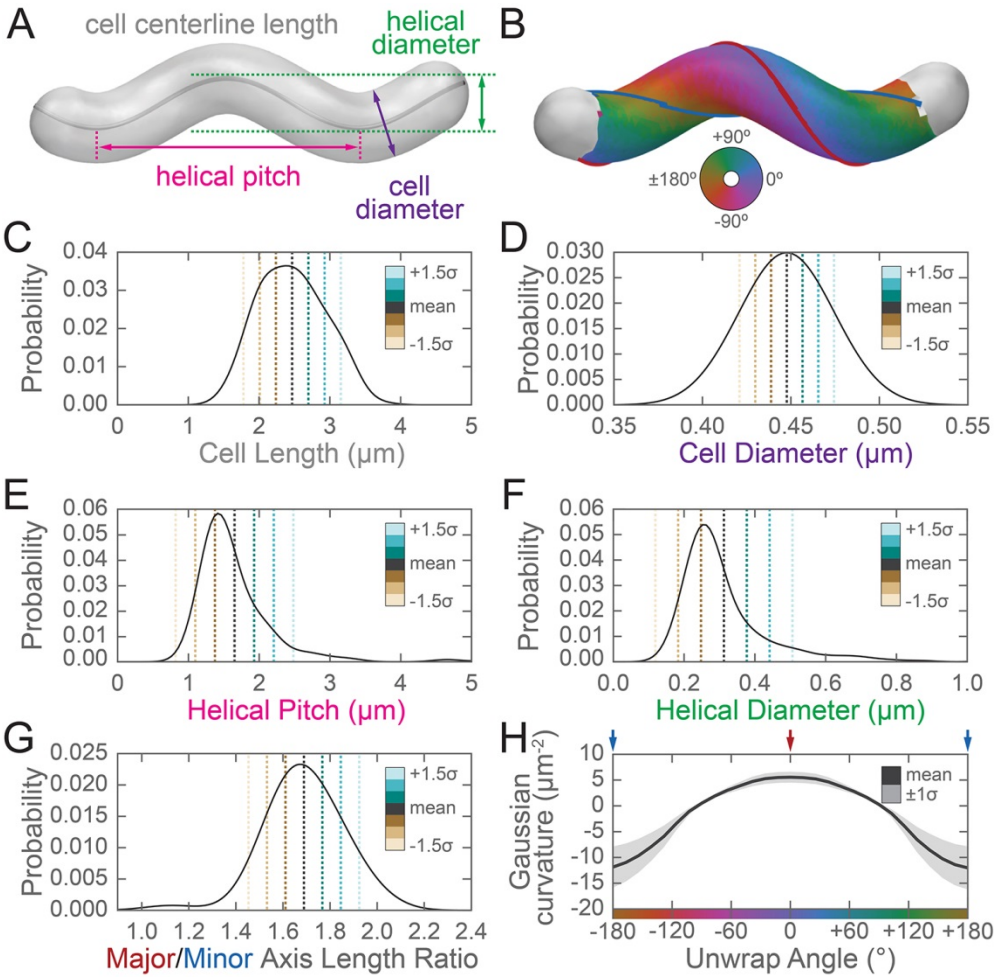

Figure 2.3. Three-dimensional shape properties of a wild-type helical population.

Analysis of the wild-type population in Figure 2.2 from the 231 wild-type cells for which the cell centerline was well-fit by a helix. (A) Schematic of helical-rod shape parameters (cell centerline length, gray; cell diameter, purple; helical pitch, pink; and helical diameter, green). (B) Example cell with helical coordinate system and the major (red line, 0°) and minor (blue line, 180°) helical axes shown on the cell sidewall. Population distributions of (C) cell centerline lengths, (D) average cell diameters, (E) helical pitch, (F) helical diameter, (G) major to minor axis length ratio, and (H) the average Gaussian curvature for a given helical coordinate system unwrap angle. Colored dotted lines in (C-G) indicate the mean ±1.5 standard deviations in 0.5 standard deviation steps. Shaded line in (H) indicates ±1 standard deviation about the mean. Distributions of parameters (C-D) are from real cells, parameters (E-F) are from helical centerline fits, and properties (G-H) are measured from the matched synthetic cell sidewalls.

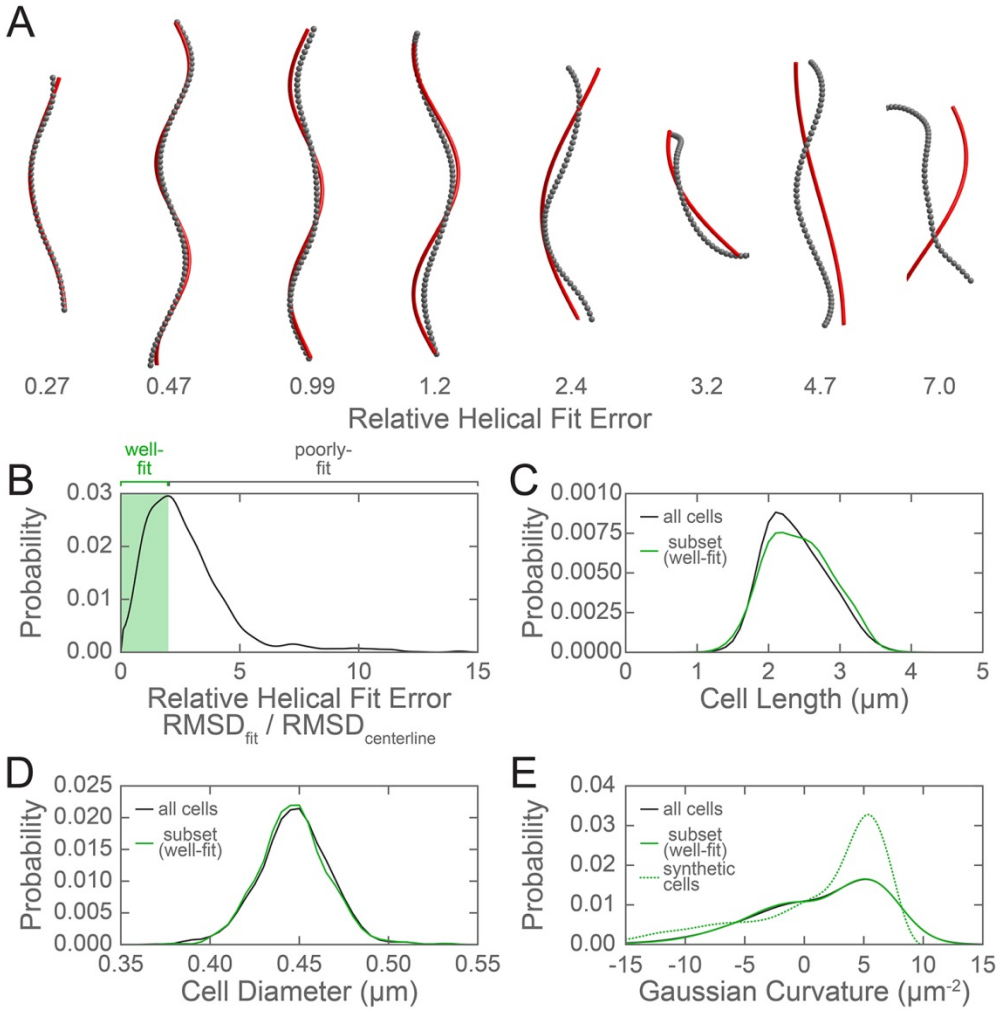

Figure 2.4. Evaluation of the subset of the wild-type population used to generate synthetic cells.

(A) Example cell centerlines (gray dots) and calculated helical fits (red lines), arranged from good (left) to poor (right) fit. (B) Histogram of the relative helical fit error for each of the cells from the wild-type population shown in Figure 2.2. Shaded green box indicates well-fit centerlines with a relative helical fit error below the selected threshold of 2, which were used for further analysis. Comparison of the population distribution of (C) cell lengths and (D) average cell diameters for the entire wild-type population (black line) and the subset of cells with a centerline that was well fit by a helix (green). (E) Comparison of the population cell surface Gaussian curvature distribution for the entire wild-type population (black line), the selected subset of wild-type cells (green line), and the synthetic cells generated based on the cell centerline helical fits of the selected subset (dotted green line).

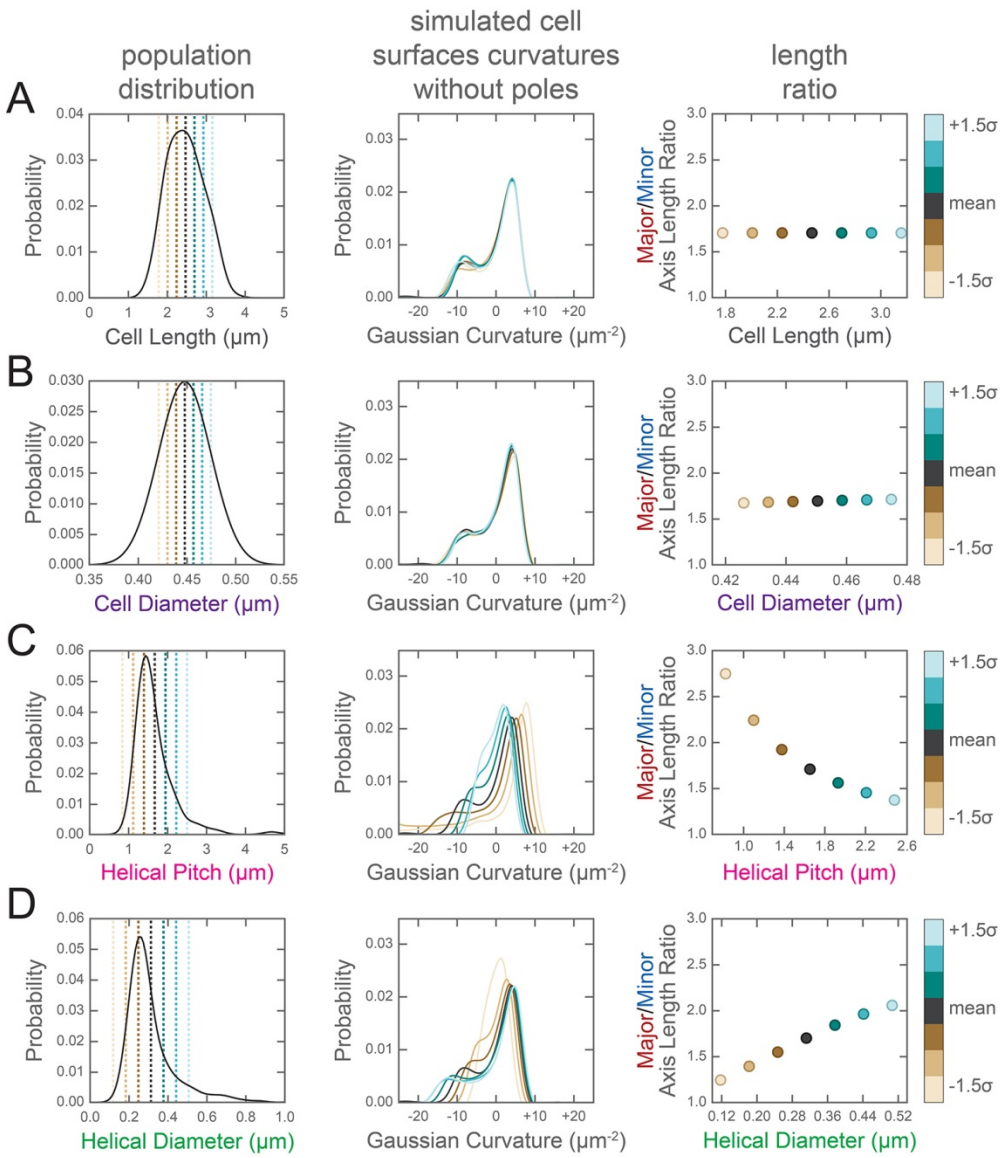

Figure 2.5. Change in the distribution of cell surface Gaussian curvatures based on modulating helical rod parameters.

Left column, distribution of population helical rod parameters from Figure 2.3 C-F. Center column, Gaussian surface curvature distribution of the synthetic cells in Figure 2.6 without poles for (A) cell centerline length, (B) cell diameter, (C) helical pitch, and (D) helical radius modulated to the mean ±1.5 standard deviations in 0.5 standard deviation increments. Right column, ratio of major to minor axis length vs. (A) cell centerline length, (B) cell diameter, (C) helical pitch, and (D) helical radius modulated to the mean ±1.5 standard deviations in 0.5

standard deviation increments. As shown in the color bar at the far right, data for the mean cell data are plotted in gray; data for cells generated with a parameter modulated to a value greater than the mean are shown in blue tones; and data for cells generated with a parameter modulated to a value less than the mean are shown in tan tones.

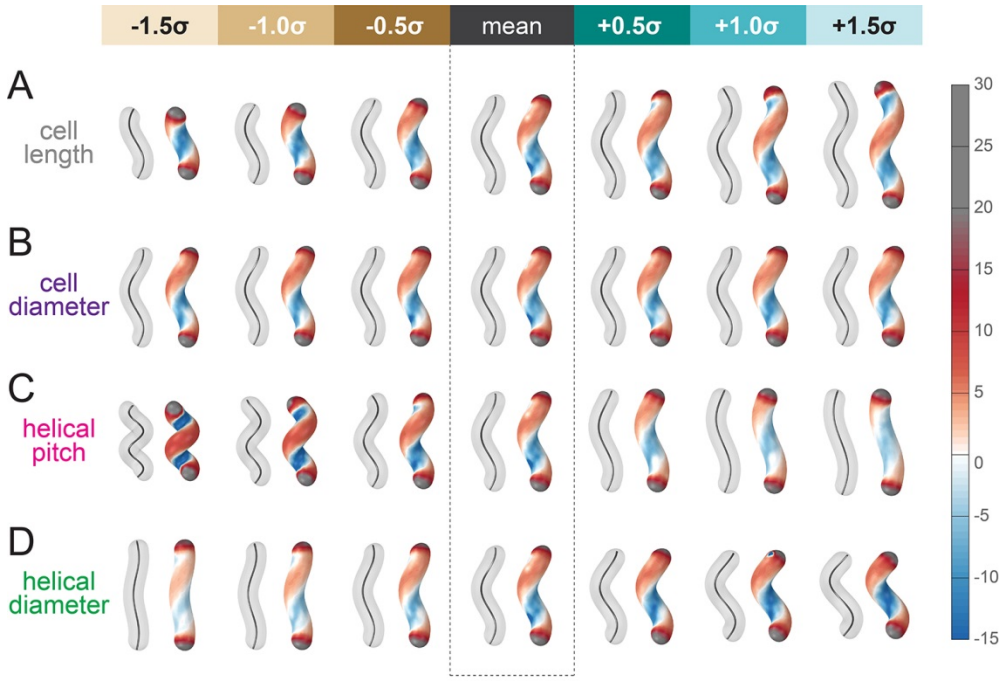

Figure 2.6. Simulated helical cells demonstrating how variation in helical parameters alters surface Gaussian curvature.

Cell centerline (paired cells, left) and cell surface Gaussian curvatures (paired cells, right) of synthetic, idealized cells with parameters taken from the distribution of wild-type shapes. The central pair of cells in each row was generated using the average value for each shape parameter shown in Figure 2.3 and is the same for all rows. Each of the parameters (A) cell centerline length, (B) cell diameter, (C) helical pitch, and (D) helical radius is increased (right of mean cell pair) and decreased (left of mean cell) up to 1.5 standard deviations in 0.5 standard deviation increments while leaving the remaining three parameters fixed at the population mean.

2.4.2 H. pylori *can incorporate modified D-alanine and modified MurNAc into peptidoglycan*

Since a helical cell must maintain large regions of positive and of negative curvatures, we hypothesized that *H. pylori* may have a different growth pattern than that of *E. coli*, where the majority of the sidewall regions have Gaussian curvature near zero. To determine where new PG is preferentially inserted, we used two metabolic probes of PG incorporation. First, we attempted labeling wild-type cells with MurNAc-alkyne (MurNAc-alk), but *H. pylori* is unable to readily use exogenous MurNAc. We then engineered a strain, HJH1, containing recycling enzymes AmgK and MurU from *Pseudomonas putida* (Gisin *et al.*, 2013) at the *rdxA* locus, a neutral locus routinely used for expression of genes in *H. pylori* (Goodwin *et al.*, 1998, Smeets *et al.*, 2000). These enzymes convert MurNAc into UDP-MurNAc, which can then be used to form PG subunit precursors (Figure 2.8). To verify that HJH1 can indeed use exogenous MurNAc, we assayed rescue from fosfomycin treatment. Fosfomycin blocks the first committed step in PG precursor synthesis by preventing the conversion of UDP-GlcNAc into UDP-MurNAc (Figure 2.8). We determined the minimum inhibitory concentration (MIC) of fosfomycin of our strain to be 25 μg/ml (Figure 2.9). Supplementation with 4 mg/ml MurNAc partially rescued growth of HJH1 in the presence of 50 μg/ml fosfomycin, but not the parental strain (LSH108) (Figure 2.7 A).

To verify that clickable MurNAc-alk is indeed incorporated into the cell wall, we purified sacculi from HJH1 labeled with MurNAc-alk for six doublings for MS/MS analysis. We positively identified MurNAc-alk-pentapeptide and MurNAc-alk-tetra-pentapeptide, the most abundant monomeric and dimeric species in the *H. pylori* cell wall, (Figure 2.7 B, C and 2.10), as well as less-abundant species (Table 2.1), confirming incorporation. Cells were labeled

without the addition of fosfomycin, indicating the HJH1 strain can use MurNAc-alk even when unmodified MurNAc is available in the cell.

Table 2.1. MurNAc-alk incorporation into PG

Muropeptide (non-reduced)	Theoretical Neutral Mass	MurNAc-alk labeled *H. pylori*			Control *H. pylori*		
		Observed Ion (charge)	Rt[1] (min)	Calculated Neutral Mass	Observed Ion (charge)	Rt[1] (min)	Calculated Neutral Mass
Di	696.270	697.289 (1+)	20.3	696.282	697.290 (1+)	20.4	696.283
Alk-Di	734.286	735.307 (1+)	30.5	734.300	-[2]	-	-
Tri	868.355	869.375 (1+)	15.8	868.368	869.374 (1+)	15.8	868.367
Alk-Tri	906.371	907.392 (1+)	25.8	906.385	-	-	-
Tetra	939.392	940.411 (1+)	20.4	939.404	940.412 (1+)	20.4	939.405
Alk-Tetra	977.408	978.428 (1+)	30.4	977.421	-	-	-
Penta	1010.429	1011.449 (1+)	22.9	1010.442	1011.449 (1+)	22.8	1010.442
Alk-Penta	1048.445	1049.464 (1+)	32.9	1048.457	-	-	-
TetraTri	1789.736	895.889 (2+)	33.4	1789.762	895.888 (2+)	33.3	1789.761
Alk-TetraTri	1827.752	914.898 (2+)	39.2	1827.781	-	-	-
TetraTetra	1860.774	931.407 (2+)	35.0	1860.799	931.407 (2+)	34.9	1860.799
Alk-TetraTetra	1898.789	950.416 (2+)	39.7	1898.817	-	-	-
TetraPenta	1931.811	966.926 (2+)	35.8	1931.837	966.925 (2+)	35.7	1931.835
Alk-TetraPenta	1969.826	985.934 (2+)	39.9	1969.853	-	-	-

[1] Rt, retention time.

[2] -, not detected.

Muropeptides detected (confirming incorporation) via LC-MS analysis of MurNAc-alk labeled versus control PG digests. The control cells displayed no evidence of any MurNAc-alkyne incorporation.

As a second strategy for labeling new PG incorporation, we used D-alanine-alkyne (D-Ala-alk) (Kuru *et al.*, 2012, Siegrist *et al.*, 2013). This probe can be incorporated through the activity of PG transpeptidases (Figure 2.8). To verify that D-Ala-alk is incorporated into the cell wall and to determine the position(s) at which it is incorporated, we purified sacculi from wild-type (LSH100) cells labeled for six doublings for analysis. D-Ala-alk was detected in only pentapeptide monomers and tetra-pentapeptide dimers, indicating that D-Ala-alk is exclusively incorporated at the pentapeptide position (Figure 2.7 D and 2.11).

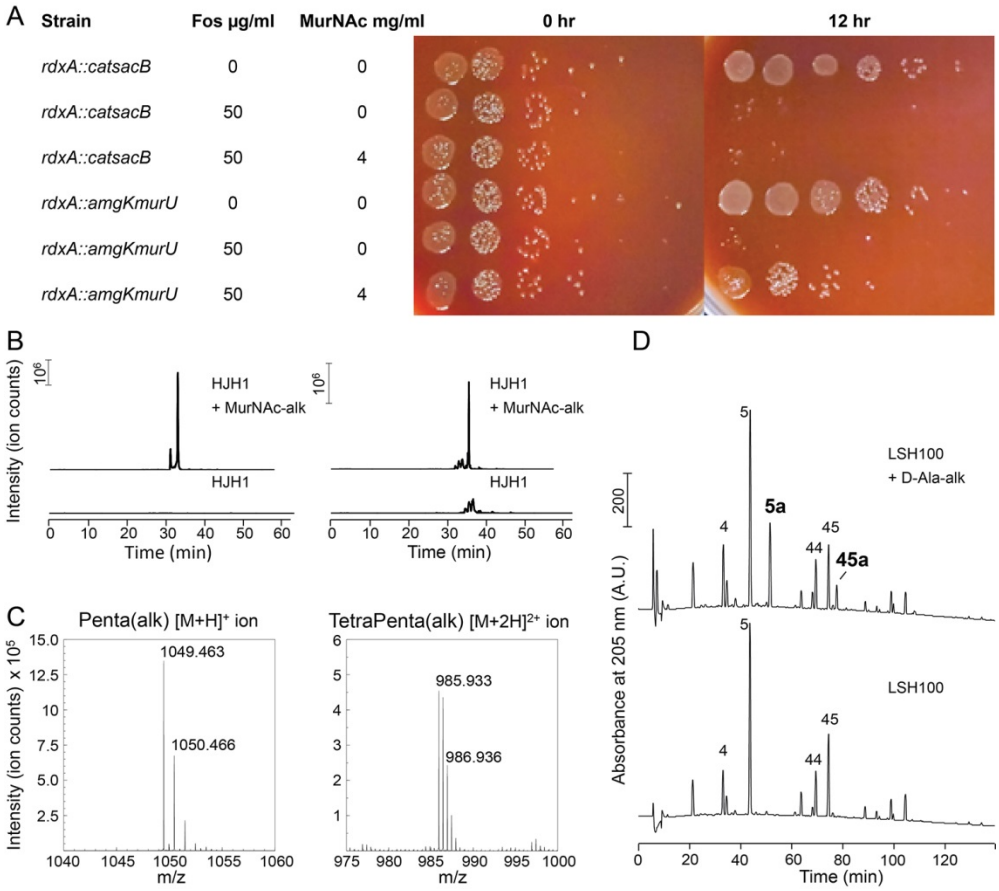

Figure 2.7. Validation of PG metabolic probes.

(A) 10-fold dilutions showing LSH108 (*rdxA::catsacB*) or HJH1 (*rdxA::amgKmurU*) treated with 50 µg/ml fosfomycin or untreated and with or without 4 mg/ml MurNAc supplementation, from one representative of three experiments. (B and C) Verification of MurNAc-alk incorporation into pentapeptides (left column) and tetra-pentapeptides (right column) by HPLC/MS/MS. (B) Extracted ion chromatograms (EICs) for the ion masses over the HPLC elution for unlabeled (lower EIC) and labeled (top EIC) sacculi. (C) Spectra of the ions observed during LC-MS for the MurNAc-alk pentapeptide (left, non-reduced, predicted $[M+H]^+$ ion m/z = 1049.452) and MurNAc-alk tetra-pentapeptide dimer (right, non-reduced, predicted $[M+2H]^{2+}$ ion m/z = 985.920). (D) Verification of D-Ala-alk incorporation into pentapeptides and tetra-pentapeptides. HPLC chromatograms of labeled (top) and unlabeled (bottom) sacculi. The main monomeric and dimeric muropeptides are labeled (4, disaccharide tetrapeptide; 5, disaccharide pentapeptide; 44, bis-disacccharide tetratetrapeptide; 45, bis-disacharide tetrapentapeptide). D-Ala-alk-modified muropeptides (top, 5a and 45a) are present only in the sample from labeled

cells and were confirmed by MS analysis of the collected peak fractions. 5a, alk-labeled disaccharide pentapeptide (neutral mass: 1036.448); 45a, alk-labelled bis-disaccharide tetrapentapeptide (neutral mass: 1959.852). Data (B, C, and D) shown are from one replicate.

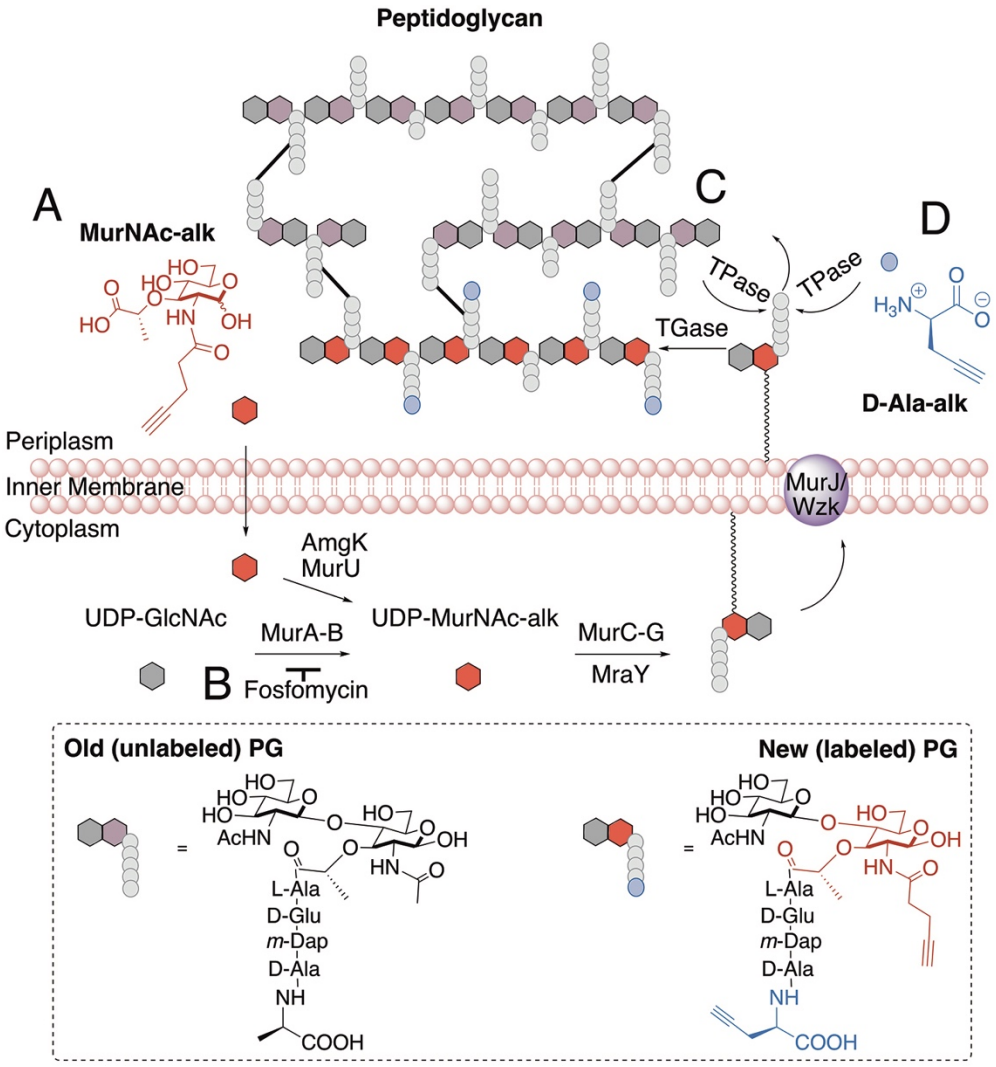

Figure 2.8. Schematic of PG synthesis and incorporation of PG metabolic probes.

(A) MurNAc-alk diffuses across the cell membrane and is converted into UDP-MurNAc-alk, which can then be used in the synthesis of PG precursors. (B) Fosfomycin inhibits the conversion of UDP-GlcNAc to UDP-MurNAc. Addition of exogenous MurNAc allows the cell to bypass this step and survive when treated with fosfomycin. To incorporate the new PG monomer into the cell wall, transglycosylases (TGase) polymerize the glycan strand. (C) To link the new strand to the existing PG, transpeptidases (TPase) form a crosslink between the tetra position D-Ala of

the new peptide stem and the m-Dap of a nearby peptide stem, resulting in loss of the penta position D-Ala of the new peptide stem. (D) In a reaction similar to forming a crosslink, TPases can replace the penta position D-Ala with D-Ala-alk. In our experiments labeling PG incorporation, we labeled cells with either MurNAc-alk or D-Ala-alk.

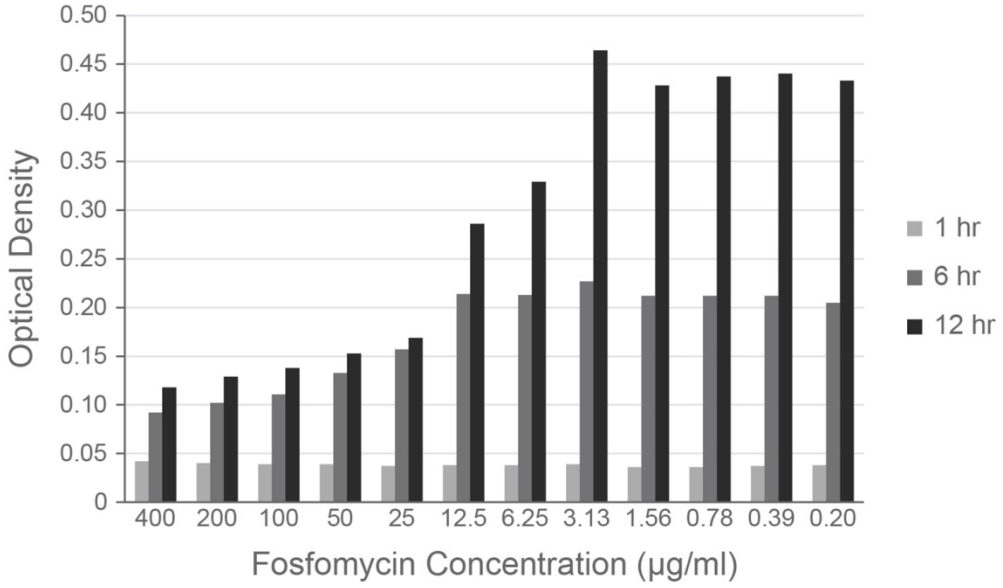

Figure 2.9. The MIC of fosfomycin in *H. pylori* is 25 µg/ml.

Optical density of wild-type *H. pylori* cultures grown in a 96-well plate with a 2-fold dilution series of fosfomycin. Optical density was measured at 1 (light gray), 6 (medium gray), and 12 (dark gray) hours of incubation. Figure shows one representative experiment of two.

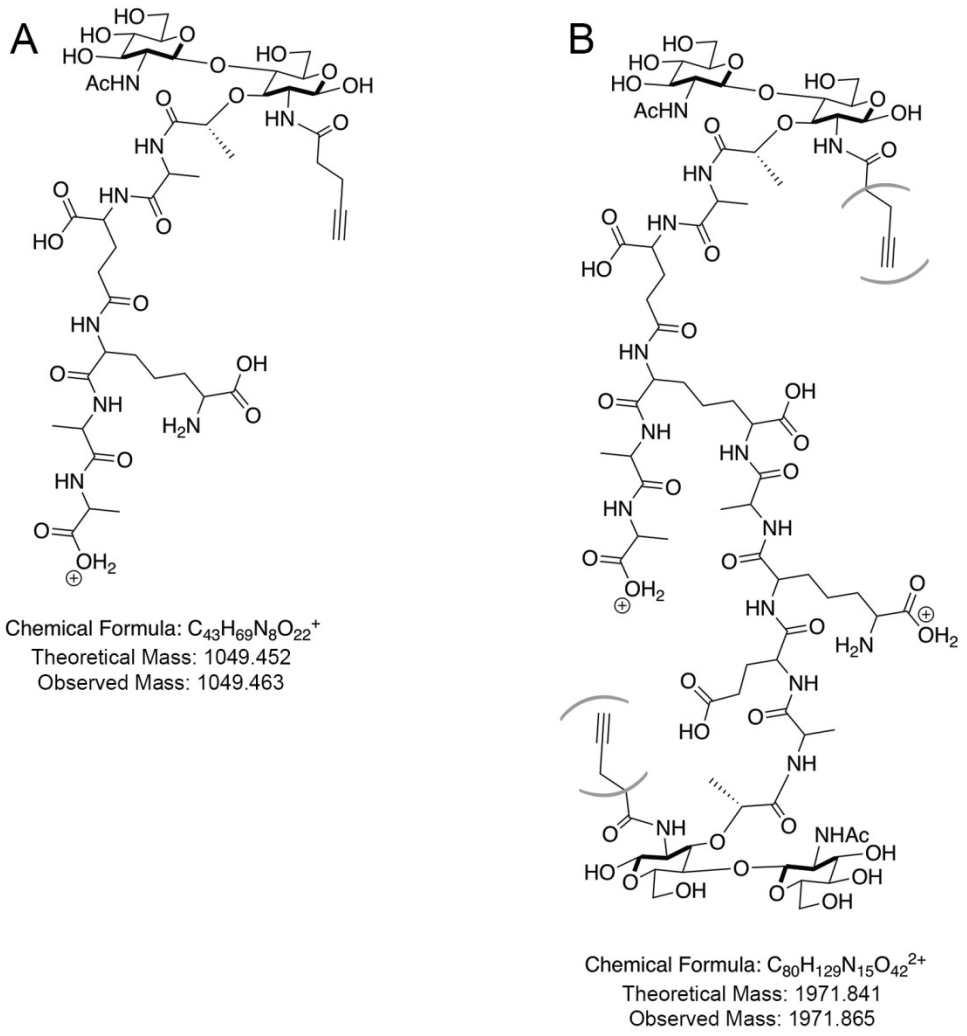

Figure 2.10. Detected MurNAc-alk labeled muropeptides.

Labeled (A) pentapeptide monomer and (B) tetra-pentapeptide dimer ions. Parentheses indicate that the MurNAc-alk could be on either the tetra or penta portion of the dimer; these two species are indistinguishable in our HPLC/MS/MS data.

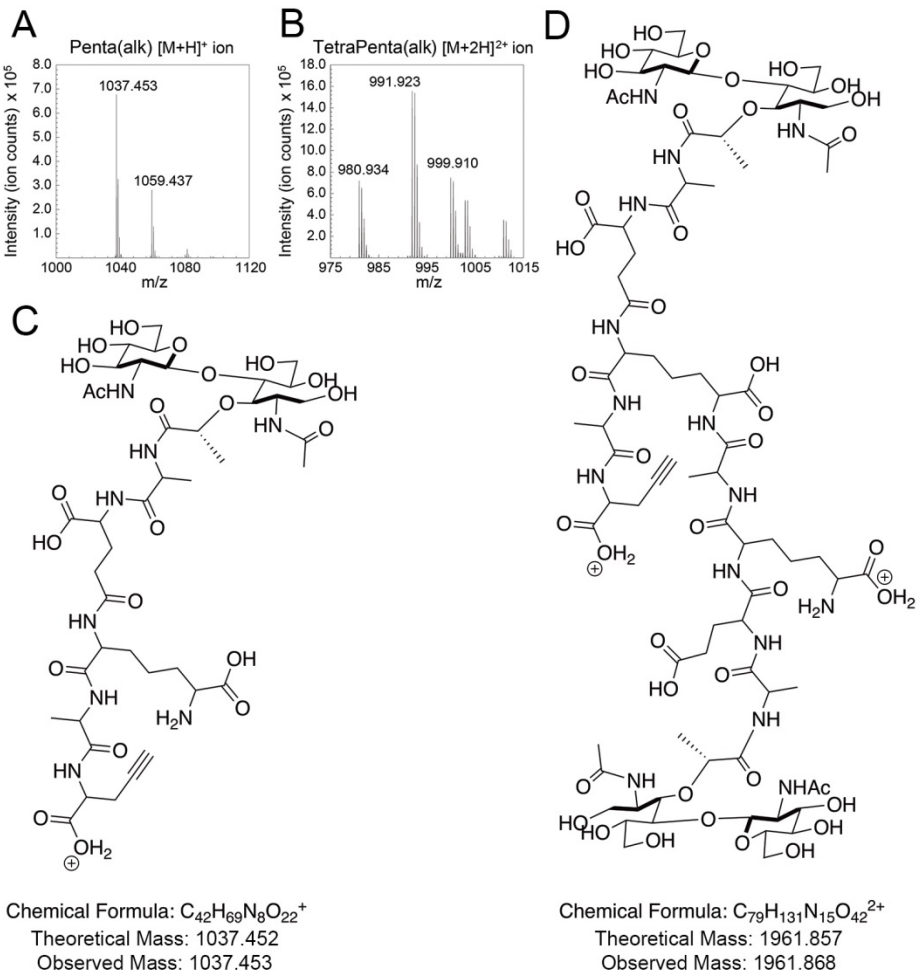

Figure 2.11. Detected D-Ala-alk labeled muropeptides.

Mass spectra for the ions observed for the reduced (A) D-Ala-alk pentapeptides (left, Peak 5a in Figure 2.8 C) and (B) D-Ala-alk tetra-pentapeptides (right, Peak 45a in Figure 2.8 C). The labeled peaks, from left to right are: (A) D-Ala-alk-pentapeptide+H^+ and D-Ala-alk-pentapeptide+Na^+ and (B) D-Ala-alk-tetra-pentapeptide+$2H^{2+}$, D-Ala-alk-tetra-pentapeptide+H^++Na^+, and D-Ala-alk-tetra-pentapeptide+H^++K^+. Schematic of (C) labeled pentapeptide monomer and (D) labeled tetra-pentapeptide dimer ions.

2.4.3 *PG synthesis is enriched at both negative Gaussian curvature and the major helical axis area*

To visualize new PG incorporation, we labeled HJH1 with either MurNAc-alk or D-Ala-alk for 18 minutes (approximately 12% of the doubling time). AF555-azide was conjugated to the alkyne groups using click chemistry and cells were counterstained with WGA-AF488. Cells were imaged using 3D SIM (Figure 2.12). As expected, labeling was seen on the boundary of the cell but not in the cytoplasmic area (Figure 2.12 D and H). For both metabolic probes, PG synthesis appeared to be excluded from the poles, dispersed along the sidewall, and present at septa. However, D-Ala-alk septal labeling appeared much brighter compared to MurNAc-alk septal labeling, indicating at least some difference between incorporation and/or turnover of the two probes. To discover if this labeling difference is due to curvature-biased transpeptidation rates, we also attempted labeling with dimers D-alanine-D-alanine-alkyne and D-alanine-alkyne-D-alanine, which is presumably incorporated predominantly through PG precursor biosynthesis in the cytoplasm, but no signal was detected (data not shown) (Liechti *et al.*, 2014).

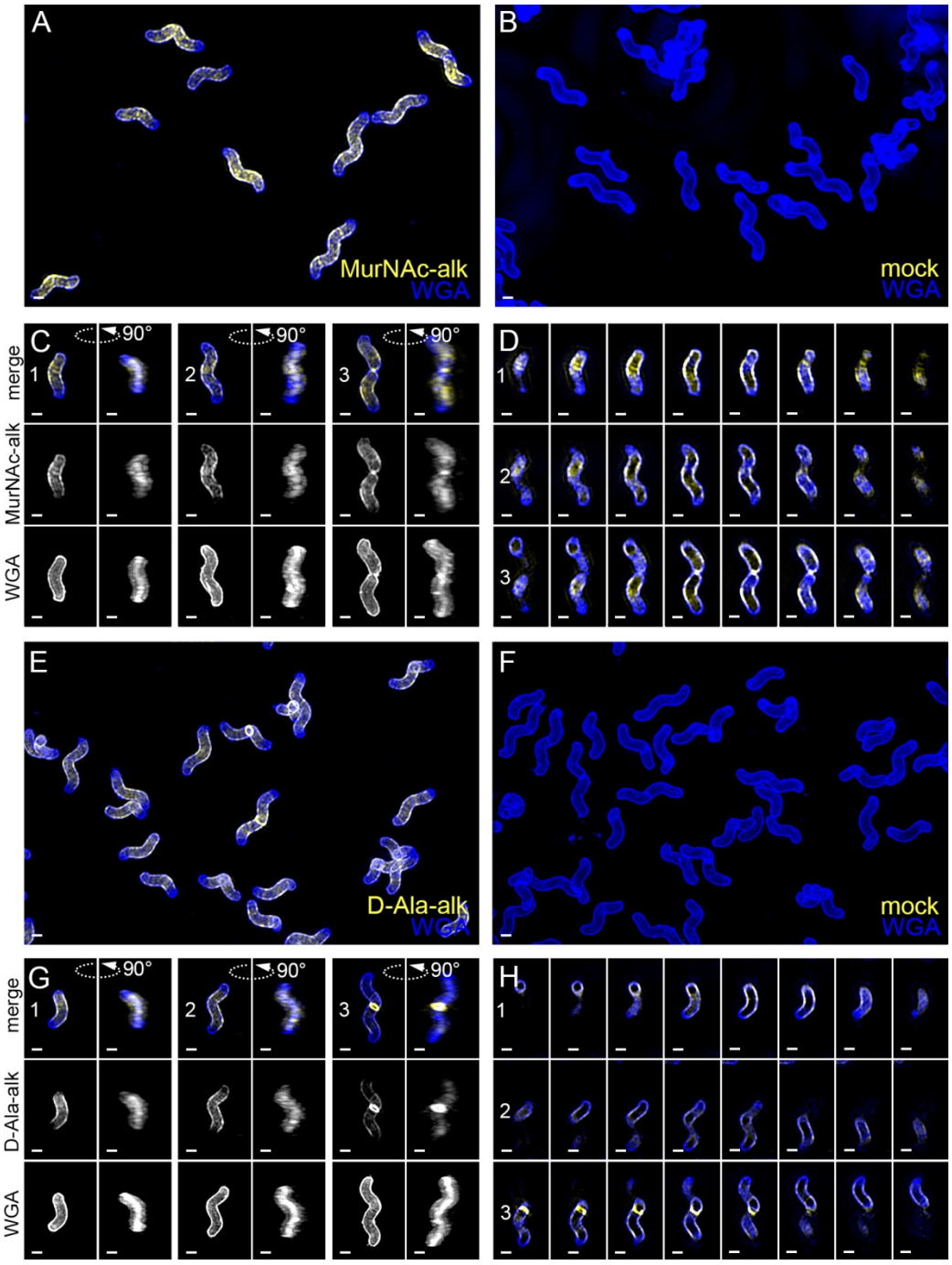

Figure 2.12. New cell wall growth appears dispersed along the sidewall, excluded from poles, and present at septa.

3D SIM imaging of wild-type cells labeled with an 18-minute pulse of MurNAc-alk (A-D, yellow) or 18-minute pulse of D-Ala-alk (E-H, yellow) counterstained with fluorescent WGA (blue). Color merged maximum projection of 18-minute MurNAc-alk (A), D-Ala-alk (E), or mock (B, F) labeling with fluorescent WGA counterstain. (C, G) Top-down (left) and 90-degree

rotation (right) 3D views of three individual cells, including a dividing cell at the right. Top: color merge; middle: 18-minute MurNAc-alk (C) or D-Ala-alk (G); bottom: fluorescent WGA. (D, H) Color merged z-stack views of the three cells in C, G, respectively (left to right = top to bottom of the cell). Numbering indicates matching cells. Scale bar = 0.5 μm. The represented images are selected from one of three biological replicates.

To quantify any curvature-based enrichment (expressed throughout as relative concentration vs. Gaussian curvature) of new cell wall synthesis, we used the fluorescent WGA signal to generate 3D cell surface reconstructions of hundreds of individual, non-septating cells labeled with MurNAc-alk, D-Ala-alk, or cells that were mock-labeled as a control. The Gaussian curvature was calculated at every location on the reconstructed 3D surface of the cell. Because the absolute amount of synthesis (or other signals of interest) can vary between cells, and because the level of illumination throughout the field of view is non-uniform, we set the average PG synthesis signal for each individual cell to one. We measured each cell's curvature-dependent PG synthesis signal intensity relative to that average value, normalized by the amount of that curvature present on the surface, since there is more surface area associated with positive Gaussian curvature than negative (Figure 2.13 A).

As a tool to facilitate understanding and interpretation of these relative enrichment plots, we generated a synthetic cell surface with the same geometric properties as the average wild-type cell (Figure 2.3), applied a variety of example intensity distributions, and generated curvature enrichment plots. We began with a uniform baseline signal (Figure 2.14, "uniform - low") and in each case added 25% extra signal intensity to specific geometries. In the enrichment profiles, a relative concentration value of one indicates that the average signal intensity at that curvature is the same as the average across the cell surface. Values greater than one indicate curvatures where normalized signal is enriched compared to average and values less than one indicate curvatures

where normalized signal is depleted compared to average. These simulations illustrate the interrelated nature of the relative enrichment plots. Because there is more cell surface area with positive Gaussian curvature, adding 25% signal to this region (Figure 2.14, "enriched at major axis") increases the average signal more than adding 25% signal at zero or negative Gaussian curvature. Thus by increasing the signal at positive curvature, the relative concentration decreases at the rest of the cell surface even though the absolute signal at these geometries remains the same. A similar change in relative concentration occurs with an increase in signal at zero or negative curvature (Figure 2.14, "enriched at zero" and "enriched at minor axis", respectively), but because there is less surface area with these curvatures, the magnitude of this change is lower. To further illustrate the implications of the interrelated nature of these plots, we added both signal with a monotonic decline profile (Figure 2.14, "monotonic decline") and signal enriched at the major axis (Figure 2.14, "enriched at major axis") to one cell surface (Figure 2.14, "monotonic decline and major axis"). By adding extra signal at the major axis area, the average concentration increases significantly, causing the rest of the relative concentrations to decrease compared to the monotonic decline profile alone. As these simulations demonstrate, relative enrichment plots must be considered holistically. The key features of interest are the overall increases, decreases, and peaks in the curves, along with the curvatures at which these occur.

We performed relative concentration enrichment analysis separately with the entire cell surface and with the sidewall only (poles removed) from the PG synthesis data. We then averaged the single cell measurements across more than 100 cells pooled from three biological replicates to obtain a profile of enrichment or depletion as a function of surface curvature.

Curvature enrichment analysis of whole cell surfaces revealed that for both metabolic probes, signal was largely absent from the poles, as seen by the drop-off of relative enrichment at curvatures above 10 μm^{-2} (Figure 2.13 B). To focus on the curvature enrichment pattern along the sidewall, we repeated the analysis after first computationally removing the poles. Looking at sidewall curvature alone, MurNAc-alk was enriched at two sites. At negative curvature, enrichment increases as curvature becomes more negative. At positive curvature, enrichment peaks near 6 μm^{-2} and then begins to decrease at higher curvatures (Figure 2.13 C, green). D-Ala-alk showed peaks of enrichment aligning with those of MurNAc-alk (Figure 2.13 C, blue), but the magnitude of the peak at positive curvature was reduced. The mock labeling control showed minimal curvature bias and is on average 3.6% of the D-Ala-alk signal and 4.5% of the MurNAc-alk signal (Figure 2.13 B and C, gray and Figure 2.15 B). This demonstrates that the fluorescent signal in the mock labeling is independent of geometry. Thus the nonspecific signal should contribute negligibly to the PG synthesis enrichment profiles. Biological replicates are shown in Figure 2.15).

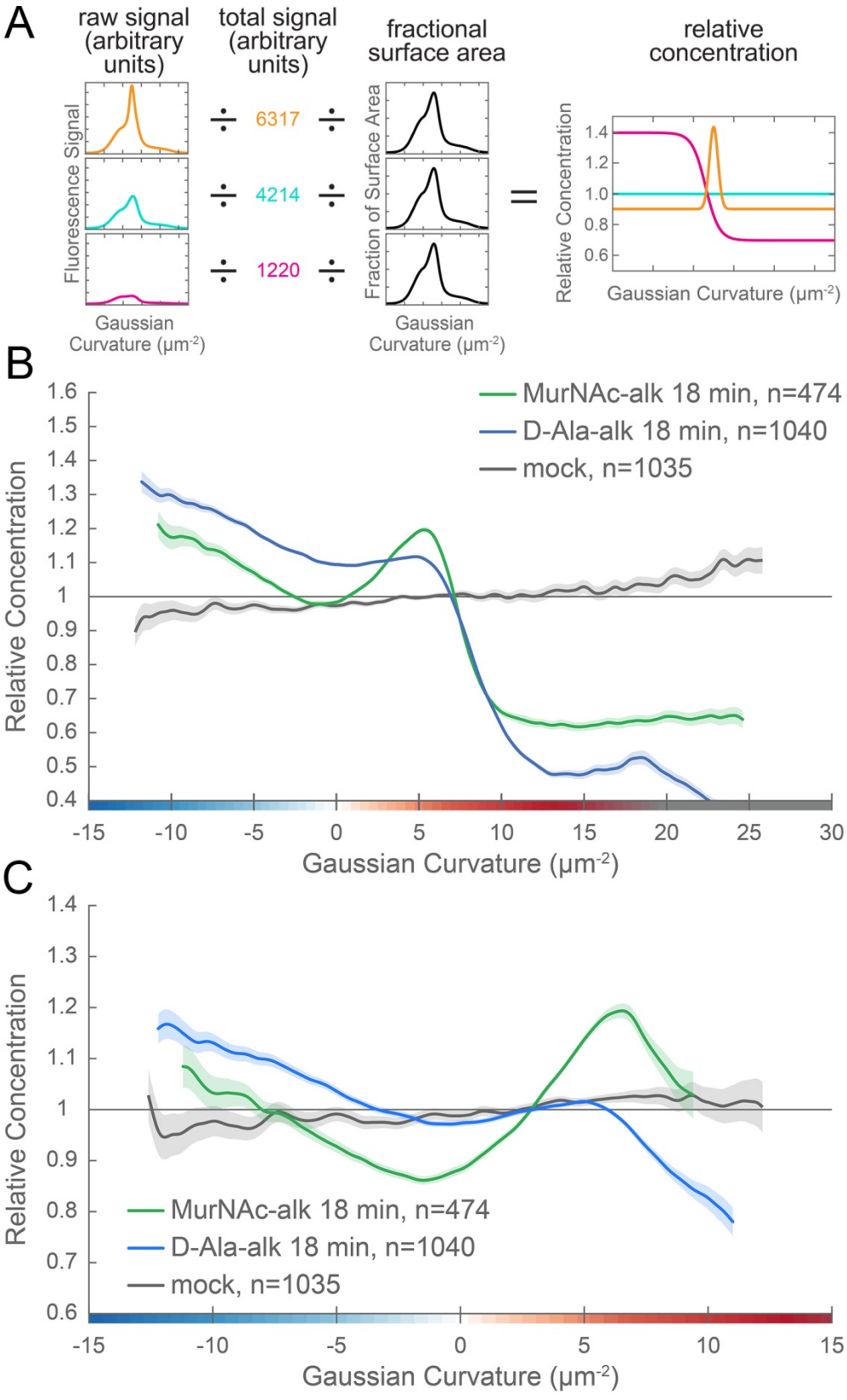
A
raw signal (arbitrary units)
total signal (arbitrary units)
fractional surface area
relative concentration
Fluorescence Signal
6317
4214
1220
Fraction of Surface Area
Relative Concentration
Gaussian Curvature (μm-2)
B
MurNAc-alk 18 min, n=474
D-Ala-alk 18 min, n=1040
mock, n=1035
Relative Concentration
Gaussian Curvature (μm-2)
C
MurNAc-alk 18 min, n=474
D-Ala-alk 18 min, n=1040
mock, n=1035
Relative Concentration
Gaussian Curvature (μm-2)

Figure 2.13. New cell wall growth is excluded from the poles and enriched at negative Gaussian curvature and the major axis area.

(A) The calculation of relative concentration for a specific probe involves two steps of normalization. First, the raw signal is summed up in bins defined by the Gaussian curvature at the surface. Then, this raw signal is normalized by dividing by the sum of the raw signal at all Gaussian curvatures (total signal). This normalizes for changes in total signal, fluorophore brightness, imaging conditions, etc. The second step is to divide by the fractional surface area, or amount of surface area contributed by each Gaussian curvature bin. This distribution is dependent on the observed shape of the cell. Following these two normalization steps, one has the concentration of the probe of interest relative to a uniformly distributed null model. For illustration, we have shown this graphical equation for three noise-free cells that have the same geometry, but different relative signal abundances. In the experimental data presented in the main text, the single cell relative concentration profile is averaged over hundreds of cells, each with their own unique geometry. Whole surface (B) and sidewall only (C) surface Gaussian curvature enrichment of relative concentration of new cell wall growth (y-axis) vs. Gaussian curvature (x-axis) derived from a population of computational cell surface reconstructions of MurNAc-alk (green), D-Ala-alk (blue) 18-minute pulse-labeled, and mock-labeled (gray) cells. 90% bootstrap confidence intervals are displayed as a shaded region about each line. The represented data are pooled from three biological replicates.

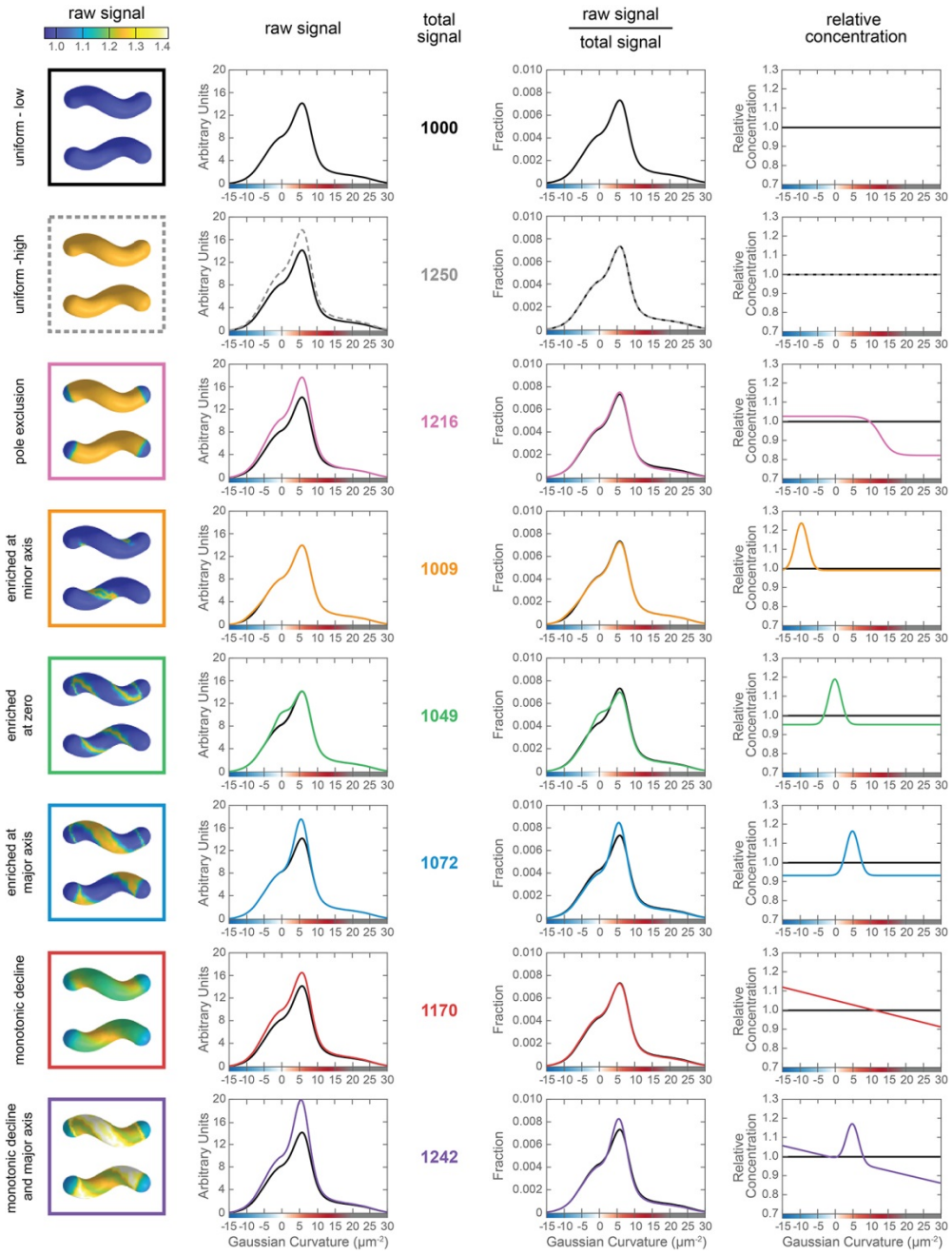

Figure 2.14. Example enrichment profiles.

For eight different example distributions (rows with brief labels to the left), five pieces of data are shown. The five columns are as follows (from left to right): two views of an example rendering of a helical rod cell colored by the intensity of the raw signal at each point on the surface; the raw signal summed across all surface elements of the same curvature; the total raw signal summed across all curvature values; the ratio of the raw signal to total signal; and the relative concentration. For plots that are functions of Gaussian curvature, the solid black line

from the ‘uniform – low’ example is included in all plots for comparison. The same idealized cell geometry was used for all the examples. The simulated example distributions were created by taking a uniformly distributed signal and adding 25% additional signal to specific geometries. This additional signal results in the raw signal being 1.25X larger at the enriched geometries than the uniform case. However, the increase in the total signal is geometry dependent and not 25%, except in the ‘uniform – high' example. Because of the normalization steps, an identical relative concentration profile could have been generated by removing material from the opposite regions.

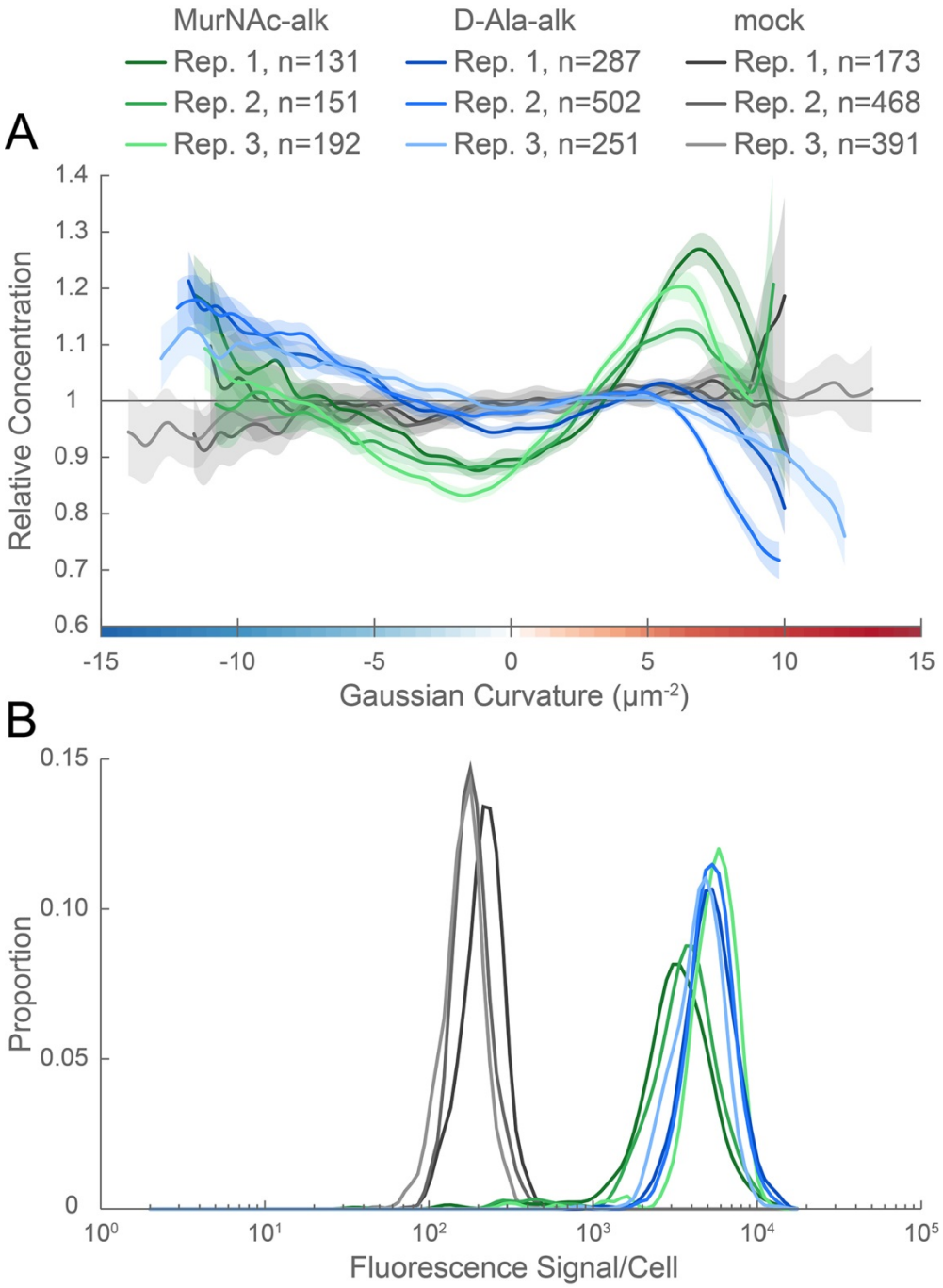

Figure 2.15. Curvature enrichment analysis of biological replicates of MurNAc-alk-, D-Ala-alk-, and mock-labeling.

(A) Sidewall only surface Gaussian curvature enrichment of relative concentration of new cell wall growth (y-axis) vs. Gaussian curvature (x-axis) of the three biological replicates pooled in Figure 2.13: MurNAc-alk (greens), D-Ala-alk (blues) 18-minute pulse-labeled, and mock-

labeled (grays) cells. 90% bootstrap confidence intervals are displayed as a shaded region about each line. (**B**) Histogram of fluorescence signal per cell divided by the number of pixels in the projected cell area for the populations in (A).

2.4.4 *MreB is enriched at negative Gaussian curvature*

The cytoskeletal protein MreB has been shown in rod-shaped organisms to preferentially localize to negative Gaussian curvatures near to and below zero and help direct PG synthesis (Bratton *et al.*, 2018, Ursell *et al.*, 2014). It has been reported that MreB is not essential in *H. pylori* and that treatment with the MreB inhibitor A22 does not alter cell shape (Waidner *et al.*, 2009), though growth inhibition only occurred at concentrations well above those used to select for A22 resistance in other organisms (Gitai *et al.*, 2005, Ouzounov *et al.*, 2016, Srivastava *et al.*, 2007, Wu *et al.*, 2011). Since multiple attempts to knock out *mreB* in wild-type LSH100 were unsuccessful, we generated IM4, a merodiploid strain with a second copy of *mreB* at a neutral intergenic locus (McGee locus (Langford *et al.*, 2006)) (Figure 2.17 A) for comparative transformation experiments. To verify that both LSH100 and IM4 are readily transformable, we performed parallel transformations with a *ccmA* deletion cassette. LSH100 and IM4 showed similar transformation efficiencies ($2.4x10^{-4}$ and $1.2x10^{-4}$, respectively) (Figure 2.16 A). We transformed LSH100 and IM4 with an *mreB::CAT* deletion cassette (Figure 2.16 A and Figure 2.17 A) and obtained *mreB* targeting transformants in strain IM4 at a frequency of $2.3x10^{-4}$. The CAT resistance cassette integrated into *mreB* at either the native locus or the McGee locus (19 and 5 of 24 clones tested, respectively) (Figure 2.17 B). In contrast, we obtained two colonies after transformation of LSH100 (frequency of $6.7x10^{-7}$). Sequencing revealed that an amplification event at the mreB locus occurred for each of these clones, such that an uninterrupted copy of *mreB* was present in addition to a copy of *mreB::CAT* (Figure 2.17 D).

Western blotting revealed that MreB was produced at wild-type levels in clone #2, but only a faint band was observed for clone #1 (Figure 2.17 C). In clone #1, the terminal four amino acids were replaced due to the recombination event (GFSE to FLAN). One of the four epitopes used to generate the anti-MreB antibody includes the four terminal amino acids (Nakano *et al.*, 2012) likely explaining the discrepancy between the sequencing results and western blot detection. While we requested the previously published *mreB* mutant strains (Waidner *et al.*, 2009), they could not be revived from frozen stocks. We thus conclude that MreB is essential in LSH100 and perhaps all *H. pylori* strains.

We investigated MreB localization to determine if an altered curvature preference might account for the PG synthesis pattern we observed. Immunofluorescence labeling with 3D SIM imaging revealed that MreB is present at the cell periphery as many individual foci and some short arcs that appear to be oriented approximately circumferentially and excluded from the poles (Figure 2.16 B, D, and E). Only sparse foci were seen with immunofluorescence using the preimmune serum (Figure 2.16 B). Curvature enrichment analysis of non-dividing cells confirmed that MreB localization is depleted at the poles (Figure 2.16). Regardless of whether the poles were included in the analysis, we observed as Gaussian curvature became more negative, relative MreB concentration increased monotonically (Figure 2.16 F and 2.18). Biological replicates are shown in Figure 2.19 A. This echoes the enrichment of PG synthesis at negative Gaussian curvature; as Gaussian curvature became more negative (below -2 μm^{-2}), relative PG synthesis increased monotonically. Preimmune serum signal was 36.4% of the MreB signal (Figure 2.19 B), but did not show a curvature preference (Figure 2.16 F, gray and Figure 2.18, gray). Thus, MreB may promote the enhanced PG synthesis observed at negative curvature.

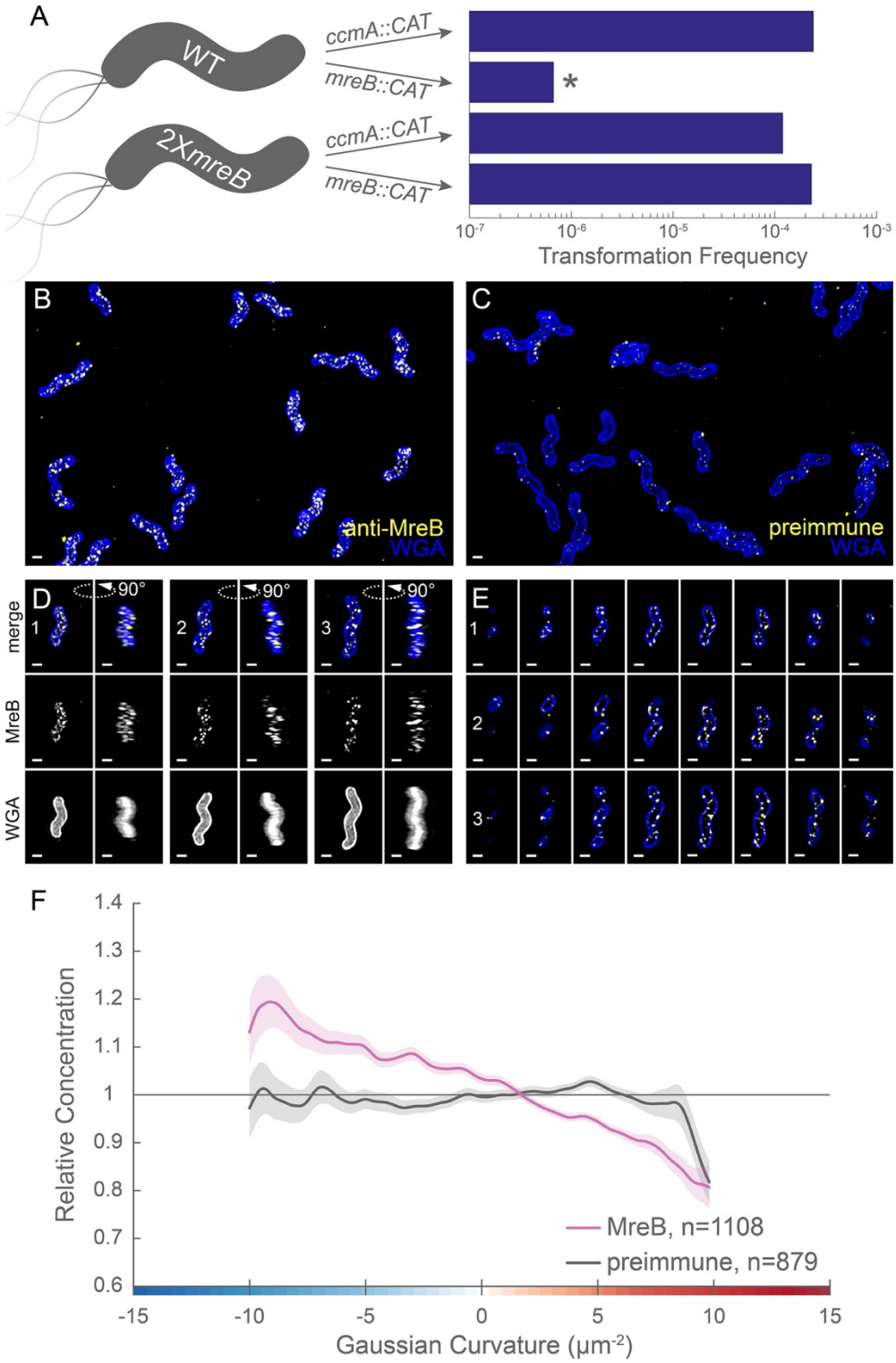

Figure 2.16. MreB is essential in LSH100 and is present as small foci enriched at negative Gaussian curvature.

(A) Schematic of transformation experiment testing MreB essentiality in LSH100 (WT) and IM4 (2X*mreB*) (left) and corresponding transformation frequencies (right). * = two recombinant clones with *mreB* duplication (see Figure 7 - supplement 1 for details). 3D SIM imaging of wild-type cells immunostained with anti-MreB (B, D, E, yellow) or preimmune serum (C, yellow) and counterstained with fluorescent WGA (blue). (B, C) Color merged maximum projections (D) Top-down (left) and 90-degree rotation (right) 3D views of three individual cells. Top: color merge; middle: anti-MreB; bottom: fluorescent WGA. (E) Color merged z-stack views of the three cells in A. (left to right = top to bottom of the cell). Numbering indicates matching cells. Scale bar = 0.5 μm. (F) Sidewall only surface Gaussian curvature enrichment plots for a population of cells immunostained with anti-MreB (pink), or pre-immune serum (gray). Smooth line plot (solid line) of relative MreB concentration (y-axis) vs. Gaussian curvature (x-axis) derived from a population of computational cell surface reconstructions with poles excluded. 90% bootstrap confidence intervals are displayed as a shaded region about each line. The represented images are selected from one of three biological replicates and the data shown in (F) are pooled from the three biological replicates.

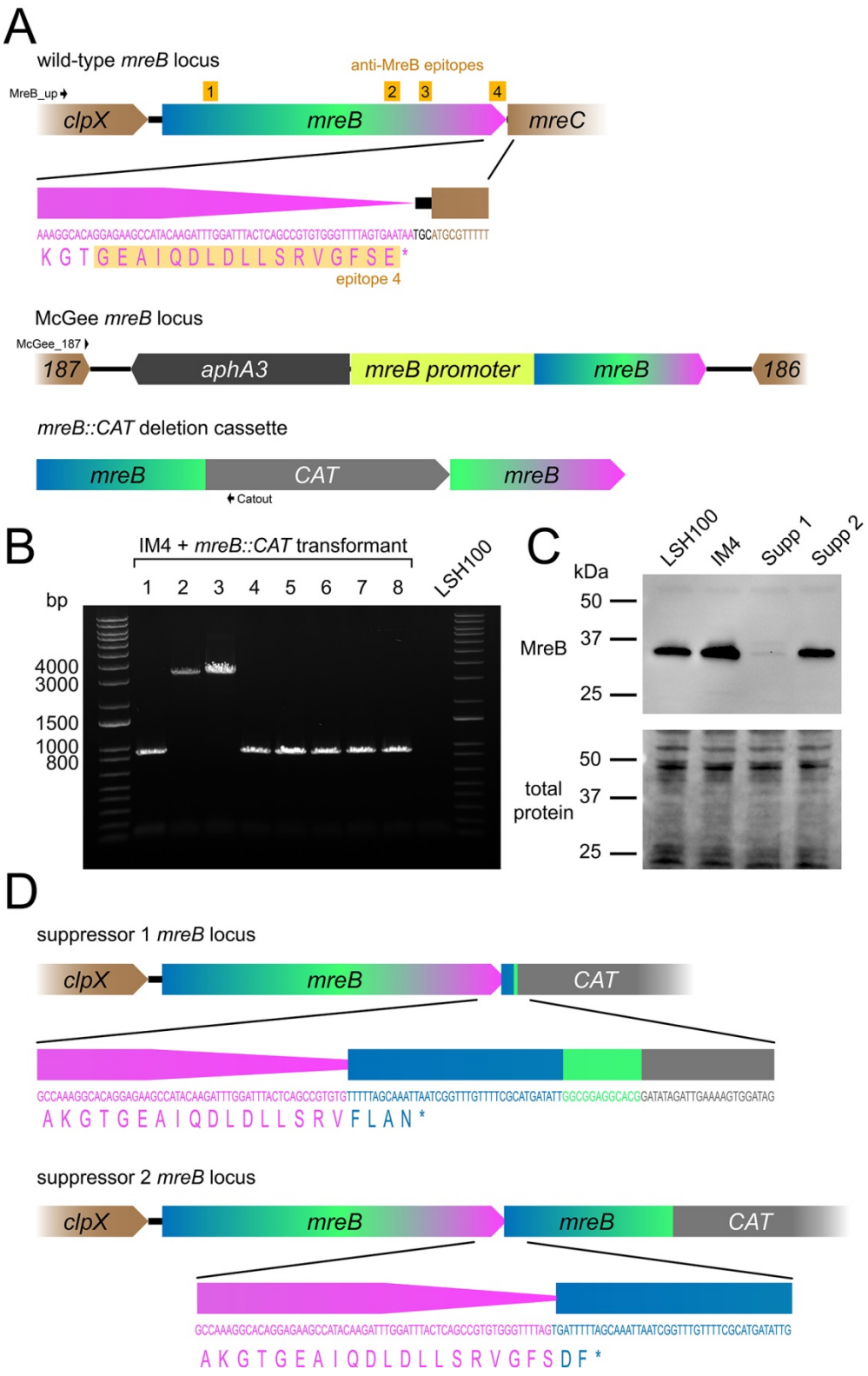

Figure 2.17. MreB is essential in the G27 derivative LSH100.

(A) (Top) Schematic of the LSH100 native *mreB* locus with DNA and protein sequence for a small region at the C-terminus. Anti-MreB epitopes are annotated in yellow. (Middle) Schematic of McGee locus with *mreB* in strain IM4. (Bottom) *mreB::CAT* deletion cassette used for transformations. Black arrows: primers MreB_up, McGee_187, and Catout used for CAT insertion site characterization in (B). (B) PCR to determine the integration site of *mreB::CAT* into IM4. Native locus expected size = 899 bp; McGee locus expected size = 3320 bp. (C) Western blot of MreB expression (top) and total protein levels (bottom) in LSH100 (wild-type), IM4 (2X*mreB*), and *mreB* recombinant clone #1 and #2. One of two representative experiments. (D) Schematic of the *mreB* duplications in MreB suppressor clone #1 (top) and #2 (bottom) with DNA and protein sequence for a small region at the C-terminus. Schematics are to scale; McGee *mreB* locus schematic is presented at ½ scale.

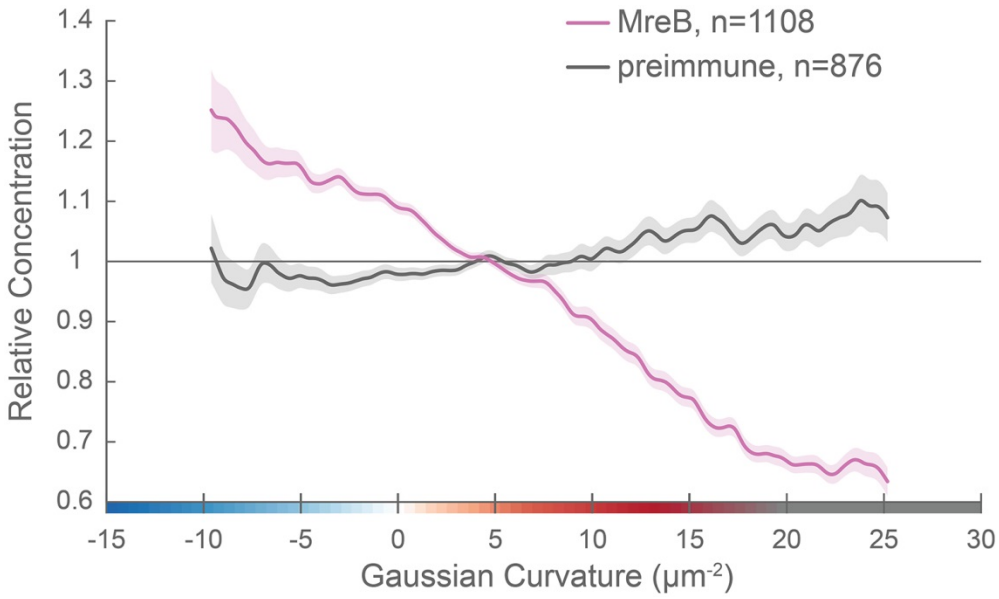

Figure 2.18. MreB enrichment decreases with increasing positive Gaussian curvature.

Whole surface (sidewall and poles) Gaussian curvature enrichment of relative MreB concentration (y-axis) vs. Gaussian curvature (x-axis) of computational cell surface reconstructions of a population of cells immunostained with anti-MreB (pink), or pre-immune serum (gray). 90% bootstrap confidence intervals are displayed as a shaded region about each line. The represented data are pooled from three biological replicates.

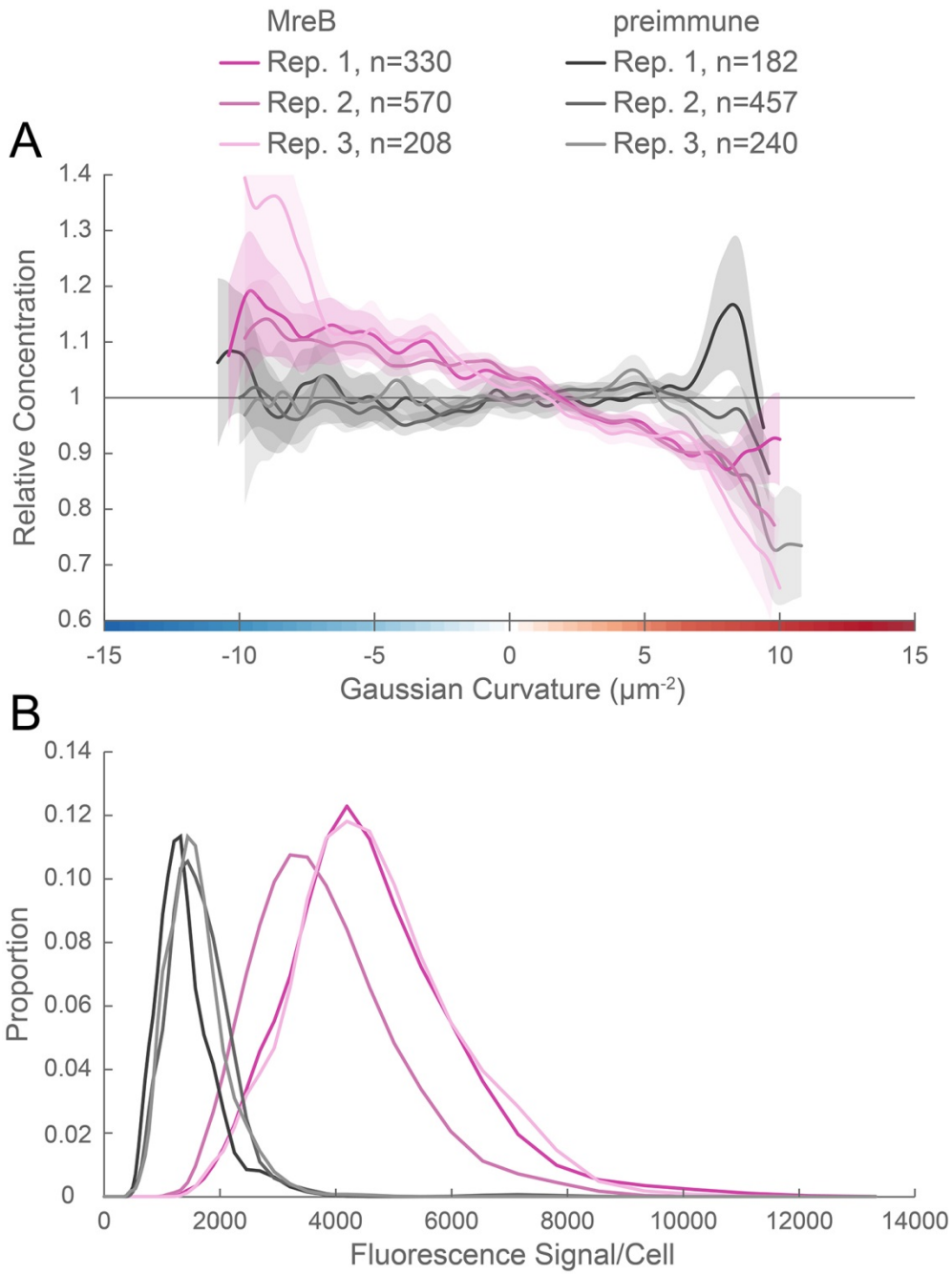

Figure 2.19. Curvature enrichment analysis of biological replicates of MreB.

(A) Sidewall only surface Gaussian curvature enrichment of relative MreB concentration (y-axis) vs. Gaussian curvature (x-axis) of the three biological replicates pooled in Figure 2.16 F: anti-MreB (pinks) and preimmune serum (grays) immunostained cells. 90% bootstrap confidence

intervals are displayed as a shaded region about each line. (B) Histogram of fluorescence signal per cell divided by the number of pixels in the projected cell area for the populations in (A).

2.4.5 *The bactofilin CcmA forms filaments, bundles, and lattices in vitro*

We reasoned that another cytoskeletal element might promote the higher relative PG synthesis observed at the major axis area. While both coiled-coil rich proteins (Ccrp) and the bactofilin homolog CcmA have been implicated in *H. pylori* cell shape (Specht *et al.*, 2011, Sycuro *et al.*, 2010, Waidner *et al.*, 2009), only loss of CcmA, and not individual Ccrps, results in a drastic cell shape defect in our strain background (Yang *et al.*, 2019); Δ*ccmA* cells are nearly straight. To verify CcmA's status as a cytoskeletal filament, we tested its ability to form higher-order structures in vitro. Negative staining of recombinant wild-type CcmA purified from *E. coli* revealed filaments of varying length, long helical bundles of filaments, and lattice structures (Figure 2.20 A-B and 2.21 A). Fast Fourier transform analysis of the lattice structures revealed a filament spacing of 5.5 nm (Figure 2.22), similar to that previously observed for *C. crescentus* BacA lattices (5.6 nm) (Vasa et al., 2015). While BacA forms orthogonal lattices, the CcmA lattices are skewed (acute angle = 71.5°; obtuse angle = 106.2°).

To begin to assess the importance of higher-order structures and localization for CcmA cell shape functions, we constructed two point mutant variant proteins, located in the predicted hydrophobic core of the protein (I55A and L110S) (Shi *et al.*, 2015). Homologous residues (75 and 130, respectively) were shown to be important for polar localization of the bactofilin BacA in *C. crescentus* (Vasa *et al.*, 2015). While both proteins could be expressed and purified from *E. coli* (Figure 2.21 D), the recombinant proteins either fail to form any higher order structures under any buffer condition tested (I55A; Figure 2.20 C) or form no lattice structures and many

individual filaments in addition to bundles that are straighter, narrower, and shorter than those of wild-type CcmA in vitro (L110S; Figure 2.20 D and 2.21 B). When expressed as the sole copy of *ccmA* in *H. pylori*, both mutant proteins could be detected in whole cell extracts (Figure 2.20 E).The I55A variant showed lower steady-state protein levels than wild-type, while the L110S variant consistently showed higher steady-state protein levels than wild-type. In both cases, the mutant strains displayed a morphology indistinguishable from a *ccmA* null strain (Figure 2.20 F and 2.21 C), suggesting that formation of higher-order structures by CcmA may be necessary for cell shape-determining functions.

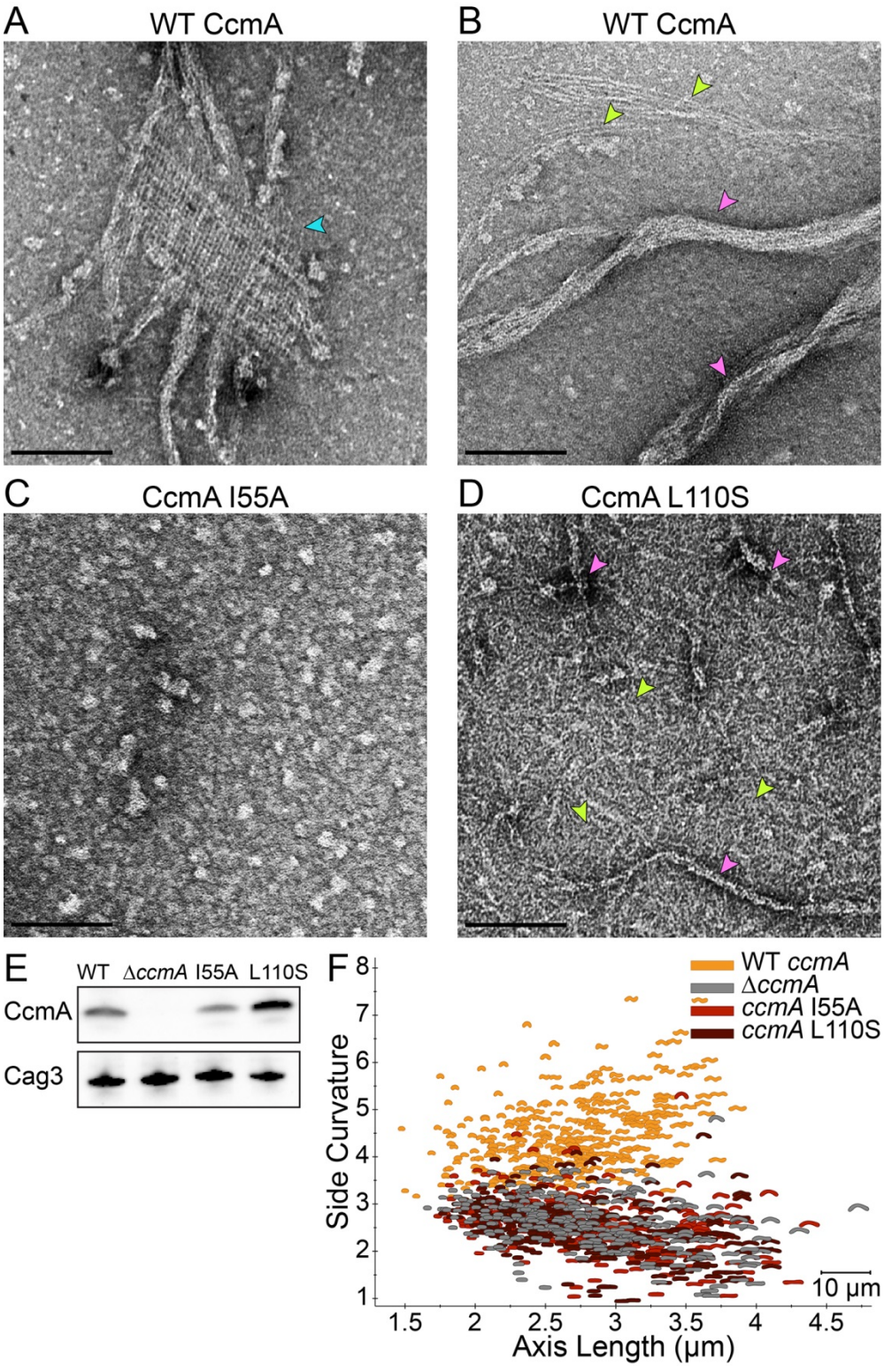

Figure 2.20. Amino acid substitution mutations in CcmA cause altered polymerization in vitro and alter cell shape in vivo.

Negatively stained TEM images of purified CcmA. Scale bars = 100 nm, with representative images from one of three experiments. Wild-type CcmA lattices (A, blue arrows) and helical bundles (B, pink arrows), which are comprised of individual filaments (lime green arrows). (C) The I55A variant does not form ordered structures in vitro. (D) CcmA^{L110S} filament bundles (pink arrows) and individual filaments (lime green arrows). (E) Immunoblot detection of CcmA expression (top) in *H. pylori* lysates using Cag3 as loading control (bottom); representative of four experiments. (F) Scatterplot displaying axis length (x-axis) and side curvature (y-axis) of wild-type (gold), Δ*ccmA* (gray), *ccmA*^{I55A} (red), and *ccmA*^{L110S} (dark red) strains. Data are representative of two independent experiments. Wild-type, n=346; Δ*ccmA*, n=279; *ccmA*^{I55A}, n=328; and *ccmA*^{L110S}, n=303.

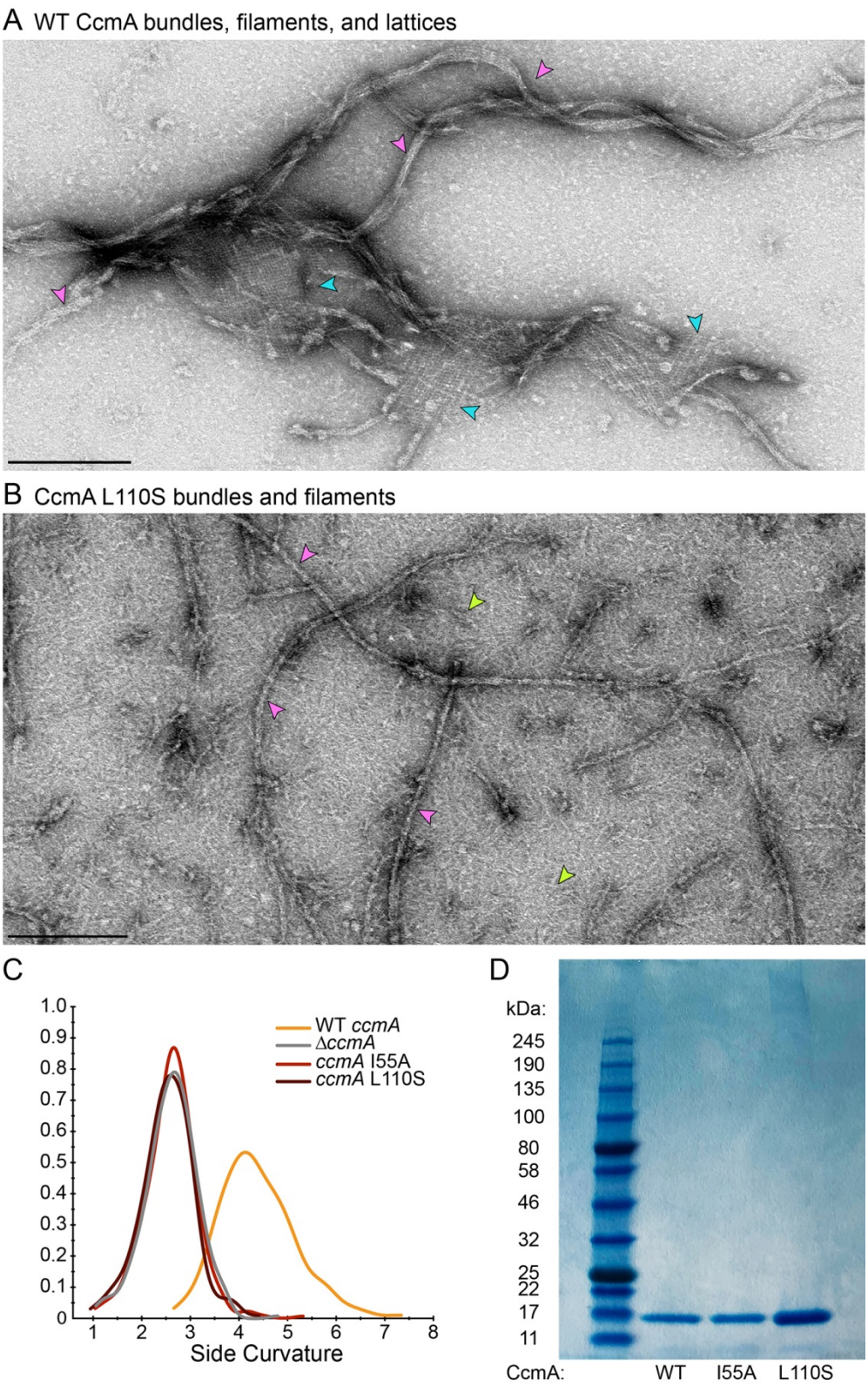

Figure 2.21. CcmA lattices and bundles.

Negatively stained TEM images of purified CcmA. Scale bars= 200 nm. Lower magnification view than in Figure 2.20 of (A) wild-type CcmA, displaying both lattices (blue arrows) and extended helical bundles (pink arrows) and (B) $CcmA^{L110S}$, displaying both individual filaments (green arrows) and bundles (pink arrows). (C) Smooth histogram of population side curvature (x-axis) of cells in Figure 2.20 F (one representative of two biological replicates). (D) Coomassie stained SDS-PAGE gel showing purified wild-type CcmA, $CcmA^{I55A}$, and $CcmA^{L110S}$.

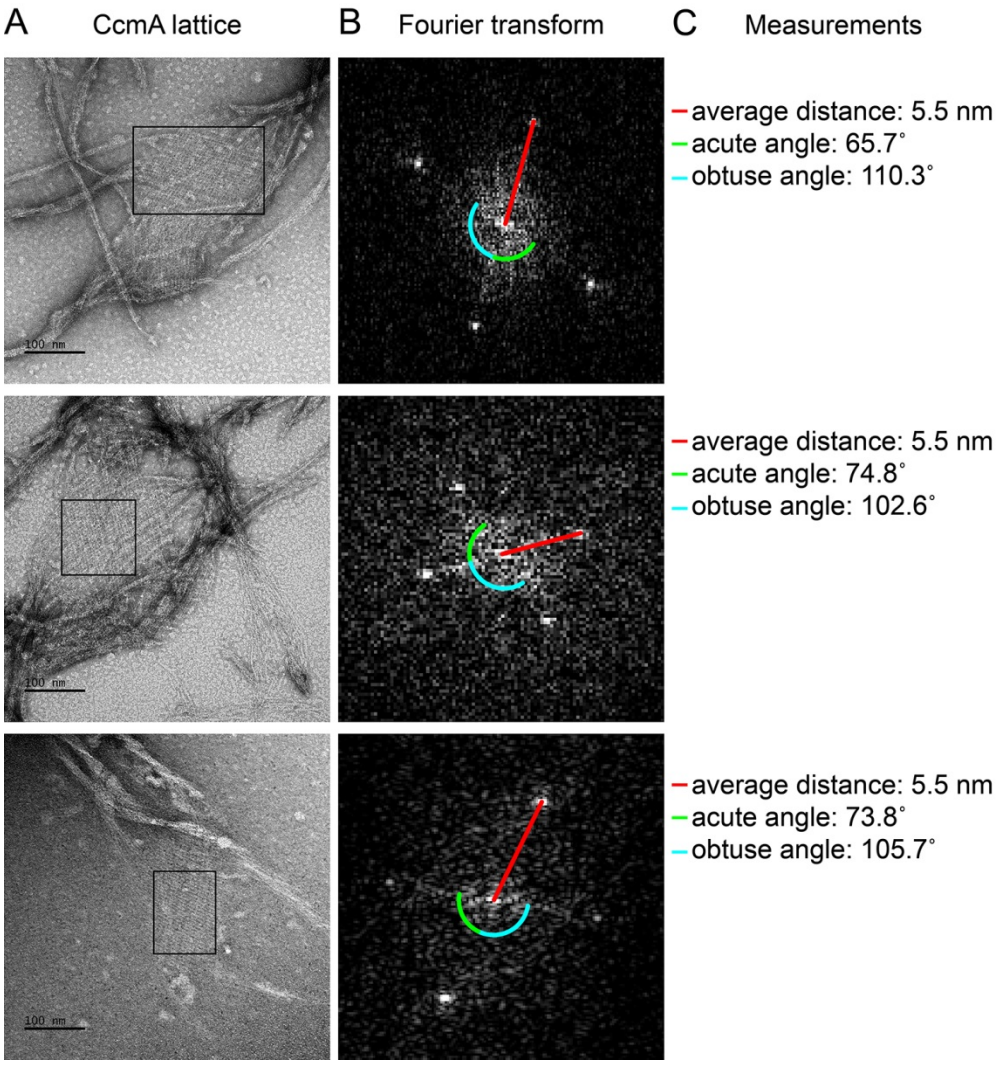

Figure 2.22. Fast Fourier transform of CcmA lattices shows regular alignment and spacing. (A) Lattices formed from purified WT CcmA in 25 mM Tris pH 8. Scale bars = 100 nm. (B) Fast Fourier transform of the region inside each corresponding box in (A) performed using Fiji

(Schindelin et al., 2012). After transformation, images were adjusted to enhance visualization (min: 134, gamma: 0.53, max: 172). (C) Average distance of bright spots from the center represents the distance between individual filaments in each lattice. Angle measurements between spots indicate the relative orientation of filaments within lattices. Average of the measurements from the three lattices: distance = 5.5 nm; acute angle = 71.5°; obtuse angle = 106.2°. Images shown are from one of three representative experiments.

2.4.6 *CcmA localization to positive curvature correlates with cell wall synthesis, CcmA polymerization, and helical cell shape*

To determine the subcellular localization of CcmA, we performed immunofluorescence of HJH1 cells expressing a 2X-FLAG epitope tag at the native locus under endogenous control as the sole copy of CcmA (Figure 2.23 A, C, and D). As shown previously (Blair et al., 2018), helical morphology is retained upon addition of the 2X-FLAG tag to the wild-type protein. Wild-type CcmA was observed at the cell boundary as puncta and short arcs and was largely absent from the center of the cell, indicating an association with the cell membrane (Figure 2.23 D). Puncta were in some cases present as lines of dots roughly parallel to the helical (long) axis of the cell, but were also found distributed along the cell surface. Immunofluorescence was also performed on cells expressing wild-type or polymerization defective CcmA ($CcmA^{I55A}$ and $CcmA^{L110S}$) using antisera raised against *H. pylori* CcmA (Figure 2.23 B, E-J). Immunostaining with CcmA preimmune serum showed background signal in the interior of wild-type and mutant cells (Figure 2.23 and 2.24). In contrast to cells expressing the wild-type version of CcmA, the mutant CcmA proteins localized as puncta at the center with minimal signal at the cell boundary (Figure 2.23 G-J).

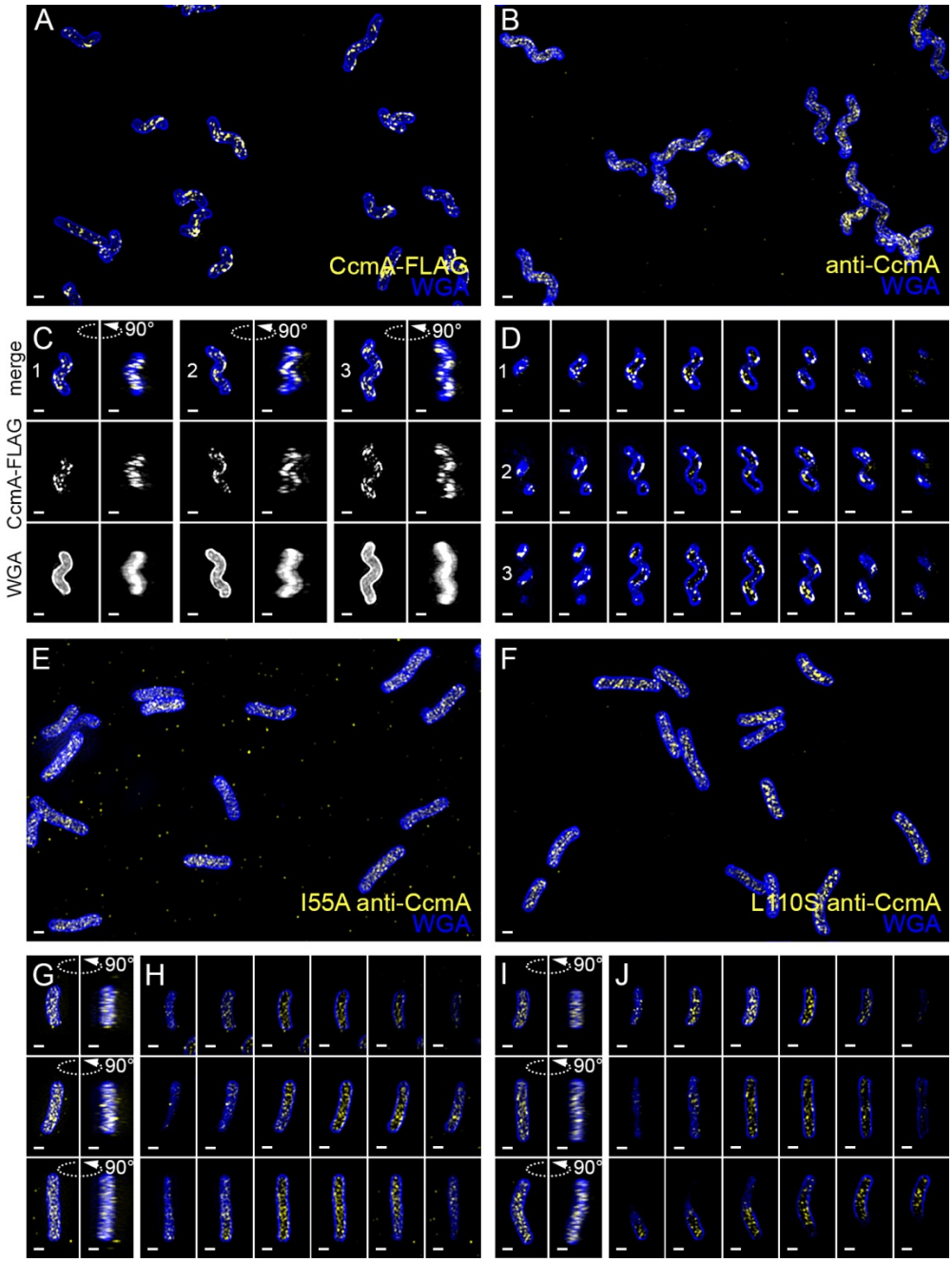

Figure 2.23. Wild-type CcmA appears as short foci on the side of the cell, but CcmA mutants I55A and L110S appear as foci in the interior of the cell.

3D SIM imaging of CcmA-FLAG cells immunostained with M2 anti-FLAG (A, C, D, yellow) or wild-type or CcmA point mutant cells immunostained with anti-CcmA (B, E-J, yellow); cells counterstained with fluorescent WGA (blue). (A) Color merged maximum projection of CcmA-FLAG immunostained with anti-FLAG and counterstained with fluorescent WGA. (B) Color merged field of view of wild-type cells immunostained with anti-CcmA and

counterstained with fluorescent WGA. (C) Top-down (left) and 90-degree rotation (right) 3D views of three individual CcmA-FLAG cells. Top: color merge; middle: anti-FLAG; bottom: fluorescent WGA. (D) Color merged z-stack views of the three CcmA-FLAG cells in C. (left to right = top to bottom of the cell). Numbering indicates matching cells. (E, F) Color merged field of view of I55A or L110S CcmA, respectively, immunostained with anti-CcmA and counterstained with fluorescent WGA. Top-down (left) and 90-degree rotation (right) 3D views of three individual I55A (G) or L110S (I) cells. (H, J) Color merged z-stack views of the three I55A cells in (G) or L110S cells in (I), respectively (Left to right = top to bottom of the cell). Scale bar = 0.5 µm. The represented images are selected from one of three biological replicates.

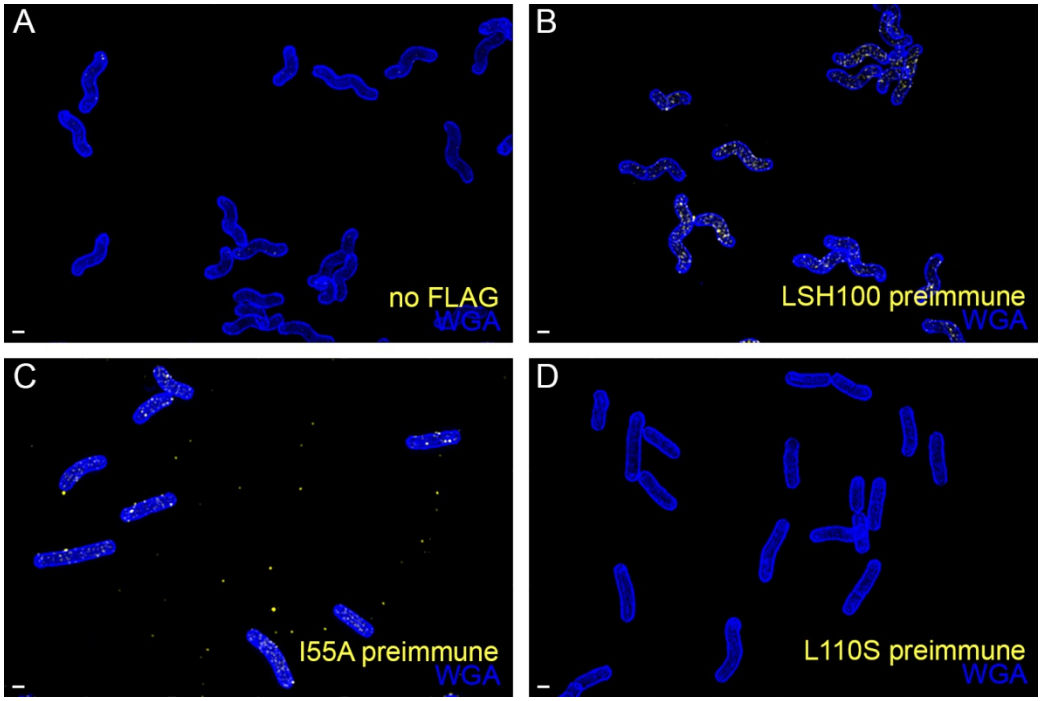

Figure 2.24. There is low signal in the no-FLAG and preimmune serum controls. (A) Wild-type (no-FLAG) cells immunostained with M2 anti-FLAG (yellow) and counterstained with fluorescent WGA (blue). (B) wild-type, (C) I55A, or (D) L110S CcmA cells immunostained with CcmA preimmune serum (yellow) and counterstained with fluorescent WGA (blue). Scale bar = 0.5 µm. The represented images are selected from one of three biological replicates.

To determine if wild-type CcmA localization corresponds to the peak of higher relative PG synthesis at the major axis area, we performed curvature enrichment analysis of CcmA-2X-FLAG immunofluorescence images of non-dividing cells. CcmA was depleted at the poles (Figure 2.26). With or without the poles, we saw a marked preference for the positive helical axis area (Figure 2.25 and Figure 2.26, red line and shaded box) that overlapped with the positive curvature enrichment peaks of MurNAc-alk and D-Ala-alk (Figure 2.23). The wild-type (no FLAG) negative control was 28.9% of the CcmA-FLAG signal (Figure 2.27 B). While the negative control showed a small peak at 5 μm^{-2}, the magnitude of the CcmA-FLAG peak was far greater (Figure 2.25 A and 2.26 A). Biological replicates are shown in Figure 2.27 A. We also performed curvature enrichment analysis on cells expressing wild-type, I55A, and L110S CcmA immunostained with anti-CcmA. Wild-type had a similar major axis area peak as CcmA-2X-FLAG (Figure 2.28 A, gold), with a lower magnitude due to a lower signal to noise ratio and an enrichment of background (preimmune) staining at negative Gaussian curvature (Figure 2.28 A, dotted gray). Preimmune signal was 33.0% of the anti-CcmA signal in wild-type (Figure 2.28 B). There was no distinguishable curvature preference for I55A or L110S CcmA compared to preimmune serum (Figure 2.28 A, red and dark red vs. dotted light pink and dotted mauve, respectively), indicating that these proteins are unable to localize preferentially to positive Gaussian surface curvature. Preimmune signal was 50.6% and 26.7% of anti-CcmA signal in I55A and L110S, respectively (Figure 2.28 B).

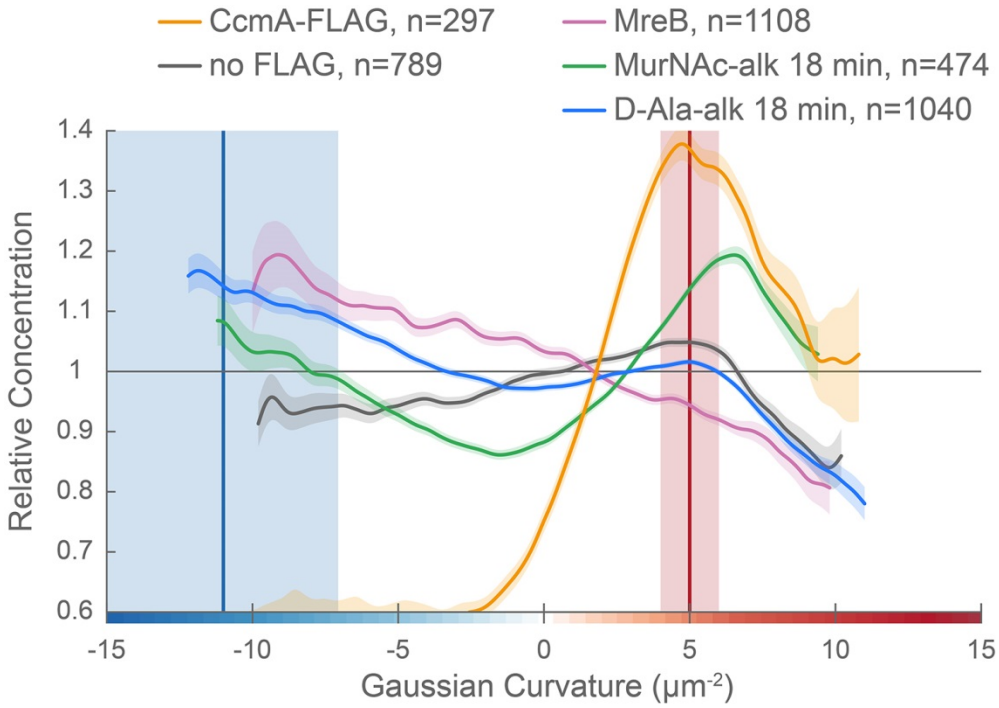

Figure 2.25. CcmA curvature preference correlates with the peak of new PG incorporation at the major axis area and MreB curvature preference correlates with new PG enrichment at negative Gaussian curvature.

(A) Overlay of sidewall only surface Gaussian curvature enrichment of relative concentration (y-axis) vs. Gaussian curvature (x-axis) from a population of computational cell surface reconstructions with poles excluded of CcmA-FLAG (gold), no-FLAG control (gray), MreB (pink, from Figure 2.16 F), MurNAc-alk (green, from Figure 2.13 C), and D-Ala-alk (blue, from Figure 2.13 C). The represented data are pooled from three biological replicates. Blue and red vertical lines and shaded regions indicate the average ±1 standard deviation Gaussian curvature at the minor and major helical axis, respectively.

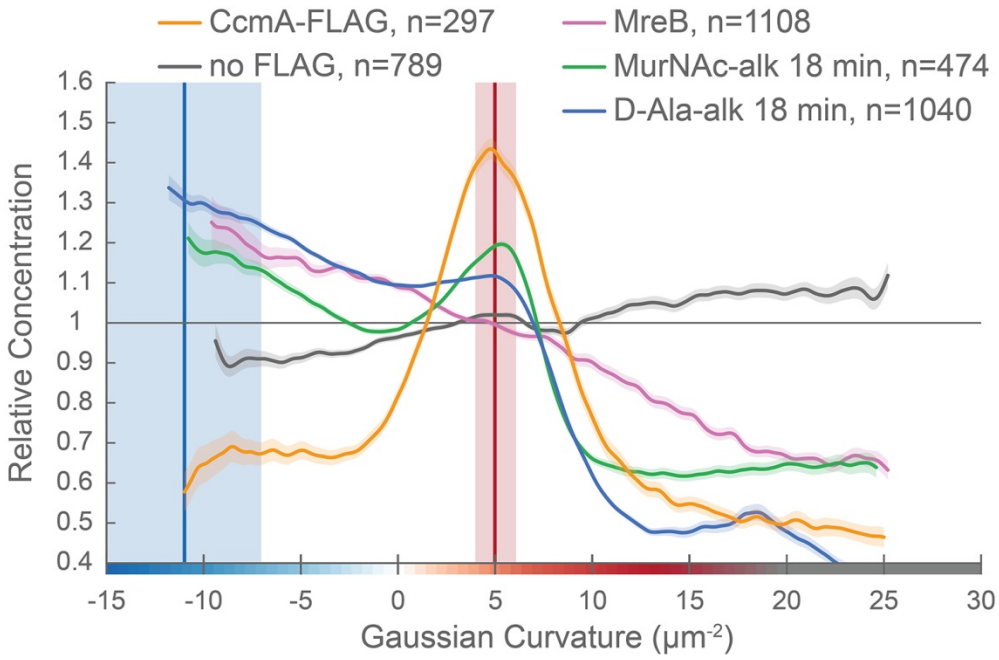

Figure 2.26. CcmA is excluded from the poles.

Whole surface (sidewall and poles) Gaussian curvature enrichment of relative signal abundance (y-axis) vs. Gaussian curvature (x-axis) derived from a population of computational cell surface reconstructions of CcmA-FLAG (gold), no-FLAG (gray), MreB (pink, from Figure 2.18), MurNAc-alk (green, from Figure 2.13 B), and D-Ala-alk (blue, from Figure 2.13 B). 90% bootstrap confidence intervals are displayed as a shaded region about each line. The represented data are pooled from three biological replicates. Blue and red vertical lines and shaded regions indicate the average ±1 standard deviation Gaussian curvature at the minor and major helical axis, respectively.

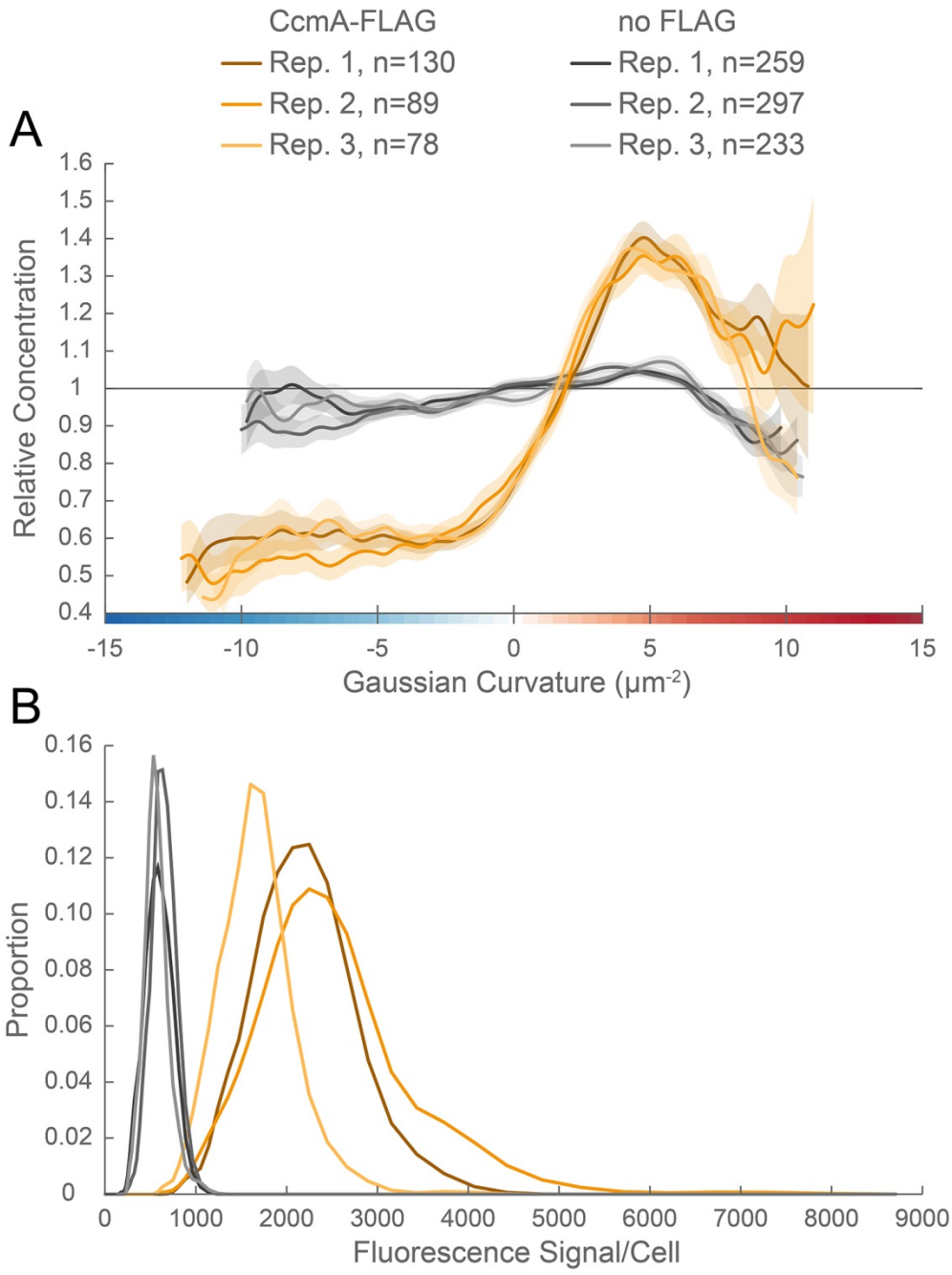

Figure 2.27. Curvature enrichment analysis of biological replicates of CcmA-FLAG. (A) Sidewall only surface Gaussian curvature enrichment of relative signal abundance (y-axis) vs. Gaussian curvature (x-axis) of the three biological replicates pooled in Figure 2.25: CcmA-FLAG (golds) and no-FLAG (grays) cells. 90% bootstrap confidence intervals are displayed as a shaded region about each line. (B) Histogram of fluorescence signal per cell divided by the number of pixels in the projected cell area for the populations in (A).

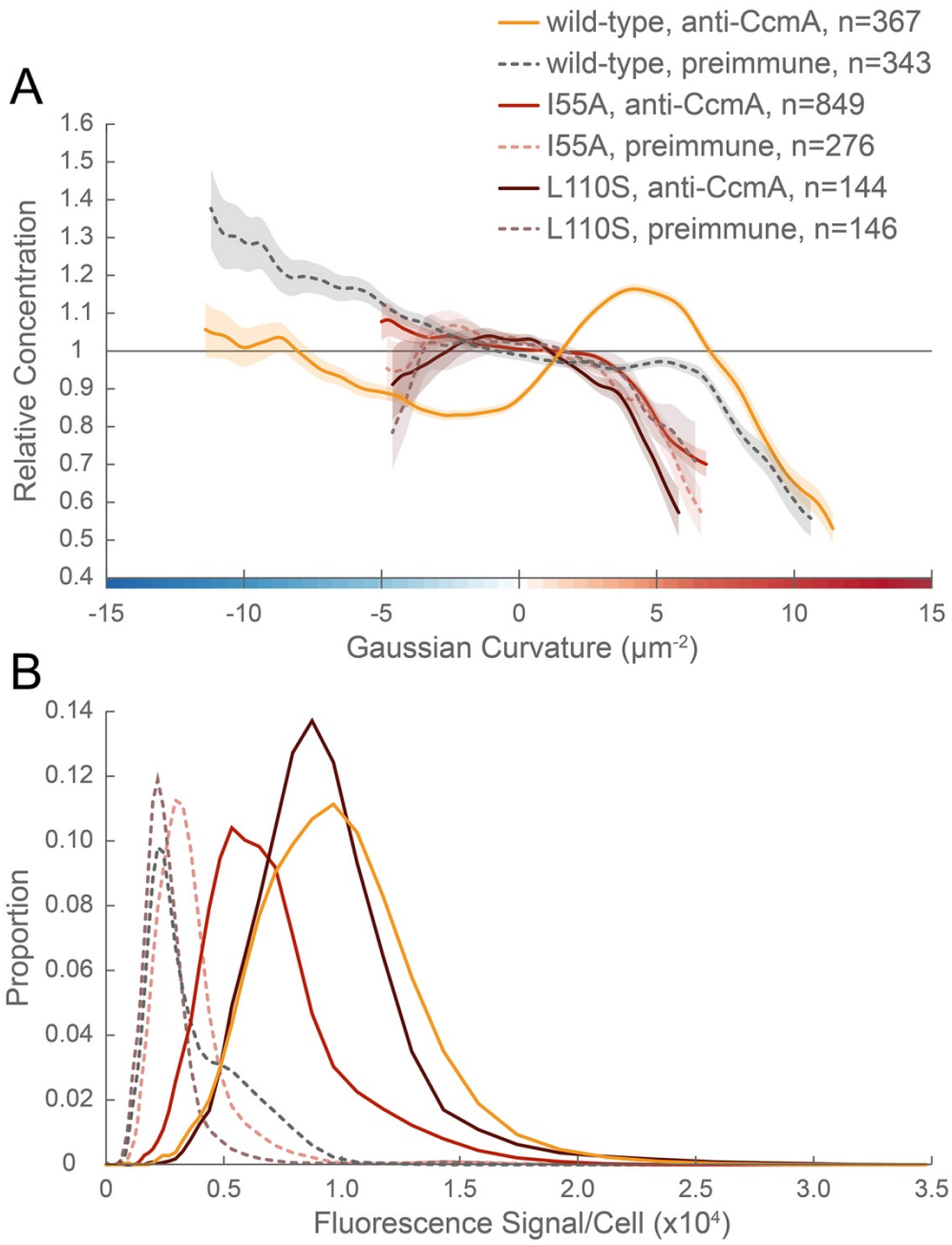

Figure 2.28. CcmA mutants are not enriched at positive Gaussian curvature.

(A) Sidewall Gaussian curvature enrichment of relative signal abundance (y-axis) vs. Gaussian curvature (x-axis) for a population of computational cell surface reconstructions with poles excluded of wild-type LSH100 cells immunostained with anti-CcmA (gold) or preimmune serum (dotted gray); CcmA I55A cells immunostained with anti-CcmA (red) or preimmune serum (dotted light pink); or CcmA L110S cells immunostained with anti-CcmA (dark red) or

preimmune serum (dotted mauve). 90% bootstrap confidence intervals are displayed as a shaded region about each line. (B) Histogram of fluorescence signal per cell divided by the number of pixels in the projected cell area for the populations in (A). The represented data are pooled from three biological replicates.

To ascertain the impact of deleting *ccmA* on MreB localization and cell wall synthesis patterning, we performed immunostaining for MreB and 18-minute MurNAc-alk and D-Ala-alk pulse labeling on Δ*ccmA* cells (JTH6, *amgK murU* Δ*ccmA*, Figure 2.29 and 2.30; dark pink, dark green, and dark blue, respectively). In Δ*ccmA* cells, MreB is present as small foci (Figure 2.31). New cell wall labeling with MurNAc-alk is present as dispersed sidewall labeling with some subtle circumferential banding, while labeling with D-Ala-alk is present as clear circumferential bands along the length of the sidewall (Figure 2.32). MreB curvature preference appears largely similar in both wild-type (HJH1, *amgK murU*, light pink) and Δ*ccmA* with poles excluded (JTH6, *amgK murU* Δ*ccmA*, dark pink) (Figure 2.29 A). When poles are included in the analysis, MreB curvature preference differs more between wild-type and Δ*ccmA*, though the general pattern of enrichment at negative Gaussian curvature remains (Figure 2.30 A). In contrast, MurNAc-alk and D-Ala-alk patterning change with loss of CcmA; there is greater relative enrichment at low magnitude negative Gaussian curvature in Δ*ccmA* cells (dark green and dark blue) compared to wild-type cells (light green and light blue). Additionally, in Δ*ccmA* cells the enrichment at positive Gaussian curvature is both less pronounced and shifted to lower Gaussian curvature than that of wild-type (Figure 2.29 B and 2.30 B). There is a small peak for MreB at approximately 3 μm^{-2}, however interpretation of the MreB peak is complicated by the presence of a peak at the same curvature range for the preimmune signal. For Δ*ccmA*, mock signal was 2.8% of the D-Ala-alk signal, 0.6% of the MurNAc-alk signal, and preimmune signal was 34.6% of anti-MreB signal (Figure 2.30 C), dotted and solid dark blue and dotted and solid dark pink,

respectively). These data suggest that proper localization of CcmA to the major helical axis may be required for promoting extra cell wall synthesis at the major axis area and patterning helical cell shape.

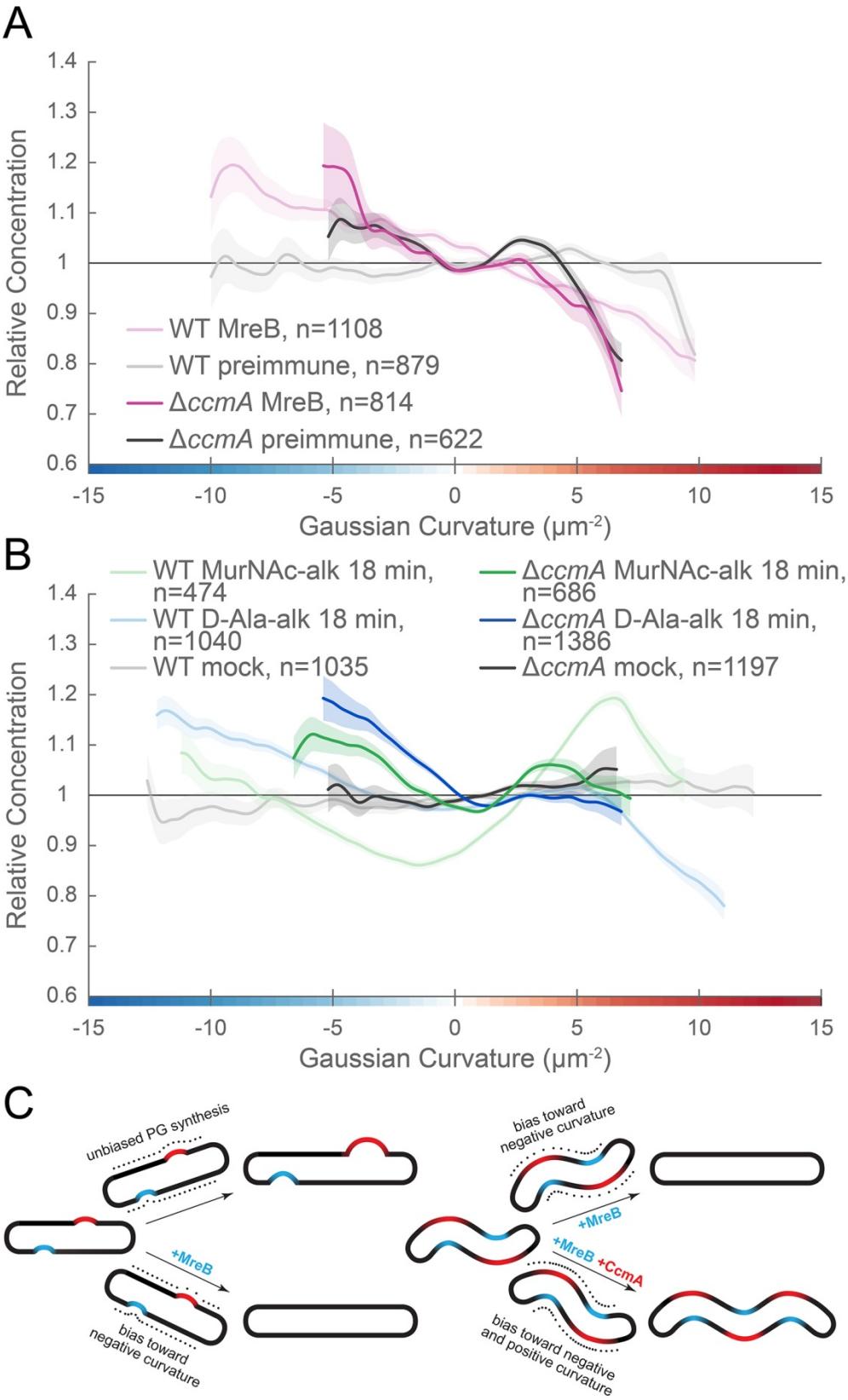
A
Relative Concentration
1.4
1.3
1.2
1.1
1
0.9
0.8
0.7
0.6
WT MreB, n=1108
WT preimmune, n=879
ΔccmA MreB, n=814
ΔccmA preimmune, n=622
-15
-10
-5
0
5
10
15
Gaussian Curvature (μm-2)
B
WT MurNAc-alk 18 min, n=474
WT D-Ala-alk 18 min, n=1040
WT mock, n=1035
ΔccmA MurNAc-alk 18 min, n=686
ΔccmA D-Ala-alk 18 min, n=1386
ΔccmA mock, n=1197
Relative Concentration
Gaussian Curvature (μm-2)
C
unbiased PG synthesis
+MreB
bias toward negative curvature
bias toward negative curvature
+MreB
+MreB +CcmA
bias toward negative and positive curvature

Figure 2.29. MreB and CcmA contribute to cell wall synthesis patterning. (A, B) Sidewall only Gaussian curvature enrichment of relative concentration (y-axis) vs. Gaussian curvature (x-axis) from a population of computational cell surface reconstructions of HJH1 (*amgK murU*) and JTH6 (*amgK murU* Δ*ccmA*) of cells immunostained with (A) anti-MreB (HJH1, light pink; JTH6, dark pink) or preimmune serum (HJH1, light gray; JTH6, dark gray) or (B) 18-minute MurNAc-alk (HJH1, light green; JTH6, dark green) or D-Ala-alk (HJH1, light blue; JTH6, dark blue) pulse-labeled or mock-labeled (HJH1, light gray; JTH6, dark gray) cells. 90% bootstrap confidence intervals are displayed as a shaded region about each line. The represented data are pooled from three biological replicates. (C) Model of the contribution of synthesis patterning to rod and helical shape maintenance. Dots indicate different densities of cell wall synthesis that can decrease or propagate non-zero Gaussian curvature. Colored shading indicates local regions of positive (red) and negative (blue) Gaussian curvature.

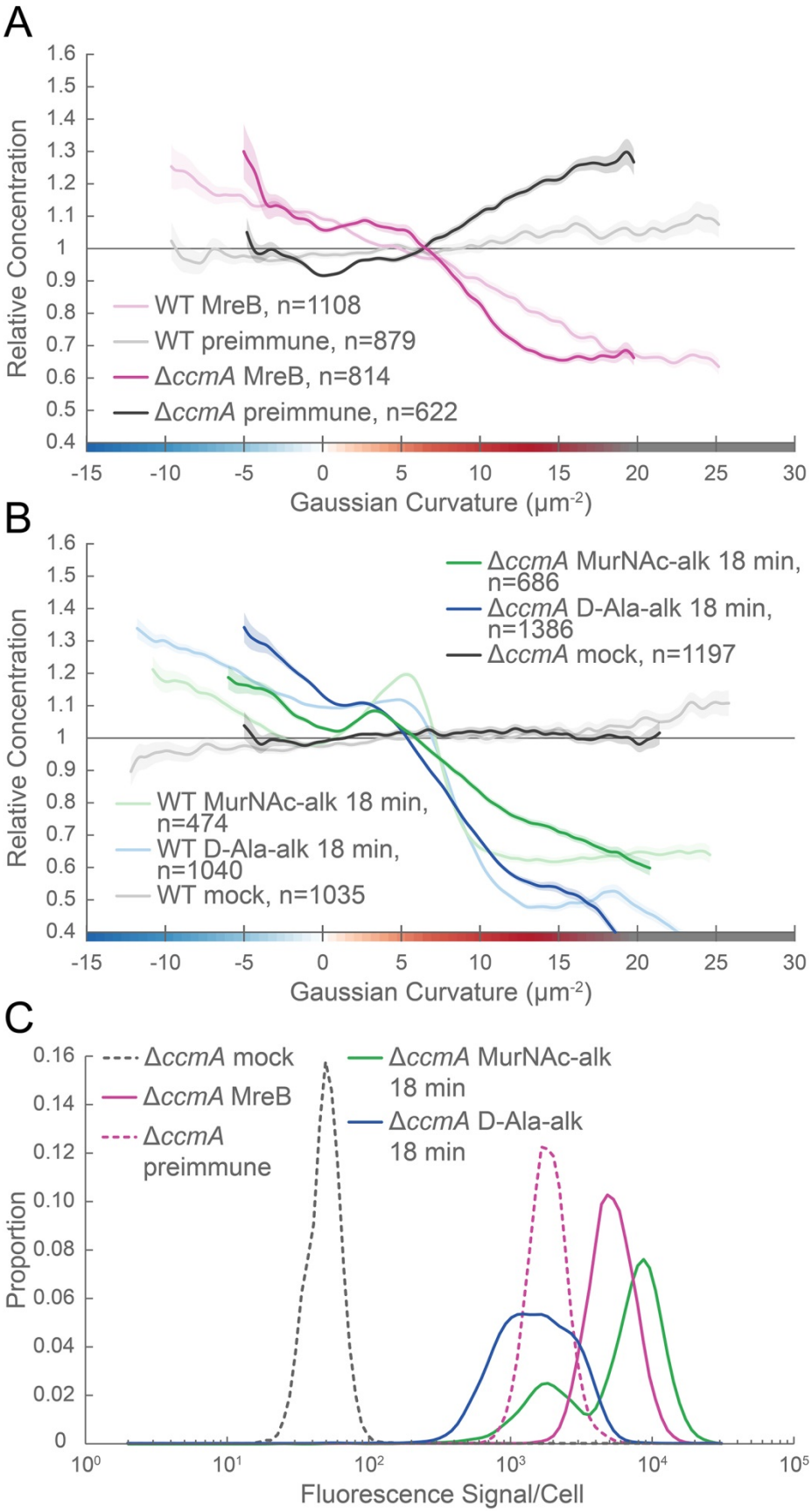
A
Relative Concentration
WT MreB, n=1108
WT preimmune, n=879
ΔccmA MreB, n=814
ΔccmA preimmune, n=622
Gaussian Curvature (μm-2)
B
Relative Concentration
ΔccmA MurNAc-alk 18 min, n=686
ΔccmA D-Ala-alk 18 min, n=1386
ΔccmA mock, n=1197
WT MurNAc-alk 18 min, n=474
WT D-Ala-alk 18 min, n=1040
WT mock, n=1035
Gaussian Curvature (μm-2)
C
Proportion
ΔccmA mock
ΔccmA MreB
ΔccmA preimmune
ΔccmA MurNAc-alk 18 min
ΔccmA D-Ala-alk 18 min
Fluorescence Signal/Cell

Figure 2.30. Cell wall synthesis patterning but not MreB curvature preference is altered by loss of CcmA.

(A, B) Whole surface (sidewall and poles) Gaussian curvature enrichment of relative concentration (y-axis) vs. Gaussian curvature (x-axis) from a population of computational cell surface reconstructions of wild-type (WT, HJH1, *amgKmurU*) and Δ*ccmA* (Δ*ccmA*, JTH6, Δ*ccmA amgKmurU*) of cells immunostained with (A) anti-MreB (wild-type, light pink; Δ*ccmA*, dark pink) or preimmune serum (WT, light gray; Δ*ccmA*, dark gray) or (B) 18-minute MurNAc-alk (HJH1, light green; JTH6, dark green) or D-Ala-alk (HJH1, light blue; JTH6, dark blue) pulse-labeled or mock-labeled (HJH1, light gray; JTH6, dark gray) cells. 90% bootstrap confidence intervals are displayed as a shaded region about each line. (C) Histogram of fluorescence signal per cell divided by the number of pixels in the projected cell area for the JTH6 populations in (A, 18 minute D-Ala-alk and mock labeling, solid and dotted dark blue, respectively) and (B, anti-MreB and preimmune immunostaining, solid and dotted dark pink, respectively). The represented data are pooled from three biological replicates.

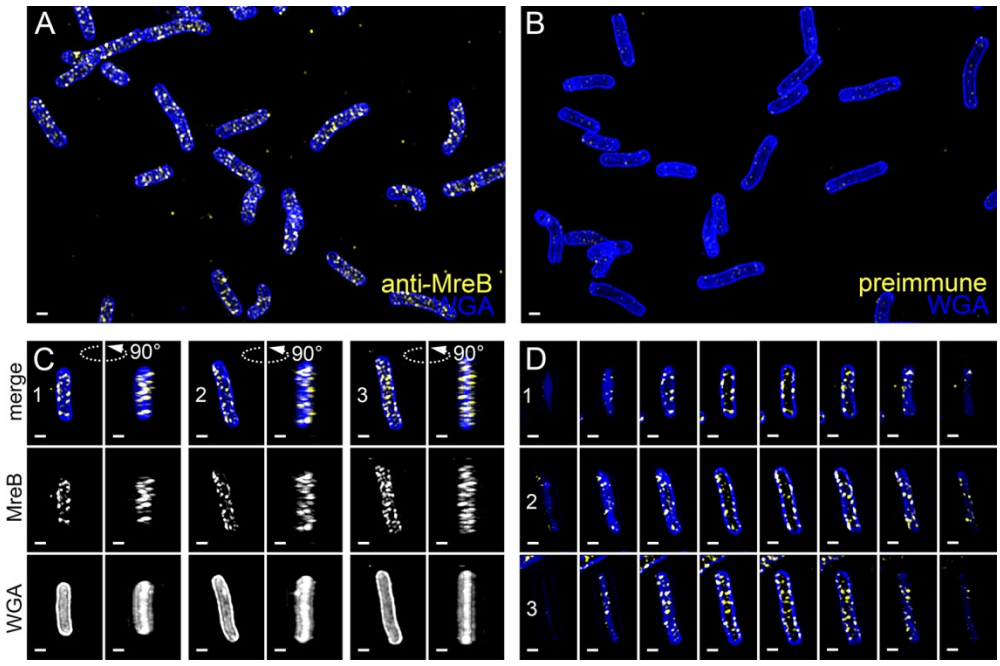

Figure 2.31. MreB is present as small foci along the sidewall in Δ*ccmA*

3D SIM imaging of Δ*ccmA* cells immunostained with anti-MreB (A, C, D, yellow) or preimmune serum (B) and counterstained with fluorescent WGA (blue). Color merged maximum projection of anti-MreB (A) or preimmune (B). (C) Top-down (left) and 90-degree rotation (right) 3D views of three individual cells. Top: color merge; middle: anti-MreB (C); bottom: fluorescent WGA. (D) Color merged z-stack views of the three cells in C, (left to right = top to bottom of the cell). Numbering indicates matching cells. Scale bar = 0.5 μm. The represented images are selected from one of three biological replicates.

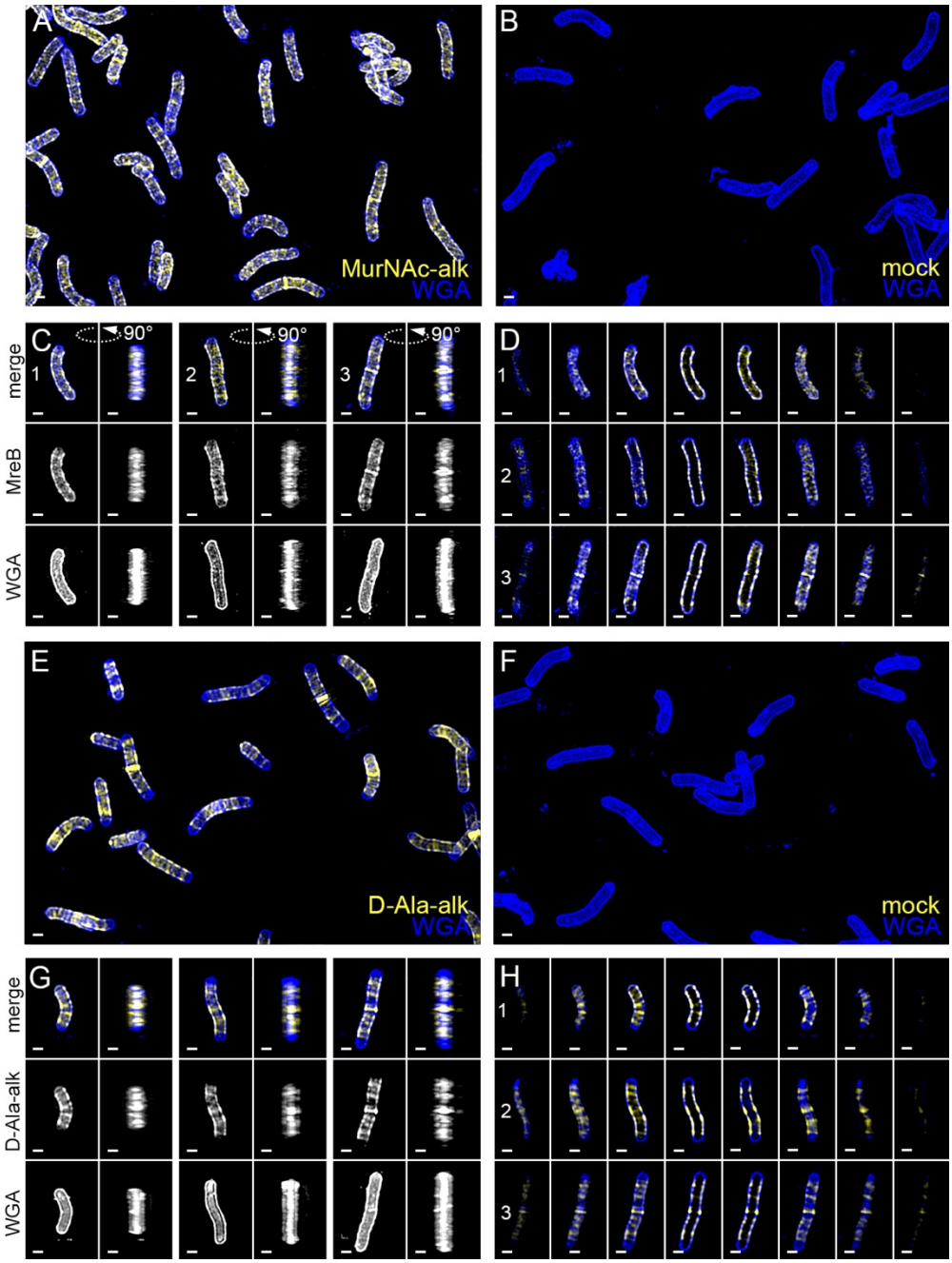

Figure 2.32. New cell wall growth appears as diffuse labeling and circumferential bands dispersed along the sidewall, excluded from poles, and present at septa in Δ*ccmA*.

3D SIM imaging of Δ*ccmA* cells labeled with an 18-minute pulse of MurNAC-alk (A, C, D, yellow) or D-Ala-alk (E, G, H, yellow) or mock labeled (B, F) and counterstained with fluorescent WGA (blue). Color merged maximum projection of MurNAc-alk (A), D-Ala-alk (E), or mock (B, F) labeling with fluorescent WGA counterstain. (C, G) Top-down (left) and 90-degree rotation (right) 3D views of three individual cells, including a dividing cell (C, G, right).

Top: color merge; middle: 18-minute MurNAc-alk (C) or 18-minute D-Ala-alk (G); bottom: fluorescent WGA. (D, H) Color merged z-stack views of the three cells in C, G, respectively (left to right = top to bottom of the cell). Numbering indicates matching cells. Scale bar = 0.5 μm. The represented images are selected from one of three biological replicates.

2.5 DISCUSSION

Bacterial cell shape is driven by patterning the cell wall. Maintenance of a cylindrical rod form in a variety of bacteria relies on the action of the actin-like protein MreB, which helps to pattern PG synthesis along the sidewall (Typas *et al.*, 2012, Zhao *et al.*, 2017). Detailed analysis of MreB localization in the Gram-negative straight-rod *E. coli* indicates that centerline straightness and diameter uniformity rely on MreB curvature enrichment (Bratton *et al.*, 2018, Ursell *et al.*, 2014), which may result from circumferential motion about the cell (Wong *et al.*, 2019). One working model is that MreB localization and cell wall synthesis are enhanced at cell wall dimples (negative Gaussian curvature), cylindrical regions (zero Gaussian curvature), and limited at cell wall bulges (positive Gaussian curvature). This pattern minimizes local curvature as growth progresses (Figure 2.29 C, left). While such a growth pattern is at odds with maintaining areas of negative and positive Gaussian curvature required for curved- and helical-rod shapes, MreB is present in many bacteria with these shapes. To be able to maintain curvature in the presence of MreB, the curved-rod shaped Gram-negative Proteobacteria *Caulobacter crescentus* and *Vibrio cholerae* appear to limit the relative levels of PG synthesis at negative curvatures through the action of long, cell-spanning cytoskeletal filaments (CreS and CrvA) that preferentially localize to the minor axis (negative Gaussian curvature) and enable cells to increase relative synthesis rates on the opposite side of the wall (positive Gaussian curvature) (Bartlett *et al.*, 2017, Cabeen *et al.*, 2009). We propose that the helical Proteobacterium *H. pylori*

uses different mechanisms than *C. crescentus* and *V. cholerae* to maintain the even higher levels of negative and positive Gaussian curvature required for its helical cell shape; *H. pylori* leverages the bactofilin CcmA, which localizes preferentially to the major helical axis area, to promote synthesis at positive Gaussian curvatures on the sidewall, and supplements the MreB-associated enhanced synthesis that is enriched at negative Gaussian curvatures (the minor helical axis) (Figure 2.29 C, right). Adding the contribution of CcmA to the PG synthesis patterning allows *H. pylori* to maintain curvatures in the presence of MreB-associated PG synthesis.

To probe cell wall synthesis patterns in *H. pylori*, we used distinct metabolic probes to label the sugar (MurNAc-alk) and peptide (D-Ala-alk) portions of the polymer. While both probes indicate enhanced synthesis at the major and minor helical axes relative to the rest of the sidewall, there were considerable differences in enrichment peak magnitudes between the MurNAc-alk and D-Ala-alk probes. Modified D-alanine is thought to be incorporated into the cell wall through the action of synthesis-associated D-D-transpeptidases and cell wall-modifying L-D-transpeptidases, potentially complicating interpretation of this label. *H. pylori* does not have any known functional L-D-transpeptidases and no detectable 3-3 crosslinks, a hallmark of L-D-transpeptidase activity (Costa *et al.*, 1999, Sycuro *et al.*, 2010). Thus, signal from D-Ala-alk likely reports on D-D-transpeptidase activity. It is possible that D-D-transpeptidation may also occur separately from synthesis to promote cell wall remodeling or that the rates of synthesis-associated transpeptidation activity may vary on different sides of the cell. We only observed D-Ala-alk incorporation at the penta position (Figure 2.7 C and Figure 2.10). *H. pylori* has a pentapeptide-rich cell wall and it is unclear if *H pylori* actively regulates pentapeptide trimming. However, the cell shape determining protein Csd3/HdpA has been shown to have weak pentapeptide carboxypeptidase activity in vitro (Bonis *et al.*, 2010). Pentapeptides can also be

trimmed via transpeptidase-mediated hydrolysis (Ghuysen, 1991). Curvature-biased trimming by either mechanism could also contribute to the difference between the D-Ala-alk and MurNAc-alk curvature enrichment profiles. The MurNAc probes have none of these complications as they are embedded in the glycan.

We provide the first example of MreB curvature enrichment analysis in a curved- or helical-rod bacterium and show that enrichment at negative Gaussian curvature is retained, even across the broad range of curvatures represented on the *H. pylori* sidewall. While there has been report of MreB being non-essential in *H. pylori* (Waidner *et al.*, 2009), the mutated strains could not be revived from frozen stocks when requested. In our strain, we could only knock out *mreB* if we first supplied the cells with a second copy of *mreB* at separate locus, indicating that MreB is functional and important. We propose that MreB promotes the peak of PG synthesis we observed at negative Gaussian curvature given its preference for this curvature in *H. pylori* and its role in localizing PG synthesis activity in other organisms. To enable maintenance of high sidewall curvature in the presence of the MreB-driven straight-rod cell growth pattern, we suggest that *H. pylori* augments the default rod pattern by means of enhanced growth at the major axis area that is independent of MreB (Figure 2.29 C).

A major outstanding question is how *H. pylori* enhances PG synthesis activity at the major axis area. Our 3D analysis establishes that the average Gaussian curvature along the major axis is distinct from that along the minor axis (5 vs. -11 μm^{-2}, respectively) and that the major axis is on average 70% longer than the minor axis in the strain used here. Cytoskeletal elements can form higher-order structures that reach a sufficient size scale to be able to sense surface curvature, providing a potential mechanism for targeting synthesis to a specific range of positive Gaussian curvature. The bactofilin CcmA is the only non-essential cytoskeletal protein we have identified

in our strain background that makes an indispensable and non-redundant contribution to helical shape maintenance. In contrast to the cell spanning filaments CreS in *C. crescentus* and CrvA in *V. cholerae*, which reside at the minor axis, we show that CcmA is present in cells as numerous puncta that have a preference for the major axis area. We propose that CcmA acts to enhance synthesis on its preferred cell face by promoting PG synthesis locally (at positive Gaussian curvature). In support of this hypothesis, the bactofilins BacA and BacB in *C. crescentus* recruit the PG synthase PBPC to assist in stalk elongation, indicating that they help recruit PG synthesis (Kühn *et al.*, 2010). Additionally, our group recently showed that CcmA co-purifies with Csd5 and MurF, an enzyme involved in PG precursor synthesis (Blair *et al.*, 2018), and separately that both CcmA and MurF are within the top 20 mass spec hits of a Csd7 immunoprecipitation(Yang *et al.*, 2019). Furthermore, we demonstrate that in the absence of CcmA, similarly to in wild-type, MreB is still enriched at negative Gaussian curvature, but that MurNAc-alk and D-Ala-alk synthesis patterning shift to more closely resemble the MreB curvature enrichment profile. In Δ*ccmA*, synthesis at negative Gaussian curvature plays a much more significant contribution to the overall synthesis pattern than does synthesis at positive curvature, as seen by the greater relative concentration at Gaussian curvature values below 0 μm^{-2}. The MurNAc-alk and D-Ala-alk signals do show a subtle peak at low magnitude positive Gaussian curvature (approximately 3 μm^{-2}), however the peak is far less prominent (greatly reduced peak to trough distance). Given that there is still some curvature in Δ*ccmA* cells, it is not necessarily surprising that there is still some enrichment at positive Gaussian curvature. CcmA is one of a suite of proteins required for helical cell shape maintenance; it is possible that other cell shape proteins can influence PG synthesis to promote some limited curvature in the absence of CcmA, consistent with multiple complementary mechanisms being required for helical shape maintenance.

It is possible that CcmA may also help promote localized crosslink trimming, as loss of CcmA results in an increased degree of crosslinking in the sacculus (Sycuro *et al.*, 2010). Crosslink trimming may help promote synthesis but could also play some other role in helical shape maintenance. CcmA dynamics could also influence its ability to promote cell shape. While CcmA does not require a nucleotide cofactor for polymerization, it may be mobile through coupling with the motion of PG synthesis machinery. In other organisms, MreB filaments travel in a roughly circumferential path around the cell and we expect MreB to behave similarly in *H. pylori*.

Loss of CcmA results in cells with highly diminished cell curvature and without significant helical twist. Beyond helping promote curvature by localized PG synthesis, it is possible that CcmA also helps generate twist. We observed helical bundles of filaments in vitro by TEM. These bundles are far longer than the foci we see by immunofluorescence, but foci within the cell may consist of short twisted filament bundles and/or skewed lattices. While it remains unclear how filament or lattice twist would be coupled to cell wall twist, the bactofilin LbbD modulates helical pitch in the spirochete *Leptospira biflexa* (Jackson *et al.*, 2018). Both CcmA point mutant variants show altered or no polymerized structures under a variety of buffer conditions in vitro and fail to localize to the cell envelope in vivo. It is still unclear which structures are relevant and if altering higher-order structures abolishes CcmA function by disrupting protein-protein interactions and/or CcmA localization.

Overall, our results are consistent with a model in which MreB-patterned straight-rod shape is the default pattern for *H. pylori* cells and helical shape is facilitated by adding major axis area PG synthesis via CcmA to augment straight-rod cell wall patterning. The enrichment of new cell wall synthesis to both negative Gaussian curvature, as expected for straight-rod shape, and to the

major axis area indicates one mechanism for achieving helical shape, but it is not apparent how this growth pattern on its own could be sufficient for helical shape maintenance. The lower relative amount of synthesis at Gaussian curvatures corresponding to the sides of the cell body in comparison to the major and minor axis areas is both unexpected and counterintuitive; it suggests additional mechanisms may be required to maintain helical shape. Indeed, the noted difference between enrichment of D-Ala-alk and MurNAc-alk suggests that spatially-coordinated cell wall modification occurs. Curvature-dependent differences in crosslinking could alter cell wall mechanical properties and PG density; perhaps the PG at the side of the cell is less dense, thus requiring less PG synthesis during growth. Furthermore, our labeling strategy allowed us to determine the curvature bias of new PG insertion, spatially-regulated turnover of old PG may also contribute to cell wall homeostasis. We also do not know if super-twisting of the cell wall occurs during growth: does PG on the major axis remain at the major axis as the cell grows?

We employed sophisticated computational tools to demonstrate that *H. pylori* must achieve a much broader distribution of sidewall Gaussian curvature than the curved-rod bacteria *C. crescentus* and *V. cholerae* and that it uses distinct mechanisms to achieve these curvatures. In elucidating the spatial patterning of new cell wall synthesis, we have revealed one of the downstream mechanisms of *H. pylori*'s cell shape-determining program.

2.6 Materials and Methods

Table 2.2. Strains used in this study

Key Resources Table				
Reagent type (species) or resource	**Designation**	**Source or reference**	**Identifiers**	**Additional information**

antibody	Monoclonal ANTI-FLAG® M2 antibody produced in mouse	Sigma	Cat# F1804, RRID:AB_262044	IF(1:200)
antibody	Goat anti-Mouse IgG (H+L) Highly Cross-Adsorbed Secondary Antibody, Alexa Fluor 488	Invitrogen	Cat# A-11029, RRID:AB_2534088	IF(1:200)
antibody	Goat anti-Rabbit IgG (H+L) Cross-Adsorbed Secondary Antibody, Alexa Fluor 488	Invitrogen	Cat#: A-11008; RRID: AB_143165	IF(1:200)
antibody	Polyclonal rabbit αCcmA	(Blair et al., 2018)		IF (1:200); WB (1:10,000)
antibody	Polyclonal rabbit αMreB (*H. pylori*)	(Nakano et al., 2012)		IF (1:500); WB (1:25,000)
commercial assay, kit	Click-iT Cell Reaction Buffer Kit	Invitrogen	Cat# C10269	
chemical compound, drug	Alexa Fluor™ 555 Azide, Triethylammonium Salt	Invitrogen	Cat# A20012	
chemical compound, drug	D-Ala-alk ((R)-2-Amino-4-pentynoic acid)	Boaopharma	Cat# B60090	
chemical compound, drug	MurNAc-alk	(Liang et al., 2017)		
chemical compound, drug	MurNAc	Sigma	Cat# A3007	

chemical compound, drug	Wheat Germ Agglutinin, Alexa Fluor 488 Conjugate	Invitrogen	Cat# W11261	
chemical compound, drug	Wheat Germ Agglutinin, Alexa Fluor 555 Conjugate	Invitrogen	Cat# W32464	
other	ProLong Diamond Antifade Mountant	Invitrogen	P36961	

2.6.1 *Cultures and growth*

H. pylori (LSH100 and derivatives, Table 2.2) was grown on horse blood (HB) agar plates (Humbert & Salama, 2008) incubated at 37°C under micro-aerobic conditions in either 90% air, 10% CO2 (dual-gas) or in 10% CO2, 10% O2, 80% N2 (tri-gas). For resistance marker selection, HB agar plates were supplemented with 15 µg/ml chloramphenicol, 25 µg/ml kanamycin, or 30 mg/ml sucrose, as appropriate. Liquid *H. pylori* cultures were grown shaking in Brucella broth (BD Biosciences, Sparks, MD) supplemented with 10% heat-inactivated fetal bovine serum (Gemini Bio-Products, West Sacramento, CA) (BB10) at 37°C in tri-gas conditions. For plasmid selection and maintenance, *E. coli* cultures were grown in lysogeny broth (LB) or agar supplemented with 100 µg/ml ampicillin or as described at 37°C.

Table 2.3. Strains used in this study

Strain	**Genotype/description**	**Construction**	**Reference**
LSH100	Wild-type: mouse-adapted G27 derivative	-	Lowenthal et al., 2009
LSH141 (*Δcsd2*)	LSH100 *csd2::cat*	-	Sycuro et al., 2010
TSH17 (*Δcsd6*)	LSH100 *csd6::cat*	-	Sycuro et al., 2013
LSH108	LSH100 *rdxA::aphA3sacB*	-	Sycuro et al., 2010
HMJ_Ec_pLC292-	*E. coli* TOP10 pLC292-KU	Transformation of TOP10	This study

KU		with pLC292-KU	
HJH1	LSH100 *rdxA::amgKmurU*	Integration of pLC292-KU into LSH108	This study
IM4	LSH100 *mcGee:mreB*	Integration of pIM04 into LSH100	This study
JTH3	LSH100 *ccmA:2X-FLAG:aphA3*	-	Blair et al., 2018
JTH5	LSH100 *ccmA:2X-FLAG:aphA3 rdxA::amgKmurU*	Natural transformation of HJH1 with JTH3 genomic DNA	This study
KGH10	NSH57 *ccmA::catsacB*	-	Sycuro et al., 2010
LSH117	LSH100 *ccmA::catsacB*	Natural transformation of LSH100 with KGH10 genomic DNA	This study
SSH1	LSH100 $ccmA^{I55A}$	Natural transformation with *ccmA I55A* PCR product	This study
SSH2	LSH100 $ccmA^{L110S}$	Natural transformation with *ccmA L110S* PCR product	This study
LSH142 (Δ*ccmA*)	LSH100 *ccmA::cat*	-	(Sycuro *et al.*, 2010)
JTH6	LSH100 *rdxA::amgKmurU ccmA::cat*	Natural transformation of HJH1 with LSH142 genomic DNA	This study

2.6.2 *AmgK MurU strain construction*

AmgK and MurU-encoding sequences were PCR amplified from expression plasmid pBBR-KU (Liang *et al.*, 2017) using primers AmgK_BamHI_F and MurU_HindIII_R (Table 2.3). The

AmgK MurU amplification product and plasmid pLC292 (Terry *et al.*, 2005) were digested with BamHI-HF and HindIII-HF (New England BioLabs, Ipswich, MA) at 37°C for 1 hour and cleaned up with the QIAquick PCR Purification Kit (Qiagen, Valencia, CA) according to manufacturer instructions. Insert and vector were then ligated with T4 ligase (New England BioLabs) for 10 minutes at room temperature, inactivated at 65°C for 20 minutes, and stored at -20°C. 1 µl of the ligation mixture was transformed into OneShot TOP10 competent cells (Invitrogen, Carlsbad, CA) according to manufacturer instructions. Cells were plated on LB-ampicillin plates and incubated overnight at 37°C. Colonies were screened by colony PCR using primers AmgK_BamHI_F and MurU_HindIII_R. Plasmid pLC292-KU was purified from the resulting clone, HMJ_Ec_pLC292-KU, using the QIAprep Spin Miniprep Kit (Qiagen) according to manufacturer instructions. Recipient *H. pylori* containing a *aphA3sacB* cassette at the *rdxA* locus(LSH108 (Sycuro *et al.*, 2010)) were transformed with the purified plasmid. Transformants were selected on sucrose plates and kanamycin sensitivity was verified. Genomic DNA was purified using the Wizard Genomic DNA Purification Kit (Promega, Fitchburg, WI) and insertion of *amgK murU* at *rdxA* was verified by PCR amplifying and sequencing the locus using primers RdxA_F1P1 and RdxA_dnstm_RP2. The resulting confirmed strain was named HJH1. JTH6, Δ*ccmA* with *amgK murU* was generated by natural transformation of HJH1 with genomic DNA from LSH142 and selection on chloramphenicol plates. Deletion of *ccmA* was confirmed by PCR.

2.6.3 mreB *merodiploid stran construction and quantitative transformation assays*

To generate the *mreB* merodiploid strain IM4, the promoter of the operon containing *mreB* and a 5’ KpnI site was amplified from LSH100 genomic DNA using primers O#9 ProMreB (KpnI_5') and O#10 ProMreB_R. The *mreB* coding sequence with a 3’ XhoI site was PCR amplified using

primers O#11 ProMreB_F and O#12 ProMreB (XhoI_3'). These products were joined using PCR SOEing (Horton, 1995). A modified Bluescript SK vector, pDCY40, containing the RK6 origin and *aphA3* flanked by two 550 bp segments of DNA from a previously characterized neutral locus (McGee locus) located between HPG27_186 and HPG27_187 (Langford *et al.*, 2006). pDCY40 was constructed using isothermal assembly (Gibson *et al.*, 2009) of six pieces amplified using primers O#68 McGee-1F, O#69 McGee-1, O#70 MCS-kan-F, O#71 MCS-kan-R, O#72 McGee-2, O#73 McGee-2R, O#74 McGee-R6K-F, O#75 McGee-R6K-R, O#76 R6K-amp-F, O#77 R6K-amp-R, O#78 MCS fragment, O#79 McGee-MCS-F, and O#80 McGee-MCS-R. The PCR SOEing product and pDCY40 were digested with KpnI and XhoI and ligated to generate vector pIM04DY containing the promotor-*mreB* fusion with flanking *mcGee* locus sequences. pIM04DY was transformed into Chung competent DH5αλpir cells and selected on LB plates with 50 µg/ml ampicillin and 0.2% glucose. The pIM04DY insert was sequence confirmed using primers O#36 pMcGee-Insert-F, O#45 MreBC-seq-F2, O#47 MreB-seq-F2, O#28 MreBseq-F3, and O#37 pMcGee-Insert-R. Linear DNA was PCR amplified from pIM04DY using primers O#73 McGee-2R and O#68 McGee-1F. LSH100 was transformed with this PCR product and kanamycin resistant clones were verified by Sanger sequencing. IM4 was generated by back-crossing LSH100 with genomic DNA from one of these verified clones.

ccmA::CAT linear DNA was PCR amplified from LSH142 (Δ*ccmA*) genomic DNA (Sycuro *et al.*, 2010) using primers csd1F and G1480_DnStrmP2. *mreB::CAT* linear DNA was generated using previously published methods (Sycuro *et al.*, 2010). Briefly, PCR products were amplified from LSH100 genomic DNA using primers MreB_start_F and MreB_cat_up_R for the upstream fragment and Cat_mreB_dn_F and MreB_end_R for the downstream fragment. The CAT cassette was amplified from LSH123 (Δ*csd5*) genomic DNA (Sycuro *et al.*, 2012) using primers

C1 and C2. These products were annealed using PCR SOEing (Horton, 1995). For transformations, LSH100 and IM4 were grown up to mid-log phase in liquid. $4.5x10^5$ cells in liquid were spotted onto plates, allowed to dry, and were incubated three hours prior to transformation. Each transformation was performed in triplicate. 300 ng of either *mreB::cat* or *ccmA::cat* linear DNA was mixed with each cell patch. Transformations were incubated overnight and then each cell patch was resuspended in BB10, serially diluted, and spread on non-selective plates for colony counts and chloramphenicol plates for selection of transformants. Colonies were counted after six days. Plates without colonies after six days were incubated for three weeks to allow for any slowly growing colonies to arise. Genomic DNA was purified from the two transformants of LSH100 (clone 1 and 2) with *mreB::cat*. Sanger sequencing was performed on recombinant clone 1 and 2. For sequencing clone1, sequencing template was PCR amplified from genomic DNA using primers FabZ_up_F and Cat_mid_R and sequenced using primers Supp1_Junction1_R and MreB_up. Additional sequencing template for clone 1 was PCR amplified using primers MreB_mid_dn_F and Cat_mid_R and sequenced using primer MreB_mid_dn_F. For sequencing clone 2, template was PCR amplified from genomic DNA using primers Supp2_junc1_R_mid and MreB_up and sequenced using primers Supp2_junc1_R_mid and MreB_up. Additional sequencing template was PCR amplified using primers MreB_mid_dn_F and Cat_mid_R and sequenced using primers MreB_mid_dn_F and Cat_mid_R. Genomic DNA was purified from eight transformants per transformation of IM4 with *mreB::cat*. PCR with primers Catout, MreB_up, and McGee_187 was used to determine which copy of *mreB* in each clone was disrupted.

2.6.4 *ccmA point mutation strain construction in* H. pylori

Strains containing CcmA point mutants were created based on previously published methods (Sycuro *et al.*, 2010). Briefly, PCR products were amplified from pKB69H (I55A) or pKB72D (L110S) using primers CcmA SDM mi F and CcmA SDM mi R (Table 2.3). Those products were annealed using PCR SOEing (Horton, 1995) to fragments amplified from WT *H. pylori* flanking the CcmA locus using primers Csd1F and CcmA SDM up R (upstream fragment, 810 bp flanking) and CcmA SDM dn F and CcmA SDM dn R (downstream fragment, 540 bp flanking). PCR product was transformed into a *catsacB ccmA* knockout strain LSH117 (LSH100 naturally transformed with KGH10 (Sycuro *et al.*, 2010) genomic DNA) and colonies resistant to sucrose and susceptible to chloramphenicol were validated using PCR and Sanger. Single clones of colonies containing correct mutations were used for all experiments.

Table 2.4. Primers used in this study

Primer name	**Sequence (5’ to 3’)**
AmgK_BamHI_F	GATAGGATCCTGACCCGCTTGACGGCTA
MurU_HindIII_R	GTATAAGCTTTCAGGCGCGCTCGC
RdxA_F1P1	CAATTGCGTTATCCCAGC
RdxA_dnstm_RP2	AAGGTCGCTTGCTCAATC
O#9 ProMreB (KpnI_5’)	TATTGGTACCCGCTTGATGTATTCATCAAAG
O#10 ProMreB_R	GATTAATTTGCTAAAAATCATAAAATAAACTCCTTGTTTTG
O#11 ProMreB_F	CAAAACAAGGAGTTTATTTTATGATTTTTAGCAAATTAATC
O#12 ProMreB (XhoI_3’)	TATTCTCGAGTTATTCACTAAAACCCACAC
O#36 pMcGee-Insert-F	CTGCCTCCTCATCCTCTTCATCCTC
O#45 MreBC-seq-F2	GCACCTATTTTGGGGTTTGAAACC
O#47 MreB-seq-F2	CATTGAGCGCTGGTTTTAAGGCGGTC
O#28 MreBseq-F3	CGATCGTGTTAGTCAAAGGGCAGGGC
O#37 pMcGee-Insert-R	GGTGTACAAACATTTAAAGGTAGAG
O#68 McGee-1F	CATTTCCCCGAAAAGTGCCACGAGCTCGAAGGAGTATTGATGAAAAAGG
O#69 McGee-1R	CTAGAGCGGCCCCACCGCGGCCATCATTAACATCATTATCG
O#70 MCS-kan-F	CTCGAGGGGGGGCCCGGTACCCACAGAATTACTCTATGAAGC
O#71 MCS-kan-R	CCATTCTAGGCACTTATCCCCTAAAACAATTCATCCAGTAA
O#72 McGee-2F	TTACTGGATGAATTGTTTTAGGGGATAAGTGCCTAGAATGG
O#73 McGee-2R	CGGATATTATCGTGAGATCGCTGCAGACTGGGGGGAAACTCATGGG
O#74 McGee-R6K-F	CCCATGAGTTTCCCCCCAGTCTGCAGCGATCTCACGATAATATCCG

O#75 McGee-R6K-R	GTAACTGTCAGACCAAGTTTACTGCGGCCGCGCAAGATCCGGCCACGATGCG
O#76 R6K-amp-F	CGCATCGTGGCCGGATCTTGCGCGGCCGCAGTAAACTTGGTCTGACAGTTAC
O#77 R6K-amp-R	CCTTTTTCATCAATACTCCTTCGAGCTCGTGGCACTTTTCGGGGAAATG
O#78 MCS fragment	CCGCGGTGGGGCCGCTCTAGAACTAGTGGATCCCCCGGGCTGCGGAATTCGCTTATCG
O#79 McGee-MCS-F	CGATAATGATGTTAATGATGGCCGCGGTGGGGCCGCTCTAG
O#80 McGee-MCS-R	GCTTCATAGAGTAATTCTGTGGGTACCGGGCCCCCCCTCGAG
Csd1F	GAGTCGTTACATTAATGTGCATATCT
G1480_DnStrmP2	AAGGGTGCAATAACGCGCTAA
MreB_start_F	ATGATTTTTAGCAAATTAATCGG
MreB_cat_up_R	CACTTTTCAATCTATATCCGTGCCTCCGCCAATATC
C1	GATATAGATTGAAAAGTGGAT
C2	TTATCAGTGCGACAAACTGGG
Cat_mreB_dn_F	AGTTTGTCGCACTGATAAACTGAAATTGGCG
MreB_end_R	TTATTCACTAAAACCCACACGGCTGA
FabZ_up_F	GCTATCCCATGCTATTGATAGAC
Cat_mid_R	GTCGATTGATGATCGTTGTAACTCC
MreB_mid_dn_F	GATCAAAGCATCGTGGAATACATCC
Supp2_junc1_R_mid	AATTTGCTAAAAATCACTAA
MreB_up	AATACCAGCAACTTTTCAAAA
Supp1_Junction1_R	ATTTGCTAAAAACACACGGC
Catout	CCTCCGTAAATTCCGATTTGT
McGee_187	GCGAGTATTACCACAAGTTTTC

CcmA SDM mi R	AGACTAGATTGGATCATTCCCTATTTATTTTCAATTTTCT
CcmA SDM mi F	ATAAAGAAAGGAGCATCAGATGGCAATCTTTGATAACAAT
CcmA SDM up R	ATTGTTATCAAAGATTGCCATCTGATGCTCCTTTCTTTAT
CcmA SDM dn F	AGAAAATTGAAAATAAATAGGGAATGATCCAATCTAGTCT
CcmA SDM dn R	GCTCATTTGAGTGGTGGGAT
SDM 155A F	ATTCTAAAAGCACGGTGGTGgcCGGACAAACCGGCTCGGTAG
SDM 155A R	CTACCGAGCCGGTTTGTCCGgcCACCACCGTGCTTTTAGAAT
SDM L110S F	TGGTGGAAAGGAAGGGGATTtcGATTGGGGAAACTCGCCCTA
SDM L110S R	TAGGGCGAGTTTCCCCAATCgaAATCCCCTTCCTTTCCACCA

2.6.5 *Fosfomycin rescue with MurNAc*

Overnight liquid cultures of HJH1 and parent strain LSH108 grown to 0.3-0.5 OD_{600}/ml were diluted in BB10, BB10 containing fosfomycin, or BB10 containing fosfomycin and MurNAc to yield cultures at 0.002 OD_{600}/ml, with 50 μg/ml fosfomycin, or 50 μg/ml fosfomycin and 4 mg/ml MurNAc, as appropriate. Cultures were grown shaking in 5 ml polystyrene tubes. Samples were taken initially and after 12 hours 10 μl of culture was diluted into 30 μl of BB10 and a 10-fold dilution series was performed from this initial dilution. 4 μl of each dilution for each experimental condition was spotted on plates and plates were incubated 5-6 days. One biological replicate is defined as beginning with a new overnight liquid culture.

2.6.6 *Synthesis and characterization of MurNAc-alk*

MurNAc-alk was synthesized and characterized as previously described (Liang *et al.*, 2017). and underwent multiple rounds of purification using our previously-described autopur preparatory HPLC purification strategy until no more than 5% N hydroxysuccinimide (NHS) remained in the product as judged by H NMR, chemical shift 2.6 ppm. The final MurNAc-alk product was then

solubilized in water or DMSO or water (200mg/mL) for subsequent bacterial PG labeling experiments.

2.6.7 *PG preps and analysis for D-Ala-alk and MurNAc-alk*

330 ml of liquid cultures were grown for six doublings to an optical density at 600 nm (OD600) reading of 1 with 100 µg/ml D-alanine-alk ((R)-2-Amino-4-pentynoic acid, Boaopharma, Woburn, MA), 62.5 µg/ml MurNAc-alk, or no additions. Cells were harvested and sacculi were purified as previously described (Blair *et al.*, 2018). Briefly, cells were harvested by centrifugation at 4°C, resuspended in PBS, and added dropwise to boiling 8% SDS. SDS was then removed by ultracentrifugation and washing. Then sacculi were resuspended in 900 µl of 10 mM Tris HCl with 10 mM NaCl pH 7.0 and 100 µl of 3.2M imidazole pH 7.0 and incubated with 15 µl α-amylase (10 mg/ml) (Sigma, St. Louis, MA) for 2 hours at 37°C and 20 µl Pronase E (10 mg/ml) (Fisher Scientific, Pittsburgh, PA) for 1 hour at 60°C. 500 µl of 8% SDS was added and samples were boiled for 15 minutes. SDS was again removed by ultracentrifugation and washes with water. The purified PG was suspended in 20 mM sodium phosphate pH 4.8 (D-Ala-alk samples) or 20 mM ammonium formate pH 4.8 (MurNAc-alk samples) and incubated overnight with 10 µg of cellosyl (kind gift from Hoechst, Frankfurt am Main, Germany) at 37^0C on a Thermomixer at 900 rpm. Following this incubation, the samples were placed in a dry heat block at 100^0C for 10 min and centrifuged at room temperature for 15 min at 16,000×g. The supernatant was retrieved. D-Ala-alk labeled digests were reduced with sodium borohydride (Merck KGaA, Darmstadt, Germany) and separated by RP-HPLC, peaks collected and analyzed using offline electrospray mass spectrometry as previously described (Bui *et al.*, 2009).

MurNAc-alk labeled digests (non-reduced) were analyzed via injection onto a capillary (0.5 X 150 mm) ACE Ultracore 2.5 super C18 column (Hichrom, Lutterworth, UK). The LC-MS

instrument configuration comprised a NanoAcquity HPLC system (Waters, Milford, MA) and QTOF mass spectrometer (Impact II, Bruker, Billerica, MA). Buffer A was 0.1% formic acid (VWR, Lutterworth, UK) in water (VWR). Buffer B was 0.1% formic acid in acetonitrile (VWR). RP-HPLC conditions were as follows: 0 % buffer B for 3 min, 1.5 % B at 20 min, 3.0 % B at 35 min, 15 %B at 45 min, 45% B at 50 min, followed by 2 min at 85% B and finally 15 min re-equilibration at 0 %B. The flow rate was 0.02 ml/min and the capillary column temperature was set at 35°C.

MS data was collected in positive ion mode, 50 – 2000 m/z, with capillary voltage and temperature settings of 3200 V and 150°C respectively, together with a drying gas flow of 5 L/min and nebulizer pressure of 0.6 Bar. The resulting MS spectral data was analyzed using Compass DataAnalysis™ software (Bruker).

2.6.8 *18-minute pulses with D-Ala-alk and MurNAc-alk*

400 µl of HJH1 overnight liquid cultures in BB10 grown to 0.3-0.5 OD_{600}/ml was added to a 5 ml polystyrene round bottom tube and equilibrated in the 37°C Trigas incubator for 15 minutes before addition of the metabolic probe. 8 µl of a 200 mg/ml MurNAc-alk (synthesized and characterized as previously described (Liang *et al.*, 2017)) stock in DMSO or ddH_2O (final concentration = 4mg/ml) or 4 µl of a 100 mM stock of D-Ala-alk ((R)-2-Amino-4-pentynoic acid, Boaopharma) in ddH_2O was added to the culture. The culture was incubated for 18 minutes and growth was arrested by adding 4 µl of 10% sodium azide and placing cultures on ice for 5 minutes. Cells were transferred to a 1.5 ml microcentrifuge tube, pelleted in a microcentrifuge for 5 minutes at 5000 rpm, and resuspended in 1 ml Brucella broth. Paraformaldehyde was added to a final concentration of 4%. Cells were fixed at room temperature for 45 minutes, pelleted, and resuspended in 70% ethanol. Cells were permeabilized on ice for 30 minutes, pelleted, and

resuspended in PBS. Cell suspension density was normalized between samples using a hemocytometer and cells were spun onto clean glass coverslips at 500 rpm for 5 minutes in a Hettich Rotana 460R swinging bucket centrifuge. Click chemistry was performed on coverslips using the Click-iT Cell Reaction Buffer Kit (Invitrogen) according to manufacturer instructions (without BSA washes) with 8 µg/ml Alexa Fluor 555 Azide (Invitrogen). Coverslips were washed two times with 0.05% Tween-20 in PBS (PBST) for 10 minutes each and were then stained with 30 µg/ml WGA-Alexa Fluor 488 (Invitrogen) in PBS for 30 minutes at room temperature. Coverslips were washed an additional four times in PBST and mounted on slides with Prolong Diamond antifade (Invitrogen). Slides were cured for a week before imaging. One biological replicate is defined as beginning with a new overnight liquid culture.

2.6.9 *Immunofluorescence (CcmA-FLAG, CcmA, MreB)*

Overnight liquid cultures in BB10 grown to 0.3-0.5 OD_{600}/ml were fixed at room temperature for 45 minutes with 4% paraformaldehyde. Cells were pelleted in a TOMY TX-160 micro centrifuge for 5 minutes at 5000 rpm and resuspended in 0.1% Triton X-100 in PBS for one hour at room temperature to permeabilize the cells. Cells were then pelleted in an Eppendorf microfuge at 2400 rpm for 10 minutes and resuspended in PBS. Cell suspension density was normalized using a hemocytometer and cells were spun onto clean glass coverslips at 500 rpm for 5 minutes in a Hettich Rotana 460R swinging bucket centrifuge. Coverslips were stained with 30 µg/ml WGA-Alexa Fluor 555 (Invitrogen) in PBS for 30 minutes at room temperature, washed four times with 0.05% Tween-20 in PBS (PBST) for 10 minutes each, blocked for two hours with 5% goat serum (Sigma) in PBST at room temperature, and then incubated overnight at 4°C in primary antibody in 5% goat serum PBST. Mouse anti-FLAG M2 (Sigma, RRID:AB_262044), rabbit anti-CcmA (Blair *et al.*, 2018), and CcmA preimmune serum were used at a 1:200 dilution. Rabbit anti-

MreB and MreB preimmune serum (a gift from Dr. Hong Wu and Dr. Kouichi Sano (Nakano *et al.*, 2012)) were used at a 1:500 dilution. After primary antibody incubation, coverslips were washed four times in PBST and incubated with 1:200 Alexa Fluor 488 anti-mouse (A-11029, Invitrogen, RRID:AB_2534088) or 1:200 Alexa Fluor 488 anti-rabbit (A-11008, Invitrogen, RRID:AB_143165) in PBST for 45 minutes at room temperature. After secondary antibody incubation, coverslips were washed four times in PBST and mounted on slides with Prolong Diamond antifade (Invitrogen). Slides were cured for a week before imaging. For CcmA-FLAG immunofluorescence, strain JTH5 was used. JTH5 was generated by natural transformation HJH1 with genomic DNA from JTH3 (Blair *et al.*, 2018) and selection on kanamycin blood plates. HJH1 was used as the corresponding no-FLAG control, as well as for the anti-MreB and MreB preimmune immunofluorescence. Wild-type LSH100 (Lowenthal *et al.*, 2009) was used for anti-CcmA and CcmA preimmune immunofluorescence. One biological replicate is defined as beginning with a new overnight liquid culture.

2.6.10 *3D structured illumination imaging*

Slides for cell surface curvature profiles for LSH100, Δ*csd2*, and Δ*csd6* were imaged on a DeltaVision OMX V4 BLAZE 3D microscope (GE Healthcare Life Sciences, Chicago, IL) equipped with Photometrics Evolve 512 emCCD cameras and an Olympus UPlanApo 100x/1.42 oil objective with oil matched for the sample refractive index. 512 x 512 pixel images were collected with 3 msec exposure and 170 EMCCD gain using a 100 mW 488 nm laser with 10% transmission. Z-plane images were acquired with 125 nm spacing. The remaining SIM microscopy was performed on a DeltaVision OMX-SR equipped with PCO scientific CMOS cameras, 488 nm and 568 nm lasers, and an Olympus 60x/1.42 U PLAN APO oil objective with oil matched for the sample refractive index. 512 x 512 pixel Z-plane images with 125 nm

spacing and 3 μm thickness were collected. For HJH1 D-Ala-alk samples, images were collected with 5% 488 and 15% 568 laser power for 20 msec and 100 msec exposures, respectively. For JTH6 D-Ala-alk samples, images were collected with 5% 488 and 30% 568 laser power for 20 msec and 100 msec exposures, respectively. For MurNAc-alk samples, images were collected with 10% 488 and 15% or 2% 568 laser power for 2 msec and 80 msec exposures, respectively. For α-FLAG immunostained samples, images were collected with 10% 488 and 10% 568 laser power and 40 msec and 25 msec exposure, respectively. For HJH1 α-MreB immunostained samples, images were collected with 10% 488 and 10% 568 laser power and 70 msec and 25 msec exposure, respectively. For JTH6 α-MreB immunostained samples, images were collected with 20% 488 and 20% 568 laser power and 25 msec and 25 msec exposure, respectively. For α-CcmA immunostained samples, images were collected with 15% 488 and 15% 568 laser power and 30 msec and 40 msec exposure, respectively. Images were processed using included Softworx software. Figures were generated by opening files in Fiji (Schindelin *et al.*, 2012), adjusting brightness and contrast, and assembling in Adobe Photoshop. Intensity scaling of maximum projection and Z-slice images are equal for all samples within a set (D-Ala-alk and mock; MurNAc-alk and mock; α-FLAG M2; α-MreB and preimmune serum; and α-CcmA and preimmune serum), with the exception of the I55A CcmA anti-CcmA and preimmune images, which were brightened in comparison to other anti-CcmA and preimmune images to compensate for the reduced expression of I55A CcmA. Intensity scaling is equal for I55A CcmA anti-CcmA and preimmune images.

2.6.11 *3D reconstructions and curvature enrichment*

3D cell surfaces were generated from the 3D-SIM OMX software reconstructions using existing software (Bartlett *et al.*, 2017, Bratton *et al.*, 2018) with parameters optimized for the difference

in imaging modality and file formats. This method minimizes the difference between the observed image and a forward convolution model of the true intensity distribution and the microscope's transfer function. While the images generated by 3D-SIM are not precisely equal to the convolution of the true intensity distribution, we consider the observed images as if they had been generated with an effective blurring function that we parameterize as a 3D Gaussian blur. For each individual cell, the reconstruction algorithm returns the 3D shape of the cell as a collection of vertex positions $\{V_i\}$ and a collection of faces defining which vertices are connected to each other. These faces and positions allow us to calculate geometric properties including the volume, surface area, local principal curvatures, etc. (Bratton *et al.*, 2018, Rusinkiewicz, 2004). The Gaussian curvature at any point on the surface is the product of the principal curvatures and is therefore independent of the sign convention chosen for the principal curvatures. Following reconstruction, each cell surface undergoes a visual inspection quality control step. To estimate the diameter of each cell, we use the distance from each surface point to its nearest centerline point as a proxy for the local radius. The cell diameter is then the weighted average of twice the local radius, weighted by the surface area represented by each vertex.

In addition to the geometric properties of the surface, we calculate the intensity of a secondary fluorophore at the coordinates of the surface, for example D-Ala-alk, MurNAc-alk, or immunofluorescence. For each individual cell, the average surface concentration was calculated as the surface area weighted sum of the fluorescence at the surface divided by the total surface area of that cell. This normalization sets the concentration scale for the enrichment analysis; a value of one is the same concentration as if all the intensity was uniformly spread on the surface, concentrations greater than one are enriched and concentrations less than one are depleted. When considering the entire cell surface, the normalization included all surface vertices. When only

considering the sidewalls of the cell, we first removed all the vertices in the polar regions. These regions were defined as all the points on the surface whose nearest centerline point was closer to the pole than 0.75 of the cell diameter (Figure 2.1 B). Following normalization, we calculated the geometric enrichment in each individual cell by averaging the concentration across all the vertices of a particular Gaussian curvature. This enrichment profile was then averaged across the entire population of cells. We truncate the analysis to Gaussian curvatures which have sufficient representation (>4e-4). For error estimation, we report 90% confidence intervals from bootstrap analysis across cells and plot this interval, along with the mean, using cubic smoothing splines (Figure 2.13, lines). Each sample is the composite dataset from three biological replicates.

We approximated the total fluorescent signal from each cell including the contributions from inside the cell and surface intensities. This total signal is a good proxy for the selectivity of the labeling experiments. As a first step, the entire z-stack was summed to make a 2D projection. A thresholded, binary mask of each cell was generated using Otsu's method on the color channel used to generate the computation cell surface reconstruction and dilated by 3 pixels to make sure that we captured all the intensity in the cell. The total intensity in the corresponding pixels of the other color channel were added together to calculate the total intensity in the cell. To normalize for effects of cell size, this total intensity was divided by the number of pixels in the mask, resulting in the total fluorescence signal/cell.

The MATLAB scripts used to reconstruct cell surfaces and perform the geometric enrichment analyses are publicly available under a BSD 3-clause license at https://github.com/PrincetonUniversity/shae-cellshape-public and archived at https://doi.org/10.5281/zenodo.1248978.

2.6.12 *Determining helical fits of 3D centerlines*

To examine the helical parameters of the cell centerlines, we adapted the helical fitting algorithm from Nievergelt (Nievergelt, 1997). The first step in the routine is to estimate a right-cylindrical surface on which all the data lie. This is defined by four parameters, three of which define a vector parallel to the helical axis (X_a, Y_a, Z_a) and the fourth is the cylinder diameter (D). The remaining four parameters are determined in a subsequent step. These define a point on the helix (X_o, Y_o, Z_o) and the helical pitch (P). The algorithm takes advantage of the speed of singular value decomposition (SVD) by framing the best fit as a linear algebra problem. The modifications that we made to the algorithm were in a preconditioning step as well as steps 2 and 3. The center of mass of the data was subtracted off from all the observations and then added back into X_0, Y_0, and Z_0. For our real cells the two smallest singular values in step 2.3 are sometimes of similar magnitude and are both checked to see which right-singular vector is more consistent with a cylinder. The use of SVD instead of eigenvalue decomposition does not retain the right-handed convention of space forcing us to switch step 2.4 to an eigenvalue decomposition. In estimating the pitch of the helix in step 3.2, the algorithm by Nievergelt did not support helical data that covered more than one helical turn. This type of data presents a phase wrapping issue. To solve this issue, we first sorted the data by its projected position along the helical axis. We assumed that the relative phase difference between any two subsequent points was close to zero and calculated an absolute phase at each point by summing the relative phase differences along the whole curve. This then allowed us to calculate the relative slope of the helical phase. Here we again had to break from Nievergelt's SVD approach and used simple linear regression to retain the right-handed convention of space.

For each cell that was independently reconstructed, we estimate the best fit helical parameters for the centerline. Because we do not consider the orientation and offset of the helix to be shape parameters, we do not present any statistics on them. To estimate if the best fit helix was consistent with the centerline, we calculated the root mean squared deviation (RMSD) between the observed centerline coordinates and the best fit helix. One third (402/1137) of the cells had centerlines consistent with single helix. From the one third of the population that matched a single helix, we generated synthetic helical rods with the same helical parameters as each individual cell. From these, we compared the simulated and reconstructed cells in terms of their surface area, volume, volume of the convex hull, and Euclidean distance from pole to pole. If any of the parameters from the simulated cell deviated from the measured value by more than 10%, we excluded that cell from the analysis. In the end, we were left with almost 20% (231/1137) of the wild-type cells that were consistent with our model that cell shape is close to a spherocylinder wrapped around a helical centerline.

Synthetic cells were generated using two major components, a helical centerline and a cylindrical coordinate system about that centerline. In cylindrical coordinates (R, θ, L), a cylinder with hemispherical endcaps has a simple form of a constant radius in the cylinder region and parabolic dependence in the endcaps. We then wrap the coordinate system around a helical axis by calculating the Frenet-Serret frame at each point of the helical centerline from the local tangent, normal, and their cross-product, the binormal. This wraps a fixed angular coordinate θ around the centerline, generating the helical rod surface of interest. However, these surfaces are still in a rectangular format, meaning that they are stored as three matrices {x,y,z} each as a function of the (θ, L). This surface is resampled into a triangular approximation of the surface with approximately equilateral triangles using the surface reconstruction tools that we have

previously developed (Bartlett *et al.*, 2017, Bratton *et al.*, 2018). Some geometric parameters, including the Gaussian curvature at each point on the surface and the surface area and the volume of the cells, can be calculated for both real cell reconstructions and the synthetic cells (Figure 2.3 C-F, supplement 2.4 C-E, and 2.5, left column). For these, we defined the pole surface area as the surface within 0.75 cell diameters of the end. Because of their intrinsic unwrap coordinate system, synthetic cells have defined surface helical axes, which allows us to compute the length of the major and minor axes as well as the Gaussian curvature at these axes. Since the decrease in local diameter near the pole changes both the curvature and the length of the helical axis, we calculate the major and minor axis lengths and Gaussian curvatures from the central 50% of the cell, where the measurements are not influenced by the poles (Figure 2.3 G-H and 2.5, middle and right columns). Decreasing the total length of the cell proportionally decreases both the sidewall portion of the cell (including surface curvature properties) and the length of the major and minor axes, retaining the same ratio of major axis to minor axis length measurements as the ratio of the two axis lengths, we can justify this approach. As shown in Figure 2.5A (center and right columns), the length of the cell has negligible influence on the distribution of surface curvatures and the ratio of major to minor axis length, further validating our aggressive threshold for removing the ends of the cells for these measurements.

The MATLAB scripts used to fit helical centerlines are publicly available under a BSD 3-clause license at https://github.com/PrincetonUniversity/shae-cellshape-public and archived at https://doi.org/10.5281/zenodo.1248978.

2.6.13 *Purification of recombinant 6His-CcmA and variants*

Plasmids containing N-terminal 6-histidine fusions to WT CcmA (pKB62) and CcmA containing point mutations were generated using site directed mutagenesis primers (Table 2.3) to generate

CcmA I55A (pKB69H; primers SDM 155A F and SDM I55A R) and CcmA L110S (pKB72D; primers SDM L110S F and SDM L110S R). Plasmids were transformed into E. coli protein production host BL21. Strains were grown in liquid culture overnight at 37°C in LB with 0.2% glucose and 100 µg/ml ampicillin. The next day, cells were diluted 1/1000 into fresh media without glucose, grown to mid-log (0.5-0.75), chilled on ice for 15 minutes, then induced for protein expression by adding 1.0 mM IPTG. Flasks were transferred to room temperature and incubated with shaking for 3.5-4 hours. Cells were harvested by centrifugation and either used immediately for protein purification or frozen at -80°C. For purification, cells were re-suspended in 2/5 culture volume of lysis buffer (25 mM Tris pH8.0, 2 M urea, 500 mM NaCl, 2% glycerol, 0.5 mg/mL lysozyme) supplemented with ¼ EDTA-free protease inhibitor tablet (Pierce, Waltham, MA) and 2 U Benzonase nuclease (EMD Millipore, Burlington, MA) and incubated at room temperature with gentle rolling for 1 hour. After lysing, cells were sonicated at 20% power with 15 second pulses until all cells were lysed. Lysates were cleared at 5000 x g at 4°C, then applied to equilibrated TALON metal affinity resin (TaKaRa, Shiga, Japan) and incubated for 2 hours at room temperature with gentle rolling. The protein bound to resin was washed twice with wash buffer (25 mM Tris pH8.0, 2 M urea, 500 mM NaCl, 2% glycerol, 7.5 mM imidazole), and proteins eluted from the resin using 25 mM Tris pH8.0, 2 M urea, 500 mM NaCl, 2% glycerol, 250 mM imidazole). Fractions were analyzed by SDS-PAGE for purity and yield. Protein concentration was determined using a Nanodrop 1000 (Thermo Fisher Scientific, Waltham, MA) using the Protein A280 program. One biological replicate is defined as beginning with a new overnight liquid culture.

2.6.14 *Immunoblotting* H. pylori *extracts*

Whole cell extracts were prepared by harvesting 1.0 OD_{600} of log phase (0.3-0.7 OD_{600}) *H. pylori* liquid culture by centrifugation for 2 minutes at max speed in a microcentrifuge and resuspending in 2x protein sample buffer (62.5 mM Tris pH 8, 2% SDS, 0.02% bromophenol blue, 20% glycerol) or Lämmli buffer at 10.0 OD_{600} per ml and boiled for 10 minutes. Whole cell extracts were separated on 4-15% gradient BioRad TGX gels or 4-15% mini-PROTEAN TGX Stain-Free gels (used according to manufacturer instructions) by SDS-PAGE and transferred onto PVDF membranes using the BioRad Turbo-transfer system according to the manufacturer's instructions (BioRad, Hercules, CA). Membranes were blocked for 2 hours at room temperature with 5% non- fat milk in TBST (0.5 M Tris,1.5 M NaCl, pH 7.6, plus 0.05% Tween 20). Membranes were incubated with primary antibody for 2 hours at room temperature or overnight at 4°C with 1:10,000 α-CcmA primary antibody, 1:20,000 dilution for α-Cag3 (Pinto-Santini & Salama, 2009), or 1:25,000 dilution for α-MreB, in TBST. Six washes with TBST over a 30 minute period were followed by a 1 hour incubation at room temperature with horseradish peroxidase- conjugated anti-rabbit immunoglobulin G (Santa Cruz Biotechnology, Dallas, TX) antibody at 1:20,000 dilution in TBST. After six washes with TBST over a 30 minute period, antibody detection was performed with ECL Plus (Pierce) detection kit, or Immobilon Western Chemiluminescent HRP substrate (Millipore), following the manufacturer's protocol and imaged with the BioRad Gel Documentation System. One biological replicate is defined as beginning with a new liquid culture.

2.6.15 *2D* H. pylori *quantitative cell shape analysis*

Phase-contrast microscopy was performed on cells grown in shaken liquid culture until mid-log phase (OD_{600} 0.3.-0.6), fixed in a 4% PFA/PBS + 10% glycerol solution and mounted on glass

slides. Resulting images were acquired using a Nikon TE 200 microscope with at 100X oil-immersion objective and Nikon CoolSNAP HQ CCD camera controlled by MetaMorph software (MDS Analytical Technologies, Sunnyvale, CA). Images were thresholded using the ImageJ software package. Quantitative analysis of thresholded images were used to measure both side curvature and central axis length with the CellTool software package as described previously (Sycuro *et al.*, 2010). One biological replicate is defined as beginning with a new liquid culture.

2.6.16 *Transmission electron microscopy*

For TEM 10 μM WT, I55A, or L110S CcmA was dialyzed overnight at 4°C against 25 mM Tris pH 8. The proteins were applied to glow-discharged carbon-coated grids and negatively stained with 0.75% uranyl acetate. Images were acquired with JEOL 1400 transmission electron microscope using a Gatan UltraScan 1000xp camera with 2K x 2K resolution.

2.7 ACKNOWLEDGEMENTS

This research was supported in part by US National Institutes of Health R01 AI136946 (NRS), U01 CA221230 (CLG and NRS), T32 CA009657 (KMB), T32 GM95421 (SRS), T32 GM008550 (KED), GM113172 (MSV) the FHCRC Cellular Imaging and Genomics and Bioinformatics Shared Resources of the NCI Center Support Grant P30 CA015704, the Stanford Imaging Award Number 1S10OD01227601 from the National Center for Research Resources (NCRR), the Life Sciences Research Foundation (EK), and the Wellcome Trust grant 101824/Z/13/Z (WV).This work was supported by the National Science Foundation Graduate Research Fellowship Program under Grant No. DGE-0718124 (JAT) and DGE-1256082 (JAT and KMB), the Department of Defense (DoD) through the National Defense Science & Engineering Graduate Fellowship (NDSEG) Program (JAT), and the GO-MAP Graduate

Opportunity Program Research Assistantship Award (GOP Award) (SRS). This work was supported by National Science Foundation PHY-1734030 (BPB and JWS), the Glenn Centers for Aging Research (BPB) and National Institutes of Health NIH R21 AI121828 (BPB and JWS).

The opinions, findings, and conclusions or recommendations expressed in this material contents are solely the responsibility of the authors and do not necessarily represent the official views of the NCRR, the National Institutes of Health, the Department of Defense, or the National Science Foundation. The authors have no conflicts of interest to report.

We would like to thank Laura Sycuro, Desirée Yang, and Irina Mavrodi for strain construction; Dr. Cintia Santiago for assistance with NAM purification and compound shipment; Patrina Pellett (GE Healthcare) for assistance with OMX imaging; the David Baker Lab (University of Washington) for OMX access and use; and Sloan Siegrist (University of Massachusetts Amhurst) for the D-alanine-D-alanine-alkyne and D-alanine-alkyne-D-alanine reagents. We kindly thank Dr. Hong Wu and Dr. Kouichi Sano (Osaka Medical College) for the anti-MreB and corresponding preimmune sera used in this study; Anson Chan (University of British Columbia) for consultation on CcmA mutant design; and Zachary Jones for assistance in synthesizing the MurNAc sugars.

2.8 APPENDIX

Selecting a subset of wild-type cells whose geometry is consistent with the four parameter model of helical-rod shape. We generated a set of simulated helical cells based on the three-dimensional reconstructions of the wild-type population shown in Figure 2.2. Inputs to this simulation are the measured pole-pole cell lengths along the curved centerlines (Figure 2.3 A and C, gray); the diameters of the cells (Figure 2.4 A and D, purple); the helical pitches of the centerlines (Figure 2.3 A and E, pink); and the helical diameters of the centerlines (Figure 2.3 A

and F, green). To determine the helical pitch and radius from each reconstructed cell, we borrowed heavily from previous algorithms designed to calculate the best fit helix to a set of observations (Nievergelt, 1997). We modified these algorithms to accommodate helices longer than one helical repeat and to allow the pitch to be a signed value, with positive pitches corresponding to right-handed helices and negative to left-handed ones. Not all centerlines fit well to a single helical fit as some centerlines have kinks or variable pitch along their long axis. We calculated the relative error of the helical fit as the root mean squared deviation (RMSD) of the error in the fit to the RMSD between two subsequent points along the centerline. This relative error is unitless; we set a threshold value of two for satisfactory fits (Figure 2.4 A). About one quarter of the centerlines had a good fit to a single helix (402/1137). Wild type *H. pylori* cells have been shown to be right handed (Yoshiyama & Nakazawa, 2000). Our algorithm finds that 96% of the cells with satisfactory fits are right handed (387/402). Infrequently (15/402), the algorithm returned a left-handed helix as the best fit. Upon visual inspection, none of these centerlines were globally left-handed and were thus discarded.

From the four calculated 3D shape parameters, we generated synthetic cells to mimic the original wild-type population. Just as we ignored cells whose centerlines were not well fit by a single helix, we also removed cells whose simulated counterpart differed from the real cell reconstruction by more than 10% in surface area, volume, volume of the convex hull, or Euclidean distance from pole to pole. For roughly 20% of the total wild-type population (231/1137), the observed geometry of the cell was consistent with the simple four parameter model (see Methods and Figure 2.4 A and B). It is not reasonable to look at the distribution of helical parameters for centerlines that do not have satisfactory fits. The distribution of cell lengths, cell diameters, and surface curvatures for the entire population and the population subset

are closely matched (Figure 2.4 C-E), indicating that the subset adequately represents the population. Both wild-type and synthetic cells share a multimodal distribution of Gaussian curvatures with peaks around 5 μm^{-2} and between -5 and -10 μm^{-2}. However, there is a notable difference in the widths and magnitudes of these peaks between the wild-type and corresponding synthetic cells, consistent with the fact that, unlike real cells, the synthetic cell surfaces are perfectly smooth.

Using this subset of simulated cells, we then proceeded to characterize the major and minor helical axes. Because we simulated these cells based on a model of a cylinder wrapped and twisted about a helical axis, they inherently have a natural unwrap helical coordinate system (Figure 2.3 B and 2.4 A). We chose to set the unwrap angle of the major helical axis to 0° and the minor helical axis to 180° allowing us to measure the relative length of the major to minor helical axes as well as measure the average Gaussian curvature along the helical axes. The average Gaussian curvature at the major axis is $5 \pm 1\ \mu m^{-2}$, and the average Gaussian curvature at the minor axis is $-11 \pm 4\ \mu m^{-2}$. There was substantially more variation in the average curvature at the minor axis than at the major axis (Figure 2.3 H).

2.9 BIBLIOGRAPHY

Bartlett, T.M., Bratton, B.P., Duvshani, A., Miguel, A., Sheng, Y., Martin, N.R., Nguyen, J.P., Persat, A., Desmarais, S.M., VanNieuwenhze, M.S., Huang, K.C., Zhu, J., Shaevitz, J.W., and Gitai, Z. (2017) A Periplasmic Polymer Curves *Vibrio cholerae* and Promotes Pathogenesis. *Cell* **168**: 172-185 e115.

Blair, K.M., Mears, K.S., Taylor, J.A., Fero, J., Jones, L.A., Gafken, P.R., Whitney, J.C., and Salama, N.R. (2018) The *Helicobacter pylori* cell shape promoting protein Csd5 interacts with the cell wall, MurF, and the bacterial cytoskeleton. *Mol Microbiol* **110**: 114-127.

Bonis, M., Ecobichon, C., Guadagnini, S., Prevost, M.C., and Boneca, I.G. (2010) A M23B family metallopeptidase of *Helicobacter pylori* required for cell shape, pole formation and virulence. *Mol Microbiol* **78**: 809-819.

Bratton, B.P., Shaevitz, J.W., Gitai, Z., and Morgenstein, R.M. (2018) MreB polymers and curvature localization are enhanced by RodZ and predict *E. coli*'s cylindrical uniformity. *Nat Commun* **9**: 2797.

Bui, N.K., Gray, J., Schwarz, H., Schumann, P., Blanot, D., and Vollmer, W. (2009) The peptidoglycan sacculus of *Myxococcus xanthus* has unusual structural features and is degraded during glycerol-induced myxospore development. *J Bacteriol* **191**: 494-505.

Cabeen, M.T., Charbon, G., Vollmer, W., Born, P., Ausmees, N., Weibel, D.B., and Jacobs-Wagner, C. (2009) Bacterial cell curvature through mechanical control of cell growth. *EMBO J* **28**: 1208-1219.

Correa, P. (1988) A Human Model of Gastric Carcinogenesis. *Cancer Research* **48**: 3554-3560.

Costa, K., Bacher, G., Allmaier, G., Dominguez-Bello, M.G., Engstrand, L., Falk, P., de Pedro, M.A., and García-del Portillo, F. (1999) The Morphological Transition of *Helicobacter pylori* Cells from Spiral to Coccoid Is Preceded by a Substantial Modification of the Cell Wall. *Journal of Bacteriology* **181**: 3710-3715.

Ghuysen, J.-M. (1991) Serine beta-lactamases and penicillin-binding proteins. **45**: 37-67.

Gibson, D.G., Young, L., Chuang, R.Y., Venter, J.C., Hutchison, C.A., 3rd, and Smith, H.O. (2009) Enzymatic assembly of DNA molecules up to several hundred kilobases. *Nat Methods* **6**: 343-345.

Gisin, J., Schneider, A., Nagele, B., Borisova, M., and Mayer, C. (2013) A cell wall recycling shortcut that bypasses peptidoglycan *de novo* biosynthesis. *Nat Chem Biol* **9**: 491-493.

Gitai, Z., Dye, N.A., Reisenauer, A., Wachi, M., and Shapiro, L. (2005) MreB actin-mediated segregation of a specific region of a bacterial chromosome. *Cell* **120**: 329-341.

Goodwin, A., Kersulyte, D., Sisson, G., Veldhuyzen van Zanten, S.J.O., Berg, D.E., and Hoffman, P.S. (1998) Metronidazole resistance in *Helicobacter pylori* is due to null mutations in a gene (*rdxA*) that encodes an oxygen-insensitive NADPH nitroreductase. *Molecular Microbiology* **28**: 383-393.

Höltje, J.-V. (1998) Growth of the Stress-Bearing and Shape-Maintaining Murein Sacculus of *Escherichia coli*. *Microbiology and Molecular Biology Reviews* **62**: 181-203.

Holtrup, S., Heimerl, T., Linne, U., Altegoer, F., Noll, F., and Waidner, B. (2019) Biochemical characterization of the *Helicobacter pylori* bactofilin-homolog HP1542. *PLoS One* **14**: e0218474.

Horton, R.M. (1995) PCR-mediated recombination and mutagenesis. SOEing together tailor-made genes. *Mol Biotechnol* **3**: 93-99.

Humbert, O., and Salama, N.R. (2008) The *Helicobacter pylori* HpyAXII restriction-modification system limits exogenous DNA uptake by targeting GTAC sites but shows asymmetric conservation of the DNA methyltransferase and restriction endonuclease components. *Nucleic Acids Res* **36**: 6893-6906.

Hussain, S., Wivagg, C.N., Szwedziak, P., Wong, F., Schaefer, K., Izore, T., Renner, L.D., Holmes, M.J., Sun, Y., Bisson-Filho, A.W., Walker, S., Amir, A., Lowe, J., and Garner, E.C. (2018) MreB filaments align along greatest principal membrane curvature to orient cell wall synthesis. *eLife* **7**.

Jackson, K.M., Schwartz, C., Wachter, J., Rosa, P.A., and Stewart, P.E. (2018) A widely conserved bacterial cytoskeletal component influences unique helical shape and motility of the spirochete *Leptospira biflexa*. *Mol Microbiol* **108**: 77-89.

Kühn, J., Briegel, A., Morschel, E., Kahnt, J., Leser, K., Wick, S., Jensen, G.J., and Thanbichler, M. (2010) Bactofilins, a ubiquitous class of cytoskeletal proteins mediating polar localization of a cell wall synthase in *Caulobacter crescentus*. *EMBO J* **29**: 327-339.

Kuru, E., Hughes, H.V., Brown, P.J., Hall, E., Tekkam, S., Cava, F., de Pedro, M.A., Brun, Y.V., and VanNieuwenhze, M.S. (2012) *In situ* probing of newly synthesized peptidoglycan in live bacteria with fluorescent D-amino acids. *Angew Chem Int Ed Engl* **51**: 12519-12523.

Langford, M.L., Zabaleta, J., Ochoa, A.C., Testerman, T.L., and McGee, D.J. (2006) In vitro and in vivo complementation of the *Helicobacter pylori* arginase mutant using an intergenic chromosomal site. *Helicobacter* **11**: 477-493.

Liang, H., DeMeester, K.E., Hou, C.W., Parent, M.A., Caplan, J.L., and Grimes, C.L. (2017) Metabolic labelling of the carbohydrate core in bacterial peptidoglycan and its applications. *Nat Commun* **8**: 15015.

Liechti, G.W., Kuru, E., Hall, E., Kalinda, A., Brun, Y.V., VanNieuwenhze, M., and Maurelli, A.T. (2014) A new metabolic cell-wall labelling method reveals peptidoglycan in *Chlamydia trachomatis*. *Nature* **506**: 507-510.

Lowenthal, A.C., Hill, M., Sycuro, L.K., Mehmood, K., Salama, N.R., and Ottemann, K.M. (2009) Functional analysis of the *Helicobacter pylori* flagellar switch proteins. *J Bacteriol* **191**: 7147-7156.

Martinez, L.E., Hardcastle, J.M., Wang, J., Pincus, Z., Tsang, J., Hoover, T.R., Bansil, R., and Salama, N.R. (2016) *Helicobacter pylori* strains vary cell shape and flagellum number to maintain robust motility in viscous environments. *Mol Microbiol* **99**: 88-110.

Meeske, A.J., Riley, E.P., Robins, W.P., Uehara, T., Mekalanos, J.J., Kahne, D., Walker, S., Kruse, A.C., Bernhardt, T.G., and Rudner, D.Z. (2016) SEDS proteins are a widespread family of bacterial cell wall polymerases. *Nature* **537**: 634-638.

Morgenstein, R.M., Bratton, B.P., Nguyen, J.P., Ouzounov, N., Shaevitz, J.W., and Gitai, Z. (2015) RodZ links MreB to cell wall synthesis to mediate MreB rotation and robust morphogenesis. *Proc Natl Acad Sci U S A* **112**: 12510-12515.

Nakano, T., Aoki, H., Wu, H., Fujioka, Y., Nakazawa, E., and Sano, K. (2012) Fine visualization of filamentous structures in the bacterial cytoplasm. *J Microbiol Methods* **90**: 60-64.

Nievergelt, Y. (1997) Fitting helices to data by total least squares. *Computer Aided Geometric Design* **14**: 707-718.

Ouzounov, N., Nguyen, J.P., Bratton, B.P., Jacobowitz, D., Gitai, Z., and Shaevitz, J.W. (2016) MreB Orientation Correlates with Cell Diameter in *Escherichia coli*. *Biophys J* **111**: 1035-1043.

Pinto-Santini, D.M., and Salama, N.R. (2009) Cag3 is a novel essential component of the *Helicobacter pylori* Cag type IV secretion system outer membrane subcomplex. *J Bacteriol* **191**: 7343-7352.

Rusinkiewicz, S. (2004) Estimating Curvatures and Their Derivatives on Triangle Meshes. *Proceedings. 2nd International Symposium on 3D Data Processing, Visualization and Transmission*.

Sauvage, E., Kerff, F., Terrak, M., Ayala, J.A., and Charlier, P. (2008) The penicillin-binding proteins: structure and role in peptidoglycan biosynthesis. *FEMS Microbiol Rev* **32**: 234-258.

Schindelin, J., Arganda-Carreras, I., Frise, E., Kaynig, V., Longair, M., Pietzsch, T., Preibisch, S., Rueden, C., Saalfeld, S., Schmid, B., Tinevez, J.Y., White, D.J., Hartenstein, V., Eliceiri, K., Tomancak, P., and Cardona, A. (2012) Fiji: an open-source platform for biological-image analysis. *Nat Methods* **9**: 676-682.

Shi, C., Fricke, P., Lin, L., Chevelkov, V., Wegstroth, M., Giller, K., Becker, S., Thanbichler, M., and Lange, A. (2015) Atomic-resolution structure of cytoskeletal bactofilin by solid-state NMR. *Science Advances* **1**.

Siegrist, M.S., Whiteside, S., Jewett, J.C., Aditham, A., Cava, F., and Bertozzi, C.R. (2013) (D)-Amino acid chemical reporters reveal peptidoglycan dynamics of an intracellular pathogen. *ACS Chem Biol* **8**: 500-505.

Smeets, L.C., Bijlsma, J.J.E., Boomkens, S.Y., Vandenbroucke-Grauls, C.M.J.E., and Kusters, J.G. (2000) *comH*, a Novel Gene Essential for Natural Transformation of *Helicobacter pylori*. *Journal of Bacteriology* **182**: 3948-3954.

Specht, M., Schatzle, S., Graumann, P.L., and Waidner, B. (2011) *Helicobacter pylori* possesses four coiled-coil-rich proteins that form extended filamentous structures and control cell shape and motility. *J Bacteriol* **193**: 4523-4530.

Srivastava, P., Demarre, G., Karpova, T.S., McNally, J., and Chattoraj, D.K. (2007) Changes in nucleoid morphology and origin localization upon inhibition or alteration of the actin homolog, MreB, of *Vibrio cholerae*. *J Bacteriol* **189**: 7450-7463.

Sycuro, L.K., Pincus, Z., Gutierrez, K.D., Biboy, J., Stern, C.A., Vollmer, W., and Salama, N.R. (2010) Peptidoglycan crosslinking relaxation promotes *Helicobacter pylori*'s helical shape and stomach colonization. *Cell* **141**: 822-833.

Sycuro, L.K., Rule, C.S., Petersen, T.W., Wyckoff, T.J., Sessler, T., Nagarkar, D.B., Khalid, F., Pincus, Z., Biboy, J., Vollmer, W., and Salama, N.R. (2013) Flow cytometry-based enrichment for cell shape mutants identifies multiple genes that influence *Helicobacter pylori* morphology. *Mol Microbiol* **90**: 869-883.

Sycuro, L.K., Wyckoff, T.J., Biboy, J., Born, P., Pincus, Z., Vollmer, W., and Salama, N.R. (2012) Multiple peptidoglycan modification networks modulate *Helicobacter pylori*'s cell shape, motility, and colonization potential. *PLoS Pathog* **8**: e1002603.

Terry, K., Williams, S.M., Connolly, L., and Ottemann, K.M. (2005) Chemotaxis plays multiple roles during *Helicobacter pylori* animal infection. *Infect Immun* **73**: 803-811.

Tomb, J.-F., White, O., Kerlavage, A.R., Clayton, R.A., Sutton, G.G., Fleischmann, R.D., Ketchum, K.A., Klenk, H.-P., Gill, S., Dougherty, B.A., Nelson, K., Quackenbush, J., Zhou, L., Kirkness, E.F., Peterson, S., Loftus, B., Rischardson, D., Dodson, R., Khalak, H.G., Glodek, A., McKenney, K., Fitzegerald, L.M., Lee, N., Adams, M.D., Hickey, E.K., Berg, D.E., Gocayne, J.D., Utterback, T.R., Peterson, J.D., Kelley, J.M., Cotton, M.D., Weidman, J.M., Fujii, C., Bowman, C., Watthey, L., Wallin, E., Hayes, W.S., Borodovsky, M., Karp, P.D., Smith, H.O., Fraser, C.M., and Venter, J.C. (1997) The complete genome sequence of the gastric pathogen *Helicobacter pylori*. *Nature* **388**: 539-547.

Typas, A., Banzhaf, M., Gross, C.A., and Vollmer, W. (2012) From the regulation of peptidoglycan synthesis to bacterial growth and morphology. *Nat Rev Microbiol* **10**: 123-136.

Ursell, T.S., Nguyen, J., Monds, R.D., Colavin, A., Billings, G., Ouzounov, N., Gitai, Z., Shaevitz, J.W., and Huang, K.C. (2014) Rod-like bacterial shape is maintained by feedback between cell curvature and cytoskeletal localization. *Proc Natl Acad Sci U S A* **111**: E1025-1034.

Vasa, S., Lin, L., Shi, C., Habenstein, B., Riedel, D., Kühn, J., Thanbichler, M., and Lange, A. (2015) beta-Helical architecture of cytoskeletal bactofilin filaments revealed by solid-state NMR. *Proc Natl Acad Sci U S A* **112**: E127-136.

Waidner, B., Specht, M., Dempwolff, F., Haeberer, K., Schaetzle, S., Speth, V., Kist, M., and Graumann, P.L. (2009) A novel system of cytoskeletal elements in the human pathogen *Helicobacter pylori*. *PLoS Pathog* **5**: e1000669.

Wong, F., Garner, E.C., and Amir, A. (2019) Mechanics and dynamics of translocating MreB filaments on curved membranes. *eLife* **8**.

Wu, X., Iwai, N., and Chen, W.L. (2011) Effects of S-(3,4-dichlorobenzyl) isothiourea on different cellular events in the cyanobacterium *Anabaena* sp. strain PCC 7120. *Res Microbiol* **162**: 375-381.

Yang, D.C., Blair, K.M., Taylor, J.A., Petersen, T.W., Sessler, T., Tull, C.M., Leverich, C.K., Collar, A.L., Wyckoff, T.J., Biboy, J., Vollmer, W., and Salama, N.R. (2019) A Genome-Wide *Helicobacter pylori* Morphology Screen Uncovers a Membrane-Spanning Helical Cell Shape Complex. *J Bacteriol* **201**.

Yoshiyama, H., and Nakazawa, T. (2000) Unique mechanism of *Helicobacter pylori* for colonizing the gastric mucus. *Microbes and Infection* **2**: 55-60.

Zhao, H., Patel, V., Helmann, J.D., and Dörr, T. (2017) Don't let sleeping dogmas lie: new views of peptidoglycan synthesis and its regulation. *Mol Microbiol* **106**: 847-860.

Chapter 3. STRUCTURE AND ELASTICITY OF THE *HELICOBACTER PYLORI* CELL WALL

3.1 INTRODUCTION

As described in Chapter 2, *H. pylori* uses asymmetric peptidoglycan (PG) synthesis as one mechanism for maintaining helical cell shape (Taylor *et al.*, 2020). However, as we noted, this is likely not the sole mechanism used for shape maintenance. We observed higher relative rates of new PG incorporation at both negative Gaussian curvature, corresponding to the minor helical axis, and at the range of moderate positive Gaussian curvature that corresponds to the major helical axis. One outstanding question from these results is how helical cell shape is maintained with the lower relative amounts of synthesis between the two axes and if structural heterogeneity in the PG might further explain how helical cell shape is maintained given this growth pattern.

In our previous studies on incorporation of new PG into the *H. pylori* cell wall, we noted differences between the D-alanine-alkyne (D-Ala-alk) and *N*-acetylmuramic acid-alkyne (MurNAc-alk) labeling patterns (Taylor *et al.*, 2020). D-Ala-alk is likely incorporated into the PG by transpeptidases while MurNAc-alk is incorporated into PG subunits through the cytosolic steps of the PG biosynthetic pathway. The differences in labeling might reflect subcellular heterogeneity in the amount of crosslinking in the cell wall and thus possibly structural heterogeneity.

PG is a heteropolymer composed of relatively stiff glycan strands that are thought to be oriented roughly circumferentially and interconnected by crosslinks connecting the flexible peptide stems (Vollmer & Seligman, 2010). Given this organization, cells should become shorter in hyper-osmotic conditions and longer in hypo-osmotic conditions, with only small decreases or increases in width, respectively, as the flexible peptide stems should stretch and relax in response

to changes in turgor pressure. Indeed, the model organism *Escherichia coli* responds this way in response to hyper-osmotic shock, with extreme levels of hyper-osmotic shock leading to plasmolysis (Rojas *et al.*, 2014). Beyond the orientation of the PG strands, decreases in crosslinking density and decreases in glycan strand lengths have been shown to reduce cell stiffness (Trivedi *et al.*, 2018, Loskill *et al.*, 2014, Auer *et al.*, 2019).

While most of the work to date examining the mechanical properties of Gram-negative bacteria has focused on PG cell wall, it is becoming increasingly apparent that other cell envelope or cell envelope-associated components play significant roles in force equilibrium. The actin-like cytoskeletal protein MreB has been shown to contribute approximately as much as the cell wall to cell stiffness (Wang *et al.*, 2010). Braun's lipoprotein, which is covalently linked to PG and connects it to the outer membrane (OM), also impacts cell elasticity (Rojas *et al.*, 2018), but is notably absent from *H. pylori* PG (Costa *et al.*, 1999, Sycuro *et al.*, 2013). In addition to proteins, the outer membrane itself contributes substantially to force equilibrium. While it appears to exert little force under normal growth conditions, the force from compression of the OM reduces cell shrinkage due to hyper-osmotic shock (Rojas *et al.*, 2018). It is unclear how cytoskeletal elements and the OM might contribute to force equilibrium in helical *H. pylori* cells.

Here we undertook a detailed examination of the *H. pylori* cell envelope responses to osmotic and detergent perturbations. Comparison of the behavior of wild-type and of several mutants known to influence cell morphology reveals asymmetry in cell envelope structure corresponding to helical cell features. Interesting this asymmetry cannot be attributed to the PG sacculus. Unlike other studied rod-shaped bacteria, the *H. pylori* cell wall shows an approximately isotropic response to loss of turgor pressure.

3.2 RESULTS

3.2.1 H. pylori *shows an anisotropic response to turgor pressure perturbation inconsistent with a circumferential arrangement of PG glycan strands*

To investigate the elastic properties of the cell envelope, we loaded wild-type *H. pylori* into a microfluidic device, exposed the cells to both hyper- and hypo-osmotic conditions to alter turgor pressure, and measured the change in length and width for individual cells before and after shock. We subjected cells to 25, 50, 100, or 200 mM NaCl hyperosmotic shock (Figure 3.1). Changes in cell dimensions are reported as mean ± standard deviation. Unexpectedly, under hyper-osmotic conditions, cell length increased (absolute change: 0.13 ± 0.08, 0.16 ± 0.07, 0.16 ± 0.08, 0.18 ± 0.10 μm; percent change 4.59 ± 2.67, 5.54 ± 2.29, 5.61 ± 2.70, 5.96 ± 3.37, respectively) and cell width decreased (absolute change: 0.04 ± 0.03, 0.05 ± 0.03, 0.06 ± 0.03, 0.10 ± 0.02 μm; percent change 5.75 ± 4.69, 8.01 ± 3.78, 9.33 ± 4.25, 15.99 ± 3.52, respectively).

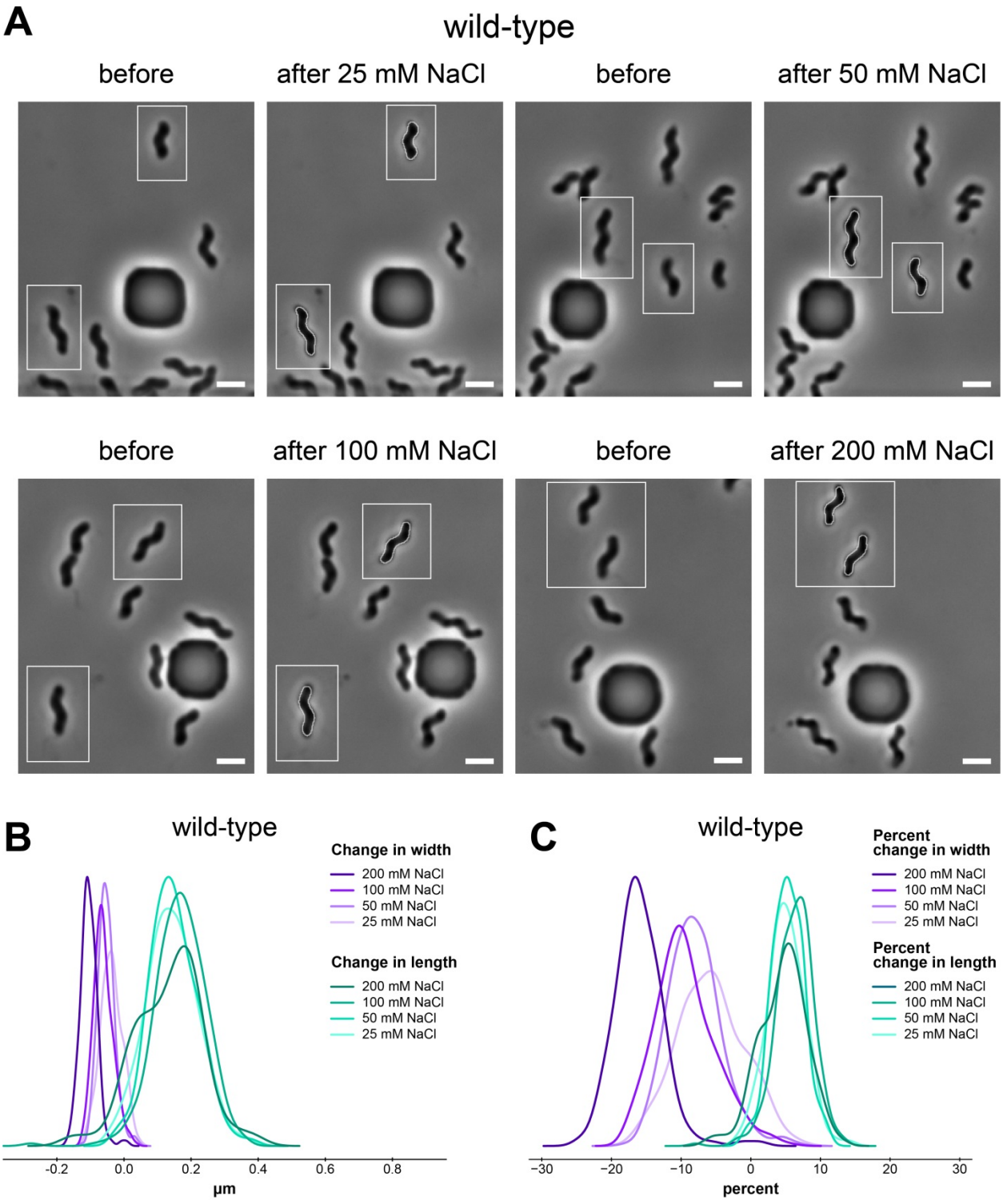

Figure 3.1. Wild-type *H. pylori* cells respond anisotropically to hyper-osmotic shock. A. Paired example phase contrast images of before and after hyper-osmotic shocks with 25, 50, 100, and 200 mM NaCl (upper left to lower right). Light outlines of the contour of two example

cells before shock are shown superimposed on the two matching cells after shock. White rectangles are drawn around these example cells. Scale bars = 2 μm. Smooth histogram of the B. absolute change in μm or C. percent change after osmotic shock in width (purples) and length (aqua tones). (n= 130, 337, 305, and 167 for 25, 50, 100, and 200 mM NaCl shocks, respectively.)

Conversely, cell length decreased (absolute change: 0.04 ± 0.05, 0.11 ± 0.07, 0.20 ± 0.09 μm; percent change 1.17 ± 1.58, 3.77 ± 2.04, 7.09 ± 2.52, respectively) and cell width increased (absolute change: 0.005 ± 0.02, 0.09 ± 0.02, 0.12 ± 0.02 μm; percent change 0.76 ± 2.68, 13.66 ± 3.44, 18.06 ± 3.93, respectively) under hypo-osmotic conditions with 50%, or 25% BB10 media, or with H_2O, respectively (Figure 3.2). Unexpectedly, there was a slight increase in length (0.02 ± 0.06 μm, 0.55 ± 1.97 %) and a slight decrease in width (0.02 ± 0.04 μm, 3.35 ± 5.29%) when exposing cells to 75% BB10 media. However, we follow the osmotic shocks with 4% paraformaldehyde added to the osmotic perturbation. Cells treated with 4% paraformaldehyde added to regular media also increased in length (0.05 ± 0.06 μm, 2.01 ± 2.02 %) and decreased in width (0.05 ± 0.02 μm, 6.83 ± 2.74 %) (Figure 3.3, gray).

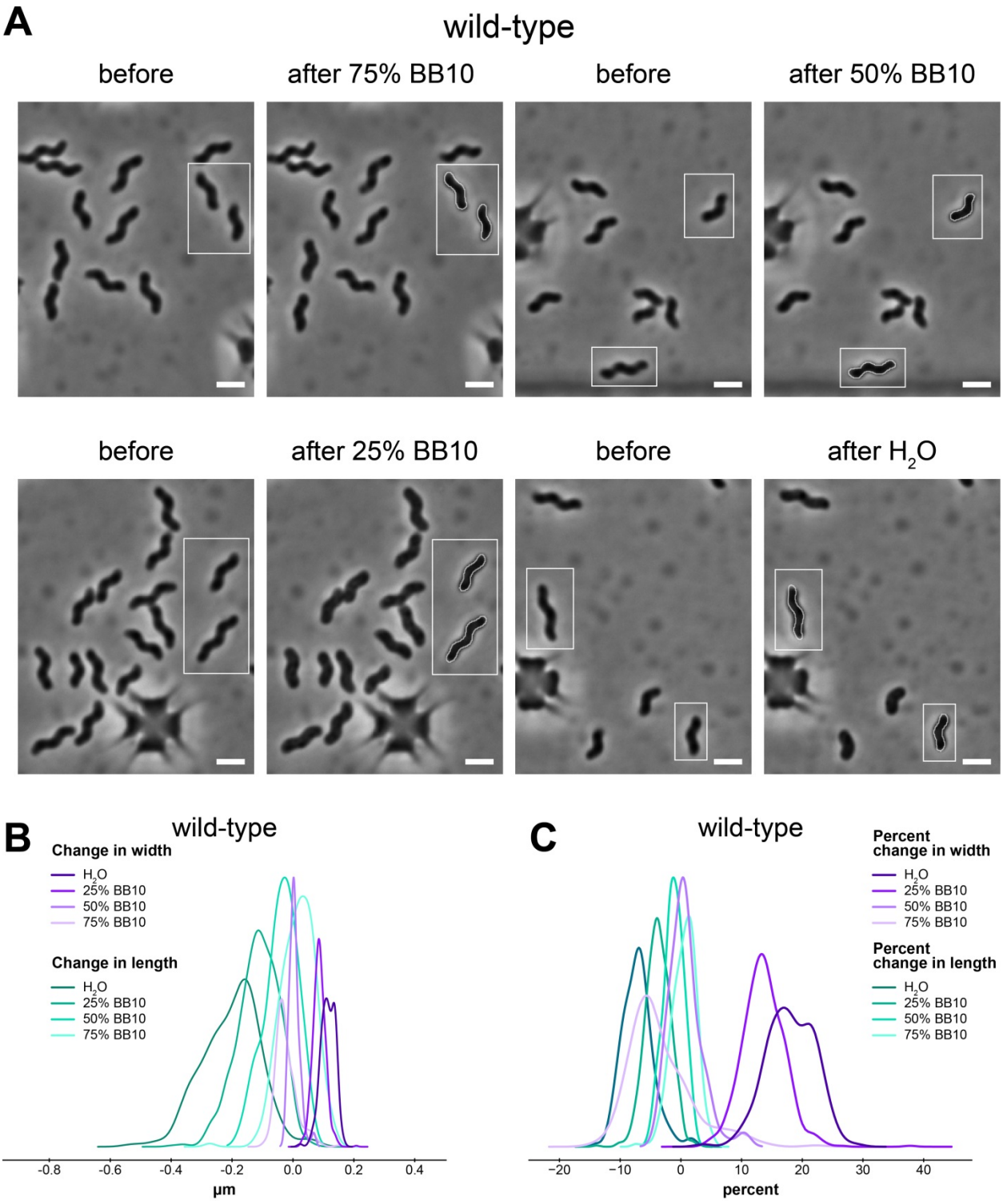

Figure 3.2. Wild-type *H. pylori* cells respond anisotropically to hypo-osmotic shock. A. Paired example phase contrast images of before and after hypo-osmotic shocks with 75%, 50%, and 25% BB10, and H_2O (upper left to lower right). Light outlines of the contour of two

example cells before shock are shown superimposed on the two matching cells after shock. White rectangles are drawn around these example cells. Scale bars = 2 µm. Smooth histogram of the B. absolute change in µm or C. percent change after osmotic shock in width (purples) and length (aqua tones). (n= 257, 78, 711, and 182 for 75, 50, 25 % BB10, and H_2O, respectively.)

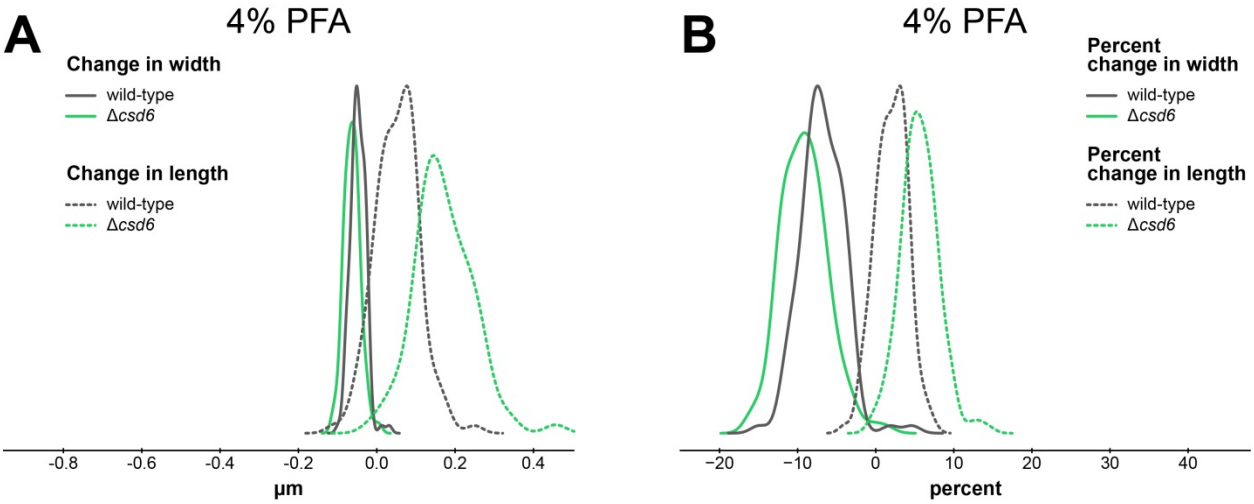

Figure 3.3. Paraformaldehyde fixation increases cell length and decreases cell width. Smooth histogram of the A. absolute change in µm or B. percent change after treatment with 4% paraformaldehyde in BB10 in width (solid lines) and length (dotted lines) for wild-type (gray, n = 122) or Δ*csd6* (green, n = 171).

3.2.2 *Anisotropic behavior does not depend on helical cell shape or cell shape-associated PG modification*

To determine if this unexpected response to osmotic shock is dependent on helical cell shape, we similarly performed hyper- (25, 50, 100, or 200 mM NaCl) and hypo-osmotic shocks (75, 50, or 25% media, or H_2O) on the straight rod mutant Δ*csd6*. As with wild-type, cells become longer (absolute change: 0.30 ± 0.10, 0.27 ± 0.09, 0.37 ± 0.11, 0.37 ± 0.13 µm; percent change 10.20 ± 2.70, 8.93 ± 2.80, 12.47 ± 3.12, 12.05 ± 3.54, respectively) and narrower (absolute change: 0.10

± 0.02, 0.11 ± 0.02, 0.12 ± 0.02, 0.12 ± 0.03 µm; percent change 15.34 ± 2.35, 16.22 ± 2.37, 18.05 ± 2.48, 18.24 ± 3.68, respectively) under hyper-osmotic conditions (Figure 3.4).

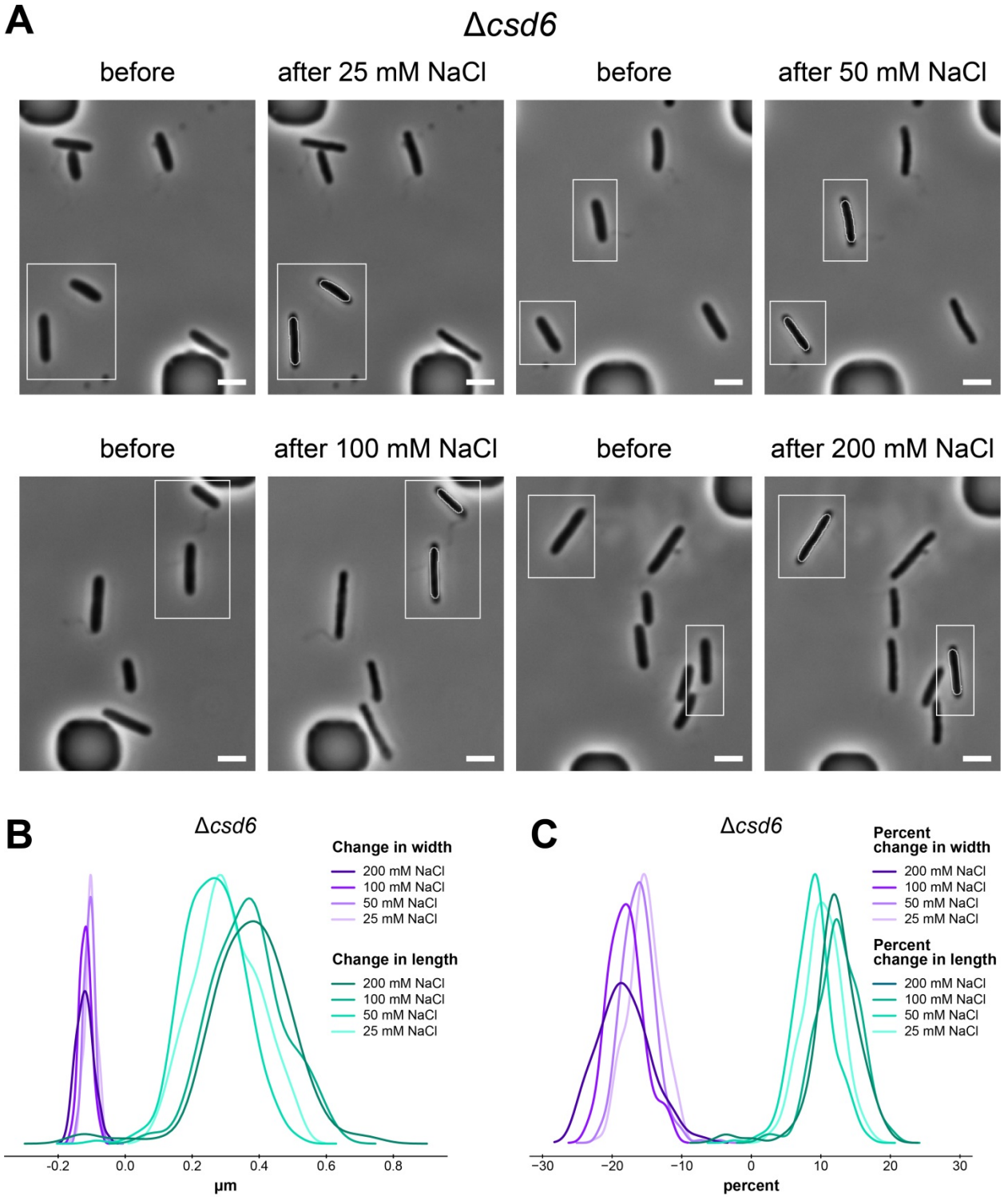

Figure 3.4. Δ*csd6* straight rod mutant *H. pylori* cells respond anisotropically to hyperosmotic shock.

A. Paired example phase contrast images of before and after hyperosmotic shocks with 25, 50, 100, and 200 mM NaCl (upper left to lower right). Light outlines of the contour of two example cells before shock are shown superimposed on the two matching cells after shock. White rectangles are drawn around these example cells. Scale bars = 2 μm. Smooth histogram of the B. absolute change in μm or C. percent change after osmotic shock in width (purples) and length (aqua tones) (n= 192, 300, 202, and 113 for 25, 50, 100, and 200 mM shocks, respectively.)

Conversely, Δ*csd6* cell length decreased (absolute change: 0.16 ± 0.07, 0.30 ± 0.14 μm; percent change 5.04 ± 2.24, 9.22 ± 3.89, respectively) and cell width increased (absolute change: 0.05 ± 0.02, 0.10 ± 0.03 μm; percent change 7.35 ± 3.16, 14.49 ± 5.09, respectively) under hypo-osmotic conditions with 25% BB10, or H_2O (Figure 3.5). Likely due to the effect of paraformaldehyde, length increased by 0.09 ± 0.08 μm, or 2.93 ± 2.56%, and width decreased by 0.03 ± 0.03 μm, or 4.29 ± 4.07% with 75% BB10. Average length decreased very subtly by 0.04 ± 0.06 μm, or 1.15 ± 2.14% and average width decreased by 0.02 ± 0.02 μm, or 3.68 ± 2.81% after exposure to 50% BB10. Cells treated with 4% paraformaldehyde added to regular media increased in length (0.17 ± 0.08 μm, 5.64 ± 2.44 %) and decreased in width (0.06 ± 0.02 μm, 9.12 ± 3.00%) (Figure 3.3, green).

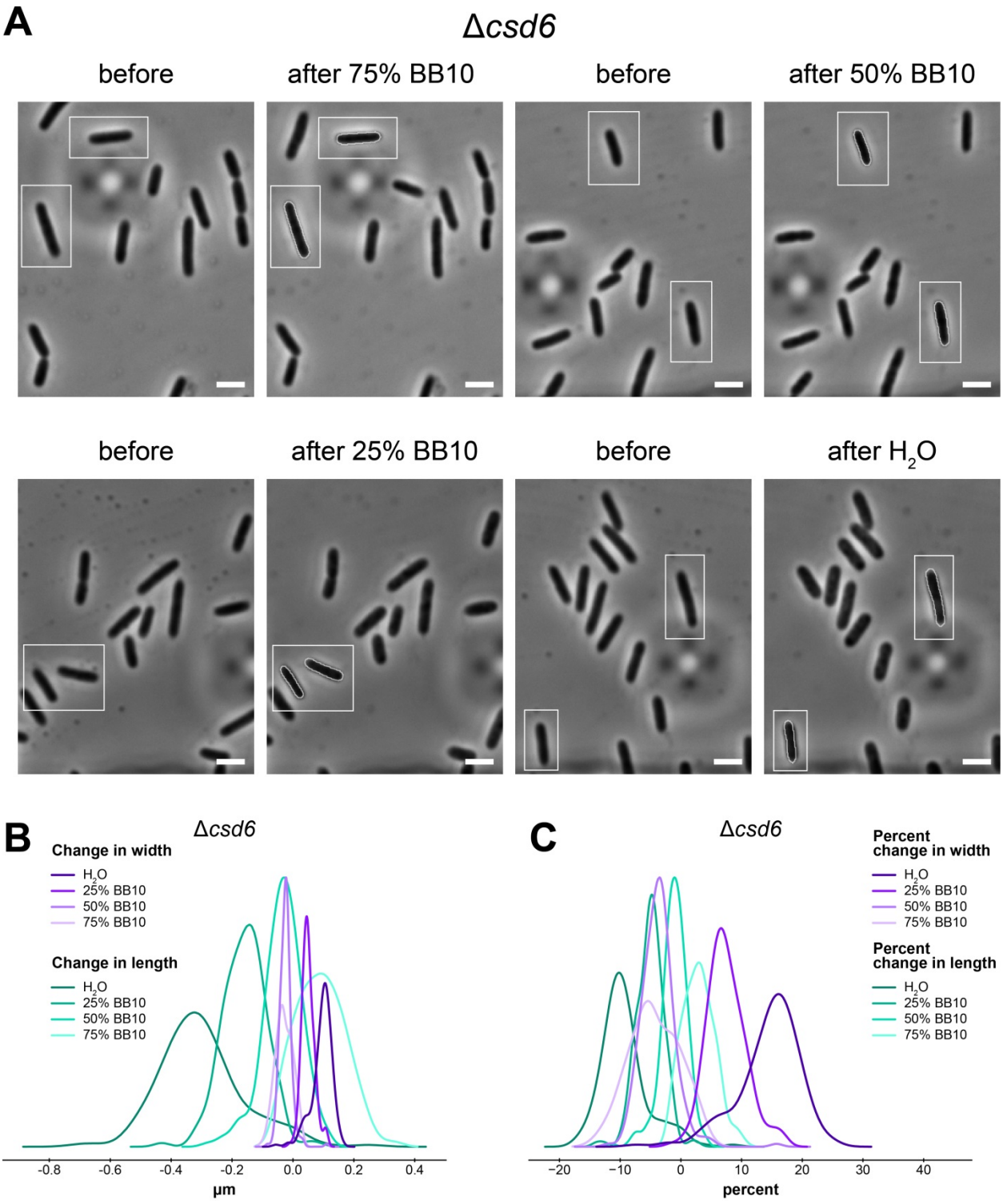

Figure 3.5. Δ*csd6* straight rod mutant *H. pylori* cells respond anisotropically to hypo-osmotic shock.

A. Paired example phase contrast images of before and after hypo-osmotic shocks with 75%, 50%, and 25% BB10, and H_2O (upper left to lower right). Light outlines of the contour of two example cells before shock are shown superimposed on the two matching cells after shock. White rectangles are drawn around these example cells. Scale bars = 2 μm. Smooth histogram of the B. absolute change in μm or C. percent change after osmotic shock in width (purples) and length (aqua tones). (n= 206, 203, 273, and 207 for 75, 50, 25 % BB10, and H_2O, respectively.)

3.2.3 *The major and minor helical axes have different responses to osmotic perturbation*

Upon looking more carefully at the shape of wild-type *H. pylori* cells after exposure to 200 mM NaCl, we noticed that movement of the minor axis appears to be the major contributor to the observed decrease in width, while the position of the major axis appears to largely stay fixed. To analyze this difference in detail, we approximated the major and minor axes as computationally defined peak and trough points, respectively, of the contours derived from the 2D phase contrast images (Figure 3.6). We analyzed shifts resulting from 25, 50, 100, or 200 mM NaCl hyper-osmotic shocks. We used the contours of cells after hyper-osmotic shock since the peaks and troughs were more pronounced and thus easier to accurately define. We then measured the distance from each of these axis points to the nearest point on the corresponding pre-shock cell contour to approximate how much the major and minor axes shifted. The peak displacement was on average 0.03 ± 0.01, 0.03 ± 0.02, 0.03 ± 0.02, and 0.04 ± 0.03 μm, respectively. In contrast, the trough displacement was on average 0.06 ± 0.03, 0.06 ± 0.03, 0.07 ± 0.03, and 0.10 ± 0.03 μm, respectively).

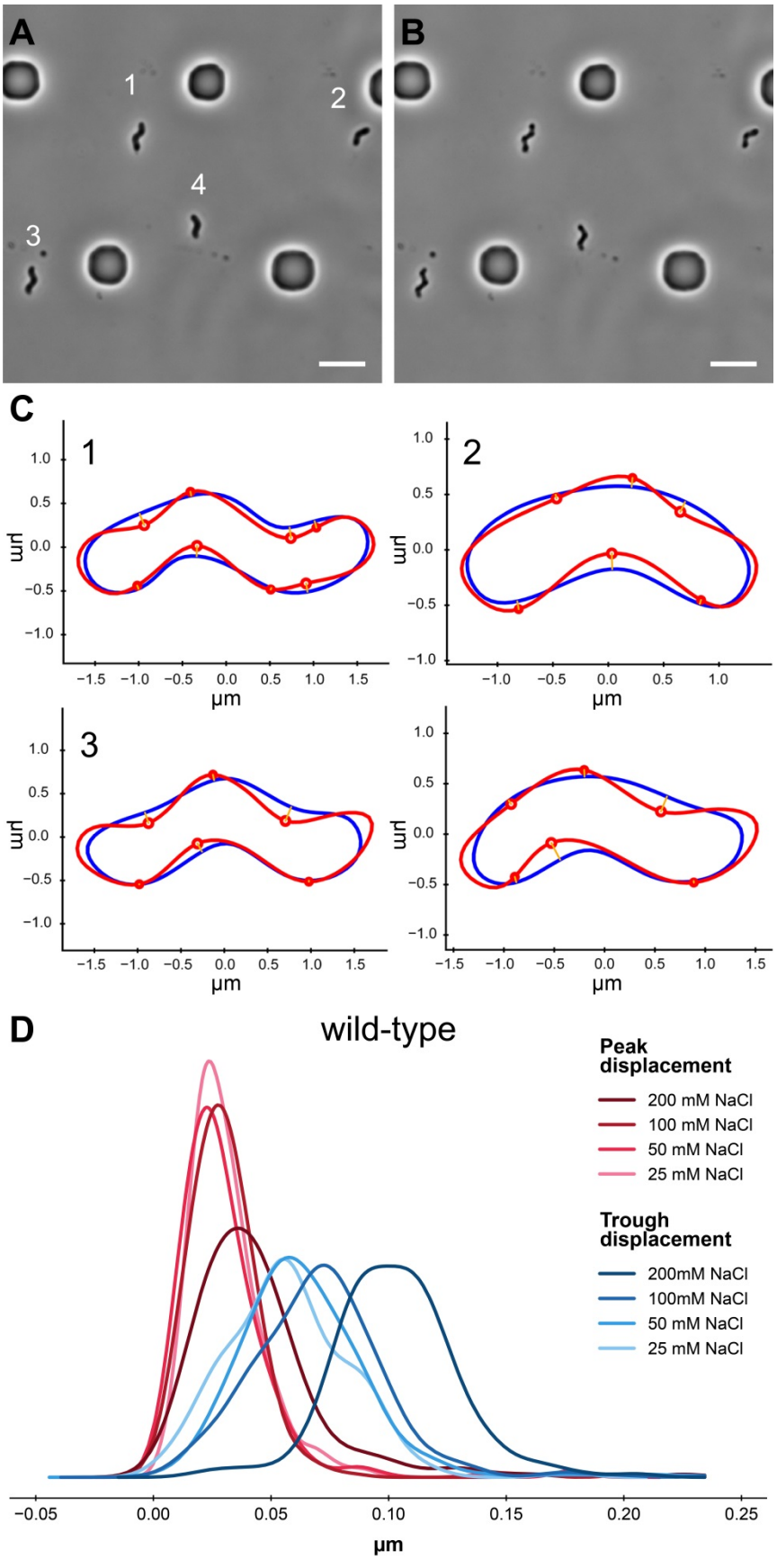
A
1
2
3
4
B
C
1
2
3
μm
D
wild-type
Peak displacement
200 mM NaCl
100 mM NaCl
50 mM NaCl
25 mM NaCl
Trough displacement
200mM NaCl
100mM NaCl
50 mM NaCl
25 mM NaCl
μm

Figure 3.6. The major and minor axes exhibit different responses to hyperosmotic shock. Phase contrast image of four example cells A. before and B. after 200 mM NaCl hyperosmotic shock. Scale bars = 5 μm. C. Cell contours before (blue) and after (red) 200 mM NaCl hyperosmotic shock. Peak and trough points (proxies for the major and minor helical axes, respectively) from the post-osmotic shock contour are shown in red dots and distance to the nearest point on the pre-shock contour displayed as yellow lines. D. Smooth histogram of the displacement of the cell contour peaks (reds) and troughs (blues) in μm for 25, 50, 100, and 200 mM NaCl hyperosmotic shocks. (n= 130, 337, 305, 167, respectively.)

3.2.4 *Increased PG crosslinking of the sacculus alters the response to osmotic perturbation*

We then asked if the cytoskeletal bactofilin CcmA was responsible for the apparent rigidity at the major helical axis. CcmA is required for helical cell shape; loss of CcmA causes cells to become gently curved rods. We recently demonstrated that CcmA preferentially localizes to the narrow range of positive Gaussian curvature corresponding to the major axis. We performed hyper-osmotic shocks with 200 mM NaCl (Figure 3.7 and 3.8) and hypo-osmotic shocks with 25% BB10 media (Figure 3.9) on Δ*ccmA* cells.

We observed that, unlike wild-type and Δ*csd6* cells, Δ*ccmA* cells decreased in both length and width after hyper-osmotic shock (Figure 3.7). We determined that there was less of a decrease in width for Δ*ccmA* compared to wild-type and Δ*csd6*. Length decreased by 0.19 ± 0.09 μm, or 5.70 ± 2.64%, and width decreased by 0.10 ± 0.02 μm, or 15.26 ± 2.16 % for Δ*ccmA* (compared to 0.11 ± 0.10 μm, 3.50 ± 3.17% length increase, and 0.12 ± 0.02 μm, 18.31 ± 2.22% width decrease for LSH100; and 0.44 ± 0.11 μm, 14.23 ± 3.51% length increase, and 0.15 ± 0.03 μm, 22.21 ± 3.99% width decrease for Δ*csd6*).

In response to hypo-osmotic perturbation with 25% BB10, Δ*ccmA* length decreased by 0.06 ± 0.05 μm, or 1.83 ± 1.54%, and width increased by 0.04 ± 0.01 μm, or 6.28 ± 2.16% (compared

to 0.08 ± 0.06 μm, 2.63 ± 2.26% length decrease, and 0.06 ± 0.02 μm, 8.55 ± 2.47% width increase for LSH100; and 0.18 ± 0.08 μm, 6.01 ± 2.07% length decrease, and 0.08 ± 0.02 μm, 11.08 ± 3.17% width increase for Δ*csd6*) (Figure 3.9).

Δ*ccmA* cells have a global increase in tetra–pentapeptide crosslinks within the PG sacculus (Sycuro *et al.*, 2010), which could contribute to the altered response to turgor pressure perturbations. To determine if the difference in crosslinking could explain why Δ*ccmA* cells respond differently to osmotic shock than wild-type and Δ*csd6* cells, we similarly performed 200 mM NaCl hyper- and 25% BB10 media hypo-osmotic shocks on Δ*csd1* cells, which still express CcmA, but have a similar degree of crosslinking to Δ*ccmA* cells (Sycuro *et al.*, 2010, Yang *et al.*, 2019). The Δ*csd1* cells responded similarly to the Δ*ccmA* cells. In response to 200 mM NaCl, length decreased 0.04 ± 0.09 μm, or 6.87 ± 3.31%, and width decreased 0.10 ± 0.02 μm, or 14.10 ± 3.05% (Figure 3.7). In response to 25% BB10, length decreased 0.04 ± 0.05 μm, or 1.17 ± 1.70%, and width decreased 0.04 ± 0.01 μm, or 6.27 ± 2.47% (Figure 3.9). However, we observed that the centerline of highly-curved Δ*csd1* cells became more curved after hyper-osmotic shock (Figure 3.8). Since cells often shift during treatment, the matched before and after cell contours are translated and rotated to achieve optimal alignment. Therefore, we cannot measure the true displacement of the major and minor axes and cannot determine if there is an asymmetric response. Additionally, since Δ*ccmA* cells are only slightly curved and because slightly curved Δ*csd1* cells do not appear to become more curved, it is not clear if this behavior is a difference between the two strains.

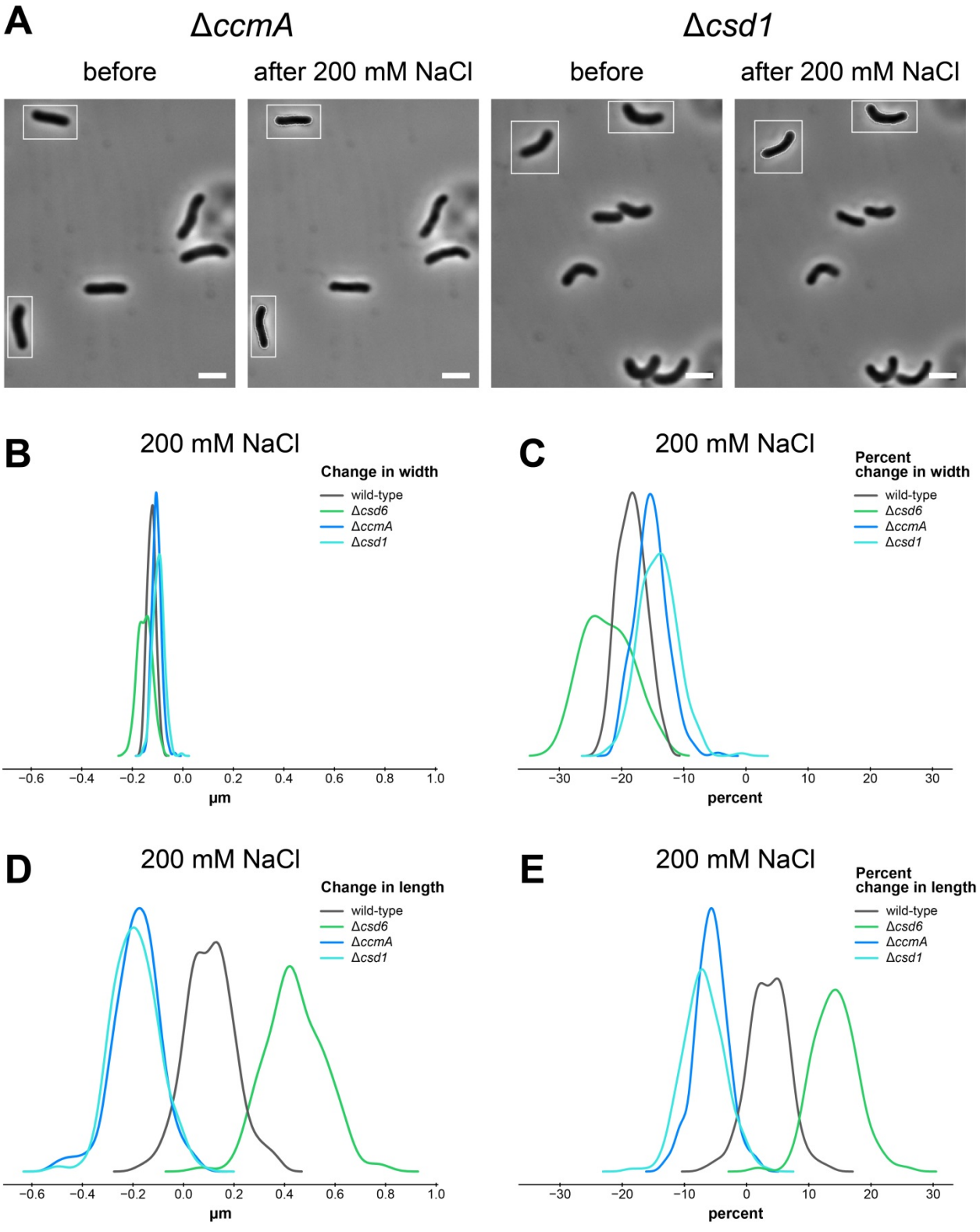

Figure 3.7. Δ*ccmA* and Δ*csd1* curved rod mutant *H. pylori* cells decrease in both length and width in response to 200 mM NaCl hyper-osmotic shock.

A. Paired example phase contrast images of Δ*ccmA* (left) and Δ*csd1* (right) before and after hyper-osmotic shocks with 200 mM NaCl. Light outlines of the contour of two example cells before shock are shown superimposed on the two matching cells after shock. White rectangles are drawn around these example cells. Scale bars = 2 µm. Smooth histogram of the absolute change in µm in width (B.) and length (D.) or percent change in width (C.) and length (E.) after osmotic shock for Δ*csd6* (green), wild-type (gray), Δ*ccmA* (medium blue), and Δ*csd1* (light blue). (Δ*csd6* n = 136; wild-type n = 187; Δ*ccmA* n = 238; Δ*csd1* n = 243). Matched cell contours from Δ*ccmA* (D.) and Δ*csd1* (E.) cells before (blue) and after (red) 200 mM hyperosmotic shock.

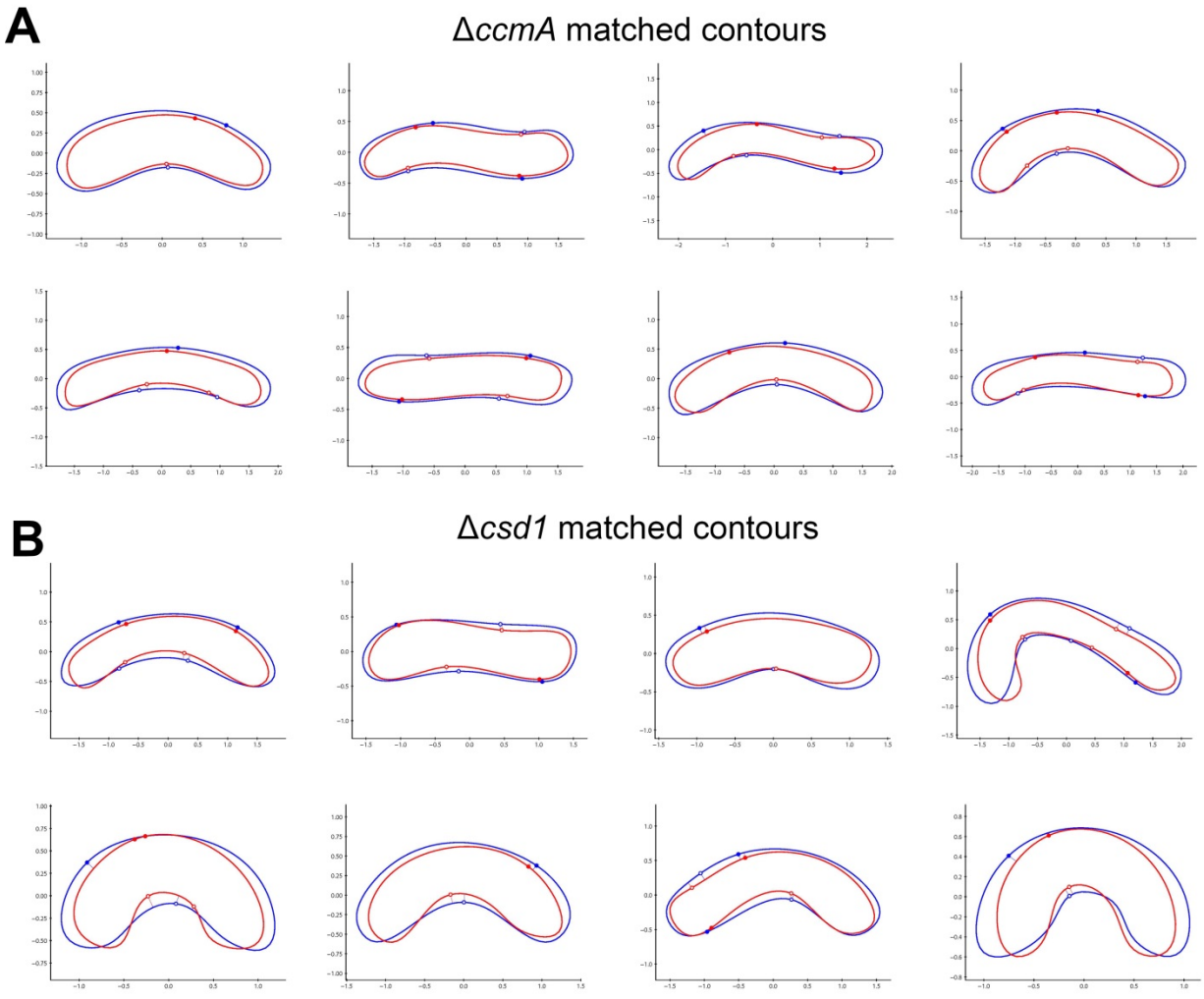

Figure 3.8. Highly-curved Δ*csd1* cells become more curved after hyper-osmotic shock with 200 mM NaCl.

Matched cell contours of A. Δ*ccmA* and B. Δ*csd1* cells before (blue) and after (red hyper-osmotic shock with 200 mM NaCl. Units = μm.

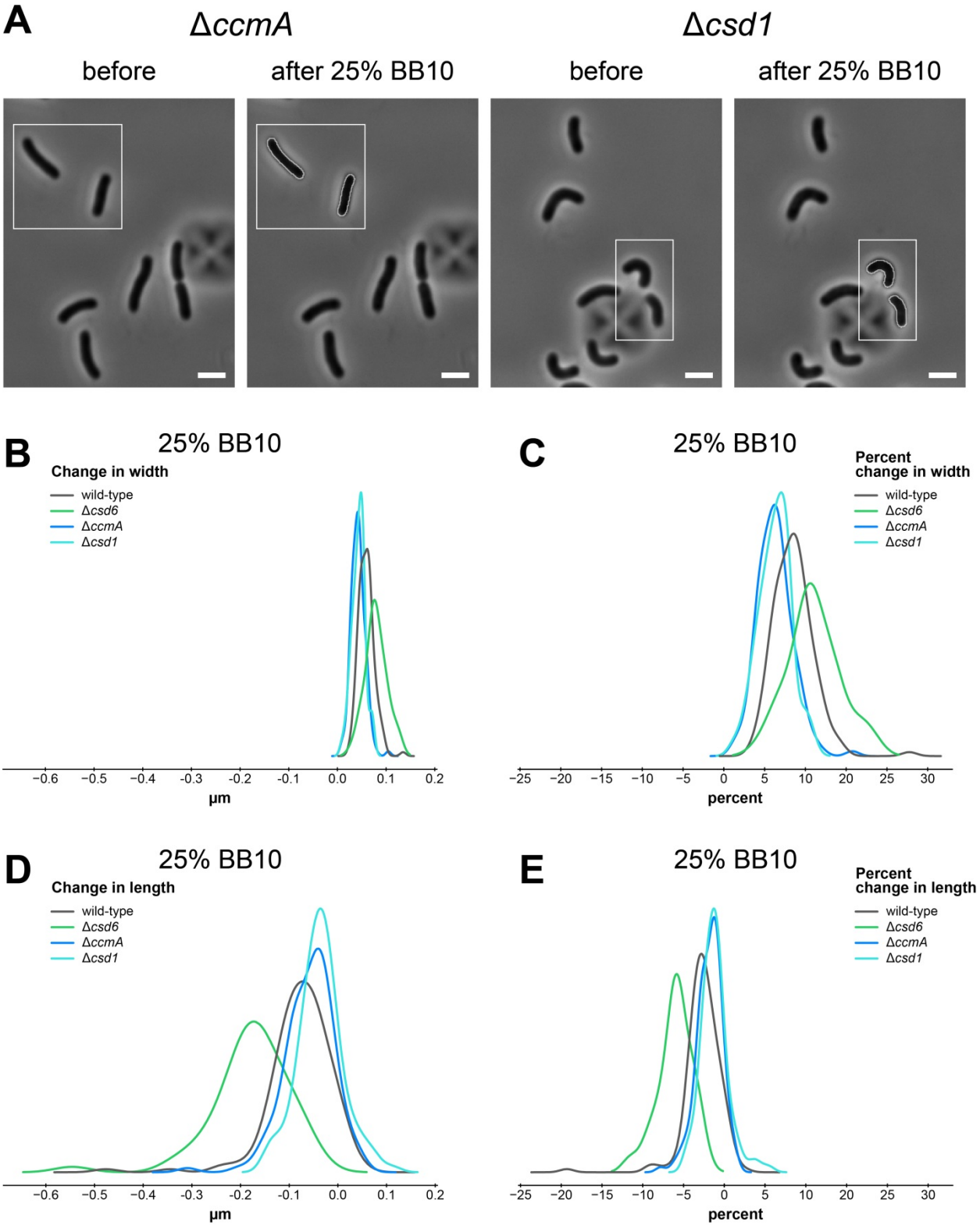

Figure 3.9. Δ*ccmA* and Δ*csd1* curved rod mutant *H. pylori* cells decrease in length and increase in width in response to hypo-osmotic shock with 25% BB10.

A. Paired example phase contrast images of Δ*ccmA* (left) and Δ*csd1* (right) before and after hypo-osmotic shock with 25% BB10. Light outlines of the contour of two example cells before shock are shown superimposed on the two matching cells after shock. White rectangles are drawn around these example cells. Scale bars = 2 μm. Smooth histogram of the absolute change in μm in width (B.) and length (D.) or percent change in width (C.) and length (E.) after osmotic shock for Δ*csd6* (green), wild-type (gray), Δ*ccmA* (medium blue), and Δ*csd1* (light blue). (Δ*csd6* n = 54; wild-type n = 146; Δ*ccmA* n = 134; Δ*csd1* n = 113).

3.2.5 *Known cytoskeletal elements contribute minimally to cell envelope elasticity*

We previously showed that CcmA preferentially localizes to Gaussian curvatures that correspond to the major helical axis. We performed similar curvature enrichment analyses of CcmA localization in Δ*csd2* and Δ*csd6* cells. Unexpectedly, CcmA was enriched at negative Gaussian curvature in both Δ*csd2* and Δ*csd6* without a peak of enrichment at positive Gaussian curvature (Figure 3.10). While both mutants have considerably less curvature than wild-type, the similarly altered localization of CcmA in these mutants, which have distinct responses to osmotic shock, suggests that CcmA contributes to cell envelope elasticity primarily through indirect effects on PG crosslinking.

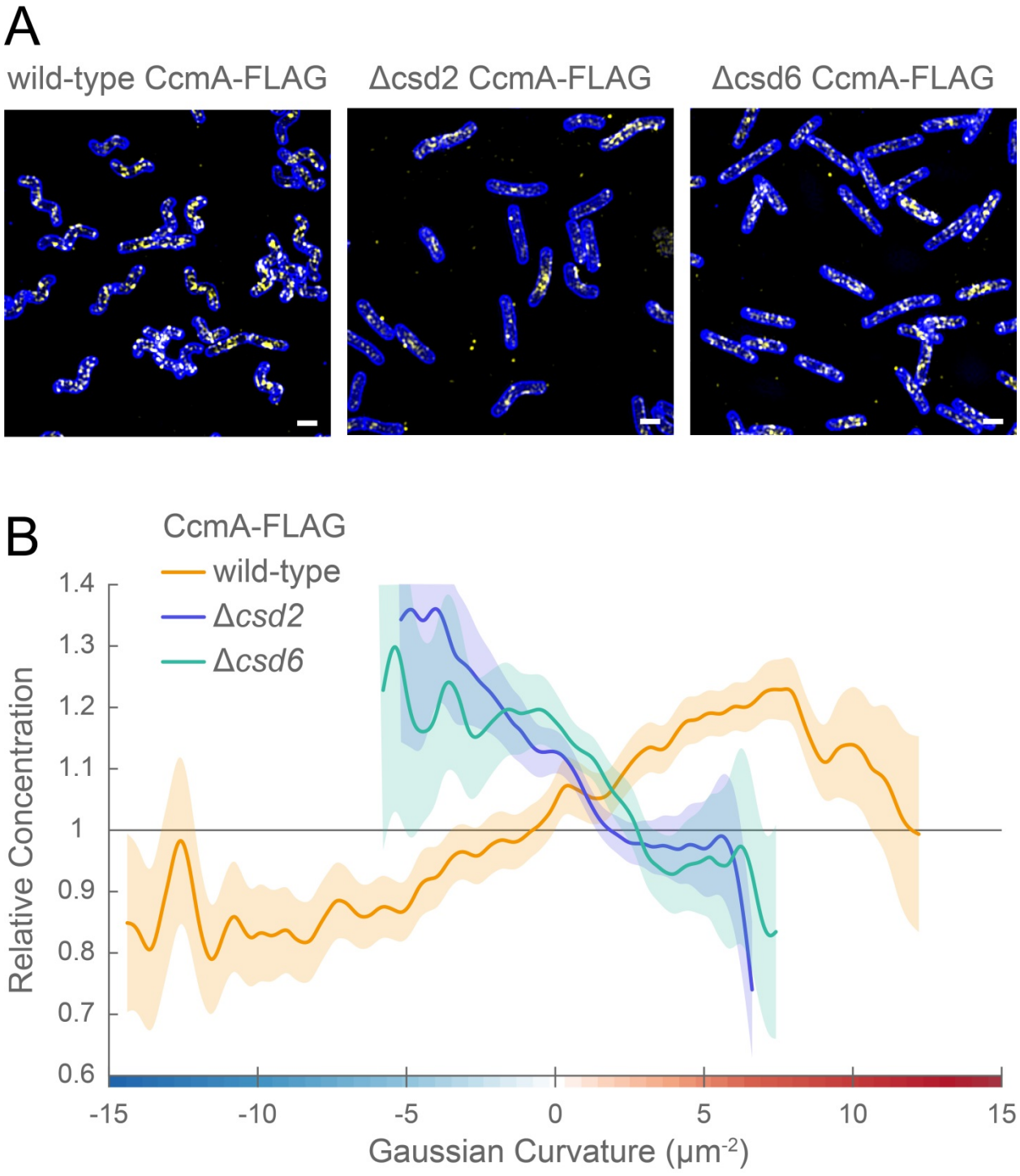

Figure 3.10. CcmA localizes preferentially to negative Gaussian curvature in Δ*csd2* and Δ*csd6* cells.

A. Maximum intensity projections of 3D SIM images in wild-type *ccmA-FLAG*, Δ*csd2 ccmA-FLAG*, and Δ*csd6 ccmA-FLAG* cells with fluorescent WGA labeling (blue) and CcmA-FLAG immunostaining (yellow). Scale bar = 1 μm. B. Curvature enrichment plot of CcmA-FLAG signal in wild-type *ccmA-FLAG* (gold), Δ*csd2 ccmA-FLAG* (blue), and Δ*csd6 ccmA-FLAG* (teal) cells.

An additional set of four cytoskeletal proteins, termed coiled-coil rich proteins (Ccrps), Ccrp58, 59, 1142, and 1143 (*HP0058, HP0059, HP1142, HP1143*) have been reported to be individually essential for proper helical shape in some but not all strains of *H. pylori* (Waidner *et al.*, 2009, Schatzle *et al.*, 2015, Yang *et al.*, 2019). We reasoned that the Ccrps could contribute to the rigidity of the major axis. Using BlastP, we identified homologues in our strain, a G27 derivative, of Ccrp58 (*HPG27_53*), Ccrp59 (*HPG27_54*), and Ccrp1143 (*HPG27_1088*). Ccrp1142 appears to be a pseudogene in G27 due to a frameshift mutation, but would otherwise have gene number *HPG27_1087*. Since individual Ccrps do not influence cell shape in our strain background (Yang *et al.*, 2019), we proceeded to knock out all Ccrps and the Ccrp pseudogene. We generated strains JTH7 *HPG27_53-54::CAT*, JTH8 *HPG27_1087-1088::aphA3*, and JTH9 *HPG27_53-54::CAT HPG27_1087-1088::aphA3*. We then collected 2D phase contrast images of cells grown in liquid culture and analyzed the shape parameters using Celltool (Sycuro *et al.*, 2010). There was no difference in helical shape between wild-type and any of the Ccrp deletion strains (Figure 3.11 A-C). We then took images of JTH9 cells before and after hyper-osmotic shock with 200mM NaCl. As with wild-type, cells become longer and narrower, and the minor axis appears to move far more than the major axis (Figure 3.11 D).

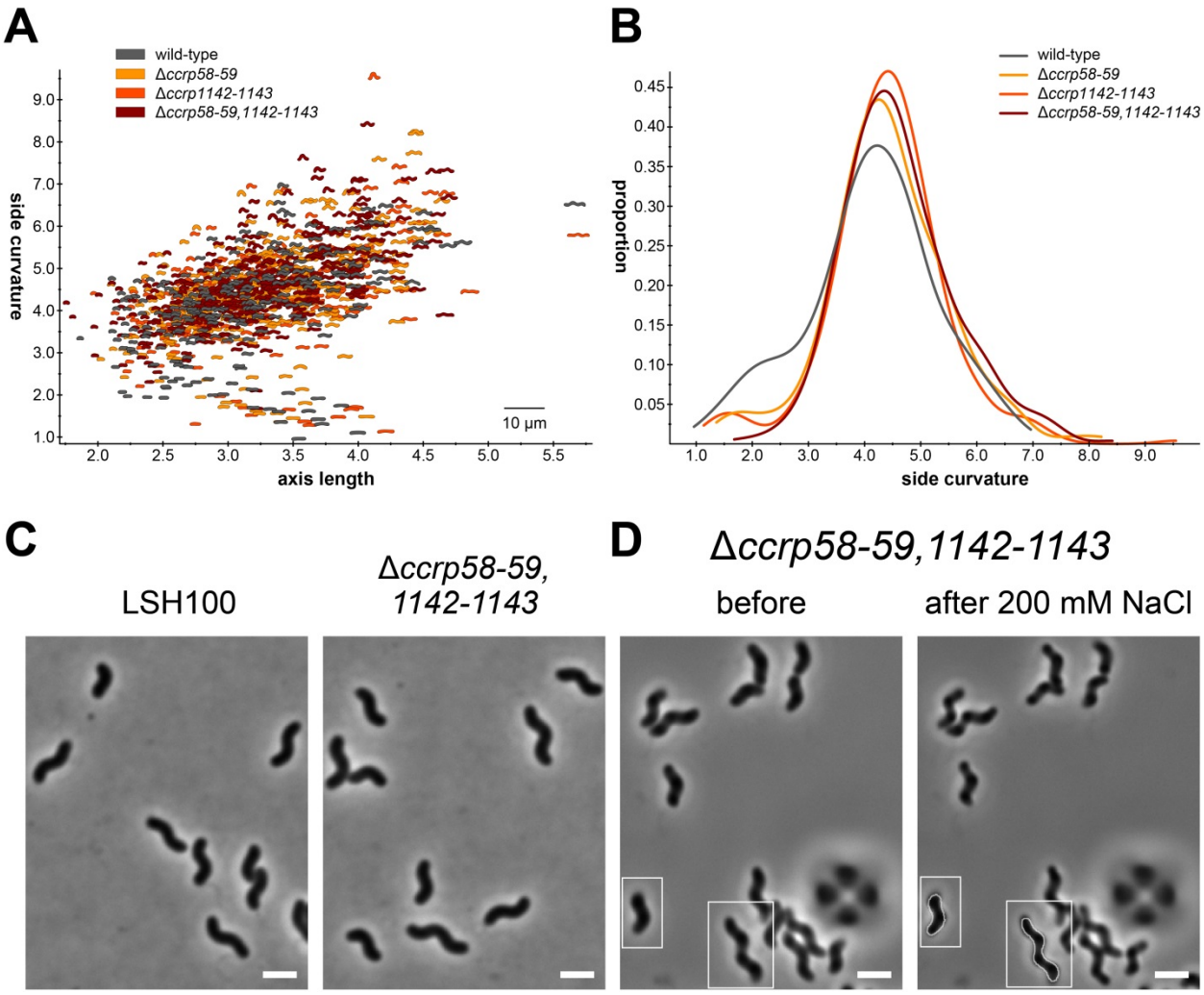

Figure 3.11. Coiled-coil proteins do not contribute to shape or response to hyper-osmotic shock in G27 derivative LSH100.

A. Scatterplot of side curvature vs. axis length and B. smooth histogram of side curvature from phase contrast images of wild-type LSH100 (gray, n = 237), Δ*ccrp58-59* (JTH7, gold, n = 331), Δ*ccrp 1142-1143* (JTH8, orange, n = 300), and the complete Ccrp knockout Δ*ccrp58-59, 1124-1143* (JTH9, red, n = 352). C. Example phase contrast images of LSH100 and Δ*ccrp58-59, 1124-1143*. D. Example paired phase contrast images of Δ*ccrp58-59, 1124-1143* before (left) and after (right) 200 mM NaCl hyper-osmotic shock. Light outlines of the contour of two example cells before shock are shown superimposed on the two matching cells after shock. White rectangles are drawn around these example cells. Scale bars = 2 μm.

3.2.6 *Identification of a cell wall feature that correlates with the major helical axis*

Since the apparent rigidity at the major axis cannot be simply attributed to cell shape-associated non-essential cytoskeletal proteins, we looked for sub-cellular heterogeneity in the cell wall composition. Taking advantage of the ability to specifically label the pentapeptides and tetrapeptides by in vitro D-Ala-alk labeling via the transpeptidases PBP4 from *Staphylococcus aureus* and LdtA from *Vibrio cholerae*, respectively, we looked for subcellular PG heterogeneity (Kuru *et al.*, 2019). Unlike many organisms, *H. pylori* has a high abundance of pentapeptide species in its cell wall (Costa *et al.*, 1999). In wild-type, pentapeptides appeared to be uniformly distributed throughout the cell wall (Figure 3.12 A). Unexpectedly, tetrapeptides were enriched at a discrete band tracing the major helical axis in wild-type (Figure 3.12 B). We labeled the penta- and tetrapeptides in Δ*csd6*, Δ*ccmA*, and Δ*csd1* cells; while pentapeptides remained uniformly distributed as in wild-type cells, tetrapeptides were localized with discrete patterns. In Δ*csd6* cells, tetrapeptides appear to be enriched in circumferential sections of the cell. Tetrapeptides in both Δ*ccmA*, and Δ*csd1* cells form discrete bands approximately parallel to the long axis of the cell. In Δ*ccmA*, the bands appear to be usually present at the major (positive Gaussian) curvature of the cell, while in Δ*csd1* cells, the bands appear mostly at the minor (negative Gaussian) curvature. Since Δ*csd6* cells increase in length and decrease in width, and since Δ*ccmA*, and Δ*csd1* cells decrease in both dimensions in response to hyper-osmotic shock we reasoned that the tetrapeptide ribbon was not responsible for the anisotropic shape change observed upon turgor modulation.

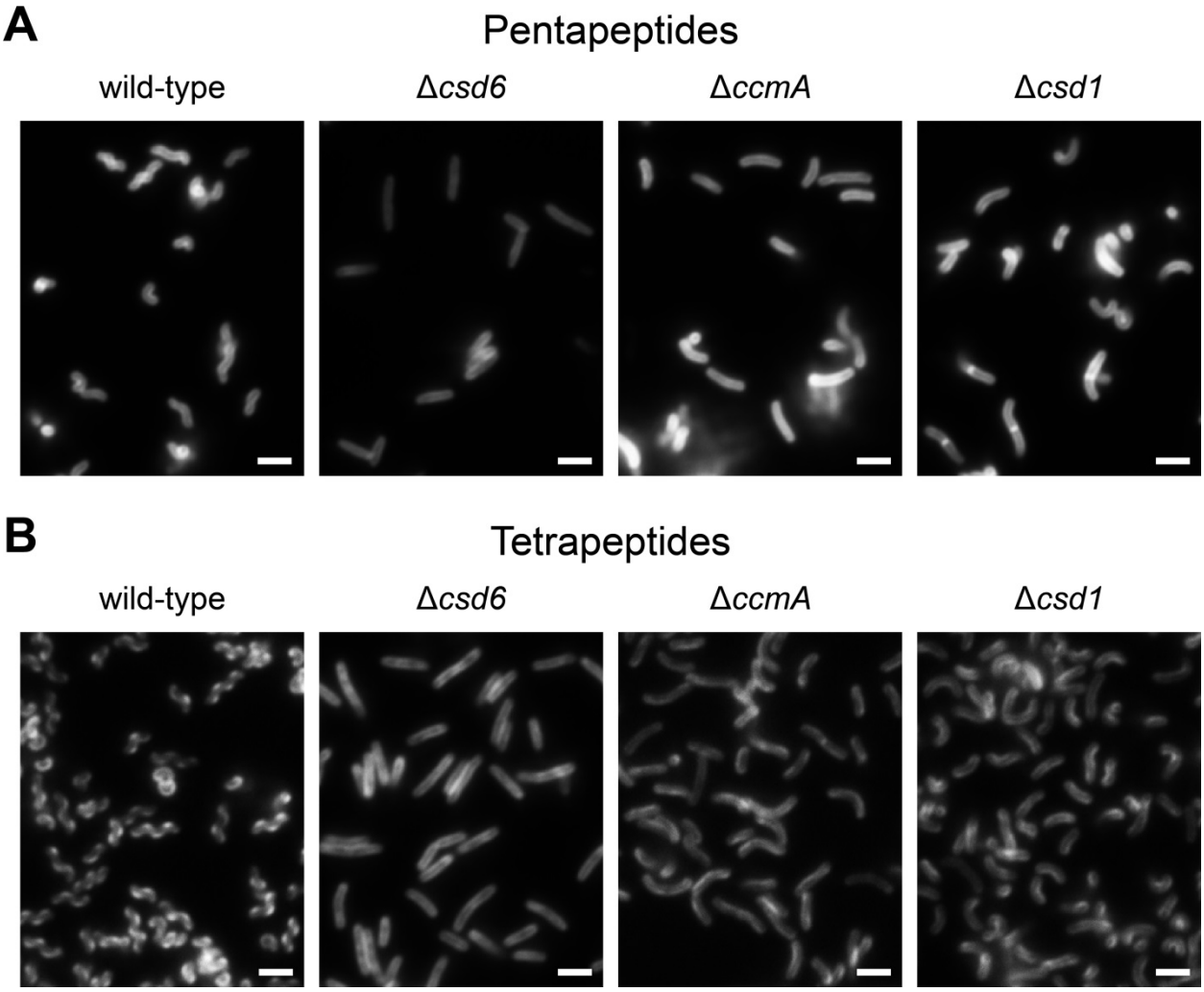

Figure 3.12. Tetrapeptides but not pentapeptides are asymmetrically distributed in *H. pylori* cell walls.

Widefield fluorescence images of D-Ala-alk-labeled A. pentapeptides or B. tetrapeptides in wild-type, Δ*csd6*, Δ*ccmA*, or Δ*csd1* cells (left to right). Scale bars = 2 μm

3.2.7 *The* H. pylori *PG sacculus has an approximately isotropic global response to turgor pressure*

In addition to the cell wall, the cell membranes as well as elements linked to the cell envelope contribute to the elastic response to osmotic shock (Rojas *et al.*, 2018). We therefore subjected cells to detergent treatment to sequentially disrupt various contributors to cell envelope elasticity

and to then completely relax the PG cell wall. We loaded wild-type *H. pylori* cells in a microfluidic device and then flowed in media with 0.125% SDS from an unprimed channel. As the SDS flowed into the imaging platform and the SDS concentration increased to 0.125%, the cells went through a range of discrete changes (Figure 3.13). Cells first became longer and narrower, appearing like cells after 200 mM NaCl treatment, but often with discernable plasmolysis. Then cells relaxed back to near-starting dimensions. Within one frame (0.5 s interval), cells became more phase light, and lengthened without a noticeable change in width. Pitch also appeared to increase without a corresponding change in helical radius. Cells then gradually begin to shrink in all dimensions, become increasingly phase light, and start to flow out of the microfluidic chamber. The faint remnants of cells were both substantially shorter and narrower than the initial cells. This suggests that, unlike *E. coli*, the *H. pylori* PG has an approximately isotropic structure.

When we similarly treated Δ*csd6*, Δ*ccmA*, and Δ*csd1* with 0.125% SDS in BB10, we saw similar types of transitions and a shared approximately isotropic relaxed final state among strains as we observed for wild-type (Figure 3.14). However, plasmolysis was strikingly different in Δ*ccmA* and Δ*csd1* cells; the cytoplasm retracted from large sections of the cell interior in generally one to two locations. In Δ*csd6* cells, there appeared to be numerous small regions of plasmolysis along the length of the cell. Because of the narrow depth of field, it was more difficult to assess plasmolysis in detail in wild-type, but its plasmolysis appeared to more closely resemble that of Δ*ccmA* and Δ*csd1* cells.

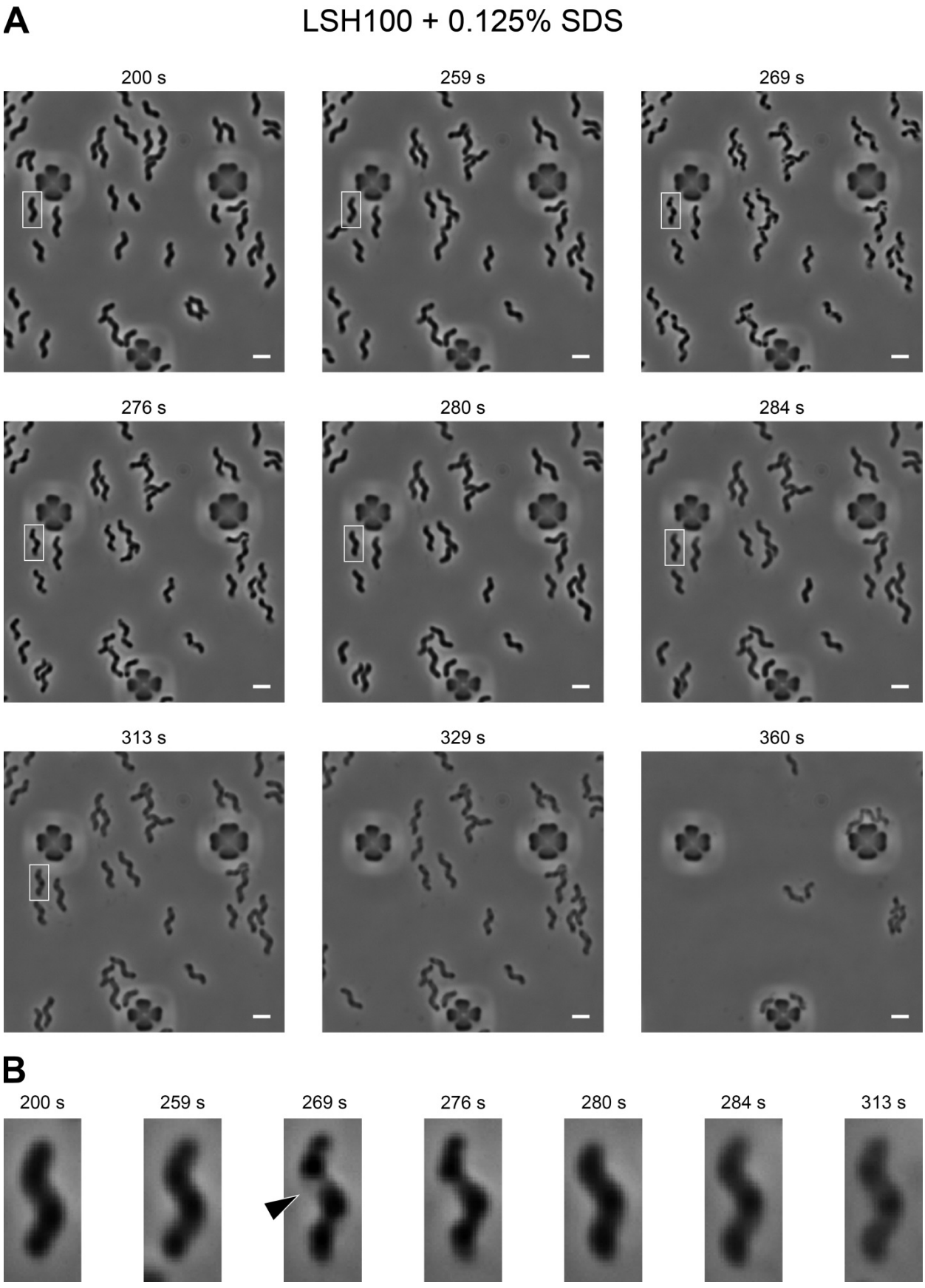
A
LSH100 + 0.125% SDS
200 s
259 s
269 s
276 s
280 s
284 s
313 s
329 s
360 s
B
200 s
259 s
269 s
276 s
280 s
284 s
313 s

Figure 3.13. LSH100 undergoes multiple transitions in response to treatment with 0.125% SDS. A. Still frames from a video of LSH100 treated with SDS increasing to a concentration of 0.125% in BB10 at 3 PSI were selected to represent each transition observed during detergent treatment. Plasmolysis is visible in most cells at 269 seconds. Near the end of treatment, cells have contracted significantly and are too small to remain trapped in the imaging chamber under flow. The time each frame was collected (seconds after initiation of flow) is annotated. Scale bars = 2 μm. B. Magnified views of example cell identified by a white rectangle in A. Arrowheads indicate apparent plasmolysis.

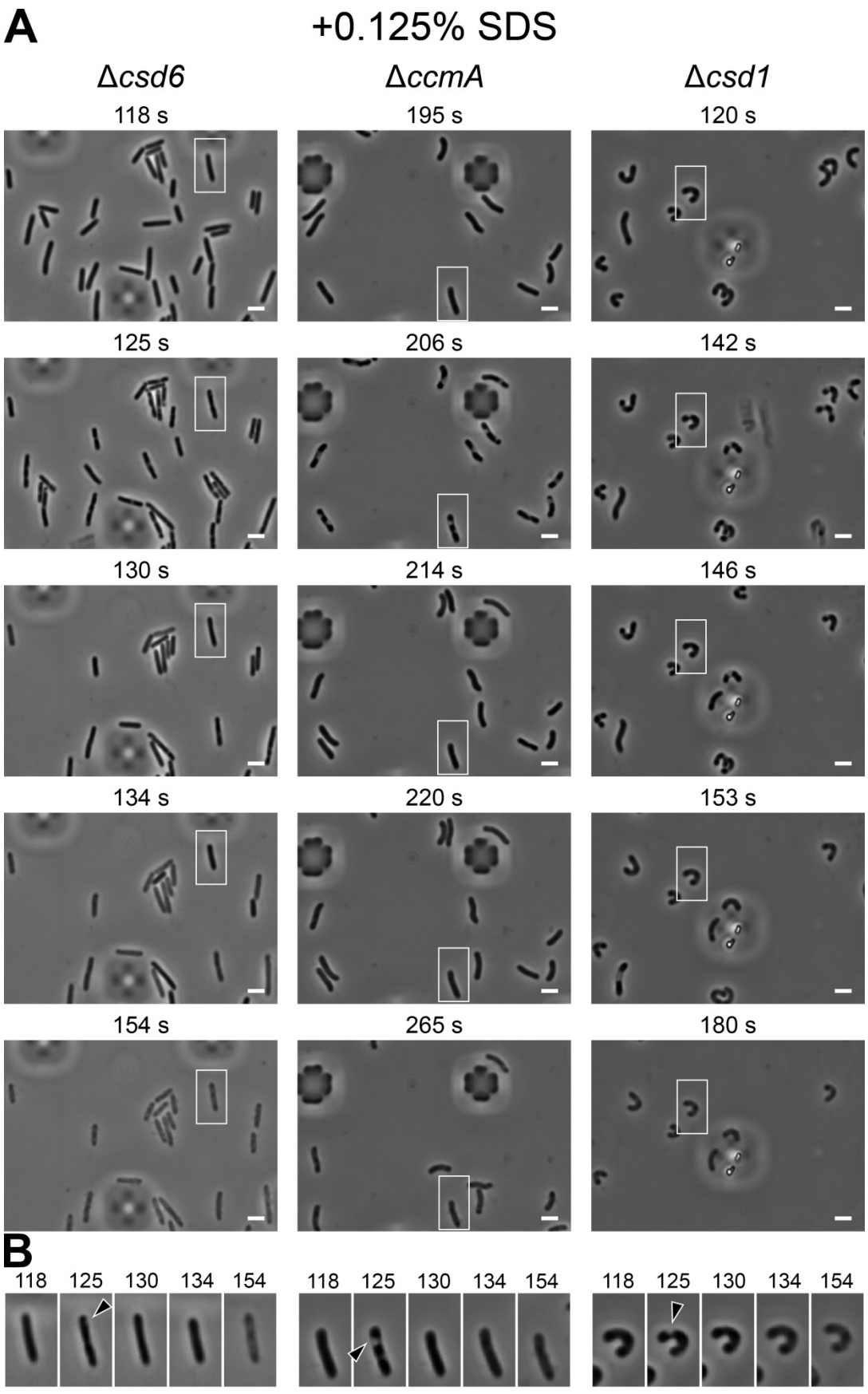
A
+0.125% SDS
Δcsd6
ΔccmA
Δcsd1
118 s
195 s
120 s
125 s
206 s
142 s
130 s
214 s
146 s
134 s
220 s
153 s
154 s
265 s
180 s
B
118 125 130 134 154
118 125 130 134 154
118 125 130 134 154

Figure 3.14. Cell shape mutants show variable plasmolysis but similar isotropic change in final state after SDS exposure.

A. Still frames from a video of Δ*csd6*, Δ*ccmA*, and Δ*csd1* (left to right) treated with SDS increasing to a concentration of 0.125% in BB10 at 3 PSI. Frames were selected to represent the major shared transitions observed during detergent treatment. Plasmolysis is visible in all strains in the images shown in the second row. Near the end of treatment, cells have contracted significantly and are too small to remain trapped in the imaging chamber under flow. The time each frame was collected (seconds after initiation of flow) is annotated. Scale bars = 2μm. B. Magnified view of one example cell from the still frames in A. for each strain, designated by white rectangle. Arrowheads indicate apparent plasmolysis.

To further investigate the structure of the *H. pylori* PG cell wall, we purified wild-type and Δ*csd6* sacculi as well as *E. coli* sacculi and imaged them using atomic force microscopy (AFM). *H. pylori* sacculi were thinner than *E. coli* sacculi (Figure 3.15 A) and the edges of both wild-type and Δ*csd6* sacculi were noticeably rougher than those of *E. coli* sacculi (Figure 3.15 A and B). Unlike in *E. coli*, there were no apparent circumferential striations and numerous pores were observed in flattened whole sacculi. This suggested that *H. pylori* sacculi may be isotropic and highly-porous. To observe single-layer PG fragments, we sonicated wild-type *H. pylori* cells, purified sacculi, and imaged them with AFM (Figure 3.15 C). Indeed, the PG appears to be riddled with pores of approximately 10 nm diameter, and there is no visually apparent geometric heterogeneity in the organization of the PG, consistent with an isotropic cell wall architecture.

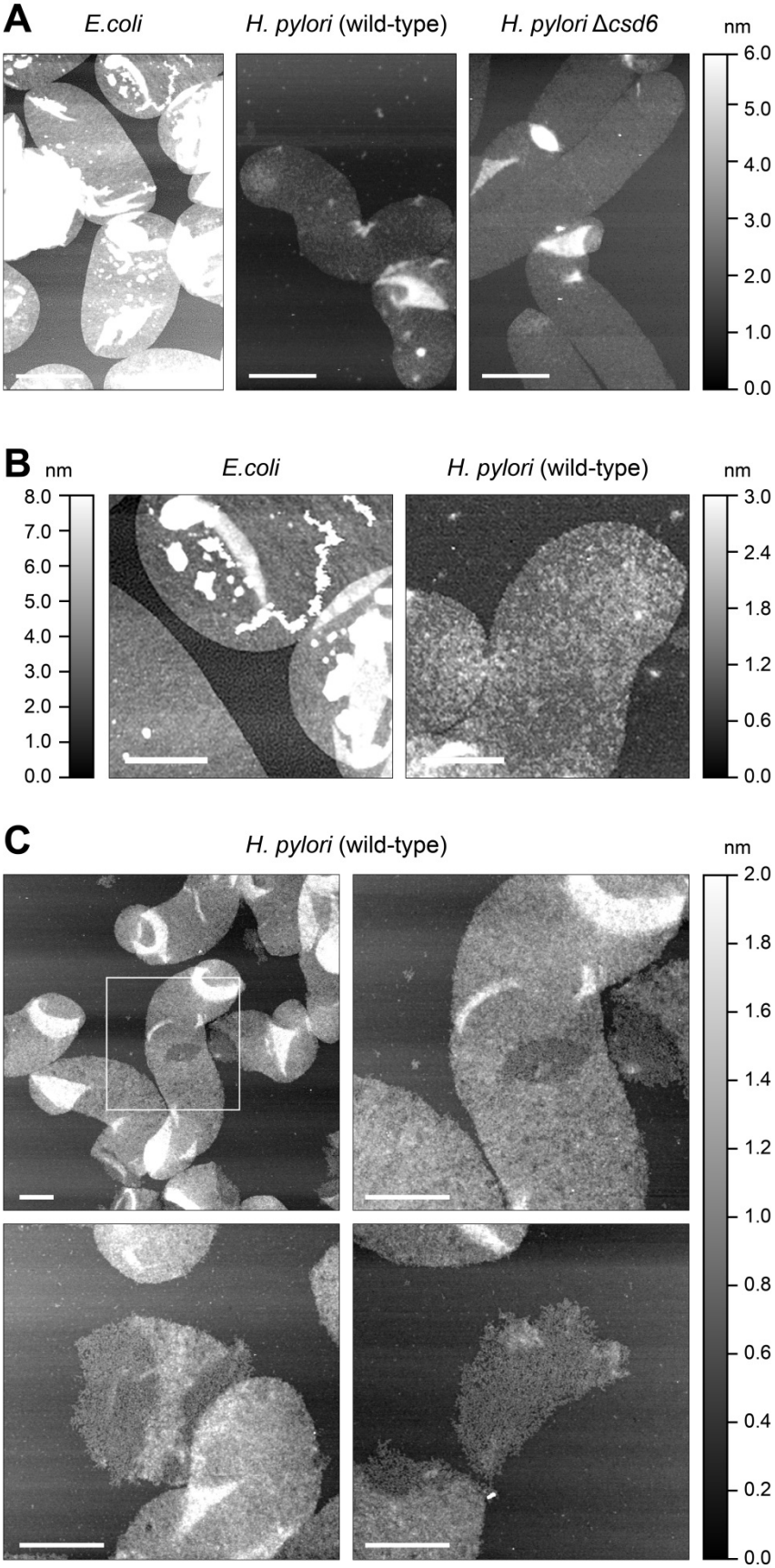
A
E.coli
H. pylori (wild-type)
H. pylori Δcsd6
nm
6.0
5.0
4.0
3.0
2.0
1.0
0.0
B
nm
8.0
7.0
6.0
5.0
4.0
3.0
2.0
1.0
0.0
E.coli
H. pylori (wild-type)
nm
3.0
2.4
1.8
1.2
0.6
0.0
C
H. pylori (wild-type)
nm
2.0
1.8
1.6
1.4
1.2
1.0
0.8
0.6
0.4
0.2
0.0

Figure 3.15. *H. pylori* sacculi have a porous organization without circumferential banding. A. AFM images of *E. coli* (left), wild-type *H. pylori* (middle), and straight rod mutant Δ*csd6 H. pylori* (right) whole sacculi. Images are scaled equally (topographic color scale at the right; scale bars = 1 μm). B. Zoomed in view of *E. coli* (left) and wild-type *H. pylori* (right) sacculi from A. with altered topographic scaling (left topographic color scale for *E. coli*, right topographic color scale for *H. pylori*, Scale bars = 0.5 μm). C. AFM images of sonicated wild-type *H. pylori* sacculi. Top right image is a zoomed in view of the top left image, as indicated by the white box. Image topography is scaled equally (topographic color scale at the right; scale bars = 1 μm).

3.3 DISCUSSION

In this work, we sought to address whether structural heterogeneity in the PG cell wall might be a contributing factor to helical cell shape maintenance. In following this line of investigation, we discovered that in addition to the PG cell wall, numerous other components contribute in unique ways to mechanical force equilibrium in intact *H. pylori* cells. Furthermore, we present evidence that the PG cell wall is highly elastic and approximately isotropic.

We observed that in response to hyper- and hypo-osmotic shock, length and width changes are inversely related for both helical wild-type cells and straight rod mutant Δ*csd6* cells, yet it remains unclear what drives this behavior. The magnitude of the shift, both in terms of absolute and percent change, is greater for Δ*csd6* than wild-type. However, with 2D images, it is not possible to completely accurately measure helical centerline length (because z-height changes do not contribute to the measured length) and cell diameter (because the narrow depth of field makes areas of the cell that are out of the focal plane appear fainter and thus narrower). These systematic biases would cause an underestimation of both centerline length and cell width. 3D measurements would be required to accurately compare wild-type and Δ*csd6*. Furthermore,

analyzing 3D images would allow us to quantify more nuanced shape transitions, particularly those influenced by the rigidity at the major axis, such as how the lengths of the major and minor axes, number of helical turns, and pitch change in response to hyper-osmotic shock and detergent treatment.

We posited that the bactofilin CcmA, which we previously demonstrated localizes preferentially to the major helical axis in wild-type, could be responsible for the observed rigidity at the major axis. We did not observe a line of rigidity at the major curvature with 200 mM NaCl treatment in Δ*ccmA*, although this could be more difficult to identify on gently-curved cells. Δ*ccmA* cells exhibit a different type of response to osmotic perturbations than wild-type and Δ*csd6*, with a decrease in both width and length under hyper-osmotic shock with 200 mM NaCl. In response to hypo-osmotic shock with 25% BB10, there is an increase in width and a slight decrease in length. The magnitude of the changes in response to hyper- and hypo-osmotic shock is lower than in wild-type and Δ*csd6*. Δ*csd1* cells show a decrease in length and width almost identical to Δ*ccmA*, despite still expressing CcmA. One notable difference between the two strains is that clearly curved Δ*csd1* cells become more curved in response to hyper-osmotic shock. In Δ*csd2* cells, which lack stable Csd1, CcmA preferentially localizes to negative Gaussian curvature. However, CcmA shows a similar localization preference in Δ*csd6*, thus CcmA mislocalization is unlikely to explain the striking difference in how Δ*ccmA* and Δ*csd1* respond to osmotic perturbation. Δ*ccmA* and Δ*csd1* cells both have a higher degree of crosslinking than wild-type and Δ*csd6*. This suggests that crosslinking characteristics of the cell wall contribute either directly or indirectly to the inverse relationship between length and width changes in response to turgor perturbation.

H. pylori cells subjected to SDS treatment went through a series of changes as SDS concentration increased. Wild-type and the three shape mutants we tested all transitioned through analogous changes: a decrease in width (though whether length increased or decreased during this phase was strain-dependent) accompanied by plasmolysis; relaxation back to a shape resembling the initial shape of the cells; an abrupt elongation and phase lightening of cells; and a gradual but substantial decrease in both length and width, and an increase in phase lightness that was accompanied by what appeared to be outer membrane sloughing. This indicates that all four strains likely have the same contributors to force equilibrium, but that there are differences in at least one contributor that affects the cell's response to perturbations. We would expect based on mechanical studies of *E. coli* that the cell wall would resist force from an increase in turgor pressure and that the outer membrane would resist compressive forces from a decrease in turgor pressure (Rojas *et al.*, 2014, Rojas *et al.*, 2018). At the end of the detergent treatment transitions, membrane can be observed sloughing off the cells as the phase light remnants of the cells gradually contract in length and width; this is consistent with the reported role of the outer membrane in resisting compressive forces.

The cell wall PG itself is anisotropic, with glycan strands roughly 5 times stiffer than peptide stems (Huang *et al.*, 2008). In *E. coli*, cells shrink primarily in length in response to treatment with SDS, leading to the conclusion that in these cells, glycan strands are on average oriented approximately circumferentially while peptide stems are oriented along the longitudinal axis (Rojas *et al.*, 2014, Vollmer & Seligman, 2010). This interpretation is further supported by AFM images of purified sacculi, which reveal striations orthogonal to the long axis of the cell (Gan *et al.*, 2008). This architecture has been thought to be the universal organization of PG for rod-shaped organisms. Our results, both the relaxation in length and width at the end of SDS

treatment and AFM images of purified *H. pylori* sacculi, indicate that *H. pylori* PG is organized approximately isotropically. This may be a consequence of the very short average glycan strand length in *H. pylori* PG (Costa *et al.*, 1999). Reducing glycan length has been shown to reduce cell stiffness in *Proteus mirabilis* and *Vibrio parahaemolyticus* (Auer *et al.*, 2019). It is possible that *H. pylori* depends on short glycans to achieve the high degree of surface curvature required for helical shape.

Given that the cell wall in isolation (at the end of detergent treatment) behaves approximately isotropically, the responses we observed after osmotic perturbation reveal that other components at the cell surface must play a contributing role in force equilibrium. This is consistent with the distinct transitions observed with SDS treatment. The SDS experiments hold much promise for connecting these transitions with the cell envelope components contributing to force equilibrium. By fluorescently labeling the cytoplasm and the periplasm, we plan to explore when each of these components ruptures, which should help us understand which of these transitions are dictated by which membranes. Additional components, perhaps such as proteins that bridge the cell wall, membranes, and/or cytoskeletal elements, are likely to mediate some of the transition dynamics and could be much more difficult to identify. *H. pylori* has no known L-D-transpeptidases, no detectable 3-3 crosslinks, and no evidence of Braun's lipoprotein or other proteins covalently linked to the cell wall (Costa *et al.*, 1999, Sycuro *et al.*, 2013). A recently-published method for screening for stiffness-modulating mutants may be effective in identifying putative mediators of force equilibrium in *H. pylori* (Auer *et al.*, 2016).

We discovered that in wild-type *H. pylori*, there is a helical ribbon of a much higher abundance of tetrapeptides that traces the major helical axis. It is possible that this ribbon is a feature recognized by proteins contributing directly or indirectly to PG remodeling; proteins

linked to the membrane that bind to this feature could contribute to the enhanced rigidity at the major axis. Since the asymmetric response of the major axis does not remain through the end state of SDS treatment, we conclude that the tetrapeptide ribbon alone does not substantially alter major axis rigidity.

Overall, we determined that *H. pylori* has as strikingly different cell wall architecture than previously studied organisms. While there is no clear subcellular mechanical heterogeneity in the sacculus, it is clear that such heterogeneity is present in the cell envelope at large, and many components may contribute to these mechanical properties. Our work underscores the importance of considering the mechanical properties of all the envelope components holistically and demonstrates that there is hitherto unappreciated diversity in cell wall organization.

3.4 METHODS

3.4.1 *Growing cultures*

H. pylori (LSH100 and derivatives, Table 1) was grown on horse blood (HB) agar plates (Humbert & Salama, 2008) incubated at 37°C under micro-aerobic conditions in either 90% air, 10% CO_2 (dual-gas) or in 10% CO_2, 10% O_2, 80% N_2 (tri-gas). For resistance marker selection, HB agar plates were supplemented with 15 μg/ml chloramphenicol, 25 μg/ml kanamycin, or both, as appropriate. Liquid *H. pylori* cultures were grown shaking in Brucella broth (BD Biosciences, Sparks, MD) supplemented with 10% heat-inactivated fetal bovine serum (BB10) (Gemini Bio-Products, West Sacramento, CA) (BB10) at 37°C in tri-gas conditions.

Table 3.5. Strains used in this study

Strain	**Genotype/description**	**Construction**	**Reference**
LSH100	Wild-type: mouse-adapted	-	Lowenthal et al.,

	G27 derivative		2009
LSH142 (*Δccm*A)	LSH100 *ccmA::cat*	-	Sycuro et al., 2010
LSH113 (Δ*csd1*)	LSH100 *csd1::cat*	-	Sycuro et al., 2010
LSH141 (*Δcsd2*)	LSH100 *csd2::cat*	-	Sycuro et al., 2010
TSH17 (*Δcsd6*)	LSH100 *csd6::cat*	-	Sycuro et al., 2013
JTH3	LSH100 *ccmA:2X-FLAG:aphA3*	-	Blair et al., 2018
JTH10	LSH100 *ccmA:2X-FLAG:aphA3 csd2::cat*	Natural transformation of JTH3 with LSH141 genomic DNA	This study
JTH11	LSH100 *ccmA:2X-FLAG:aphA3 csd6::cat*	Natural transformation of JTH3 with TSH17 genomic DNA	This study
JTH7	LSH100 *HPG27_53-54::cat*	Natural transformation of LSH100 with *HPG27_53-54::cat* stitch product	This study
JTH8	LSH100 *HPG27_1087-1088::aphA3*	Natural transformation of LSH100 with *HPG27_1087-1088::aphA3* stitch product	This study
JTH9	LSH100 *HPG27_53-54::cat HPG27_1087-1088::aphA3*	Natural transformation of JTH7 with *HPG27_1087-1088::aphA3* stitch product	This study

3.4.2 *CellASIC osmotic and detergent treatments*

For matched-cell osmotic shocks and detergent treatment videos, CellASIC B04A plates were first primed with BB10, running columns 1-6 at 4 PSI for 15 min and then columns 1-5 at 4 PSI

for 30 min. Columns 6-8 were emptied by vacuum aspiration. 100 µl of liquid *H. pylori* culture at OD_{600} 0.3-0.5 was added to column 6 and 100 µl of BB10 was added to column 8. 200 µl of osmotic or detergent treatment media was added to wells in column 1-5 as appropriate. For osmotic shocks, the appropriate column was run at 3 PSI for 1.33 min and then 50 µl of 20% PFA was added to fix cells after shock. *H. pylori* cells were gently loaded into visualization platforms by manually applying pressure to column 6 until a sufficient density of cells was loaded. For osmotic shock matched cells, cells at the left-hand side in rows 3-5 were imaged with phase contrast microscopy using a Nikon TE 200 microscope with at 100X oil-immersion objective and Nikon CoolSNAP HQ CCD camera controlled by MetaMorph software (MDS Analytical Technologies, Sunnyvale, CA), depending on the loading density, both before and after shock. For detergent treatment, one field of view was imaged every 0.5 s for up to six minutes until most cells had washed out of the field of view; images were converted to 8-bit using FIJI (Schindelin *et al.*, 2012) and figures were assembled using Adobe Photoshop.

3.4.3 *Matched pair cell shape analysis*

Phase contrast images from before and after osmotic shock were thresholded using FIJI. Structural features from the microfluidic device, cells without a corresponding match in the before/after images, cells that moved significantly during osmotic shock, and cells close enough to microfluidic device structural features to have their thresholded mask be influenced by the structural feature halos were manually removed. Cells were computationally matched and cell shape parameters were determined and changes compared using a modified version of the Celltool software.

To match corresponding cells in before and after images, the centroid of each cell was calculated, and all pairwise distances between before-cells and after-cells were calculated. We

applied the Hungarian algorithm to find the pairing of before and after cells that minimized the sum of distances between all (before, after) pairs. From this pairing we estimated the image shift from before to after as the mean displacement vector between paired before and after cells. We then un-shifted the cells by subtracting this displacement vector from the position of the after cells and re-calculated the pairing. This second step was empirically necessary to deal with large shifts between images that could otherwise leave cells systematically mis-paired.

Outlines of each cell were brought into alignment with the mean cell outline from strain NSH57 by finding the point ordering of the outline leading to the best rigid alignment between outlines, as calculated by the Procustes method of point-set alignment (allowing for rotation, translation, and reflection). This produced cell outlines for which the point ordering was consistent. Before and after pairs of outlines were brought into optimal alignment with the Procustes method, allowing for only rotation and translation. Centerlines to each cell outline were fit as previously described (Sycuro *et al.*, 2010).

The mean diameter of each cell was calculated by stepping along the cell centerline at multiple positions (excluding the poles) and calculating the intersection points of the cell outline with the line perpendicular to the centerline at each position on the centerline. The distance between these intersection points yields the cell diameter at that position on the centerline; the mean of this across the centerline was measured and compared across matched before and after cell pairs. Centerline length was also directly calculated as the cumulative distance along the poly-line defining the cell centerline and compared across cell pairs.

To approximate displacement of the major and minor axes of wild-type cells after hyper-osmotic shock, the 2D projection of the helical shape of the bacteria was characterized from cell outlines by examining the position of "peaks" and "troughs" of the outline: positions of

maximum inward and outward bending of the projected shape, with respect to the centerline. Troughs were identified as local minima of the (signed) curvature of the outline, indicating regions with the most tightly outwardly curving boundary. Peaks were identified as the local maxima of the curvature roughly opposite each trough position, and excluding the cell poles which are of high inward curvature regardless. For each peak or trough along a cell outline given image (before or after), the nearest point on the cell outline from the corresponding image (after or before, respectively) was identified. To summarize these deformations, the average distance from all peaks (from before or after images) to their nearest corresponding points was calculated, as was the average distance from all troughs to their nearest points.

3.4.4 *Quantitative analysis of CcmA curvature enrichment profiles*

To determine the curvature-based enrichment of CcmA in Δ*csd2* and Δ*csd6* cells, we generated strains JTH10 and JTH11 by transforming JTH3 (CcmA 2X-FLAG) with genomic DNA from LSH141 (Δ*csd2*) or TSH17 (Δ*csd6*), respectively, and selecting on Cm + Kan plates. We performed immunofluorescence, SIM imaging, and quantitative image analysis as described previously (Taylor *et al.*, 2020). Briefly, we grew cells in liquid culture to OD_{600} 0.3-0.5, fixed 45 min with 4% paraformaldehyde, permeabilized 1 hr in PBS + 0.1% Triton X-100, and centrifuged onto clean glass coverslips. Coverslips were stained with 30 µg/ml WGA-Alexa Fluor 555 (Invitrogen) in PBS for 30 min, washed with PBS + 0.05% Tween 20 (PBST), blocked 2 hr with PBST + 5% goat serum (Sigma), and incubated overnight at 4°C with 1:200 mouse anti-FLAG M2 (Sigma, RRID:AB_262044) in PBST. Coverslips were then washed four times with PBST, incubated with 1:200 Alexa Fluor 488 anti-mouse (A-11029, Invitrogen, RRID:AB_2534088) in PBST 45 min at room temperature, washed four times with PBST, and

mounted on slides with Prolong Diamond antifade (Invitrogen). Slides were cured for a week before imaging.

Slides were imaged on a DeltaVision OMX V4 BLAZE 3D microscope (GE Healthcare Life Sciences) equipped with Photometrics Evolve 512 emCCD cameras and an Olympus UPlanApo 100x/1.42 oil objective with oil matched for the sample refractive index. 3D triangular mesh cell surfaces were generated from the 3D-SIM OMX software reconstructions using published software (Taylor *et al.*, 2020). Using the Gaussian curvature values and CcmA-FLAG fluorescence intensities, we calculated the relative enrichment of CcmA-FLAG signal at each Gaussian curvature value for the population.

3.4.5 *Generating Ccrp deletion strains and analyzing shape parameters*

Homologues of Ccrp58, 59, and 1143 in LSH100 were identified by a BlastP search. The homologue of Ccrp 1142 appears to be a pseudogene in LSH100. We generated deletion mutants of these strains by assembling deletion cassettes using PCR SOEing (Horton, 1995) and natural transformation. The *HPG27_53-54::cat* (Ccrp58-59) cassette was generated using primers G27_53_up_F1P1, G27_53_Cat_up_R, C1, C2, Cat_G27_54Dn_F, and HPG27_55_R_P2. The *HPG27_1087-1088::aph3* (Ccrp1142-1143) cassette was generated using primers G27_1089_F1P1, G27_1088_Kan_R, O#251 kan5'F, O#256 kan3'RC, Kan_G27_1087_Dn_F, and G27_1086_R-P2. LSH100 was transformed using the *HPG27_53-54::cat* cassette, selected on Cm plates to generate strain JTH7, and was confirmed by PCR using primers Cat_mid_F and HPG27_55_R. LSH100 was transformed using the *HPG27_1087-1088::aphA3* cassette, selected on Kan plates to generate strain JTH8, and was PCR confirmed using primers G27_1089_F1P1 and HPG27_1086_R. JTH7 was transformed using the *HPG27_1087-1088::aphA3* cassette,

selected on Cm + Kan plates to generate strain JTH9, and was PCR confirmed using primers Cat_mid_F, HPG27_55_R, G27_1089_F1P1, and HPG27_1086_R.

LSH100, JTH7, JTH8, and JTH9 were grown in liquid culture overnight to OD_{600} 0.3-0.5, spotted on 1.5% Brucella broth agarose pads, and imaged with phase contrast microscopy using a Nikon TE 200 microscope with at 100X oil-immersion objective and Nikon CoolSNAP HQ CCD camera controlled by MetaMorph software (MDS Analytical Technologies, Sunnyvale, CA). Phase contrast images were thresholded using FIJI (Schindelin *et al.*, 2012) and analyzed using Celltool as previously described (Sycuro *et al.*, 2010).

Table 3.6. Primers used in this study

Primer name	**Sequence (5' to 3')**
C1	GATATAGATTGAAAAGTGGAT
C2	TTATCAGTGCGACAAACTGGG
HPG27_52_F	GCGCAATACATGCCTAAG
G27_53_up_F1P1	GATAAAAGGAGATATTCTTATG
G27_53_Cat_up_R	CCACTTTTCAATCTATATCTTGCTTTTGTAATTCGGTATTC
Cat_mid_F	CTGCCGATATTTACGTTTGGGAAG
Cat_G27_54Dn_F	AGTTTGTCGCACTGATAATAAAGGAAATATCATGGT
HPG27_55_R_P2	CGCTTTCTTTAGACAAGCTAG
HPG27_55_R	GTGCTTTTAGTCCCAAAG
G27_1089_F1P1	GATTGAATTTGATAACACCTC
G27_1088_Kan_R	GCTTCATAGAGTAATTCTGTGATTTTCCTTTAAGATTTG
Kan_G27_1087_Dn_F	CTGGATGAATTGTTTTAGTACCTAGATCATGCGAATCGTATTTATGGGAAC
G27_1086_R_P2	CCATATCCATAAGCATGGTGC
HPG27_1089_F	GAGTTTTAAACGCTCAAG
HPG27_1086_R	GCTTGCAACCTTGCTATAC

cat_mid_F	CTGCCGATATTTACGTTTGGGAAG
O#251 kan5'F	ACAGAATTACTCTATGAAGCGCC
O#256 kan3'RC	ATCTAGGTACTAAAACAATTCATCC

3.4.6 *Pentapeptide and tetrapeptide labeling*

Total pentapeptides and tetrapeptides were labeled similarly as described (Kuru *et al.*, 2019). *H. pylori* was grown in liquid culture to OD_{600} = 0.3-0.5. Cells from 1 ml of culture were pelleted in a microcentrifuge for 5 minutes at 5000 rpm, and resuspended in 1 ml ice cold 70% EtOH for 30 minutes. Cells were then centrifuged at 2000 rpm for 5 minutes and washed twice in 1 ml Dulbecco's phosphate-buffered saline. Cells were resuspended and incubated 1 hr at 37°C in 150 µl PBP4Sa buffer (12.5 mM HEPES, pH 7.5, 2 mM $MnCl_2$, 0.25 mM Tween-20) with 2 µl D-alanine-alkyne (100 mM in H_2O) and 5 µl PBP4 (1.8 mg/ml) from *Staphylococcus aureus* for pentapeptide labeling or LdtAVc buffer (50 mM Tris HCl, pH 7.5, 100 mM NaCl) with 2 µl D-alanine-alkyne (100 mM in H_2O) and 2 µl LdtA (2.5 mg/ml) from *Vibro cholerae* for tetrapeptide labeling. Cell suspension density was normalized between samples using a hemocytometer and cells were spun onto clean glass coverslips at 500 rpm for 5 minutes in a Hettich Rotana 460R swinging bucket centrifuge. Click chemistry was performed on coverslips using the Click-iT Cell Reaction Buffer Kit (Invitrogen) according to manufacturer instructions (without BSA washes) with 8 µg/ml Alexa Fluor 555 Azide (Invitrogen). Coverslips were washed two times with 0.05% Tween-20 in PBS (PBST) for 10 minutes each and were mounted on slides using Prolong Diamond antifade (Invitrogen). Slides were imaged on a Nikon TE 200 microscope with at 100X oil-immersion objective and Nikon CoolSNAP HQ CCD camera controlled by MetaMorph software (MDS Analytical Technologies, Sunnyvale, CA). Images

were converted to 8-bit using FIJI. Contrast was increased 100% and figures were assembled in Adobe Photoshop.

3.4.7 *Sacculi purification and AFM imaging*

Sacculi were purified as previously described (Blair *et al.*, 2018). Sacculi were harvested from 330 ml of a liquid culture grown to 0.6-0.8 OD_{600}/ml by centrifugation in a TOMY TX-160 centrifuge with a TMA-27 rotor at 5000 rpm for 10 min at 4°C. Cell pellets were resuspended in 6 ml chilled Dulbecco's PBS (Gibco), added dropwise into 6 ml boiling 8% SDS, and boiled for an additional 6.5 hr. Sacculi were pelleted in a Beckman–Coulter Optima L-90K ultracentrifuge with a SW41 Ti rotor at 28000 rpm for 60 min at 28°C, resuspended in 2.5 ml of 4% SDS, and boiled for 4 hr. Sacculi were pelleted in a Beckman TL-100 ultracentrifuge with a TLA 100.3 rotor at 70000 rpm for 60 min at 25°C. Sacculi were resuspended in 2.5 ml of 1% SDS, and boiled for 4 hr, pelleted by ultracentrifugation, and resuspended in 2.5 ml of 50 mM sodium phosphate pH 7.4. Sacculi were incubated at 37°C with 0.25 mg α-chymotrypsin (Sigma, C4129) for 4 hr, then an additional 0.25 mg of α-chymotrypsin was added and sacculi were incubated overnight at 37°C. 300 µl of 10% SDS was added and samples were boiled for 4 hr. Sacculi were collected by ultracentrifugation, resuspended in 2.5 ml of 1% SDS, and boiled for 4 hr. Sacculi were washed by repeated ultracentrifugation and resuspension in ddH_2O until supernatant was demonstrated free from SDS by the Hayashi test (Hayashi, 1975). Purified SDS-free sacculi were resuspended in 500 µl of ddH_2O plus 0.02% sodium azide and stored at 4°C until use.

AFM imaging was carried out as previously described (Turner *et al.*, 2013). AFM was performed using a Multimode AFM with extended Nanoscope III controller. All imaging was carried out in tapping mode. Imaging was performed in ambient conditions using silicon

cantilevers (Olympus AC160TS). AFM image processing was carried out using Gwyddion (version 2 or later).

3.5 BIBLIOGRAPHY

Auer, G.K., Lee, T.K., Rajendram, M., Cesar, S., Miguel, A., Huang, K.C., and Weibel, D.B. (2016) Mechanical Genomics Identifies Diverse Modulators of Bacterial Cell Stiffness. *Cell Syst* **2**: 402-411.

Auer, G.K., Oliver, P.M., Rajendram, M., Lin, T.Y., Yao, Q., Jensen, G.J., and Weibel, D.B. (2019) Bacterial Swarming Reduces *Proteus mirabilis* and *Vibrio parahaemolyticus* Cell Stiffness and Increases beta-Lactam Susceptibility. *mBio* **10**.

Blair, K.M., Mears, K.S., Taylor, J.A., Fero, J., Jones, L.A., Gafken, P.R., Whitney, J.C., and Salama, N.R. (2018) The *Helicobacter pylori* cell shape promoting protein Csd5 interacts with the cell wall, MurF, and the bacterial cytoskeleton. *Mol Microbiol* **110**: 114-127.

Costa, K., Bacher, G., Allmaier, G., Dominguez-Bello, M.G., Engstrand, L., Falk, P., de Pedro, M.A., and García-del Portillo, F. (1999) The Morphological Transition of *Helicobacter pylori* Cells from Spiral to Coccoid Is Preceded by a Substantial Modification of the Cell Wall. *Journal of Bacteriology* **181**: 3710-3715.

Gan, L., Chen, S., and Jensen, G.J. (2008) Molecular organization of Gram-negative peptidoglycan. *Proc Natl Acad Sci U S A* **105**: 18953-18957.

Horton, R.M. (1995) PCR-mediated recombination and mutagenesis. SOEing together tailor-made genes. *Mol Biotechnol* **3**: 93-99.

Huang, K.C., Mukhopadhyay, R., Wen, B., Gitai, Z., and Wingreen, N.S. (2008) Cell shape and cell-wall organization in Gram-negative bacteria. *Proc Natl Acad Sci U S A* **105**: 19282-19287.

Humbert, O., and Salama, N.R. (2008) The *Helicobacter pylori* HpyAXII restriction-modification system limits exogenous DNA uptake by targeting GTAC sites but shows asymmetric conservation of the DNA methyltransferase and restriction endonuclease components. *Nucleic Acids Res* **36**: 6893-6906.

Kuru, E., Radkov, A., Meng, X., Egan, A., Alvarez, L., Dowson, A., Booher, G., Breukink, E., Roper, D.I., Cava, F., Vollmer, W., Brun, Y., and VanNieuwenhze, M.S. (2019) Mechanisms of Incorporation for D-Amino Acid Probes That Target Peptidoglycan Biosynthesis. *ACS Chem Biol* **14**: 2745-2756.

Loskill, P., Pereira, P.M., Jung, P., Bischoff, M., Herrmann, M., Pinho, M.G., and Jacobs, K. (2014) Reduction of the peptidoglycan crosslinking causes a decrease in stiffness of the *Staphylococcus aureus* cell envelope. *Biophys J* **107**: 1082-1089.

Rojas, E., Theriot, J.A., and Huang, K.C. (2014) Response of *Escherichia coli* growth rate to osmotic shock. *Proc Natl Acad Sci U S A* **111**: 7807-7812.

Rojas, E.R., Billings, G., Odermatt, P.D., Auer, G.K., Zhu, L., Miguel, A., Chang, F., Weibel, D.B., Theriot, J.A., and Huang, K.C. (2018) The outer membrane is an essential load-bearing element in Gram-negative bacteria. *Nature* **559**: 617-621.

Schatzle, S., Specht, M., and Waidner, B. (2015) Coiled coil rich proteins (Ccrp) influence molecular pathogenicity of *Helicobacter pylori*. *PLoS One* **10**: e0121463.

Schindelin, J., Arganda-Carreras, I., Frise, E., Kaynig, V., Longair, M., Pietzsch, T., Preibisch, S., Rueden, C., Saalfeld, S., Schmid, B., Tinevez, J.Y., White, D.J., Hartenstein, V., Eliceiri, K., Tomancak, P., and Cardona, A. (2012) Fiji: an open-source platform for biological-image analysis. *Nat Methods* **9**: 676-682.

Sycuro, L.K., Pincus, Z., Gutierrez, K.D., Biboy, J., Stern, C.A., Vollmer, W., and Salama, N.R. (2010) Peptidoglycan crosslinking relaxation promotes *Helicobacter pylori*'s helical shape and stomach colonization. *Cell* **141**: 822-833.

Sycuro, L.K., Rule, C.S., Petersen, T.W., Wyckoff, T.J., Sessler, T., Nagarkar, D.B., Khalid, F., Pincus, Z., Biboy, J., Vollmer, W., and Salama, N.R. (2013) Flow cytometry-based enrichment for cell shape mutants identifies multiple genes that influence *Helicobacter pylori* morphology. *Mol Microbiol* **90**: 869-883.

Taylor, J.A., Bratton, B.P., Sichel, S.R., Blair, K.M., Jacobs, H.M., DeMeester, K.E., Kuru, E., Gray, J., Biboy, J., VanNieuwenhze, M.S., Vollmer, W., Grimes, C.L., Shaevitz, J.W., and Salama, N.R. (2020) Distinct cytoskeletal proteins define zones of enhanced cell wall synthesis in *Helicobacter pylori*. *eLife* **9**.

Trivedi, R.R., Crooks, J.A., Auer, G.K., Pendry, J., Foik, I.P., Siryaporn, A., Abbott, N.L., Gitai, Z., and Weibel, D.B. (2018) Mechanical Genomic Studies Reveal the Role of D-Alanine Metabolism in *Pseudomonas aeruginosa* Cell Stiffness. *mBio* **9**.

Turner, R.D., Hurd, A.F., Cadby, A., Hobbs, J.K., and Foster, S.J. (2013) Cell wall elongation mode in Gram-negative bacteria is determined by peptidoglycan architecture. *Nat Commun* **4**: 1496.

Vollmer, W., and Seligman, S.J. (2010) Architecture of peptidoglycan: more data and more models. *Trends Microbiol* **18**: 59-66.

Waidner, B., Specht, M., Dempwolff, F., Haeberer, K., Schaetzle, S., Speth, V., Kist, M., and Graumann, P.L. (2009) A novel system of cytoskeletal elements in the human pathogen *Helicobacter pylori*. *PLoS Pathog* **5**: e1000669.

Wang, S., Arellano-Santoyo, H., Combs, P.A., and Shaevitz, J.W. (2010) Actin-like cytoskeleton filaments contribute to cell mechanics in bacteria. *Proc Natl Acad Sci U S A* **107**: 9182-9185.

Yang, D.C., Blair, K.M., Taylor, J.A., Petersen, T.W., Sessler, T., Tull, C.M., Leverich, C.K., Collar, A.L., Wyckoff, T.J., Biboy, J., Vollmer, W., and Salama, N.R. (2019) A Genome-Wide *Helicobacter pylori* Morphology Screen Uncovers a Membrane-Spanning Helical Cell Shape Complex. *J Bacteriol* **201**.

Chapter 4. APPROACHING A UNIFIED MODEL FOR HELICAL SHAPE MAINTENANCE AND GENERATION

4.1 PREFACE

"*There is grandeur in this view of life, with its several powers, having been originally breathed by the Creator into a few forms or into one; and that, whilst this planet has gone cycling on according to the fixed law of gravity, from so simple a beginning endless forms most beautiful and most wonderful have been and are being evolved.*"

-Charles Darwin, On the Origin of Species

4.2 PIECING TOGETHER A UNIFYING MODEL OF HOW *H. PYLORI* ACHIEVES HELICAL CELL SHAPE

I joined the lab at a very exciting time for studying cell shape. Laura Sycuro had identified a suite of non-essential proteins that are each individually required for helical cell shape. It was clear that peptidoglycan remodeling, both trimming crosslinks and trimming monomeric tetra- and tripeptides, was crucial for helical shape. But it was also apparent that management of global PG composition alone was insufficient for helical shape; we knew that Δ*csd5* has a global PG profile identical to that of wild-type, yet has a straight-rod cell shape.

My broad research goal was to begin to understand how these individual contributors come together at large to promote helical shape. What is the significance of trimming monomeric peptide stems down to dipeptides? What is the downstream consequence of crosslink trimming that allows the cells to be highly curved and twisted? We finally have some completely unexpected yet elegant answers and can speculate about remaining pieces to the puzzle.

4.3 WHAT IS A HELIX? HOW COULD A HELIX BE BUILT?

The first step in attempting to elucidate *H. pylori*'s helical cell shape patterning was to hypothesize what mechanisms might be involved. The logical place to start was with the cell wall, since purified cell walls maintain helical shape and since many of the cell shape proteins directly modify the cell wall. There are multiple ways to impart structure on the PG cell wall: patterning synthesis, structure, and/or turnover. Two key papers led me to hypothesize that cell wall synthesis patterning could be necessary for helical shape. Takeuchi et al. demonstrated that filamented *Escherichia coli* could be forced to adopt curved and helical shapes after growth in agarose chambers. Upon release from the chambers, cells gradually straightened over several doublings rather than immediately relaxing, suggesting that the cells grew as curved rods in the chambers (Takeuchi *et al.*, 2005). Work in *Caulobacter crescentus* indicated that mechanical forces imparted by cytoskeletal filaments could drive curvature via biased cell wall synthesis (Cabeen *et al.*, 2009). The intermediate filament crescentin (CreS) forms a cell-spanning filament at the inner, or minor, curvature of the cell. *C. crescentus* elongates primarily through a band of PG synthesis at mid-cell. In a *creS* overexpression strain (which is highly-curved) but not in the straight rod Δ*creS*, mid-cell PG synthesis occurs as a wedge, with the shorter side of the wedge on the minor curvature. When the CreS filament is disrupted in vivo by induced expression of a dominant negative CreS mutant, cells straighten gradually, a process that is growth-dependent.

4.4 TACKLING PG SYNTHESIS ANALYSIS

Studying PG synthesis in an organism that elongates via dispersed sidewall growth is quite challenging. Sites of new PG insertion were originally determined by pulse-chase labeling with

D-cysteine, sacculus purification, biotinylation and immunolabeling of D-Cys with gold particles, and imaging with TEM. This approach was not amenable for our studies. The signal:noise for the absence of signal dispersed along the sidewall would be poor. Furthermore, extracting meaningful data about the patterning of a 3D helical shape from flattened 2D purified sacculi was likely impossible. The development of two metabolic probes, florescent and clickable D-alanine (Kuru *et al.*, 2012, Siegrist *et al.*, 2013), and later, clickable *N*-acetylmuramic acid (MurNAc) (Liang *et al.*, 2017), made quantification of PG synthesis experimentally feasible. The advent of super-resolution imaging, particularly structured illumination microscopy, made imaging these labels in 3D in petite *H. pylori* cells possible.

The other half of the challenge was computational. In contemplating the geometry of a helical cell, I realized the two features I was most interested in comparing are what I have come to term the minor and major helical axes - the shortest helical path spanning the sidewall and the path 180° opposite, respectively. We needed a way to extract a 3D surface from our 3D SIM images and computationally define these axes. After several initial collaboration attempts, we engaged in a very fruitful collaboration with Ben Bratton and Joshua Shaevitz (Princeton University) and eventually had the tools to define a 3D mesh surface with Gaussian curvature and fluorescence intensity values at each vertex. From computational simulations, we determined the average Gaussian curvature at the major and minor axes for our populations.

This toolset allowed us to determine that *H. pylori* synthesizes higher relative levels of PG at the major and minor helical axes as compared to the sides and poles. Using SIM imaging and the same analysis pipeline, we showed that curvature enrichment of the actin-like cytoskeletal protein MreB is associated with the enhanced synthesis at negative Gaussian curvature and enrichment of the cytoskeletal bactofilin CcmA is associated with the enhanced synthesis at

positive Gaussian curvature. Our two initial hypotheses for PG synthesis patterning were that PG is synthesized uniformly along the whole sidewall or that PG synthesis is enhanced at the major axis area compared with the rest of the cell. Our results did not support either hypothesis and were, in fact, rather counterintuitive.

The enhanced synthesis levels at negative Gaussian curvature should, all else being equal, straighten out the cell. We postulate that the enhanced synthesis at the major axis works to counteract the straightening effect of enhanced synthesis at negative Gaussian curvature. However, one outstanding question is why there is enhanced synthesis at the minor axis - *H. pylori*'s PG synthesis strategy seems quite inefficient. One possible explanation is that, being a specialized version of a rod-shaped cell, *H. pylori* is simply stuck with the MreB-based evolutionary solution for generating a straight rod using dispersed growth along the sidewall. *H. pylori* may therefore have reached the solution of adding additional PG synthesis patterning rules to the existing cell-straightening feedback pattern for synthesis.

4.5 THE MECHANICS OF SHAPE

In analyzing PG synthesis patterning, we observed that while the general features of the labeling pattern of D-Ala-alk and MurNAc-alk were consistent, there were notable differences between the two labels. The peak of enrichment at the major axis was far more pronounced for the MurNAc-alk label than for the D-Ala-alk label. These two metabolic probes are thought to be incorporated into the PG through different routes: MurNAc-alk through the cytoplasmic PG biosynthesis pathway and D-Ala-alk through transpeptidases. While MurNAc-alk might be tolerated differently by the two structurally-unrelated *H. pylori* transglycosylases RodA and PBP1, influencing labeling, an alternative explanation is that transpeptidation activity, and thus crosslinking, may have geometrically-biased activity, resulting in sub-cellular structural

heterogeneity. If this were the case, we would expect an enhanced degree of crosslinking at the minor axis area.

To investigate if there is subcellular structural PG heterogeneity, I performed hyper- and hypo-osmotic shocks on cells trapped in a microfluidic device. Completely unexpectedly, I observed that changes in length and width were inversely related: under hyper-osmotic conditions, cells became longer and narrower, under hypo-osmotic conditions, cells became shorter and wider. We have been a cell wall-centric lab to date, and thus began to think about how organization of the PG might explain this response. Is the *H. pylori* cell wall organized like a honeycomb?

It took treating cells with a variety of detergent concentrations to realize that, while the cell wall structural organization does appear to be quite distinct from that of *E. coli*, it seems to be other components of the cell envelope that drive the unusual inverse relationship between length and width changes in response to osmotic shock. The *H. pylori* cell wall seems to be highly porous, highly elastic, and approximately isotropic (though composed of anisotropic subunits). Due to the high proportion of very short glycan strands, the *H. pylori* cell wall may simply be highly disorganized. Interestingly, new PG synthesis labeling appears by eye to be organized in a somewhat circumferential pattern, as do MreB patches. The circumferential banding of cell wall synthesis is more pronounced for D-Ala-alk labeling than for MurNAc-alk labeling, and is particularly striking for D-Ala-alk labeling of Δ*ccmA* cells (Figure 2.12 and 2.32).

Our osmotic perturbation studies have made us realize that we need to move beyond just thinking about the cell wall to thinking about the cell envelope at large. Our results have also revealed many fascinating but challenging questions. How are length and width inversely coupled, if not by the structure of the PG wall itself? The fact that Δ*ccmA* and Δ*csd1* cells have

directly coupled decreases/increases in length and width in response to hyper- or hypo-osmotic shock, respectively, could provide some insights. At the end of detergent treatment, these cell walls shrink substantially like those of wild-type. Perhaps the extra crosslinking in the Δ*ccmA* and Δ*csd1* cell walls sufficiently increases the rigidity of the cell wall to alter the force balance of the envelope after osmotic shock.

The other major outstanding question from these results is what is responsible for the line of rigidity at the major axis of wild-type cells. Since it is not the cell wall in isolation, identification of the component(s) at play will be difficult. It is still possible that CcmA, or more likely the cytoplasm-to-PG complex of which CcmA is a part, is responsible. To address this, we need to uncouple any potential mechanical effect of CcmA with its contribution to crosslinking regulation; perhaps we could engineer a dominant negative form of CcmA as was successful for studying crescentin (Cabeen *et al.*, 2009). However, several properties of CcmA do not seem to be consistent with the major axis rigidity. First, CcmA is present as puncta or very short arcs, rather than as a single cell-spanning filament. CcmA is enriched at the major axis but is still found at other sites of the sidewall. If this major axis rigidity is responsible for the inverse relationship between length and width, then it is also mysterious how CcmA in the straight rod mutant Δ*csd6* could behave analogously to how it functions in wild-type, particularly given that it is enriched at the opposite Gaussian curvature in Δ*csd6*.

We do not, however, have any other evidence to suggest that there is a cell-spanning filament at the major axis in *H. pylori*. CcmA is the only known cytoskeletal protein that is a non-essential, non-redundant contributor to cell shape. The coiled-coil rich proteins have been reported to be essential for helical cell shape in *H. pylori* (Waidner *et al.*, 2009, Specht *et al.*, 2011), but we observed no cell shape defect in either individual deletion strains (Yang *et al.*,

2019) or in a strain with all reported Ccrps knocked out (Chapter 3, Figure 3.11). Furthermore, we have seen no evidence of a cell-spanning filament in TEM or SEM images that we have collected. However, many non-pylori *Helicobacter* species have one or multiple helical cell-spanning filaments. Perhaps these filaments also exist in *H. pylori*, but just have yet to be identified and are not readily apparent in electron micrographs. Investigations in other *Helicobacter* species may prove fruitful.

4.6 AN UNEXPECTED TWIST

As a result of discussions with our collaborator Erkin Kuru about the discrepancy between the D-Ala-alk and MurNAc-alk curvature enrichment patterns, we fluorescently labeled the global distribution of penta- and tetrapeptides in the cell wall (Kuru *et al.*, 2019). At the time, I thought that the discrete ribbon of tetrapeptides at the major helical axis would be the most astonishing observation we would make about *H. pylori* cell shape. However, a short time later, I labeled tetrapeptides in a panel of our cell shape mutants and saw a helical ribbon of tetrapeptides wrapping around the body of the straight rod mutant Δ*csd5*. Here was a piece to the puzzle that we didn't know we were missing and could never have even imagined. Suddenly, so many observations clicked into place for me.

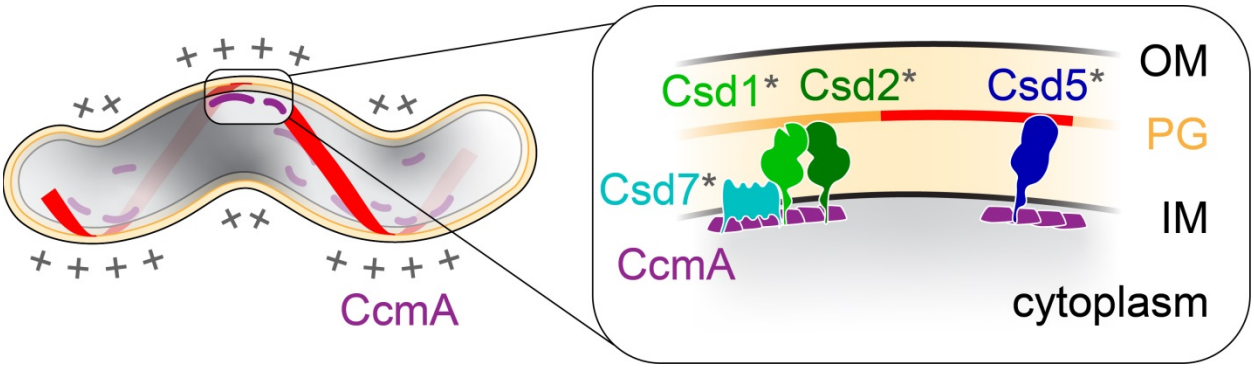

Figure 4.1. An emerging model for helical cell shape maintenance.

Diagram of a Gram-negative *H. pylori* cell (left) depicting the helical tetrapeptide ribbon (red) at the major axis. + represents enhanced rates of PG synthesis. Gold line = PG. Purple arcs = CcmA. Right: zoomed-in view of the region around the tetrapetide region, including shape proteins confirmed or predicted (denoted by asterisk) to localize preferentially to the major helical axis.

The following is an explanation of the working model I currently favor for helical cell shape (Figure 4.1). *H. pylori* forms a blueprint for helical shape that does not require an existing helical shape. This blueprint is patterned into the composition of the cell wall itself by active PG remodeling by the carboxypeptidases Csd6 and Csd4. Csd6 and Csd4 trim tetrapeptides to tripeptides and tripeptides to dipeptides, respectively. Therefore, Csd6 and Csd4 activity must be excluded from the region of the cell wall that will be the helical blueprint. It is still a very open question how this PG modification might be spatially restricted. Despite the shared straight-rod phenotype of Δ*csd4* and Δ*csd5* (Sycuro *et al.*, 2012) and in vitro data suggesting that Csd4 and Csd5 interact (Kim *et al.*, 2014), there is no in vivo indication of an interaction between Csd4 and Csd5 (Blair *et al.*, 2018), suggesting the presence of at least two separate shape systems. Because the global PG composition in Δ*csd5* cells is indistinguishable from that of wild-type and because a helical tetrapeptide ribbon is still present, I propose that the role of Csd5, which has no known enzymatic activity, is to read the helical ribbon blueprint and coordinate local enhanced PG synthesis. In support of this hypothesis, Kris Blair demonstrated that Csd5 is predicted to have a short cytoplasmic N-terminal tail, a single membrane-spanning helix, and a periplasmic domain that includes a bacterial SH3 domain. He showed that the Csd5 SH3 domain interacts with PG and that Csd5 co-purifies with CcmA and MurF, a PG precursor synthase (Blair *et al.*, 2018). By testing the interaction between the SH3 domain and purified sacculi of a few select shape mutants, Kris also demonstrated, though not quantitatively, that the amount of SH3

domain that pellets with sacculi directly correlates with the abundance of tetrapeptides in the cell wall. Additionally, Sophie Sichel has demonstrated that in vitro, fluorescently-labeled SH3 domain binds to a ribbon at the major helical axis of purified wild-type sacculi. It still remains to be definitively demonstrated that tetrapeptides rather than tripeptides are the actual species that Csd5 recognizes. Loss of either Csd6 or Csd4 results in straight-rod cells; why do muropeptides need to be trimmed down to dipeptides for the helical ribbon blueprint to be functional?

The second half of the model is far more speculative. The remaining major non-redundant, non-essential cell shape contributors are the endopeptidases Csd1 and Csd3; the catalytically-inactive endopeptidase Csd2, which is essential for Csd1 stability (Yang *et al.*, 2019); the transmembrane protein Csd7; the bactofilin CcmA; and the lytic transglycosylases Slt and Mlt. Sycuro, et al. reported that Δ*csd1*, Δ*csd2*, and Δ*ccmA* share similar, curved-rod morphologies and nearly identical global muropeptide compositions, which differ significantly from that of wild-type (Sycuro *et al.*, 2010). When I began this work, it was unclear how CcmA, which is predicted to reside in the cytoplasm, would share a phenotype with Csd1 and Csd2, which are present in the periplasm. Desiree Yang identified Csd7, an integral membrane protein essential for helical shape that interacts with Csd1, Csd2, and CcmA and links these proteins (Yang *et al.*, 2019). Csd7 also stabilizes Csd1; congruously, the global muropeptide composition of Δ*csd7* is comparable to that of Δ*csd1*. While there is now a known connection between CcmA in the cytoplasmic compartment and Csd1 in the periplasmic compartment, it is still unclear how loss of CcmA, which does not impact Csd1 protein levels, could alter the PG composition. One possibility is that CcmA activates Csd1 enzymatic activity.

Helical pitch is greatly increased in the Δ*csd1* mutant, indicating that cell twisting is greatly reduced (Sycuro *et al.*, 2010). The model I favor is that Csd1-3, Csd7, and CcmA work together

at the major axis to promote helical twist, and may even be present in complex with Csd5 and MurF. A putative mechanism for twist promotion is that CcmA filaments, linked to the cell wall via Csd1, 3, and 7 and/or Csd5 may exert mechanical force on the wall because of twist inherent to the filament. Purified CcmA forms helical bundles and skewed lattices in vitro (Taylor *et al.*, 2020). Locally trimming crosslinks could relieve this mechanical strain, resulting in strand-strand slippage to relax the filament that could generate twist, and that twist could get cemented into the cell wall by new PG synthesis. Clearly, much more work remains to test these speculations.

Interestingly, though they have the same enzymatic activity, there is only partial redundancy between Csd1 and Csd3. Csd3 has been shown to also have weak D-D-carboxypeptidase activity on pentapeptide monomers in vitro (Bonis *et al.*, 2010) The Δ*csd3* strain is polymorphic: cells are straight, gently-curved, tightly coiled, or even some combination of curvature on a single cell. There is, however, strain variability, and challenging work remains to untangle the contributions of these endopeptidases to shape maintenance. Notably, I discovered that deletion of *csd1* and *csd3* is synthetically lethal (although a knockout of both was erroneously reported; that strain is only a *csd3* knockout and phenocopies the published Δ*csd3* strain (Sycuro *et al.*, 2010)). I was able to recover one putative suppressor mutant, which has a severe morphological defect. Future investigations into *csd1*, *3* suppressors could help elucidate how these proteins contribute to both shape maintenance and cell survival.

There are a number of additional proteins that modulate helical parameters, but at this time, we lack nearly any information upon which we can reasonably base speculations. It is, however, appealing to imagine a mechanism for fine-tuning helical shape properties by means of the

balance between rates of PG synthesis at the major axis and perhaps rates of synthesis and/or turnover at the minor axis area.

With the helical blueprint model, results of an additional experiment finally made sense. Our collaborators created a small molecule inhibitor of Csd4, and we showed that it causes cells to straighten gradually and uniformly over the course of several doublings (Liu *et al.*, 2016). Later, I performed a wash out of Csd4 inhibitor in a culture of cells that I had straightened with inhibitor. I diluted the culture several times over the course of 48 hours to keep the cells growing exponentially. I had anticipated that cells would uniformly and gradually become curvier until reaching the initial wild-type shape. In contrast, the recovering population had a bimodal distribution, even at 48 hours. It appeared that there was a particular step necessary for recovery, but that after that step was achieved, cells rapidly recovered helical shape. I propose that re-establishment of the helical blueprint is the rate-limiting step, and once the ribbon is created, recovery of helical shape is a rapid process. Future experiments with the Csd4 inhibitor and tetrapeptide labeling should help reveal how the tetrapeptide ribbon is established, and experiments in which Csd5 is induced in straight cells and PG synthesis patterning is characterized before and after induction should help validate that enhanced PG synthesis at the ribbon is necessary for helical shape.

4.7 MOVING FORWARD: OUTSTANDING BIG SHAPE QUESTIONS

The results of recovery from the Csd4 inhibitor set the stage to address a second fascinating question about helical shape. Up to this point, we have focused solely on how a cell maintains helical shape, given a helical shape to begin with. However, early work in the lab clearly demonstrated that helical shape was not a prerequisite for being helical: cell shape mutants, even straight rods, could be complemented to yield a helical population. Recovery from the Csd4

inhibitor or modulation of cell shape protein expression (once we have an inducible system working in our strain) is one route for investigating helical cell shape generation. However, in both of these situations, cells would already be starting with at least a rod shape. An even more extreme challenge for cell shape generation is to recover from an amorphous shape. A talented undergraduate, Mitchell Dumais, studied how different cell wall synthesis-perturbing antibiotics influenced *H. pylori* shape. We were hoping to find a drug that could specifically perturb helical shape. While there may have been some modulation of width at sub-MIC levels a couple hours after treatment, across the board, these antibiotics caused *H. pylori* to form a "ball and whiskers" phenotype that eventually ended up looking like a round cell (Figure 4.2, first three panels). One possibility is, given that the cell wall is highly porous and elastic, it likely does not take too much of a defect in the cell wall to cause a catastrophic failure of cell wall integrity. After damage to the cell wall induced by antibiotic treatment, the cytoplasm may extrude out of the cell wall - the whiskers would be the highly-compressed remnant of the cell wall. Mitchell then washed out the antibiotics from a treated wild-type population and observed that helical cells can eventually be recovered, but that growth as a range of forms, from amorphous to branched rods, occurs in the early stages of recovery (Figure 4.2, right panel). There is a multitude of follow-up experiments using these systems that will be able to help uncover all of the rules comprising the amazingly robust helical shape generation program.

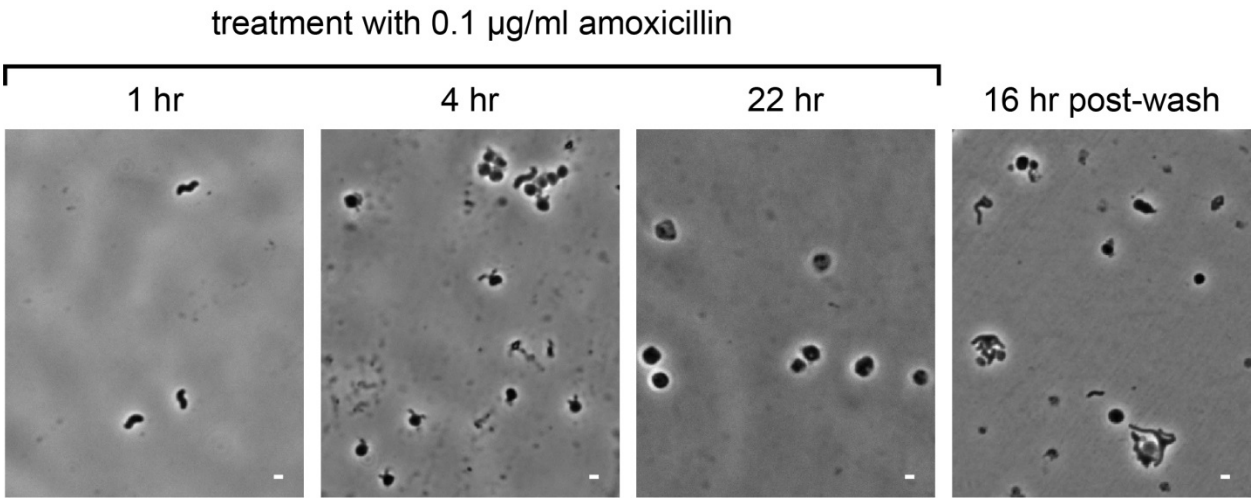

Figure 4.2. *H. pylori* undergoes morphological transitions following treatment with amoxicillin and after wash-out of amoxicillin.

Phase contrast images of wild-type *H. pylori* 1, 4, and 22 hours following treatment with 0.1 µg/ml amoxicillin (left three panels, respectively). Phase contrast image of a population of wild-type *H. pylori* treated with 0.1 µg/ml amoxicillin for 12 hours then grown for 16 hours after washing out the antibiotic (right panel). Scale bar = 1 µm.

Of the three contributors to shape maintenance we initially considered, the role of cell wall turnover remains an open question. It will take additional software and microscopy developments to build the tools necessary to determine if there are differential rates of turnover at the major vs. minor helical axis. In the field, total fluorescence quantification along the major and minor axes was used to ask if differential rates of PG turnover occur in *Vibrio cholerae*. Though technically a helical organism, *V. cholerae* cells are short enough to be treated as a curve and to define these axes in 2D. This approach is not amenable to study turnover in our highly-twisted *H. pylori* cells. Thus, the helical axes on each cell would have to be discretely determined. Also, cells would need to be imaged using a microscope appropriate for absolute fluorescence quantification. Finally, this type of analysis assumes that there is not super-twisting of the cell body. The prerequisite experiment for this analysis would have to determine if PG that

starts on the major or minor axis stays on the major or minor axis, or if it twists around the circumference as the cell elongates.

A common question we are asked is why *H. pylori* is a right-handed helix. Despite studying many cell shape mutants with a variety of phenotypes, we have never observed any left-handed helical cells. Does a cell-spanning filament drive helical handedness? Does CcmA? Does chirality of PG insertion (Wang *et al.*, 2012)? Relatedly, why is there such significant morphological heterogeneity in an isogenic wild-type population? While still the minority of the population, straight cells are observed far more frequently than random mutagenesis could explain. Of the helical cells in the population, there is notable variation in helical pitch and radius, though not in cell diameter (Figure 2.3). This variability seems inconsistent with a cell-spanning filament, whose structural properties would presumably dictate fixed helical shape parameters.

H. pylori is a fascinating organism for studying cell shape, partially because it is so different from other model organisms used to understand how bacterial cell shapes are generated and maintained. But given how different *H. pylori* is from these other organisms, is there a benefit to the field at large of studying shape in *H. pylori*, or are we just spending time on an interesting but largely irrelevant edge case? Within the Epsilonproteobacteria, there does seem to be moderate conservation of the contributors to shape of the curved members of the class. However, Csd5 has not been reported to be conserved outside *H. pylori* and *H. acinonychis*, but it may have a homologue in *Campylobacter jejuni* (Emilisa Frirdich, personal communication). However, preliminary labeling of *Campylobacter jejuni* shows the presence of a faint but discernible tetrapeptide ribbon at the major axis. Perhaps there are other adapter proteins capable of reading the helical blueprint, and conservation of the shape program at large. Studying shape in *H. pylori*

is incredibly beneficial to the shape field at large, not just to the subset of curved-rod organisms. As an organism that naturally has a broad distribution of curvatures but also retains the core machinery for dispersed growth straight rod maintenance, *H. pylori* is an excellent model for clarifying putative curvature-sensing mechanisms. MreB is a perfect example: there has been rigorous debate as to whether MreB has a particular curvature preference and if curvature enrichment is direct or simply a consequence of MreB motion along a roughly circumferential trajectory. We have already shown that MreB is clearly enriched at negative Gaussian curvature in wild-type *H. pylori*. Live cell studies will help to unravel MreB dynamics in *H. pylori* and contribute substantially to the field at large.

4.8 CONCLUDING THOUGHTS

At the beginning of most presentations or publications about *Helicobacter pylori* cell shape, we articulate that *H. pylori*'s shape is important, and is in fact part of the organism's very name. While it is of course logical to emphasize the utilitarian connection between form and function, it is equally valuable to marvel at the fundamental beauty of this organism. In pursuing scientific discoveries, we seek to improve the lives of those around us. Indeed, studying *H. pylori* cell shape could lead to the development of novel therapeutics to help more efficiently treat infection, and that is a lofty goal. But in seeking to improve the lives around us, should we not both help preserve life and also enrich it? We often act as if we must justify doing basic science by explaining that it could lay the foundation for concrete applications in the future, but this is a great injustice to the immediate value of our work. My aunt once asked me about my research goals, which led her to bluntly ask if it would make any difference at all if I didn't manage to figure out new things about how *H. pylori* keeps its helical shape. I have come to realize by stumbling upon completely unexpected mechanisms that *H. pylori* uses for shape maintenance

that the answer is yes, because the world would be decidedly less beautiful and much less awe-inspiring if we can't understand how *H. pylori* achieves its particular form, most beautiful and most wonderful.

4.9 BIBLIOGRAPHY

Blair, K.M., Mears, K.S., Taylor, J.A., Fero, J., Jones, L.A., Gafken, P.R., Whitney, J.C., and Salama, N.R. (2018) The *Helicobacter pylori* cell shape promoting protein Csd5 interacts with the cell wall, MurF, and the bacterial cytoskeleton. *Mol Microbiol* **110**: 114-127.

Bonis, M., Ecobichon, C., Guadagnini, S., Prevost, M.C., and Boneca, I.G. (2010) A M23B family metallopeptidase of *Helicobacter pylori* required for cell shape, pole formation and virulence. *Mol Microbiol* **78**: 809-819.

Cabeen, M.T., Charbon, G., Vollmer, W., Born, P., Ausmees, N., Weibel, D.B., and Jacobs-Wagner, C. (2009) Bacterial cell curvature through mechanical control of cell growth. *EMBO J* **28**: 1208-1219.

Kim, H.S., Kim, J., Im, H.N., An, D.R., Lee, M., Hesek, D., Mobashery, S., Kim, J.Y., Cho, K., Yoon, H.J., Han, B.W., Lee, B.I., and Suh, S.W. (2014) Structural basis for the recognition of muramyltripeptide by *Helicobacter pylori* Csd4, a D,L-carboxypeptidase controlling the helical cell shape. *Acta Crystallogr D Biol Crystallogr* **70**: 2800-2812.

Kuru, E., Hughes, H.V., Brown, P.J., Hall, E., Tekkam, S., Cava, F., de Pedro, M.A., Brun, Y.V., and VanNieuwenhze, M.S. (2012) *In situ* probing of newly synthesized peptidoglycan in live bacteria with fluorescent D-amino acids. *Angew Chem Int Ed Engl* **51**: 12519-12523.

Kuru, E., Radkov, A., Meng, X., Egan, A., Alvarez, L., Dowson, A., Booher, G., Breukink, E., Roper, D.I., Cava, F., Vollmer, W., Brun, Y., and VanNieuwenhze, M.S. (2019) Mechanisms of Incorporation for D-Amino Acid Probes That Target Peptidoglycan Biosynthesis. *ACS Chem Biol* **14**: 2745-2756.

Liang, H., DeMeester, K.E., Hou, C.W., Parent, M.A., Caplan, J.L., and Grimes, C.L. (2017) Metabolic labelling of the carbohydrate core in bacterial peptidoglycan and its applications. *Nat Commun* **8**: 15015.

Liu, Y., Frirdich, E., Taylor, J.A., Chan, A.C., Blair, K.M., Vermeulen, J., Ha, R., Murphy, M.E., Salama, N.R., Gaynor, E.C., and Tanner, M.E. (2016) A Bacterial Cell Shape-Determining Inhibitor. *ACS Chem Biol* **11**: 981-991.

Siegrist, M.S., Whiteside, S., Jewett, J.C., Aditham, A., Cava, F., and Bertozzi, C.R. (2013) (D)-Amino acid chemical reporters reveal peptidoglycan dynamics of an intracellular pathogen. *ACS Chem Biol* **8**: 500-505.

Specht, M., Schatzle, S., Graumann, P.L., and Waidner, B. (2011) *Helicobacter pylori* possesses four coiled-coil-rich proteins that form extended filamentous structures and control cell shape and motility. *J Bacteriol* **193**: 4523-4530.

Sycuro, L.K., Pincus, Z., Gutierrez, K.D., Biboy, J., Stern, C.A., Vollmer, W., and Salama, N.R. (2010) Peptidoglycan crosslinking relaxation promotes *Helicobacter pylori*'s helical shape and stomach colonization. *Cell* **141**: 822-833.

Sycuro, L.K., Wyckoff, T.J., Biboy, J., Born, P., Pincus, Z., Vollmer, W., and Salama, N.R. (2012) Multiple peptidoglycan modification networks modulate *Helicobacter pylori*'s cell shape, motility, and colonization potential. *PLoS Pathog* **8**: e1002603.

Takeuchi, S., DiLuzio, W.R., Weibel, D.B., and Whitesides, G.M. (2005) Controlling the shape of filamentous cells of *Escherichia coli*. *Nano Lett* **5**: 1819-1823.

Taylor, J.A., Bratton, B.P., Sichel, S.R., Blair, K.M., Jacobs, H.M., DeMeester, K.E., Kuru, E., Gray, J., Biboy, J., VanNieuwenhze, M.S., Vollmer, W., Grimes, C.L., Shaevitz, J.W.,

and Salama, N.R. (2020) Distinct cytoskeletal proteins define zones of enhanced cell wall synthesis in *Helicobacter pylori*. *eLife* **9**.

Waidner, B., Specht, M., Dempwolff, F., Haeberer, K., Schaetzle, S., Speth, V., Kist, M., and Graumann, P.L. (2009) A novel system of cytoskeletal elements in the human pathogen *Helicobacter pylori*. *PLoS Pathog* **5**: e1000669.

Wang, S., Furchtgott, L., Huang, K.C., and Shaevitz, J.W. (2012) Helical insertion of peptidoglycan produces chiral ordering of the bacterial cell wall. *Proc Natl Acad Sci U S A* **109**: E595-604.

Yang, D.C., Blair, K.M., Taylor, J.A., Petersen, T.W., Sessler, T., Tull, C.M., Leverich, C.K., Collar, A.L., Wyckoff, T.J., Biboy, J., Vollmer, W., and Salama, N.R. (2019) A Genome-Wide *Helicobacter pylori* Morphology Screen Uncovers a Membrane-Spanning Helical Cell Shape Complex. *J Bacteriol* **201**.

VITA

Jennifer Ann Taylor was born and raised in Florence, Alabama. In 2010, she graduated *magna cum laude* with high honors from the University of Georgia with a Bachelor of Science in Microbiology; Cellular Biology; and Biochemistry and Molecular Biology. During her undergraduate career, she studied *Acinetobacter baylyi* in the laboratories of Dr. Ellen Neidle and Dr. Cory Momany. After completing her undergraduate studies, she began her graduate studies in the Microbiology Department at the University of Washington. She performed her graduate thesis work in the laboratory of Dr. Nina Salama at the Fred Hutchinson Cancer Research Center focused on mechanisms of helical cell shape maintenance in *Helicobacter pylori*. She received her doctoral degree in 2020.